



A University of Sussex DPhil thesis

Available online via Sussex Research Online:

<http://sro.sussex.ac.uk/>

This thesis is protected by copyright which belongs to the author.

This thesis cannot be reproduced or quoted extensively from without first obtaining permission in writing from the Author

The content must not be changed in any way or sold commercially in any format or medium without the formal permission of the Author

When referring to this work, full bibliographic details including the author, title, awarding institution and date of the thesis must be given

Please visit Sussex Research Online for more information and further details

**Functional analysis of motor neuron disease-associated mutations in
TAR DNA-binding protein 43 and cytoplasmic dynein heavy chain 1**

Muruj Asaad Barri

Doctor of Philosophy in Biochemistry

University of Sussex

January 2015

Acknowledgement

I would like to express my gratitude to everyone who contributed distinctly to my PhD life.

First and foremost I would like to thank Dr Majid Hafezparast who significantly contributed to my research and gave me the opportunity to contribute some knowledge to the research field. From him, I learnt so much about scientific research. I would like to express my gratitude for his constructive criticism, productive advice, patience, and encouragement throughout the course.

I would like to thank my laboratory members Ryan green and Fabio Simoes for their useful discussions, support and unconditional help.

I thank my husband, Faisal Ali. He was always around during all the good and bad times, looking after our children during my time in the laboratory. He encouraged me with words and concrete acts. Without his help, I would never have been able to complete my research.

I would like to thank my parents for their eternal support. Without their unreserved help, I would never have been able to reach this position in my life.

Special thanks go to Doris Teutsch for her help and support wholeheartedly during my write-up. I would also like to thank my best friends, Hanan Ali and Randa Al-Haidary and my cousin Safinaz Barri. Hanan and Randa, for their encouraging words. Safinaz, for her constant support and attention throughout my life.



My research was generously funded by the
Saudi Arabia Ministry of Higher Education

“Thank you”

Contents	Page
Chapter 1: Introduction	
1. The central nervous system	1
2. Motor neuron diseases (MND).....	5
2.1 Diseases of upper and lower motor neurons	5
2.1.1 Amyotrophic lateral sclerosis (ALS)	5
2.1.2 Clinical features of ALS and its treatment	5
2.1.3 ALS pathology.....	10
2.1.3.1 Protein aggregate.....	10
2.1.3.2 Aberrant RNA metabolism	12
2.1.3.3 Oxidative stress	12
2.1.3.4 Glutamate excitotoxicity	13
2.1.3.5 Mitochondrial dysfunction.....	13
2.1.3.6 Impaired axonal transport.....	13
2.1.3.7 Neurofilament aggregation	14
2.1.3.8 Gliosis.....	15
2.1.3.9 Neurotrophin depletion	15
2.1.4 Molecular genetics of ALS	15
2.1.4.1 SOD1	16
Structure and function	16
SOD1 mouse models	21
The role of SOD1 in ALS.....	21
2.1.4.2 C9ORF72 and its role in ALS	24
2.1.4.3 TDP-43.....	25
Structure and function	25
The role of TDP-43 in ALS.....	29
TDP-43 mouse models	30
TARDBP knockout mouse models	36
TDP-43 transgenic mouse models.....	36
The F210I TDP-43 mutant mouse model.....	41
2.1.4.4 Peripherin.....	41
Structure and function	41
The role of peripherin in ALS.....	44
2.1.4.5 EAAT2.....	45

2.2 Diseases of upper motor neurons	46
2.2.1 Hereditary spastic paraplegia	46
2.3 Diseases of lower motor neurons	48
2.3.1 Distal hereditary motor neuropathies.....	48
2.3.2 SMA.....	50
2.3.2.1 SMA-LED and its molecular genetics	50
2.3.2.1.1 Molecular motors.....	51
Kinesins	51
Myosin	54
Dynein.....	56
The cytoplasmic dynein 1-interacting partners.....	59
2.3.2.1.2 Cytoplasmic dynein heavy chain mutation in human diseases.....	61
Arg399Gly	61
2.3.2.1.3 Cytoplasmic dynein heavy chain mutation in mouse models.....	64
<i>Loa</i> (Legs at odd angles).....	64
<i>Cra1</i> (Cramping-1).....	67
<i>Swl</i> (Sprawling).....	67
2.3.2.1.4 Dynein functions	67
2.3.2.1.4.1 Intracellular trafficking and axonal transport.....	67
2.3.2.1.4.2 Degradative pathways.....	68
2.3.2.1.4.3 Endocytic pathways.....	69
Growth factors and their signalling cascades.....	70
Brain derived neurotrophic factor.....	70
Epidermal growth factor (EGF) signalling cascade	74
2.3.2.1.4.4 Axonal pathfinding and growth dynamics	75
Migration in non-neuronal cells.....	75
Migration in neuronal cells	83
The structure of growth cones.....	83
The role of actin dynamics in growth cone motility	83
Microtubules in growth cones	86
Growth cone dynamics and axon outgrowth	87
Focal adhesion proteins	88
Focal adhesion kinase (FAK)	88
Paxillin	96

3. Research	104
Chapter 2: Materials and Methods	
2.1 Genotyping.....	107
2.1.1 DNA preparation from mouse tail biopsies	107
2.1.2 Genotyping TDP-43A315T transgenic mice	107
2.1.3 Genotyping SOD1G93A transgenic mice	107
2.1.4 Genotyping TDP-43 ^{F210I} mutant mice	109
2.1.5 Genotyping <i>Loa</i> mice.....	115
2.2 Dissection and cell culture	117
2.2.1 Isolation and culture of mouse embryonic fibroblasts	117
2.2.2 Motor neuron isolation and culture	117
2.2.3 Cell assay	119
2.3 Biochemistry	119
2.3.1 Preparation of lysates from tissues	119
2.3.2 Neurofilament extraction.....	121
2.3.3 Preparation of lysates from cell culture	122
2.3.4 Determination of protein concentration.....	122
2.3.5 SDS-PAGE electrophoresis.....	123
2.3.6 Immunoblotting and analysis	123
2.3.7 Immuno-precipitation	125
2.3.8 Immunocytochemistry	125
2.3.9 Cell spreading assay	128
2.3.10 Wound healing/scratch assay	129
2.3.11 RNA extraction and cDNA preparation.....	131
2.4 Cloning and transfection	133
2.4.1 Transformation of the chemically competent cells DH5 alpha.....	133
2.4.2 Miniprep isolation of plasmid DNA	134
2.4.3 Midiprep isolation of plasmid DNA	135
2.4.4 Transfecting mammalian cells by electroporation	135
2.4.5 Replacing EGFP with m-Cherry in TRIP-Syn-G-W lentivirus plasmid and EB1 cloning.....	136
2.4.6 AdEasy mCherry- α -tubulin plasmid purification, isolation from HEK293 and preparation of high titre viral stock	140
2.5 Image acquisition and microscopy analysis.....	141
2.6 Measuring the pixel intensity of adhesion sites	141

Chapter 3: Aberrant expression of peripherin and GLT-1B in TDP-43 mouse models

3.1 Introduction	146
3.2 Investigating the expression of the peripherin splice variant per61 in TDP-43 ^{A315T} and SOD1 ^{G93A} transgenic mice.....	147
3.3 Investigating the expression of peripherin isoforms: per58, per56 and per45 in TDP-43 ^{A315T} and SOD1 ^{G93A} symptomatic mice.....	153
3.4 Increased expression of per45 and reduced stability of the 50 kDa polypeptide in non-symptomatic TDP-43 ^{A315T}	159
3.5 Significant down-regulation of the neuron-specific isoform of GLT-1 (GLT-1B) in both symptomatic and non-symptomatic TDP-43 ^{A315T} transgenic mice	161
3.6 Analysis of the neuron-expressed GLT-1B in the TDP-43 ^{+F210I} mouse strain	164
3.7 Chapter 3 summary.....	166

Chapter 4: Investigating the impact of the *Loa* mutation on MAP kinase signalling and autophagy during endocytic trafficking and nutrient deprivations

4.1 Introduction	168
4.2 Increased JNK activity in cultured motor neurons after BDNF stimulation without a significant difference between wild type and <i>Loa</i> heterozygotes.....	170
4.3 Aberrant p38 activation in <i>+Loa</i> starved motor neurons.....	172
4.4 C-Fos induction is ERK1/2-dependent.....	175
4.5 Altered levels of LC3-II in <i>Loa</i> heterozygous motor neurons during starvation and stimulation with BDNF	177
4.6 Reduced levels of LC3-II in <i>Loa</i> heterozygous motor neurons after bafilomycin A1 treatment.....	179
4.7 Chapter 4 summary.....	181

Chapter 5: Investigating the Impact of Mutations in Cytoplasmic Dynein on Growth Cone Remodelling and Axonal Outgrowth

5.1 Introduction	183
5.2 Aberrant focal adhesions in <i>Loa/Loa</i> MEFs	184
5.3 The immuno-precipitation of paxillin with dynein intermediate chain	190
5.4 Reduced paxillin phosphorylation at Tyr118 in <i>Loa/Loa</i> MEFs.....	193
5.5 <i>Loa/Loa</i> MEFs exhibit migration defects	197
5.6 Abnormal microtubule cytoskeleton in growth cones of <i>+Loa</i> motor neurons	200
5.7 Live cell imaging of m-Cherry-microtubules in MEFs	203
5.8 Analysis of microtubule dynamic instability in lamellipodia of wide type and <i>Loa/Loa</i> MEFs	205

5.8 Chapter 5 summary.....	207
Chapter 6: Discussion	
6.1 Investigating the effect of TDP-43 mutation A315T on RNA metabolism of peripherin and GLT-1 and their roles in ALS pathology (Chapter 3)	209
6.1.1 GLT-1 expression in Prp-TDP-43 ^{A315T} transgenic mouse model (Figure 3.8 and 3.9)	209
6.1.2 GLT-1B expression in the TDP-43 ^{+/-F210I} mutant mouse (Figure 3.10)	211
6.1.3 Per61 expression in SOD1 ^{G93A} , Prp-TDP-43 ^{A315T} transgenic and wild type mice (Figure 3.1 and 3.3)	211
6.1.4 Per45 expression in Prp-TDP-43 ^{A315T} transgenic mouse model (Figure 3.4)	212
6.1.5 The 50 kDa polypeptide (Figure 3.5)	214
6.2 Investigating the signalling cascade underlying c-Fos activation during starvation and BDNF stimulation (Chapter 4, Figure 4.2, 4.3 and 4.4).....	214
6.2.1 Autophagy during starvation (Chapter 4, Figure 4.5 and 4.6)	218
6.2.3 Autophagy in the absence of bafilomycin A1 (Chapter, Figure 4.5)	218
6.2.4 Autophagy in the presence of bafilomycin A1 (Chapter4, Figure 4.6)	219
6.3 Focal adhesions in <i>Loa/Loa</i> MEFs (Figure 5.1).....	220
6.4 Immuno-precipitation of paxillin with dynein intermediate chain (Figure 5.4).....	220
6.5 Paxillin phosphorylation in <i>Loa/Loa</i> MEFs and in DYNC1H1 ^{R399G} human fibroblasts (Figure 5.5 and 5.6)	220
6.6 Microtubule stability in +/- <i>Loa</i> growth cones (Figure 5.8)	221
6.7 Conclusion.....	225
References	226

Publications

Garrett, Caroline A, Muruj Barri, Anna Kuta, Violetta Soura, Wenhan Deng, Elizabeth M C Fisher, Giampietro Schiavo, and Majid Hafezparast. 2014. "DYNC1H1 Mutation Alters Transport Kinetics and ERK1/2-cFos Signalling in a Mouse Model of Distal Spinal Muscular Atrophy." *Brain : A Journal of Neurology* 137 (7) (July): 1883–93.

Lists of figures and tables

Figures

1.1 The internal structure of the spinal cord.....	2
1.2 Affected descending pathways in motor neuron diseases.....	4
1.3 Underlying pathogenic mechanisms that lead to demise of motor neurons in ALS.....	20
1.4 The protein structure of TDP-43.....	28
1.5 The protein structure of TDP-43 with ALS-associated mutations.....	31
1.6 Peripherin gene and protein structure.....	43
1.7 Distal wasting and weakness of dHMN patient legs.....	48
1.8 Schematic diagram of the human cytoplasmic dynein heavy chain 1.....	52
1.9 Phylogenetic tree and domain structure of mouse kinesin genes.....	53
1.10 Schematic diagram of the motor proteins kinesin and non-muscle myosin II.....	55
1.11 Schematic diagram of the human cytoplasmic dynein 1 complex.....	58
1.12 Schematic diagram of the dynactin complex.....	62
1.13 Microtubule plus end binding proteins.....	63
1.14 <i>Loa</i> mouse model exhibiting hindlimb grasping when the mouse is suspended by the tail.....	66
1.15 Schematic diagram of cytoplasmic dynein heavy chain 1 with mutations.....	66
1.16 BDNF/TrkB-mediated ERK1/2 activation signalling pathways.....	73
1.17 Interplay between dynamic actin filaments and myosin II to promote the leading edge advance.....	76
1.18 Differential pattern of FA assembly and disassembly and how this affects actin flow distribution.....	79
1.19 Schematic diagram of the leading edge growth.....	81
1.20 Growth cone structure.....	84
1.21 Schematic diagram of actin filament dynamics in the growth cone.....	85
1.22 Growth cone dynamics and axon outgrowth.....	89
1.23 FAK functional domains.....	90
1.24 Multiple signalling pathways that implicate FAK upon integrin activation.....	95
1.25 Domain structure of paxillin α	98

1.26 Signalling pathway involving Src, ERK, paxillin and FAK upon HGF receptor activation.....	102
2.1 Genotyping the TDP-43 ^{A315T} transgenic mouse.....	108
2.2 Genotyping the SOD1 ^{G93A} transgenic mouse.....	110
2.3 Schematic diagram showing genotyping of TDP-43 ^{F210I} using multiplex PCR.....	113
2.4 Sequence of the mouse <i>Tardbp</i> gene showing the annealing sites of primers.....	114
2.5 Gel electrophoresis showing bands produced from the multiplex PCR using the outer primers and the inner wild type or inner mutant specific primers.....	114
2.6 Part of the cytoplasmic dynein heavy chain gene sequence <i>Dync1h1</i> showing the primer annealing sites as well as <i>RsaI</i> restriction sites.....	115
2.7 Gel electrophoresis of wild type, +/- <i>Loa</i> and <i>Loa/Loa</i> PCR products after digesting with <i>RsaI</i>	116
2.8 Sequential extraction of neurofilaments from mouse lumbar spinal cords.....	122
2.9 Setting up the microscope stage for capturing an image with the plate being in the same position.....	130
2.10 Gel electrophoresis of purified total RNA using a column based method.....	133
2.11 Designing m-Cherry and EB1 primers for cloning into the TRIP-Syn-G-W lentivirus plasmid.....	138
2.12 Vector map of the 2 nd generation TRIP-Syn-m-Cherry-EB1 lentivirus plasmid.....	139
2.13 Freeze-thaw-vortex cycles for virus extraction.....	143
2.14 High throughput focal adhesion quantification.....	144
3.1 Expression of per61 in SOD1 ^{G93A} , TDP-43 ^{A315T} and wild type mice.....	148
3.2 DNA contamination test performed on cDNA samples.....	150
3.3 Expression of per61 at protein level.....	152
3.4 Up-regulation of per45 in symptomatic TDP-43 ^{A315T} transgenic mice.....	155
3.5 Change in stability of per56 and the 50 kDa polypeptide in the SOD1 ^{G93A} and TDP-43 ^{A315T} transgenic mice	156
3.6 No change in the stoichiometric ratio between peripherin isoforms in P3.....	158
3.7 Per45 expression level in non-symptomatic TDP-43 ^{A315T} mice.....	160
3.8 GLT-1 expression level in TDP-43 ^{A315T} transgenic mice.....	162
3.9 GLT-1B expression level in TDP-43 ^{A315T} transgenic mice.....	163

3.10 Increased levels of GLT-1B in TDP-43 ^{+F210I} mouse model.....	165
4.1 Levels of pc-Fos and pERK1/2 in motor neurons.....	169
4.2 Increased active JNK levels in BDNF-stimulated motor neurons.....	171
4.3 Increased levels of active p38 in +/-Loa during serum-starvation.....	173
4.4 c-Fos activation is ERK1/2 dependent.....	176
4.5 LC3-II levels in non-starved, starved and BDNF-stimulated motor neurons.....	178
4.6 LC3-II levels after bafilomycin A1 treatment	180
5.1 Aberrant focal adhesions in <i>Loa/Loa</i> MEFs.....	186
5.2 Analysis of point contacts in growth cones of +/-Loa versus wild type motor neurons.....	188
5.3 Impaired lamellipodia formation in <i>DYNC1H1</i> ^{R399G/R399G} human fibroblasts.....	189
5.4 Immuno-precipitation of paxillin with dynein intermediate chain in migrating and non- migrating cells.....	191
5.5 Reduced levels of paxillin phosphorylation Tyr118 (p-paxillin) in <i>Loa/Loa</i> MEFs.....	194
5.6 Reduced levels of p-paxillin in <i>DYNC1H1</i> ^{R399G} human fibroblasts.....	196
5.7 Migration is defect in <i>Loa/Loa</i> MEFs.....	198
5.8 Microtubule depletion in the P-domain of +/-Loa growth cones of motor neurons.....	201
5.9 Abnormal microtubule bundling in <i>Loa/Loa</i> MEFs.....	204
5.10 Analysis of microtubule dynamic instability in lamellipodia of wild type and <i>Loa/Loa</i> MEFs.....	206
6.1 Proposed model of signalling pathways underlying c-Fos activation in motor neurons upon serum starvation or stimulation with BDNF.....	217
6.2 Possible mechanisms underlying the effects the <i>Loa</i> mutation has on microtubule stability.....	224

Tables

1.1 Examples of various types of motor neuron diseases.....	6
1.2 UMN and LMN symptoms and signs in ALS.....	10
1.3 Proteins involved in axonal transport and affected by ALS-associated CHMP2B mutations.....	14
1.4 fALS causative genes.....	17

1.5 Causative genes in sALS.....	19
1.6 SOD1 mouse models with various mutations.....	22
1.7 Summary of TDP-43 mouse models.....	32
1.8 HSP-caused mutations.....	47
1.9 dHMN-causative genes.....	49
1.10 Cytoplasmic dynein 1-interacting partners.....	59
1.11 Paxillin binding partners at adhesion sites.....	99
2.1 Genotyping primer sequences for the TDP-43 ^{A315T} transgenic mouse.....	107
2.2 Genotyping primer sequences for the SOD1 ^{G93A} transgenic mouse.....	109
2.3 Sequences of genotyping primers of the mutant TDP-43 F210I	111
2.4 Pattern of band intensity expected from multiplex PCR for genotyping TDP-43 ^{F210I} mice.....	112
2.5 Primer sequences for genotyping the <i>Loa</i> mouse.....	115
2.6 Expected band sizes produced after <i>RsaI</i> restriction digestion of the PCR products of wild type, +/ <i>Loa</i> and <i>Loa/Loa</i>	116
2.7 The components of motor neuron culture medium as well as complete L-15 medium	118
2.8 Proteins of interest for immunoblotting.....	124
2.9 Antibodies for immunoblotting.....	127
2.10 Antibodies for immunocytochemistry.....	129
2.11 The primer sequences for mRNAs of interest.....	132
2.12 Antibiotics and their recommended concentration according to the type of plasmids.....	134
2.13 Electroporation parameters for transfecting MEFs with plasmid DNA.....	136
2.14 Primers for cloning m-Cherry and EB1 into the TRIP-Syn-G-W lentivirus plasmid.....	137
2.15 Microscopes and parameters for fixed-cell images.....	141

Abbreviations used in this study:

ALS	Amyotrophic lateral sclerosis
Akt	Protein kinase B
aPKC	Atypical protein kinase C
apoA-II	Apolipoprotein A-II
ASAP1	ArfGAP with SH3 domain, ankyrin repeat and PH domain 1
BDNF	<i>Brain-derived neurotrophic factor</i>
BICD1	Bicaudal D1
CadTK	Calcium-dependent tyrosine kinase
Cak β	Cell adhesion kinase beta
Cas	Crk-associated substrate
Cdc	Cell division control
CFTR	Cystic fibrosis transmembrane conductance regulator
C3G	Crk SH3-domain-binding guanine-nucleotide-releasing factor
CREB	cAMP response element-binding
Crk	CT10 (chicken tumor virus number 10) regulator of kinase
CrkL	Crk-like
CNS	Central nervous system
CSF	Cerebrospinal fluid
Csk	C-Src kinase
CTNF	Ciliary neurotrophic factor
DENN	Differentially expressed in normal and neoplastic cells
DAG	Diacylglycerol
DHC	Dynein heavy chain 1
DIC	Dynein intermediate chain
DLC	Dynein light chain
DLIC	Dynein light intermediate chain
DOCK	Dedicator of cytokinesis
EGFR	Epidermal growth factor receptor
ELMO	Engulfment and cell motility

ERK	Extracellular signal related kinases
FAK	Focal adhesion kinase
fALS	Familial ALS
FRNK	FAK-related nonkinase
FA	Focal adhesion
GDNF	Glial cell-derived neurotrophic factor
GEF	guanine nucleotide exchange factor
Grb2	Growth factor receptor-bound protein 2
HAP1	<i>Huntingtin-associated protein 1</i>
HGF	Hepatocyte growth factor
HIV	Human immunodeficiency virus
hnRNPs	Heterogeneous nuclear ribonucleoproteins
iCLIP	individual-nucleotide resolution Cross-Linking and ImmunoPrecipitation
IGF-1	Insulin-like growth factor 1
IP3	Tris-phosphate
JNK	c-Jun N-terminal kinase
LIM	lin-11, isl-1 and mec-3
LMN	Lower motor neuron
LIS1	Lissencephaly
MAPK	Mitogen-activated protein kinases
MC	Monoclonal
MEFs	Mouse embryonic fibroblasts
MND	Motor neuron disease
MT	Microtubule
MTOC	Microtubule organization centre
NGF	Nerve growth factor
NT3	Neurotrophin 3
NT4	Neurotrophin 4
NudE	Nuclear distribution protein E
NUM1	Nuclear migration 1

PAK	p21 GTPase-activated kinase (Kinase that is activated by GTPase such as Rho activates PAK)
p57 ^{NTR}	pan-neurotrophin receptor
PAEC	Porcine aortic endothelial cell
PBS	Paxillin binding subdomain
PC	Polyclonal
PI3K	Phosphoinositide-3-kinase
PIX	PAK-interacting exchange factor
PKC	Protein kinase C
PKL	Paxillin-kinase linker (Arf GAP)
PLC	phospholipase C
Pyk2	Proline-rich tyrosine kinase 2
RAFTK	Related adhesion focal tyrosine kinase
Rap1	Rhoptry-associated protein 1
RT	Room temperature
RTK	Receptor tyrosine kinases
sALS	Sporadic ALS
SC	Spinal cord
Shc	Src homology 2 domain-containing
SNP	Single nucleotide polymorphism
SOS	Son of sevenless
Trk	Tropomyosin-related kinase
UMN	Upper motor neuron

Abstract

Amyotrophic lateral sclerosis (ALS) and spinal muscular atrophy with lower extremity predominance (SMA-LED) are two forms of motor neuron diseases at the opposite ends of the age spectrum, with ALS being mainly an adult-onset progressive and fatal neurodegenerative disease, and SMA-LED being a childhood-onset neuromuscular disease, manifested by muscle weakness, joint contracture, abnormal gait, and in some cases combined with intellectual disability. This thesis represents my research on the role of mutant forms of two proteins, namely Tar-DNA binding protein 43 (TDP-43) and cytoplasmic dynein heavy chain 1 (DYNC1H1) in the pathogenesis of ALS and SMA-LED, respectively.

TDP-43 – an RNA/DNA binding protein – has been implicated in ALS. The function of TDP-43 in the nucleus is to regulate RNA processing, including RNA splicing and editing. Abnormal expression of the peripherin splice variant per61 has been found in transgenic mouse models of ALS. In addition, aberrant expression of EAAT2 (excitatory amino acid glutamate transporter 2) protein has been reported in some ALS cases. Thus, I investigated splicing of peripherin and GLT-1 (the murine homologue of EAAT2) RNAs, as potential targets of TDP-43 and examined whether mutations in TDP-43 alter the expression levels of the genes encoding the two proteins. My data show that per61 is expressed in wild type mice at both RNA and protein levels. This suggests a role for this isoform in the assembly of peripherin filaments. Moreover, overexpression of TDP-43^{A315T} increases the expression level of per45 (an alternative translated isoform of peripherin) and leads to the instability of the filament network. Analysis of GLT-1B, the neuronal splice variant of GLT-1, reveals significant down-regulation in TDP-43^{A315T} transgenic mice, indicating impaired RNA processing of GLT-1B. Collectively, these data show that the expression of peripherin and EAAT2 is regulated by TDP-43, and that aberrant expressions of these two genes caused by TDP-43 mutations could have a role in the pathology of ALS.

A Phe580Tyr mutation in the mouse gene *Dync1h1* impairs growth factor-induced endocytic trafficking in *Dync1h1*^{+/F580Y} mouse motor neurons, resulting in aberrant activation of extracellular-signal-related kinases 1 and 2 (ERK1/2) and phosphorylation of the immediate early gene *c-Fos*. My data show that the induction of c-Fos upon

serum starvation and/or growth factor stimulation is ERK1/2 dependent and that the mitogen-activated protein kinase p38 is also likely to be involved in c-Fos activation during starvation. Moreover, the activation of autophagy is reduced in *Dync1h1*^{+/F580Y} motor neurons, suggesting a role for cytoplasmic dynein in autophagy induction/formation.

In addition, the *Dync1h1*^{F580Y/F580Y} mouse embryonic fibroblasts (MEFs) exhibit a defect in cell migration, as manifested by a delayed wound closure and reduced levels of paxillin phosphorylation at Tyr118 (p-paxillin). They also show abnormal and increased number of focal adhesions in spreading assays. Interestingly, human SMA-LED *DYNC1H1*^{R399G/R399G} fibroblasts show defective lamellipodia formation, as well as reduced levels of p-paxillin. Moreover, *Dync1h1*^{+/F580Y} mouse motor neurons show a defect in exploratory microtubules in the peripheral domain of their growth cones. As the molecular mechanism of growth cone motility is analogous to that found in fibroblasts, the molecular pathogenesis of SMA-LED caused by mutations in cytoplasmic dynein heavy chain 1, is likely to involve impaired growth cone development and axonal pathfinding, which could be exacerbated by the aberrant endocytic trafficking and signalling in mutant motor neurons.

Chapter 1

Introduction

1. The central nervous system

The central nervous system (CNS) consists of seven basic components: cerebrum, diencephalon, midbrain, pons, cerebellum, medulla and spinal cord (Purves et al. 2008). The medulla, pons and midbrain are, together, called the brainstem which acts as a passageway for the neuronal fibres that extend between the upper and lower neurons. The diencephalon and the cerebral hemispheres are called the forebrain, whereas the cerebellum and brainstem form the hindbrain. The brainstem contains several nuclei (group of cell bodies) of which many belong to the cranial nerves. Extending from the brainstem is the spinal cord which is surrounded by the vertebral column. The spinal cord can be divided into five regions, namely: cervical, thoracic, lumbar, sacral and coccygeal. The spinal nerve (peripheral nerve) emerges from the spinal cord towards the periphery where it innervates muscles. It connects with the spinal cord through the ventral and dorsal roots which contain axons of motor neurons and sensory neurons respectively (Figure 1.1). The dorsal root ganglion is an organ located along the spinal nerves and contains a cluster of sensory cell bodies which project their axons to the spinal nerve and the spinal cord. The spinal cord consists of two types of tissue, the grey matter and the white matter. The grey matter is divided into three parts named the ventral (anterior), the dorsal (posterior) and the lateral horn. The dorsal horn contains axons of sensory neurons whereas the ventral horn contains cell bodies of motor neurons. The axons of sensory neurons synapse with motor neurons either directly (Figure 1.1, in blue and red respectively) or through inter-neurons (Figure 1.1, in purple).

Neurons which are located in the primary motor cortex, control movements through descending pathways (Carlson 2012; Siegel and Sapru 2010). The pathways can be divided into the lateral and the ventromedial group, which are named according to their location in the white matter of the spinal cord. These pathways are composed of two neuronal groups: upper motor neurons and lower motor neurons (Monkhouse 2007). The upper motor neurons can only be found in the CNS and their cell bodies are located in the motor cortex (Bhatnagar 2001). Their axons travel through the brainstem towards the ventral horn of the spinal cord where they synapse with the lower motor neurons.

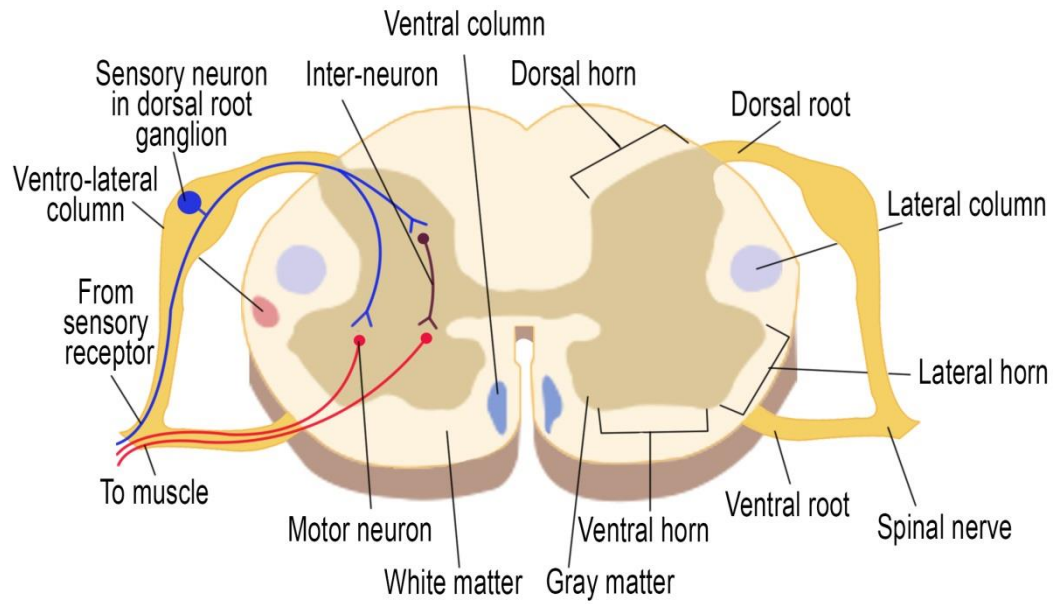
Figure 1.1

Figure 1.1 - The internal structure of the spinal cord. Note: adapted from (Purves et al. 2008) with modifications.

The lower motor neurons' cell bodies are located in the CNS and they extend their axons to the peripheral nervous system where they innervate muscles. The aforementioned cell bodies are found in two regions of the CNS: 1) in the cranial nerve motor nuclei of the brainstem and 2) in the ventral horn of the spinal cord. With regard to the descending pathways, the lateral group is comprised of the corticospinal, corticobulbar and rubrospinal tracts (Carlson 2012; Siegel and Sapru 2010). These tracts are responsible for controlling fine movements, as well as independent movements of limbs (e.g. moving the right hand in a different direction than the left hand). The ventromedial group consists of the reticulospinal, the vestibulospinal, the tectospinal and the ventral corticospinal tracts. Of relevance to motor neuron diseases are the corticospinal and the corticobulbar tracts from the lateral group and the ventral corticospinal tracts from the ventromedial group. Thus, the discussion of this thesis will focus on only these three tracts.

The corticospinal tract which is comprised of axons of cortical neurons, arises from the primary motor cortex, where their cell bodies are located and terminates in the grey matter of the spinal cord (Carlson 2012; Siegel and Sapru 2010). The axons extend through the white matter of the motor cortex, descending through the forebrain, midbrain, pons, and the medulla. The majority of axons cross to the contralateral spinal cord at the juncture between medulla and spinal cord, leading to the formation of the lateral corticospinal cord. They either directly synapse, or synapse through interneurons with the spinal motor neurons. These motor neurons are located in the gray matter of the lateral horn and innervate muscles of distal extremities such as hands, arms, fingers, lower legs, feet and toes (Figure 1.2, the light blue tract). The remaining fibres continue descending through the ipsilateral spinal cord (the ventral corticospinal tract). The axons of the ventral corticospinal tract also synapse with motor neurons on both sides of the grey matter of the ventral horn and thus innervate muscles of the upper legs and trunk (Figure 1.2, the dark blue neurons). The corticobulbar tract also starts in the motor cortex, originates in the region that is responsible for controlling the face and tongue, and terminates in the motor nuclei in the brainstem (bulbar) (Figure 1.2, the green tract). The corticobulbar tract is

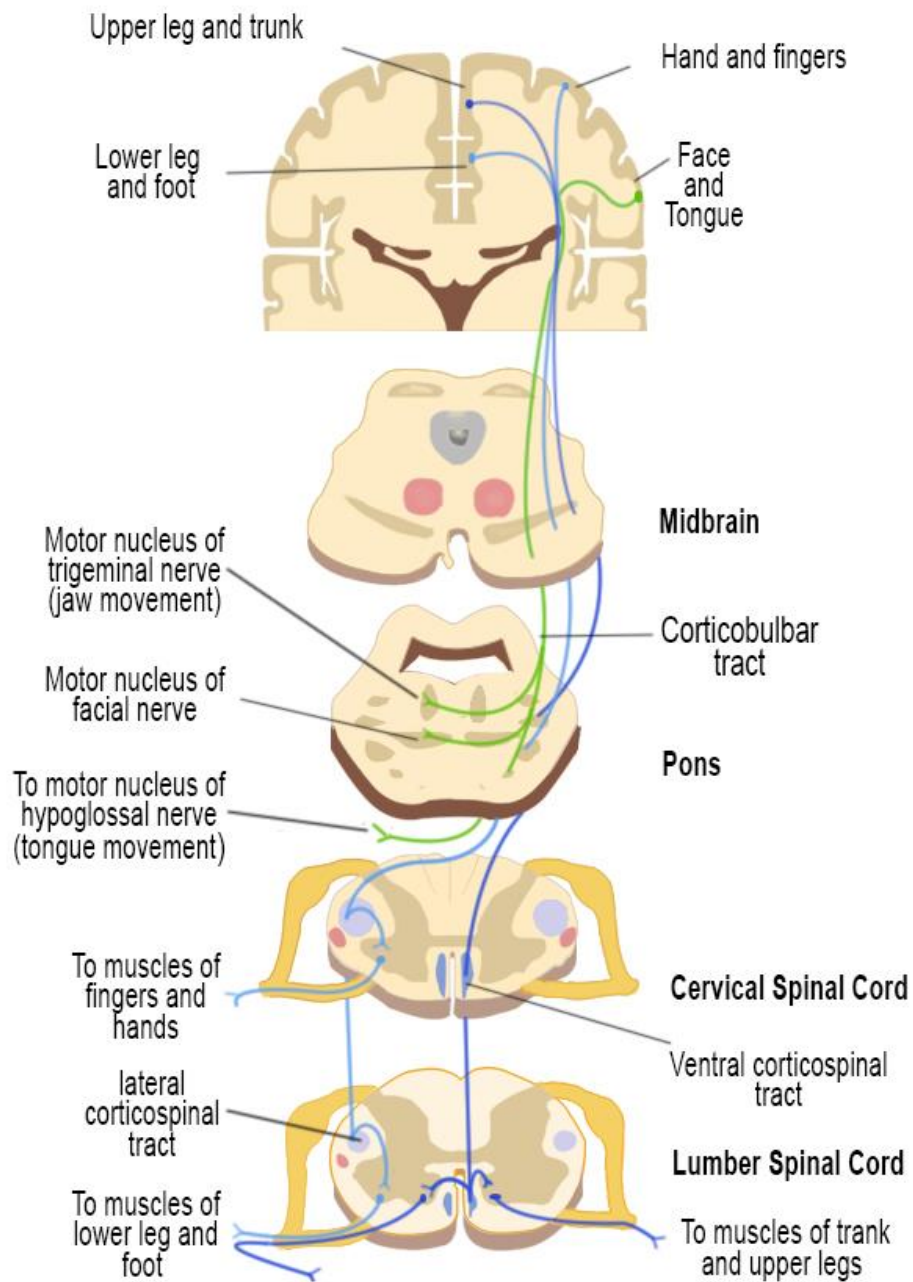
Figure 1.2

Figure 1.2 – Affected descending pathways in motor neuron diseases. The Figure shows the corticospinal and the corticobulbar tracts from the lateral group (light blue and green tracts respectively) and the ventral corticospinal tracts from the ventromedial group (dark blue tract). Note: image adapted from (Carlson 2012).

responsible for controlling the movement of the face, neck, tongue and some extraocular eye muscles.

2. Motor neuron diseases (MND)

Motor neuron diseases (MND) are neurological disorders characterized by motor neuron degeneration leading to muscle weakness and atrophy. Table 1.1 shows examples of several motor neuron diseases and their differentiating symptoms. Two forms of MNDs will be focused on in this thesis: Amyotrophic lateral sclerosis, the most common form of MND and Spinal muscular atrophy with lower extremity predominance (SMA-LED).

2.1 Diseases of upper and lower motor neurons

2.1.1 Amyotrophic lateral sclerosis (ALS)

Amyotrophic lateral sclerosis is the most common form of motor neuron degeneration affecting upper motor neurons (cerebral cortex) and lower motor neurons (brainstem and spinal cord), leading to fatal paralysis (OMIM #105400) (Renton, Chiò, and Traynor 2014; Robberecht and Philips 2013). There are two types of ALS: familial ALS and sporadic ALS. The majority of ALS cases are sporadic (sALS), while 10% are familial (fALS). The familial ALS is predominantly autosomal dominant. There are, however, rare cases of familial ALS which are X-linked or recessive.

2.1.2 Clinical features of ALS and its treatment

ALS is characterized by muscle atrophy (amyotrophic) causing muscle weakness and fasciculation manifested in the lower motor neurons (LMN). Lateral sclerosis describes the hardened state of the lateral column in the spinal cord that was found in autopsy specimens (Ferguson and Elman 2007). ALS is a late onset progressive disorder which commonly affects people between the age of 55-65. Ten percent of ALS cases show variant symptoms of either LMN manifestations (spinal muscular atrophy) or signs of degeneration in the upper motor neurons (UMN).

Table 1.1

	MND	Overview of disease characteristics	Ref.
UMN and LMN	Amyotrophic lateral sclerosis (ALS) (Lou Gehrig's disease)	Late onset, rapidly progressive. Asymmetrical weakness of extremities, muscle fasciculation and cramps, bulbar signs: dysphagia and dysarthria. (see Table 1.2 for more details)	(Ferguson and Elman 2007)
	ALS with frontotemporal dementia (FTD)	FTD symptoms: loss of vision and volition, distractibility, social disinhibition and cognitive impairment (e.g. difficulty with planning and attention)	(Kinsley and Siddique 2012)
UMN only	Primary lateral sclerosis (PLS)	Late onset, slowly progressive. Primary motor neuron loss, weakness and spasticity in one lower limb (asymmetrical onset) and bulbar affect (dysarthria followed by dysphagia), pseudobulbar affect (uncontrolled emotion e.g. sudden crying), no LMN signs.	(Singer et al. 2007)
	Hereditary spastic paraplegia (HSP)	Early childhood onset, genetically and clinically heterogeneous. Progressive spasticity and weakness in lower limbs. Pure HSP: spastic paraplegia, bladder spasticity and mildly impaired sensations. Complicated HSP: lower limb spasticity associated with other neurological or non-neurological diseases (e.g. intellectual disability and deafness respectively).	(Noreau, Dion, and Rouleau 2014; Lo Giudice et al. 2014)
LMN only	Distal hereditary motor neuropathies (dHMN)	Early adulthood onset, autosomal dominant, slowly progressive. LMN weakness or degeneration in the ventral horn of spinal cord, distal muscle wasting and weakness, reduced or no reflex response.	(Rossor et al. 2012)

Table 1.1 Cont.

	MND	Overview of disease characteristics	Ref.
LMN only	Progressive muscular atrophy (PMA)	LMN loss, prominent weakness and atrophy, no UMN signs.	(Cervenakova et al. 2000)
	Monomelic amyotrophy (MMA) (Hirayama disease)	Non-progressive. Muscle wasting and weakness in upper limb (can be bilateral), affects young males.	(Kiernan, Lethlean, and Blum 1999)
	Multifocal motor neuropathy (MMN)	Slowly progressive. No sensory involvement, asymmetric muscle weakness in upper limb.	(Ferguson and Elman 2007)
	Spinal muscular atrophy (SMA)	Onset ranges from before birth to early adulthood. Progressive, familial, autosomal recessive. LMN loss in spinal cord and brainstem, proximal muscle wasting and weakness (symmetrical).	(Prior and Russman 2013; Zanetta et al. 2014)
	Spinal and bulbar muscular atrophy (SBMA) (Kennedy's disease)	Late onset, slowly progressive, affects only males. Fasciculation of the tongue, lips or perioral region; dysphagia, dysarthria, proximal muscle weakness of the limbs, muscle spasms; no UMN signs.	(Spada 2011; Katsuno et al. 2012)
	Spinal muscular atrophy with lower extremity predominance (SMA-LED)	Congenital or early childhood onset, autosomal dominant, non-progressive or slowly-progressive motor neuron degeneration. Walking delay, waddling walk, difficulty climbing stairs, muscle weakness and wasting of proximal lower limb muscles, mild cognitive disability, no sensory involvement.	(Harms et al. 2012)

Table 1.1 Cont.

	MND	Overview of disease characteristics	Ref.
LMN only	Progressive bulbar palsy (PBP)	Progressive. Affects the motor nuclei in brainstem (bulbar motor neuron loss), dysphagia, dysarthria, tongue fasciculation, abnormal accumulation of secretions.	(Talacko and Reade 1990)
Motor and sensory	Charcot–Marie–Tooth (CMT) disease also known as Hereditary motor and sensory neuropathy (HMSN)	Genetically and clinically heterogeneous, slowly progressive. Spinal nerve involvement, muscle wasting of the toe, lower leg, forearm, and hand, Pes cavus foot deformity, sensory loss of the lower and upper extremities.	(Bucci, Bakke, and Progidia 2012)

Table 1.1 - The Table shows examples of various types of motor neuron diseases. MNDs are classified according to the affected cell type: combined Upper Motor Neuron (UMN) and Lower Motor Neuron (LMN), UMN only, LMN only and combined motor and sensory involvement.

However, the majority of patients with ALS almost always show a combination of upper and lower motor neuron manifestations. In the 10% of ALS cases where patients only show signs in either LMN or UMN, later autopsies then reveal that in fact both LMN and UMN were affected. Approximately two thirds of patients with limb onset experience asymmetrical muscle wasting and weakness which might be preceded by fasciculation or cramps (Wijesekera and Leigh 2009). Later, most patients develop bulbar symptoms and ultimately respiratory symptoms. The atrophic limbs may develop spasticity which affects manual dexterity and gait. In later stages, patients may develop flexor spasms (bending of a limb upward towards the body). People affected by ALS with bulbar onset, usually experience dysarthria, yet rarely dysphagia. Most patients with bulbar onset also develop sialorrhoea (hypersalivation) due to difficulty in saliva swallowing. Most patients also present with simultaneous development of limb symptoms, as well as bilateral facial weakness. Pseudobulbar symptoms (such as emotional lability and excessive yawning) were also observed in a significant number of patients. Up to 5% of ALS cases experience respiratory weaknesses without having significant limb or bulbar symptoms. Table 1.2 shows UMN and LMN symptoms and signs which ALS patients develop. The disease progresses to paralysis, leading to death as a result of respiratory failure. From the onset of the first symptoms, the average survival time is two to three years for sALS with bulbar onset and three to five years for patients with limb onset (Wijesekera and Leigh 2009). The average incidence rate of sALS in 1990 was 1.89 per 100,000/year in Europe and North America and the average prevalence was 5.2 per 100,000 (Worms 2001). Logroscino et al (2010) reported an incidence rate of ALS in 1998 and 1999 which was 2.16/100,000 per year for the total European population (all age groups in UK, Italy and Ireland) and which was 2.7/100,000 for the European population who are 18 years old or older (Logroscino et al. 2010).

ALS is incurable and riluzole is the only drug that has been shown to prolong the life span of patients (Wijesekera and Leigh 2009). Riluzole acts by blocking the sodium channels and thus inhibiting the release of glutamate from pre-synaptic terminals, as well as by increasing the glutamate uptake from the synaptic cleft (Fumagalli et al. 2008).

Table 1.2

	UMN	LMN
	Bulbar	
Symptoms	Dysphagia , spastic dysarthria, Laryngospasm, pseudobulbar affect, cheek biting	Difficulty chewing, sialorrhea, dysphagia, slurred speech, hoarseness
Signs	Poor palate movement, slow tongue movement, Jaw jerk, Palmomental sign, active facial reflex	Facial weakness, tongue weakness, tongue atrophy, facial/tongue fasciculation
	Limb	
Symptoms	Stiff, slow movement, clonus triggered by movement	Weakness, cramps
Signs	Spasticity, Hyperreflexia, spastic gait, pathologic reflexes (Babinski, Hoffman's)	Weakness, muscle atrophy, fasciculation, Hyporeflexia
	Axial	
Symptoms	Unsteadiness	Head drop/difficulty holding up Trouble standing erect
Signs	Absent abdominal reflexes	Neck extensor weakness, bent spine, abdominal protuberance
	Respiratory	
Symptoms	_____	Dyspnea, orthopnea, morning headache, daytime sleepiness, confusion
Signs	_____	Tachypnea, reduced volume of speech, use of accessory muscles, abdominal paradox

Table 1.2 - The Table shows UMN and LMN symptoms and signs in ALS. Note: Adapted from (Ferguson & Elman 2007).

2.1.3 ALS pathology

2.1.3.1 Protein aggregate

Cytoplasmic inclusions have been found in many neurodegenerative disorders e.g. Alzheimer's, Parkinson's, Huntington's, prion, and Pick's disease. They are formed by the abnormal accumulation of aberrant misfolded proteins (protein aggregates) in the neuronal cytoplasm. The accumulation of these protein aggregates results in selective

neuronal death in an age-dependent manner. It has been thought that these aggregates might trigger cellular stress which in turn compromises various cellular functions including cytoskeletal organization, intracellular transport, proteasome machinery, and mitochondrial function. Such cellular stress would result in axonal retraction (a dying-back neuronal phenotype) and consequently in neuronal death. In patients with ALS, protein aggregates were also observed in the cytoplasm of affected motor neurons and it is one of the hallmarks of ALS.

There are three types of inclusions found in lower motor neurons of the anterior horn and brainstem of patients with ALS: ubiquitinated inclusions (UBIs), Bunina bodies and hyaline conglomerate inclusions (HCLs) (Wijesekera and Leigh 2009; Piao et al. 2003). Ubiquitinated inclusions can be divided into two types of inclusions based on morphology: skein-like inclusions which have a filamentous structure and compact spherical inclusions named Lewy-like bodies. UBIs are the most specific type of inclusions and only exist in ALS, while the remaining (Bunina bodies and HCLs) can be found in other neurodegenerative disorders as well. Furthermore, UBIs were found in all studied cases of ALS which therefore is a strong indication for their significance in ALS pathogenesis. Bunina bodies are eosinophilic, approximately 2-3 μm in diameter and positively immunostained for cystatin C and transferrin. The presence of Bunina bodies was observed in lower motor neurons at rates ranging from 67% to 90.9% in various studies of ALS. In addition to their presence in lower motor neurons, they can be found in Betz cells of motor cortex as well as in subthalamic nuclei. HCLs are argyrophilic, most commonly observed in fALS and are immunostained against phosphorylated and nonphosphorylated neurofilaments.

Some pathogenic proteins were detected in cytoplasmic inclusions of ALS patients, one of which is the Cu-Zn superoxide dismutase 1 (SOD1), which was discovered in the hyaline inclusions in the spinal cord of fALS (Watanabe et al. 2001). It is an anti-oxidant enzyme that is involved in scavenging oxygen-derived superoxide radicals (O_2^-) from cells by metabolizing them to oxygen and hydrogen peroxide (see the Cu-Zn superoxide dismutase section for more details). Other pathogenic proteins were also identified in cytoplasmic inclusions (see below).

2.1.3.2 Aberrant RNA metabolism

Since 1993, *SOD1* remained the only causative gene for ALS until 2006 when TDP-43, the DNA/RNA binding protein (encoded by *TARDBP*) was identified in UBIs in both sporadic and familial ALS and in UBIs of patients with ALS-FTLD, suggesting that dysregulation of RNA metabolism might be an underlying cause of ALS (Lagier-Tourenne, Polymenidou, and Cleveland 2010; Wijesekera and Leigh 2009; Rosen et al. 1993). Two years later, mutations in the gene *TARDBP* were reported in ALS cases (Kabashi et al. 2008; Sreedharan et al. 2008). Approximately 48 causative mutations were identified which accounted for 3% of fALS and 1.5% of sALS (Lattante, Rouleau, and Kabashi 2013)(see section, molecular genetics of ALS). The following year, another RNA/DNA binding protein implicated in ALS was discovered and named “fused in sarcoma and trans located in liposarcoma” (Fus/TLS), further highlighting the emerging role of RNA metabolism in ALS. At least 50 mutations of Fus were identified which accounted for 5% of fALS and 1% of sALS (Lattante, Rouleau, and Kabashi 2013).

2.1.3.3 Oxidative stress

Oxidative stress is the term used to describe an imbalance between the production of free radicals and the antioxidant defence mechanisms (Barber and Shaw 2010). Most free radicals are formed as a result of electron leakage from the process called “electron transport chain in mitochondria”. As a result of this leakage, the amount of electrons required for the complete reduction of oxygen molecules during oxidative phosphorylation decreases. This leads to abnormal free radicals homeostasis which results in an accumulation of free radicals and ultimately cell death.

Oxidative stress is thought to be a contributory factor to neuronal death in ALS. Some ALS-causing mutations in the antioxidant enzyme *SOD1* support this hypothesis. Oxidative damaged proteins in the spinal cord, elevated levels of biochemical markers of oxidative stress, as well as lipid peroxidation in the cerebrospinal fluid (CSF) and in post-mortem tissue, were found in ALS patients (Niebrój-Dobosz, Dziewulska, and Kwieciński 2004; Wijesekera and Leigh 2009). Furthermore, fibroblasts and myoblasts derived from patients with ALS were found to be more susceptible to oxidative damage than the wild type (Aguirre et al. 1998; Bradley et al. 2009).

2.1.3.4 Glutamate excitotoxicity

Glutamate excitotoxicity is the term used to describe the neuronal injury provoked by the abnormal excessive activation of the postsynaptic glutamate receptors (Wijesekera and Leigh 2009). The presence of excess glutamate in the synaptic cleft, triggers glutamate receptor activation, which results in massive uncontrolled influx of calcium ions into the neurons and thus in neuronal cell death (Foran and Trotti 2009). The increased levels of intracellular calcium ions, cause mitochondrial stress and consequently an increase in free radical production, as mitochondria are no longer capable of maintaining accurate electron activity. Elevated levels of glutamate were found in the CSF of some groups with ALS (Shaw et al. 1995). The loss of excitatory amino acid glutamate transporter (EAAT2) was believed to cause increased levels of glutamate in CSF (Rothstein et al. 1995).

2.1.3.5 Mitochondrial dysfunction

Histological analysis performed on sALS samples revealed an abnormal morphology of mitochondria (swelling and vacuolation) in motor neurons, muscles and intramuscular nerves and in motor neurons of the transgenic mouse carrying the mutant human SOD1 (G93A) (Dal Canto and Gurney 1994; AK et al. 1966; T 1981; Siklos et al. 1996). An increased calcium level in mitochondria was observed in motor nerve terminals, whereas impaired activity of complex I and IV could be seen in muscle biopsies (Wiedemann et al. 1998; Siklos et al. 1996).

2.1.3.6 Impaired axonal transport

In humans, the length of motor neuron axons may extend up to one meter, which therefore requires an efficient intracellular transport system to ensure their survival (Wijesekera and Leigh 2009). There are two types of intracellular transport systems: anterograde and retrograde transport, which are mediated by the molecular motor proteins kinesin and cytoplasmic dynein-dynactin complex respectively. Both molecular motors utilize microtubules as tracks for transporting cargo along microtubules: dynein transports its cargo in the microtubule minus-end direction towards the soma, while kinesins transport their cargos in the plus-end direction towards the cell periphery. Defects in axonal transport are known to be a contributory

factor in motor neuron diseases such as ALS, HSP and CMT (type 2A). Transgenic mouse models of ALS harbouring human mutant SOD1 (G37R and G93A) exhibit defects in both anterograde and retrograde transport (Borchelt et al. 1998; Murakami et al. 2001, Kieran et al. 2005, PMID: 15911875). Moreover, mutations in charged multivesicular body protein 2B (CHMP2B), a protein involved in vesicular trafficking, are associated with 1% of ALS cases (Ikenaka et al. 2012; Cox et al. 2010). Gene expression data from microarray analysis performed on motor neurons with ALS-related CHMP2B mutations, showed down-regulation of proteins involved in transporting cargo along microtubules, which could indicate a defective axonal transport (see Table 1.3).

Table 1.3

Gene symbol	Protein
KIF1A	Kinesin family member 1A
KIF1C	Kinesin family member 1C
KIF5C	Kinesin family member 5C
DYNLRB1	Dynein light chain roadblock-type 1 (cytoplasmic dynein associated protein)
DYNLL2	Dynein light chain 2 (cytoplasmic dynein associated protein)
DYNC1H1	Cytoplasmic dynein heavy chain

Table 1.3 – The Table shows proteins that are involved in axonal transport and were identified to be affected by ALS-associated CHMP2B mutations.

2.1.3.7 Neurofilament aggregation

Neurofilament proteins have also been implicated in ALS pathogenesis.

Neurofilaments, as well as the intermediate filament protein peripherin (PRPH) were both the major components of the argyrophilic inclusions (spheroid) of spinal cord neurons in ALS (Corbo and Hays 1992). Furthermore, mutations in the highly conserved repeat region XKSPYK (X represents a single amino acid and Y represents one to three amino acids) of the neurofilament heavy gene (NF-H), are associated with ALS (Al-Chalabi et al. 1999).

2.1.3.8 Gliosis

Gliosis is one of the hallmarks observed in both familial and sporadic ALS. It is characterized by activation of astrocytes and microglia (Joyce et al. 2011; Wijesekera and Leigh 2009). Inflammatory cytokines which are secreted by both astrocytes and microglia, were observed in CSF or in spinal cord specimens of patients with ALS.

Gliosis was also observed in SOD1 and TDP-43 rodent models of ALS.

2.1.3.9 Neurotrophin depletion

A reduction in neurotrophic factors [brain derived neurotrophic factor (BDNF), Ciliary neurotrophic factor (CNTF), Glial cell line-derived neurotrophic factor (GDNF) and insulin-like growth factor (IGF-1)] has been observed post-mortem in the spinal cord and cerebral cortex of patients with ALS (Wijesekera and Leigh 2009). Furthermore, several studies on rodent models of ALS have implicated vascular endothelial growth factor (VEGF) in ALS and have shown that VEGF has a protective role in ALS. This was supported by two observations: 1) the expression of VEGF and VEGF receptor 2 were reduced in the spinal cord of symptomatic transgenic mice carrying the human SOD1^{G93A} and 2) the toxic effects induced by the mutant SOD1 was reduced in VEGF-treated motor neurons expressing the human SOD1^{G93A} and therefore indicating that VEGF has a protective role (Lunn et al. 2009). In addition to its role in angiogenesis and lymphangiogenesis, VEGF is a neuroprotective growth factor that stimulates axonal outgrowth, prevents neuronal apoptosis and has a role in neurogenesis (Keifer, O'Connor, and Boulis 2014; Lunn et al. 2009). In humans, there appears to be a significant association between the '-2578AA' single nucleotide polymorphism (SNP) of VEGF and the increased risk of ALS in males (Keifer, O'Connor, and Boulis 2014).

2.1.4 Molecular genetics of ALS

Approximately 150 pathogenic mutations in the *SOD1* gene are responsible for 20% of fALS and 4-5% of fALS are caused by mutations in the *TARDBP* and *FUS* genes (S. Chen et al. 2013). More than 40% of fALS are the result of mutations in the *C9ORF72* gene. The remaining are caused by mutations in the following genes: alsin, senataxin (*SETX*), spatacsin, angiogenin (*ANG*), vesicle associated membrane protein associated protein B (*VAPB*), factor induced gene 4 (*FIG4*) and optineurin (*OPTN*). Table 1.4 and 1.5 show

all the currently known causative genes in both fALS and sALS. Mutations in these genes cause malfunctions in various molecular pathways which then subsequently lead to motor neuron degeneration (Figure 1.3).

In this thesis, I will focus and elaborate on two causative genes for fALS: *SOD1* and *TARDBP* and on one gene for sALS which is *PRPH*.

2.1.4.1 SOD1

Structure and function

There are three types of superoxide dismutase proteins: SOD1, SOD2 and SOD3 which are mainly present in aerobic organisms (Levanon et al. 1985). Oxygen-enriched organisms produce reactive oxygen species (ROS) as part of their cellular metabolism and therefore require a defensive system against ROS (ZELKO, MARIANI, and FOLZ 2002). Superoxide dismutase proteins are antioxidant enzymes that catalyse the conversion of superoxide anions (O_2^-) into oxygen (O_2) and hydrogen peroxide (H_2O_2). Both SOD1 and SOD3 require two metals, Cu and Zn for their catalytic activity. While SOD1 can be found intracellularly in the cytoplasm, nucleus, lysosomes and within the intermembrane of mitochondria, SOD3 can be found extracellularly, for examples in plasma, lymph and CSF. SOD2 requires manganese as a cofactor and is located in the mitochondria. As human mutations of *SOD1* have been found to cause certain types of ALS, the following section will focus on this particular gene.

SOD1 is a 32 kD protein that functions as a homodimer. The *SOD1* gene is highly conserved among species and is located on chromosome 21 in humans and on chromosome 1 in mice.

Table 1.4 fALS causative genes

ALS form	Locus	Gene	Protein	Onset	Inheritance	Clinical feature	Estimated% of FALS
ALS1	21q22.1	<i>SOD1</i>	Cu/Zn SOD-1	Adult	AD/AR	Typical ALS	20%
ALS2	2q33-2q35	<i>Alsin</i>	Alsin	Juvenile	AR	Slowly progressive, predominantly UMN signs like limb, & facial spasticity	<1%
ALS3	18q21	Unknown	Unknown	Adult	AD	Typical ALS with limb onset especially lower limb	Unknown
ALS4	9q34	<i>SETX</i>	Senataxin	Juvenile	AD	Slowly progressive, distal hereditary motor neuropathy with pyramidal signs	Unknown
ALS5	15q15-21	<i>SPG 11</i>	Spatacsin	Juvenile	AR	Slowly progressive	Unknown
ALS6	16p11.2	<i>FUS</i>	Fused in Sarcoma	Juvenile/Adult	AD/AR	Typical ALS	4-5%
ALS7	20ptel-p13	Unknown	Unknown	Adult	AD/AR	Typical ALS	Unknown
ALS8	20q13.3	<i>VAPB</i>	VAPB	Adult	AD	Typical and atypical ALS	<1%
ALS9	14q11.2	<i>ANG</i>	Angiogenin	Adult	AD	Typical ALS, FTD and Parkinsonism	<1%
ALS10	1p36.2	<i>TARDBP</i>	DNA-binding protein	Adult	AD	Typical ALS	4-5%
ALS11	6q21	<i>FIG 4</i>	Phosphoinositide-5phosphatase	Adult	AD	Rapid progressive with prominent corticospinal tract signs	Unknown

Table 1.4 Cont.

ALS form	Locus	Gene	Protein	Onset	Inheritance	Clinical feature	Estimated% of FALS
ALS12	10p13	<i>OPTN</i>	Optineurin	Adult	AD/AR	Slowly progressive with limb onset and predominant UMN signs	<1%
ALS14	9p13.3	<i>VCP</i>	VCP	Adult	AD	Adult onset, with or without FTD	<1%
ALS15/ALSX	Xp11	<i>UBQLN2</i>	Ubiquilin 2	Juvenile/Adult	XD	ALSX UMN signs proceeding LMN signs	<1%
ALS16	9p13.2-21.3	<i>SIGMAR1</i>	SIGMAR1	Juvenile	AR	Juvenile onset typical ALS	Unknown
ALS-FTD1	9q21-22	unknown	unknown	Adult	AD	ALS with FTD	unknown
ALS-FTD2	9p21	<i>C9ORF72</i>	C9ORF72	Adult	AD	ALS with FTD	40-50%
NA	2p13	<i>DCTN1</i>	Dynactin	Adult	AD	Distal hereditary motor neuropathy with vocal paresis	unknown
NA	12q22-23	<i>DAO</i>	D-Amino Acid Oxidase	Adult	AD	Typical ALS	<1%

Table 1.4 - The Table shows the causative genes that have been identified so far in fALS. These genetic mutations represent different molecular pathways of motor neuron degeneration. Abbreviations: *VAPB* Vesicle associated membrane protein associated protein B, *VCP* Valosin Containing Protein, *SIGMAR1* Sigma Non Opioid Intracellular Receptor, *C9ORF72* Chromosome 9 open reading frame 72, *DAO* D-Amino Acid Oxidase, *FTD* Frontal-temporal dementia, AD, Autosomal dominant, AR, Autosomal recessive. Gray shaded rows represent rare cases of ALS. Note: adapted from (S. Chen et al. 2013; Robberecht and Philips 2013).

Table 1.5 Causative genes in sALS

Gene	Protein	Locus	Variant associated with ALS
<i>APEX1</i>	Apurinic Endonuclease DNA repair enzyme 1	14q11.2	SNP associations
<i>ATXN2</i>	Ataxin-2	12q24.12	Poly Q repeats
<i>CHMP2B</i>	Chromatin Modifying Protein 2B	3p11.2	Mutations
<i>HFE</i>	Haemochromatosis	6p22.2	SNP associations
<i>NEFH</i>	Neurofilament Heavy	22q12.2	Deletion and Insertions
<i>SMN1</i>	Survival Motor Neuron 1	5q12.2-q13.3	Abnormal copy number of genes
<i>SMN2</i>	Survival Motor Neuron 2	5q12.2-q13.3	Abnormal copy number of genes
<i>PON 1,2,3 e</i>	Paraoxonase	7q21.3	SNP associations and mutations
<i>PRPH</i>	Peripherin	12q13.12	mutations
<i>VEGF</i>	Vascular Endothelial Growth Factor	6p21	Promoter SNP's
<i>PGRN</i>	Progranulin	17q21.31	Deletions

Table 1.5 - The Table shows the causative genes reported in sALS. Abbreviation: SNP's, Single Nucleotide Polymorphisms; Poly Q, Polyglutamine. Note: adapted from (Chen et al. 2013).

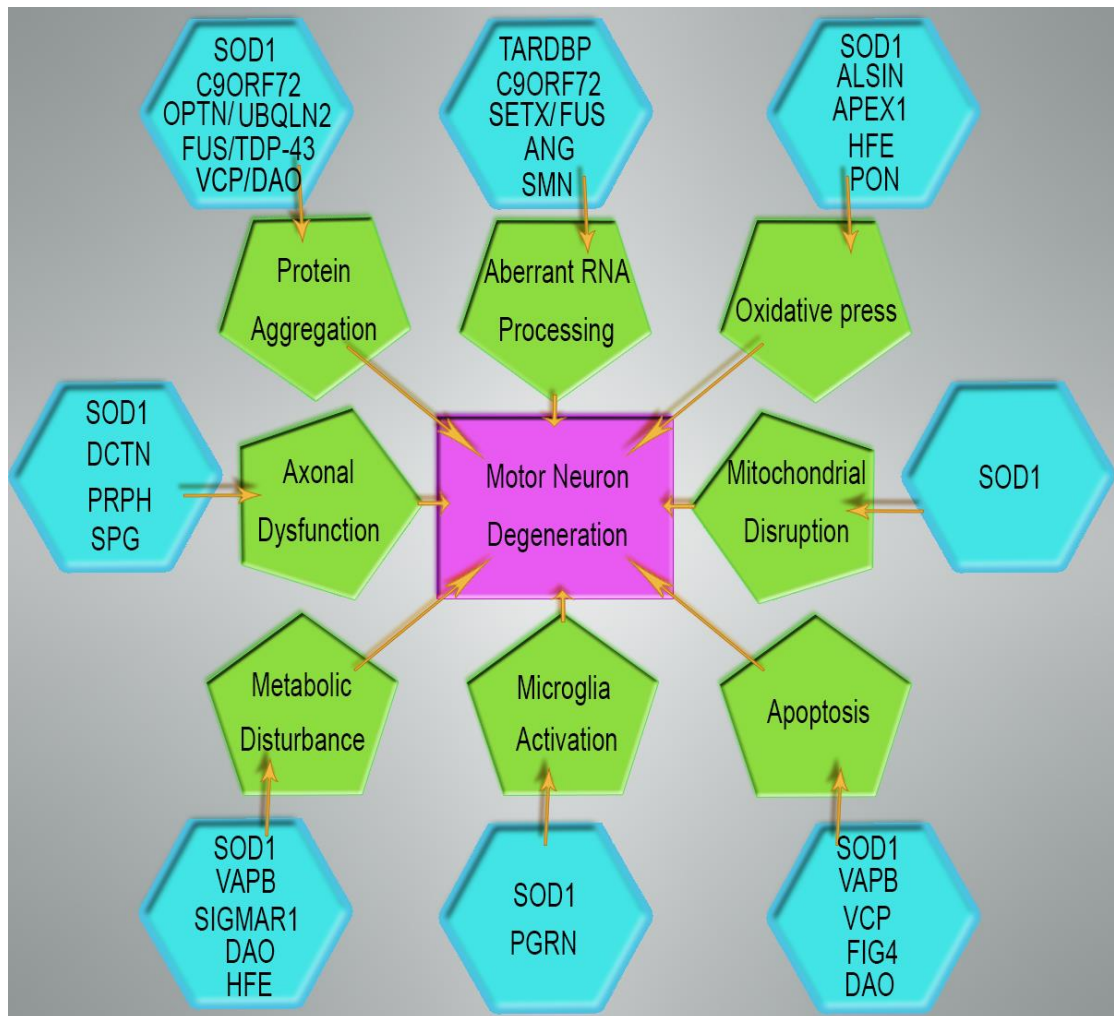
Figure 1.3

Figure 1.3 - Underlying pathogenic mechanisms that lead to demise of motor neurons in ALS. Note: adapted from (S. Chen et al. 2013) with modification.

SOD1 mouse models

In order to understand the underlying pathogenic mechanisms of ALS and how SOD1 mutations cause upper and lower motor neuron loss, mouse models were generated which display many phenotypes observed in ALS cases. In 1994, Gurney et al generated the first mouse model harbouring the mutation G93A (amino acid substitution of glycine to alanine at position 93) in the human SOD1 cDNA which had been inserted randomly into the mouse genome (Gurney et al. 1994). This transgenic mouse model, SOD1^{G93A}, has been widely used in ALS research due to exhibiting the ALS-like phenotype including autosomal dominant pattern of inheritance, gait abnormality, tremor, paralysis, gliosis, ubiquitinated SOD1 containing inclusions, swollen and vacuolated mitochondria, altered axonal transport, and axonal and motor neuron degeneration (Joyce et al. 2011). Table 1.6 summarizes SOD1 transgenic models recently reviewed by Joyce et al 2011. As can be seen from the table, mutant SOD1 mouse models exhibit slightly various pathologies depending on mutation and the level of *SOD1* transgene expression. For example, transgenic mice carrying a low (G93A^{dl}) or high copy of the human SOD1^{G93A} develop early or late onset phenotype of ALS, respectively.

The role of SOD1 in ALS

It was originally believed that the pathogenic effect of SOD1 mutations arises from toxic gain of function rather than the impairment of the antioxidant function of SOD1 (loss of function) (Julien and Kriz 2006). This stems from the fact that transgenic mice overexpressing the human mutant SOD1 (G93A, G37R or G85R) show an increased enzymatic activity and reproduce the ALS-like phenotype, whereas the SOD1 knock-out mice which have no enzymatic activity fail to develop an ALS-like phenotype. It is unlikely though that the toxic gain of function of these mutations is due to the increase in enzymatic activity, as overexpression of wild type SOD1 does not cause an ALS-like phenotype. However, recent research suggests that SOD1 loss of function might play a modifying role and therefore contribute to ALS pathogenesis (Saccon et al. 2013). Indeed, SOD1-knockout mice exhibited increased susceptibility to injury and a significant motor neuron loss compared to the wild type (Fischer et al. 2011). These

Table 1.6

Mutation	Promoter	Protein expression (fold)	Activity (fold)	Symptom onset (weeks)	Survival (weeks)	Ref.
A4V ^a	Human SOD1	nd	nd	35	48	Deng et al. (2006)
G37R	Human SOD1	nd	14	15-17	25-29	Wong et al.(1995)
H46R	Human SOD1	nd	nd	20	24	Chang-Hong et al. (2005)
H46R/H48Q	Human SOD1	nd	0	17-26	nd	Wang et al. (2002)
H46R/H48Q/H63G/H120G	Human SOD1	nd	0	35-52	nd	Wang et al. (2003)
L48V	Human SOD1	nd	nd	21-26	26-30	Tobisawa et al. (2003)
G85R	Human SOD1	1	0	35-43	37-45	Bruijn et al. (1997)
G85R	Human SOD1	1.5	nd	39.5-48	46-54	Wang et al. (2009)
G85R ^b	Mouse SOD1	nd	0	13-17	17	Ripps et al. (1995)
D90A	Human SOD1	20	6-8	52	61	Jonsson et al. (2006)
G93A	Human SOD1	17	13	13-17	17-26	Gurney et al. (1994)
G93A ^{dl}	Human SOD1	8	nd	24-26	40-50	Gurney (1997)
I113T	Human SOD1	nd	nd	52	60	Kikugawa et al. (2000)
T116X	Human SOD1	nd	nd	41	43	Deng et al. (2008)

Table 1.6 Cont.

Mutation	Promoter	Protein expression (fold)	Activity (fold)	Symptom onset (weeks)	Survival (weeks)	Ref.
L126X	Human SOD1	0-0.5 ^c	nd	28-36	nd	Wang et al. (2005)
L126Z	Human SOD1	0-1 ^c	nd	44	47	Deng et al. (2006)
L126delTT	Human SOD1	2	0	17	18	Watanabe et al. (2005)
G127X	Human SOD1	0.5-1	0	35	36	Jonsson et al. (2004)

Table 1.6 - The Table shows SOD1 mouse models with various mutations. All listed SOD1 mutations are reported in ALS cases unless stated. Superscripts: a. Double transgenic with SOD1^{wt}, b. mouse transgene, c. mRNA expression is high, protein is low, dl. G1 del-low copy. Abbreviation: nd. not described. Artificial mutations: H46R/H48Q and H46R/H48Q/H63G/H120G prevent copper binding and mutation T116X results in a truncated SOD1 protein. Note: adapted from (Joyce et al. 2011).

mice develop age dependent features (by 12-18 months), such as significant loss of grip strength and progressive distal motor neuropathy (progressive denervation in neuromuscular junction). This suggests that SOD1 plays an important role in normal neuronal function.

2.1.4.2 C9ORF72 and its role in ALS

A hexanucleotide repeat expansion GGGGCC is the most common known causative mutation for ALS so far since its discovery in 2011 (Dejesus-hernandez et al. 2011; Renton et al. 2011). These GGGGCC repeat expansions are located in the non-coding region of open reading frame 72 in chromosome 9 (C9orf72). In addition to ALS, C9orf72 has also been associated with other neurological diseases including FTD, Alzheimer's, Parkinson's, and Huntington's diseases, indicating a common pathological pathway. This further strengthens the need for understanding the molecular mechanism of disease caused by the GGGGCC repeat expansion, as well as for developing drugs to target this mutation. It is believed that GGGGCC repeat expansion causes the disease either by loss of function or by gain of function (Mizielinska and Isaacs 2014). Evidence for the former was based on findings such as reduced levels of C9orf72 transcripts in the brain of patients. Furthermore, based on homology, the structure of the C9orf72 protein is related to the DENN domain (differentially expressed in normal and neoplastic cells) containing proteins which function as Rab-activating GEFs (guanine nucleotide exchange factors) and is, therefore, involved in regulating membrane trafficking (Levine et al. 2013). Indeed, knocking down C9orf72 results in reduced endocytosis and therefore further suggesting a loss of function mechanism as a cause of the disease (Farg et al. 2014). There has been evidence indicating that the C9orf72-related disease might be caused by two gain-of-function mechanisms (Mizielinska and Isaacs 2014). In the first mechanism, the presence of RNA foci in neuronal nuclei, which contain aggregates comprised of expanded GGGGCC repeat RNA, can be observed. It has been believed that RNA foci-mediated gain of function takes place via sequestering some essential RNA-binding proteins and therefore affecting their downstream functions. The second mechanism is caused by the formation of toxic dipeptide repeat proteins generated through the translation of

repeat expansion GGGGCC transcripts. However, further studies are required to determine which pathway is responsible for neurodegeneration.

2.1.4.3 TDP-43

Structure and function

The transactive response DNA binding protein (TDP-43), 43 kDa in size, is a multifunctional protein mainly located in the nucleus which is involved in transcription, pre-mRNA splicing, RNA transport and stability, micro RNA biogenesis and DNA repair. TDP-43 is encoded by the *TARDBP* gene which is located on chromosome 1p36. The *TARDBP* gene contains 6 exons and is conserved in organisms including humans, mice, *Drosophila melanogaster*, and *Caenorhabditis elegans*. The combined information from database analysis and cDNA cloning revealed that the main transcript of TDP-43 can undergo alternative splicing in order to generate 11 splice variants. Three TDP-43 isoforms were reported and identified in the human brain and spinal cord. In addition to the full-length TDP-43 isoform (43 kDa), a second isoform exists which lacks 6 nucleotides immediately upstream the termination codon (Strong et al. 2007). The third isoform is a 28 kDa isoform which lacks the amino acid segment encoded by exon 3, as well as a significant portion of amino acids encoded by exon 6. The biological significance of the second and the third isoforms is still unknown. In 1995, TDP-43 was first identified as a protein that binds the transactive response DNA region of the HIV type 1 (the human immunodeficiency virus type 1) LTR (long terminal repeat) region. TDP-43 was shown to repress the promoter activity of the HIV LTR (Ou et al. 1995). Later, in 2001, it was discovered that TDP-43 is also involved in pre-mRNA splicing (Buratti and Baralle 2001). The first implication of TDP-43 as a splicing factor was initially reported with regard to promoting exon 9 skipping of the cystic fibrosis transmembrane conductance regulator gene (CFTR). TDP-43 was shown to preferably bind UG repeat elements at the 3' end of exon 9 and thus inhibiting its recognition by the splicing machinery, which resulted in exon 9 skipping. Further confirmation was obtained by knocking down the endogenous TDP-43, which resulted in enhancing exon 9 inclusion. A similar inhibitory role of TDP-43 for splicing was reported in exon 3 of the human apolipoprotein A-II (apoA-II) gene (Mercado et al. 2005). Deletion of TDP-43 is

embryonically lethal, reflecting the crucial multiple roles of TDP-43 in RNA processing during development (Sephton et al. 2010).

TDP-43 is structurally similar to ribonucleoproteins (hnRNPs), a group of proteins that are known to bind heterogeneous nuclear RNAs and are involved in RNA biology, including pre-mRNA splicing. Like hnRNPs, TDP-43 has two highly conserved RNA recognition motifs i.e. RRM1 and RRM2 which are involved in binding RNA and DNA, as well as in mediating protein-protein interactions (Figure 1.4). RRM1 and RRM2 are comprised of two conserved regions: an octapeptide region named RNP1 and a hexapeptide sequence called RNP2. A high degree of similarity between the aforementioned organisms was observed in a TDP-43 amino acid sequence up to the carboxyl end of RNP1 of RRM2. RRM1 is responsible for binding U/TG repeats in nucleic acids and it contains two residues i.e. Phe147 and Phe149 that are highly conserved and required for proper binding (Buratti and Baralle 2001). The N-terminal region of TDP-43 is required for the biological activity of TDP-43, since the mutant TDP-43 that lacks the amino acids 1-75, perturbs the skipping activity of exon 9 of the CFTR gene. Deletion of the first 75 amino acids of the mutant TDP-43 does not perturb its localization to nucleus. The first 75 amino acids were also found to be required for TDP-43 homodimerization which is required for binding RNA targets (Zhang et al. 2009). Zhang et al further defined the first 10 N-terminal amino acids as those required for TDP-43 exon skipping activity and homodimerization (Zhang et al. 2013). In addition, the C-terminus of TDP-43 contains a glycine-rich region which mediates the interaction of TDP-43 with other partners like hnRNPs (hnRNP A1 and hnRNP A2/B1) (Emanuele Buratti et al. 2005). Furthermore, the amino acid sequence spanning the region between 321-366 of the C-terminus of TDP-43 was found to preferentially bind hnRNP A2. This sequence is also required for its exon 9 skipping activity of the CFTR gene (D'Ambrogio et al. 2009). The glycine-rich region additionally enables the TDP-43 to go through a verifiable and controlled protein aggregation process. Such a process shows the mRNA-binding proteins' capability (such as TDP-43) to consolidate transcripts into RNA/Protein complexes, the so-called RNA granules. The RNA granules have several functions: facilitating RNA transport within neuronal processes, regulation of protein translation and RNA degradation. In addition, it was found that TDP-43 under cellular

stress, contributes to stress granule formation (SGs), which are ribonucleoprotein complexes where protein synthesis is temporarily stalled, thus stopping RNA translation and causing the RNA molecules to be stored during cellular stress (Colombrita et al. 2009). The presence of the 216-315 amino acid region, as well as RRM1 are both required for TDP-43 recruitment to SGs.

TDP-43 autoregulates its own cellular levels by directly binding to its own transcripts (Ayala et al. 2011). These RNA-binding properties of TDP-43 enable it to bind to its own 3' UTR transcripts, as well as to the amino acid residues 321 to 366. This binding of TDP-43 to its 3' UTR, does not affect the pre-mRNA splicing, but rather it promotes RNA degradation partly through the exosome. Ectopic overexpression of TDP-43 results in down-regulation of endogenous TDP-43, mediated by the TDP-43's autoregulatory system.

Although TDP-43 was mainly found in the nucleus, it also shuttles between the nucleus and cytoplasm in a transcription-dependent manner (Ayala et al. 2008). Evidence for which was confirmed by the fact that the inhibition of RNA polymerase II after treatment with actinomycin D leads to accumulation of TDP-43 in the cytoplasm. The N-terminus region of TDP-43 (at amino acid residues 82-98) contains a specific bipartite nucleus localization signal (NLS) which is comprised of two clusters of basic amino acids, separated by a sequence of 9-12 amino acids (Winton et al. 2008). NLS is required for TDP-43 entry into the nucleus. Winton et al also identified a leucine-rich TDP-43 nuclear exporting sequence spanning a region of 239-250. TDP-43 contains many potential phosphorylation sites: 41 serine, 15 threonine and 8 tyrosine amino acids, five of which are reported: Ser379, 403, 404, 409 and 410 (Gendron, Josephs, and Petrucelli 2010). TDP-43 bears three putative caspase-3 cleavage sites which generate C-terminal fragments of 42, 35 and 25 kDa (Gendron, Josephs, and Petrucelli 2010).

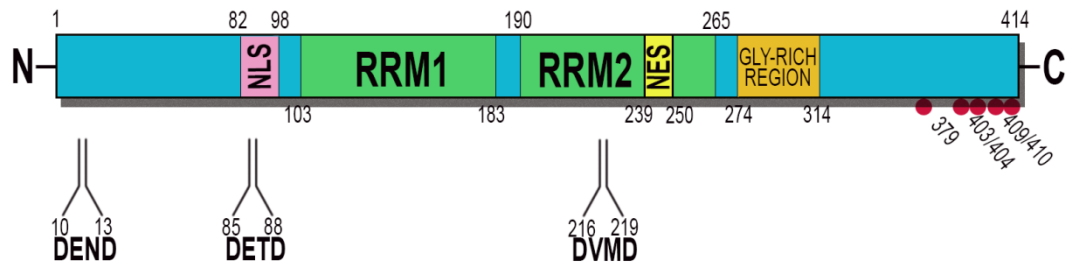
Figure 1.4

Figure 1.4 - The protein structure of TDP-43. TDP-43 consists of 414 amino acids. It contains several domains: nuclear localization signal (pink box), RRM1 and 2 (green box), nuclear exporting signal (yellow box) and glycine rich region (orange box). Red circles represent the reported serine phosphorylation sites. TDP-43 contains three putative caspase-3 cleavage sites, DEND, DETD and DVMD which generates three smaller molecular sizes of TDP-43, 42, 35 and 25 kDa respectively. Note: adapted from (Gendron, Josephs, and Petrucelli 2010).

The role of TDP-43 in ALS

TDP-43 has been implicated in several neurodegenerative disorders including FTLD and ALS. The vast majority of ALS-associated mutations have been found in the glycine rich region (Figure 1.5). TDP-43 fragmentation, phosphorylation and ubiquitination are the hallmarks of ALS. It is still unclear whether motor neuron degeneration is the result of toxic gain of function that is caused by the presence of cytoplasmic TDP-43 accumulation, or caused by loss of nuclear TDP-43 function. Nevertheless, the mechanism underlying the disease's pathology caused by TDP-43 mutations is still under investigation.

Much effort has been directed towards understanding the function of TDP-43 and thus understanding the contribution of TDP-43 mutations to the disease progression. Tollervey et al 2011 characterized the RNA targets and the binding region of TDP-43 using an iCLIP experiment performed on cortical tissues from post mortem healthy brain, as well as from brains with FTLD-TDP, neuroblastoma cells and embryonic stem cells (Tollervey et al. 2011). TDP-43 was shown to bind introns, long non-coding RNA (ncRNA) and 3' UTR of mRNAs. However, analysis of the protein binding properties of TDP-43 obtained from the brain tissues of patients with FTLD-TDP showed that there was a significant change in the binding of TDP-43 to 4 ncRNAs, 3'UTR of 7 transcripts and introns of 48 mRNAs. Also, TDP-43, from the brain tissues of FTLD-TDP patients, showed significant decreased binding to the 3'UTR region of EAAT2, a glutamate transporter gene that is required for glutamate clearance at the synaptic cleft (see section EAAT2).

In brain and spinal cord samples of patients with ALS or FTLD-U, TDP-43 cytoplasmic inclusions accompanied by loss of nuclear TDP-43, which are the hallmarks of ALS, were found, leading to the implication of loss of nuclear TDP-43 function as the cause of the disease's pathogenesis. However, Arnold et al (2013) ruled out both the loss of nuclear TDP-43 and TDP-43 cytoplasmic inclusions as the causes of motor neuron diseases. This stems from the fact that overexpression of ALS-related TDP-43 mutations, M337V or Q331K at levels similar to the endogenous TDP-43 in non-transgenic mice, causes age-dependent and mutant-dependent motor neuron degeneration without nuclear TDP-43 loss and cytoplasmic inclusions (Table 1.7). Also,

overexpression of wild type TDP-43 at levels similar to the endogenous TDP-43 does not trigger motor neuron degeneration. Instead, almost complete replacement of endogenous TDP-43 with either wild type TDP-43, Q331K mutant TDP-43 or M337V mutant TDP-43 (as a result of TDP-43 autoregulation) exhibits changes in alternative splicing of pre-mRNAs. Interestingly, the TDP-43^{Q331K} transgenic mice show mutant-dependent changes in alternative splicing on a small subset of pre-mRNAs. They show both enhanced exon exclusions, as well as loss of function (exon inclusion), leading to the supposition that the mutant Q331K confers both gain- and loss-of-function properties to TDP-43 respectively. However, another conflicting report observed either reduced or loss of nuclear TDP-43 in cultured fibroblasts transfected with ALS mutants M337V, G287S or A321V (Highley et al. 2014). It further confirmed splicing dysregulation in ALS patients with TDP-43 proteinopathy. LMN-specific pre-mRNA splicing was examined from post mortem ALS patients. Importantly, a significant down-regulation of two genes of the spliceosomes named *SNRNP25* and *SNRNP48* was observed. Splicing dysregulation was also observed in some genes associated with ALS, including *TARDBP*, *Fus*, profilin, dynactin and *C9ORF72*. Similar findings were obtained from fibroblast ALS models expressing the aforementioned TDP-43 mutants.

TDP-43 mouse models

In an attempt to model ALS that is caused by TDP-43 mutations, several mouse models have been generated. However, these mouse models show varied phenotypes and they do not exhibit all features of ALS (McGoldrick et al. 2013). Like SOD1 mouse models, development of disease phenotypes is dependent on the level of transgene expression. Unlike SOD1 mouse models, overexpression of wild type TDP-43 leads to the development of neurodegeneration, therefore making it difficult to determine the relative contribution of TDP-43 mutations to disease progression. In addition, in almost all ALS mouse models that overexpress ectopic TDP-43, down-regulation of endogenous TDP-43 was observed as a result of TDP-43 autoregulation. Table 1.7 summarizes the TDP-43 mouse models that have been generated up to date.

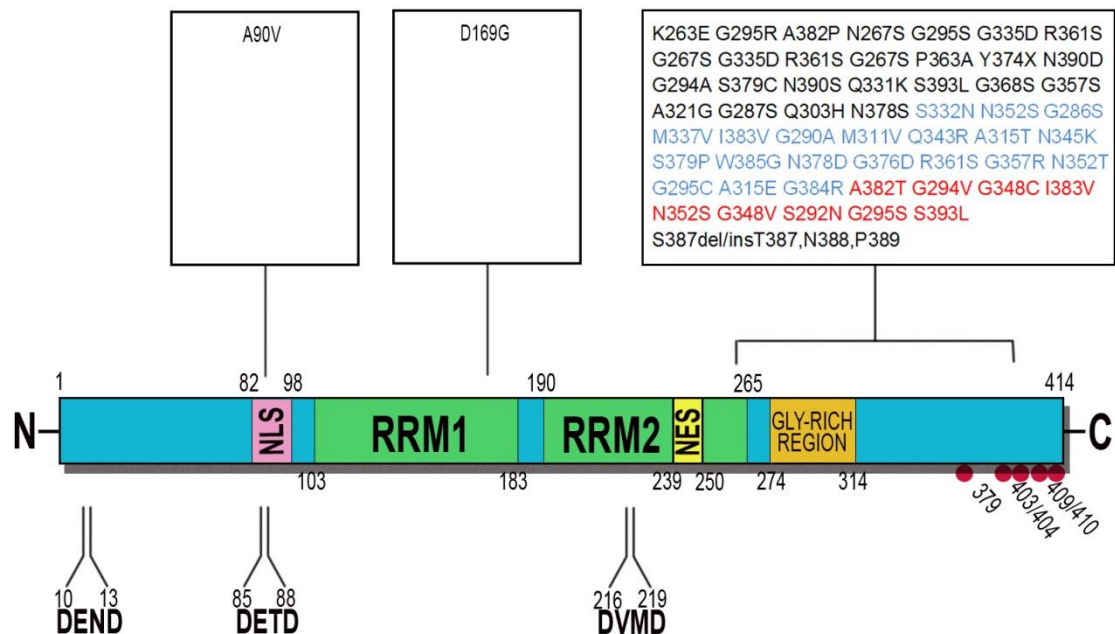
Figure 1.5

Figure 1.5 – The protein structure of TDP-43 with ALS-associated mutations. The Figure illustrates the protein structure of TDP-43, as well as mutations reported in sporadic and familial ALS cases indicated in black and blue respectively. Mutations in red are reported in both sporadic and familial ALS cases. The A90V mutation was found in both ALS and healthy controls. The structure of TDP-43 was previously described in Figure 1.4. All the aforementioned mutations resulted in dominant missense changes except Y374X which is a truncating mutation. The in-frame deletion/insertion mutation; S387del/insT387,N388,P389 is resulted from the deletion of two nucleotides (AT) at positions 1158-1159 and the insertion of CACCAACC nucleotides at the same position. Note: adapted from (Gendron, Josephs, and Petrucelli 2010; Lattante, Rouleau, and Kabashi 2013).

Table 1.7

Promoter	Protein	Protein expression (fold)	Symptom onset (weeks)	Survival (weeks)	Phenotypes								Reference
					Degeneration					Pathology			
					Abnormal motor behaviour	LMN	UMN	Cortex	Axonal	Gliosis	CTFs	Inclusion Ubiquitin/TDP-43	
Hb9:Cre	Motor neuron specific depletion	0	13	40	Yes	60% loss	nd	nd	nd	Yes	nd	Cytoplasmic: Ubiquitin (+) TDP-43 (-)	(Wu, Cheng, and Shen 2012)
Cre/loxp system	MN specific depletion	0	60	nd	Yes	Yes	nd	nd	Yes	Yes	nd	nd	(Iguchi et al. 2013)
mPrp	TDP-43 ^{A315T}	3	13	22	Yes	20% loss	Yes	nd	Yes	Yes	Yes	Cytoplasmic: Ubiquitin (+) TDP-43 (-)	(Wegorzewska et al. 2009)
mPrp	WT TDP-43	3-4 (mild)	nd	nd	No	nd	nd	nd	nd	Yes	nd	Cytoplasmic: Ubiquitin (diffuse) TDP-43 (nd)	(Stallings et al. 2010)
mPrp	TDP-43 ^{A315T}	4 (mild)	4	37.5	Yes	nd	nd	nd	nd	Yes	Yes	Cytoplasmic: Ubiquitin (+) pTDP-43 (+)	(Stallings et al. 2010)
mPrp	WT TDP-43	1.9	Not affected										(Xu et al. 2010)
mPrp	WT TDP-43	2.5	2	4-8	Yes	No	nd	nd	Yes	Yes	Yes	Cytoplasmic: Ubiquitin (+) TDP-43 (+)	(Xu et al. 2010)
mPrp	TDP-43 ^{M337V}	1.9	Not affected										(Xu et al. 2011)
mPrp	TDP-43 ^{M337V}	2.5	2	4	Yes	nd	nd	nd	Yes	Yes	Yes	Cytoplasmic: Ubiquitin (+) pTDP-43 (+)	(Xu et al. 2011)

Table 1.7 Cont.

Promoter	Protein	Protein expression (fold)	Symptom onset (weeks)	Survival (weeks)	Phenotypes								Reference
					Degeneration					Pathology			
					Abnormal motor behaviour	LMN	UMN	Cortex	Axonal	Gliosis	CTFs	Inclusion Ubiquitin/TDP-43	
mPrp	TDP-43 ^{WT}	Expressed at levels similar to endogenous TDP-43 in non-transgenic mice	Not affected										Arnold et al. 2013
mPrp	TDP-43 ^{Q337K}		12	nd	Yes	Yes	nd	nd	Yes	nd	No	No	Arnold et al. 2013
Thy1.2	TDP-43 ^{WT}	Males: 3.6	2-2.5	nd	Yes	No	nd	nd	Yes	Yes	No	Cytoplasmic: Ubiquitin (+)/TDP-43 (-) Nuclear: Ubiquitin (-)/TDP-43 (+)/Fus(+)	(Shan et al. 2010)
Thy1.2	TDP-43 ^{WT}	Female: 1.3	13	nd	Yes	No	nd	nd	nd	nd	No	No	(Shan et al. 2010)
Thy1.2	TDP-43 ^{WT}	1.9	56	nd	Yes	nd	nd	nd	nd	nd	nd	No	(Wils et al. 2010)
Thy1.2	TDP-43 ^{WT}	3.8	8	~27	Yes	10% loss	15% loss	nd	nd	Yes	Yes	nd	(Wils et al. 2010)

Table 1.7 Cont.

Promoter	Protein	Protein expression (fold)	Symptom onset (weeks)	Survival (weeks)	Phenotypes								Reference
					Degeneration					Pathology			
					Abnormal motor behaviour	LMN	UMN	Cortex	Axonal	Gliosis	CTFs	Inclusion Ubiquitin/TDP-43	
Thy1.2	TDP-43 ^{WT}	5.1	2	4	Yes	25% loss	30% loss	nd	nd	Yes	Yes	Cytoplasmic and Intracellular: Ubiquitin (+) pTDP-43 (+)	(Wils et al. 2010)
Thy1.2	TDP-25	4.7	nd	nd	nd	nd	nd	No	nd	nd	Yes	No	(Caccamo, Majumder, and Oddo 2012)
Thy1.2	TDP-43 ^{WT}	2	14	25-26 days	Yes	Yes	nd	Yes	nd	+	Yes	Cytoplasmic: Ubiquitin (+)/TDP-43 (+)/pTDP-43(+)	(Janssens et al. 2013)
Thy1.2	TDP-43 ^{M337V}	1.7	11	17-18 days	Yes	Yes	nd	Yes	nd	++	Yes	Cytoplasmic: Ubiquitin (+)/TDP-43 (++)/pTDP-43 (++)	(Janssens et al. 2013)
CaMKII	TDP-43 ^{WT}	2	8	71	Yes	nd	nd	Yes	nd	Yes	Yes	Cytoplasmic: Ubiquitin (+)/TDP-43 (+)	(Tsai et al. 2010)
CaMKII (TRE)	TDP-43 ^{WT}	0.8	8-49	nd	Yes	nd	Yes	Yes	nd	Yes	nd	Rare Cytoplasmic: Ubiquitin (nd)/TDP-43 (+)	(Igaz et al. 2011)
CaMKII (TRE)	TDP-43-ΔNLS	7.9	5	26	Yes	nd	Yes	Yes	Yes	Yes	nd	Rare Cytoplasmic: Ubiquitin (+)/pTDP-43 (+)	(Igaz et al. 2011)

Promoter	Protein	Protein expression (fold)	Symptom onset (weeks)	Survival (weeks)	Phenotypes								Reference
					Degeneration					Pathology			
					Abnormal motor behaviour	LMN	UMN	Cortex	Axonal	Gliosis	CTFs	Inclusion Ubiquitin/TDP-43	
CaMKII (TRE)	M337V TDP-43 ^{8A} (low expressor)	1.25	No	nd	No	nd	nd	No	nd	nd	Yes	Cytoplasmic: Ubiquitin (+)/TDP-43 (-) Nuclear: Ubiquitin (+)/TDP-43 (-)	(D’Alton et al. 2014)
CaMKII (TRE)	M337V TDP-43 ^{14A} (high expressor)	nd	No	nd	No	nd	nd	Yes	nd	nd	Yes	Cytoplasmic: Ubiquitin (+)/TDP-43 (-)	(D’Alton et al. 2014)
TARDBP	TDP-43 ^{WT}	3	28-32	nd	Yes	nd	nd	nd	No	Yes	nd	Cytoplasmic: Ubiquitin (+)/TDP-43 (+)	(Swarup et al. 2011)
TARDBP	TDP-43 ^{A315T}	3	28-32	nd	Yes	nd	nd	nd	No	Yes	Yes	Cytoplasmic: Ubiquitin (+)/TDP-43 (+)	(Swarup et al. 2011)
TARDBP	TDP-43 ^{G348C}	3	28-32	nd	nd	nd	nd	nd	No	Yes	Yes	Cytoplasmic: Ubiquitin (+)/TDP-43 (+)	(Swarup et al. 2011)
TARDBP	TDP-43 ^{A315T}	2.5	nd	nd	Yes	10% loss	nd	nd	nd	nd	No	Cytoplasmic: Ubiquitin (+)/TDP-43 (+)	(Stribl et al. 2014)

Table 1.7 - The Table shows a summary of TDP-43 mouse models. Abbreviation: *nd* not described, *CTFs* C-terminal fragments. Note: adapted from (McGoldrick et al. 2013) with slight modifications. Text includes more details about some mouse models but not all.

TARDBP knockout mouse models

The identification of causative mutations in *TARDBP* for ALS, raised the question whether ALS is caused by TDP-43 loss of function. Hence, *TARDBP* knockout mouse models were generated to address this question. Depletion of TDP-43 resulted in lethality during embryogenesis indicating that TDP-43 has an essential role during development (Kraemer et al. 2010; Wu et al. 2010; Sephton et al. 2010). However, disruption of one allele of *TARDBP* (*TARDBP*^{+/-}), using gene trap strategy, resulted in an age-dependant motor defect and muscle weakness. *TARDBP*^{+/-} mice exhibited decreased forelimb grip strength, compared with wild type mice (Kraemer et al. 2010). Wu et al generated conditional *TARDBP* knockout mice to specifically eliminate TDP-43 expression in motor neurons of spinal cords (Wu, Cheng, and Shen 2012). These mice were generated by crossing mice carrying the conditional allele of the *Tardbp*-floxed gene with mice harbouring a Cre-recombinase transgene under control of the HB9-promoter, which is a motor neuron specific promoter. The conditional *TARDBP* knockout mice develop ALS-like pathological phenotypes: weight loss and abnormal hindlimb clenching (at 13 weeks of age), impairment in rotarod performance (the ability to walk on a rotating rod), kyphosis (at 20 weeks of age), lower motor neuron loss, gliosis and TDP-43-negative ubiquitinated cytoplasmic inclusions.

TDP-43 transgenic mouse models

Transgenic mice expressing TDP-43 under control of mPrp

To understand the mechanisms underlying TDP-43 pathology, TDP-43 transgenic mouse models have been generated under control of tissue-specific promoters. Wegożewska et al generated the first transgenic mouse model expressing the TDP-43 transgene under the mPrp which drives the expression of TDP-43 highly in the CNS and to a lesser extent in other tissues (Wegożewska et al. 2009). This transgenic mouse expresses the coding sequence of the human mutant TDP-43 harbouring the mutation A315T (Prp-hTDP-43^{A315T}) and it is Flag-tagged at the N-terminus. The Prp-TDP-43^{A315T} expresses the TDP-43 transgene approximately 3-fold more than the endogenous TDP-43. The Prp-TDP-43^{A315T} mouse model exhibits some features of ALS such as gait

abnormality (at 13 weeks of age), weight loss (at 18 weeks of age) and swimming gait (mice unable to hold their body off the ground). It also develops some ALS pathological features: TDP-43-negative ubiquitin-positive cytoplasmic inclusions which were predominantly observed in pyramidal cells of the cortex, as well as in motor neurons of the ventral horn of the spinal cord. These ubiquitinated cytoplasmic inclusions coincided with loss of nuclear TDP-43. Also, upper and lower motor neuron loss, as well as gliosis were observed in this mouse model.

Stallings et al generated three mouse models, expressing native (without tagging) TDP-43 cDNA (human wild type, A315T or M337V) under control of the prion promoter (Stallings et al. 2010). Transgenic mice expressing high levels of the TDP-43 transgene, exhibit a severe motor dysfunction, muscle weakness, spasticity and early mortality, (ranging from 12 to 34, 14 to 49 days or a mean of survival of 19 days, respectively). Furthermore, transgenic mice expressing mild levels of the wild type or TDP-43^{A315T} (at ~ 4 folds normalized to endogenous level of TDP-43), are viable and therefore this facilitates reproducing offspring carrying the same level of the transgene, in order to perform a complete analysis. The TDP-43^{A315T} transgenic mice exhibit a progressive decrease in grip strength and a pronounced weakness in the hindlimbs. Immunofluorescence analysis revealed an increase in TDP-43 in the nucleus, as well as an increase in gliosis in the ventral horn of the spinal cord. Also, ubiquitinated cytoplasmic inclusions were observed in the ventral horn of spinal cord, with colocalization of TDP-43 when only probed with anti phospho-TDP-43 at residues 409-410 in mice that reached the late stage of the disease. The wild type TDP-43 transgenic mice, however, do not develop a motor phenotype, but they exhibit a mild level of neuronal abnormality (showed by an increase in ubiquitin that was diffused in the neurons of the ventral horn or brainstem), as well as gliosis.

However, Xu et al reported conflicting results about wild type TDP-43 transgenic mice in which overexpression of the wild type TDP-43 (at 2.5 fold normalized to TDP-43 endogenous level) results in neurodegeneration and early mortality (Xu et al. 2010). The same group reported similar findings with transgenic mice overexpressing M337V (Xu et al. 2011). Similar to the wild type TDP-43 transgenic mice, TDP-43^{M337V} transgenic mice expressing 1.9 fold of the transgene compared to the endogenous

TDP-43, were unaffected. However, when the level of the transgene increases to 2.5 fold, they exhibit motor dysfunction, axonal degeneration and early mortality.

Transgenic mice expressing TDP-43 under control of Thy1.2

Other TDP-43 mouse models were generated in which the Thy1.2 promoter was used to drive the expression of the transgene postnatally in neuronal cells (Shan et al. 2010; Caccamo, Majumder, and Oddo 2012; Wils et al. 2010). Hence, this will eliminate any deleterious effects resulting from TDP-43 overexpression during embryogenesis (McGoldrick et al. 2013). Male transgenic mice expressing wild type TDP-43 exhibit weight loss, abnormal gait, tremor and abnormal reflexes of hindlimbs (Shan et al. 2010). In addition, abnormal accumulation of mitochondria was found in cytoplasmic ubiquitinated aggregates of motor neurons and coincided with a marked reduction of mitochondria in nerve terminals at neuromuscular junctions (NMJ). Moreover, abnormal morphology of NMJ was also observed similar to that found in spinal muscular atrophy (SMA). Based on this similarity, the author also examined Gemini coiled bodies (GEMs), a nuclear structure that contains the survival of motor neuron protein (a deficiency of this protein is known to cause SMA). Abnormal distribution of GEMs was observed in the nuclei of neurons.

Similar to the prp-TDP-43^{WT} mouse model, Wils et al generated wild type TDP-43 mouse models under the control of the Thy1.2 promoter which exhibit motor neuron degeneration in a dose-dependent manner (Wils et al. 2010).

The presence of N-terminal-cleaved TDP-43 fragments which forms C-terminal fragments (25 kDa) was found in the cytoplasm of almost all TDP-43 mouse models for ALS. The role of this small molecular weight fragment of TDP-43 in the disease pathogenesis is still unclear. Therefore, Caccamo et al generated a mouse model overexpressing TDP-43-25. This mouse model developed cognitive impairment reminiscent of FTLD-TDP (Caccamo, Majumder, and Oddo 2012).

To determine the relative contribution of mutant TDP-43 to disease progression, Janssens et al established mutant transgenic mice that express a comparable level of human TDP-43^{M337V} to that expressed by wild type human TDP-43 mice, i.e. 1.7 and 2

folds respectively. The mutant showed accelerated disease onset and progression (Table 1.7).

Transgenic mice expressing TDP-43 under control of CaMKII

Other groups generated TDP-43 mouse models under control of CaMKII (calcium-calmodulin-dependent kinase II) which limits the expression of TDP-43 to the forebrain (Tsai et al. 2010; Igaz et al. 2011; Cannon et al. 2012). Tsai et al generated a mouse model overexpressing wild type TDP-43 at 2 fold compared to the endogenous TDP-43. This mouse develops cognitive abnormalities from 8 weeks of age. Interestingly, the mouse also develops motor dysfunction by 26 weeks of age manifested by abnormal hindlimb reflexes, decreased grip strength and rotarod deficits. This coincided with loss of cortical neurons, as well as cortical atrophy.

Igaz et al generated conditional transgenic mouse models under the control of CaMKII and the tetracycline response element system (TRE). Briefly, transgenic hTDP-43 mouse lines were first generated containing either hTDP-43^{WT} or TDP-43-ΔNLS (lacking the nuclear localisation signal domain), fused with a tetracycline-responsive promoter element (tetO). These mice were bred to Camk2a-tTA mice carrying the tetracycline-controlled trans activator (tTA) under control of the promoter Camk2a. The bigenic mice carrying both Camk2a-tTA and tetO-hTDP-43 were given doxycycline-containing food. Doxycycline (dox) blocks the promoter until 28 days of age when mice were fed dox-free food to allow the transcription of tTA which then binds to tetO to activate the expression of TDP-43.

In both bigenic lines, hTDP-43^{WT} or TDP-43-ΔNLS, the induction of their respective TDP-43 expression led to neuron loss in selected regions of the forebrain (cortex and hippocampus), corticospinal tract degeneration and spastic motor impairment that was measured by abnormal clasping. The tetO-hTDP-43-ΔNLS line facilitates the investigation of the impact of mislocalized TDP-43 on neuronal viability. Indeed, the cytoplasmic ubiquitinated phosphorylated TDP-43 was rarely observed. Furthermore, overexpression of the transgene TDP-43 resulted in a dramatic down-regulation of endogenous TDP-43. Taking all the above findings into account, this suggests that the

neuronal loss is more likely caused by the nuclear TDP-43 loss of function than by cytoplasmic inclusions.

Other transgenic mice expressing the human mutant M337V and using the TRE system were generated by D'Alton et al 2014. The two lines which expressed the highest level of the transgene were used in this study, namely hTDP-43^{8A} and hTDP-43^{14A}. The hTDP-43^{14A} mice express high amounts of the transgene compared to hTDP-43^{8A} (D'Alton et al. 2014). These mice do not develop any overt phenotypes. The hTDP-43^{14A} mice, on the other hand, exhibit abnormal brain development at postnatal age of P0 without detection of TDP-43 aggregation. Furthermore, active caspase 3 was extensively detected in the cortex of hTDP-43^{14A} indicating high levels of cell death as a result of overexpression of the mutant M337V. Ubiquitinated inclusions were detected in the cytoplasm of the cortex of hTDP-43^{14A} and in the nuclear and cytoplasm of the cortex of hTDP-43^{8A}. Small molecular weight species of TDP-43 (25 kDa and 35 kDa) were also detected in both lines.

TDP-43 transgenic mice using a bacterial artificial chromosome

Swarup et al using a bacterial artificial chromosome generated TDP-43 mutant (A315T and G348C) and wild type transgenic mice by inserting the entire human TDP-43 gene under the control of its own promoter into the mouse genome (Swarup et al. 2011). In a nutshell, all transgenic lines, as well as the transgenic wild type TDP-43, express the transgene at 3 fold more than the endogenous TDP-43. The mice develop cognitive abnormalities and motor impairments by 26 and 42 weeks of age, respectively. Furthermore, peripherin aggregates were observed in the cross-sections from brain and spinal cord tissues of these mice.

TDP-43 transgenic knock-in mice using recombinase-mediated cassette exchange

Stribl et al generated a transgenic knock-in mouse model expressing the human TDP-43^{A315T} cDNA under the control of its own promoter (Stribl et al. 2014). The homozygotes die whereas the heterozygotes are viable. The heterozygotes express the transgene hTDP-43^{A315T} at 2.5 fold greater than the endogenous TDP-43. As a result, the level of the endogenous TDP-43 decreased to 20% in comparison to the control non-transgenic mice. The heterozygotes exhibited body weight loss by 10%, as well as

insoluble TDP-43 inclusions that were detected in the brain lysate in an age dependent manner. The mice also exhibited a 10% reduction of motor neurons which correlated with a slight motor impairment. In addition, colocalization of TDP-43 with ubiquitin was observed in the cytoplasm of the brain (cortex) and in the anterior horn of the spinal cord. Furthermore, transmission electron microscopy (TEM) performed on the cortex of heterozygotes at 18-month of age revealed an abnormal morphology of mitochondria.

The F210I TDP-43 mutant mouse model

F210I is a missense mutation located in the RRM2 of TDP-43. Heterozygotes are viable whereas homozygotes are lethal. At E14.5 embryonic stage, the heterozygous embryos appear normal compared to the wild type, whereas the homozygotes appear to be less developed in contrast to the wild type. Ricketts investigated the negative impact of the F210I mutation on TDP-43 function by examining the RNA splicing role of TDP-43^{F210I} using a CFTR mini gene assay (Ricketts 2012). TDP-43^{F210I} exhibited a deficiency of exon 9 exclusion of the CFTR gene. Heterozygotes showed a significant reduction in the ability of exon 9 skipping activity (by 67.7%) whereas the homozygotes showed an almost complete loss of this activity. As a result, TDP-43^{F210I} cellular localization was determined using cell fractionation. Similar to the wild type, TDP-43^{F210I} is predominantly localized to the nucleus. In addition, the binding affinity between TDP-43 and the hnRNP family was not affected by F210I mutation. However, TDP-43^{F210I} showed a significant reduction in the ability to bind the UG repeats which is known to be required for exon 9 skipping activity. Also, TDP-43^{F210I} showed a reduced ability to bind its own 3' UTR sequence.

2.1.4.4 Peripherin

Structure and function

Peripherin is a type III intermediate filament expressed mostly in the peripheral nervous system (PNS) and in some neuronal populations in the central nervous system (Eriksson et al. 2008; Yuan et al. 2012). This classification as a type III intermediate filament is based on its structural properties, as well as on its ability to self-assemble or coassemble with either vimentin or neurofilament proteins. During neuronal

development, peripherin is up-regulated and then postnatally down-regulated, suggesting that peripherin has an influence on neurite elongation. Also, peripherin is up-regulated after brain damage which indicates that it also might play a role in axonal regrowth. Nevertheless, the exact physiological function of peripherin is still unknown.

The peripherin gene is comprised of 9 exons (Figure 1.6A, blue boxes) that can be alternatively spliced to generate three different splice variants. Similar to neurofilaments, peripherin contains a conserved alpha helical rod domain flanked by non-alpha-helical head and tail domains (Figure 1.6B). The rod domain is subdivided into three coil domains: 1a, 1b, and 2 which are connected by non-alpha helical linker sequences (Figure 1.6B, thin red boxes). Both the rod and N-terminal domains are required for filament assembly whereas the C-terminal domain is dispensable for filament formation.

Peripherin isoforms were first characterized in murine neuroblastoma cells in which the three peripherin cDNAs were entirely sequenced and characterized: Per58, per61 and per56 (Figure 1.6B) (Landon, Wolff, and Nechaud 2000; Landon et al. 1989). The coding sequence is highly conserved between the three isoforms. Per58 is the predominant isoform and is comprised of 457 amino acids that are encoded by all nine exons. Per61 is generated by inclusion of 32 amino acids within the coil 2 domain as a result of the retention of intron 4. Per56 is generated by the presence of a cryptic acceptor site located at the start of exon 9. The use of this cryptic acceptor site leads to a deletion of 62 bp (21 amino acids) (Figure 1.6A, grey box). This deletion results in a change in the reading frame and thus the stop codon used in per58 and per61 is no longer the stop codon for per56. Instead, a new stop codon located 20 bp downstream from the original stop codon is generated, resulting in the replacement of 21 amino acids with 8 amino acids. Per45 is an alternatively translated isoform translated from the same per58 transcript. While the second start codon is used to translate per58, per45 is translated from the third start codon. In humans, however, per58 is translated from the first ATG, whereas per45 is generated from the second ATG. Regarding per61, the murine per61 is generated by the insertion of 96bp long intron 4. In the humans,

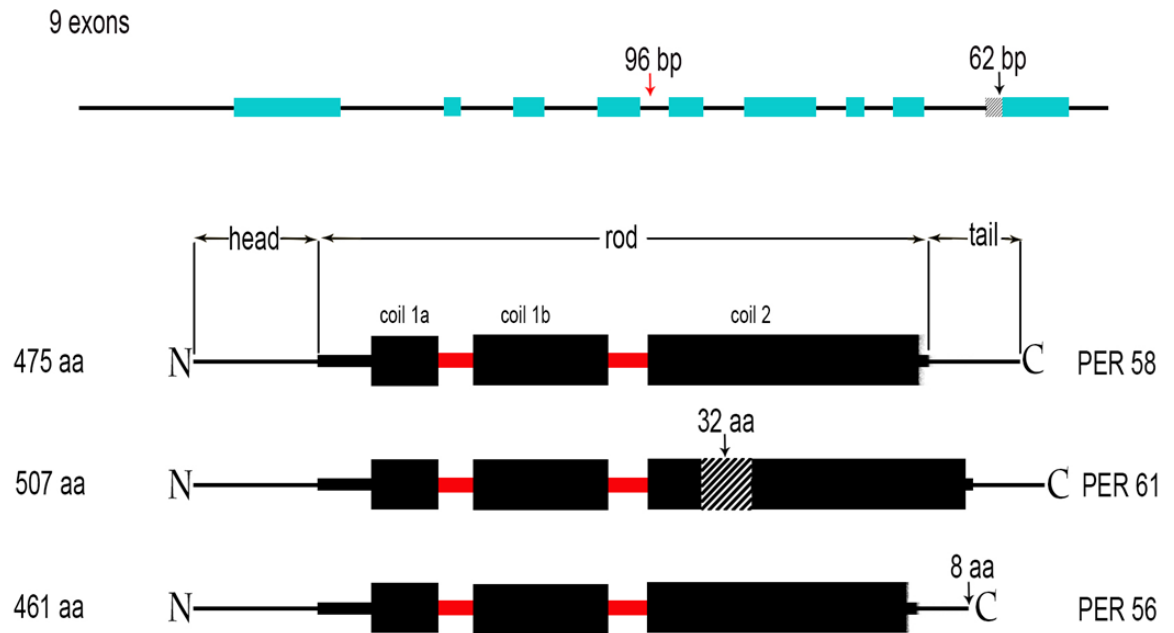
Figure 1.6

Figure 1.6 – Peripherin gene and protein structure. (A) Thick blue boxes represent exons while thin black boxes represent introns. The red arrow refers to the position of intron 4. The grey box represents the deletion of 62 bp in the per56 splice variant as a result of the use of a cryptic site at the start of exon 9. (B) Figure showing the structure of peripherin isoforms. Thick black boxes represent coil domains while thin red boxes represent linker sequences. Stripped box represents the 32 amino acid inclusion. Note: adapted from (Robertson et al. 2003).

however, intron 4 of peripherin consists of 91 bp. If the insertion of 91 bp occurred, this would result in a frameshift and therefore in the formation of a C-terminally truncated protein, 32kDa in size. Hence, per61 cannot exist in humans (Xiao et al. 2008). Moreover, per28 was found to be expressed at low stoichiometric levels in humans. Per28 results from the retention of intron 3 and 4 at RNA levels. However, due to the presence of a stop codon in intron 3, which is located 30 bp downstream of the start of intron 3, a ten amino acid sequence gets included in the translated product per28 and intron 4 is therefore untranslated.

The role of peripherin in ALS

Peripherin was found to be associated with hyaline conglomerate inclusions in ALS. Also, axonal spheroid (large swellings observed at the proximal axons of affected motor neurons) was immunostained for peripherin, (McLean et al. 2008; Corbo and Hays 1992).

Stoichiometric expression of peripherin isoforms is required for the formation of a proper cytoskeletal network. Changes in the ratio of peripherin isoforms may trigger aggregate formation (Xiao et al. 2008). For instance, per28 was found to be up-regulated in ALS cases. Up-regulation of per28 results in changes in stoichiometric levels of peripherin, leading to aggregate formation.

Peripherin isoforms contribute to the formation of filament networks through intra-isoform association that are tissue-specific and post-transcriptionally regulated (McLean et al. 2008; McLean et al. 2010). Per45 is required for a proper network establishment of per58. Without per45, per58 would be unable to form a proper neurofilament network (McLean et al. 2008).

The ability of each peripherin isoform to form filaments was first characterized when they were ectopically and individually expressed in the SW13 vim(-) cell line (Robertson et al. 2003). Per58 and per56 were both able to assemble neurofilaments, whereas per61 was not. Per61 also had a toxic effect on cultured motor neurons. In addition, abnormal expression of per61 was detected in the ALS transgenic mouse model SOD1^{G37R}. This might be due to a disruption of the heptad repeat of coil 2 by inclusion of 32 amino acids in per58. This repeat is required for the formation of a

coiled-coil structure (the basic building block of neurofilaments) which leads to the dimerization of peripherin (Goldman et al. 2011).

A heterozygous frameshift deletion of 1 bp in exon 1 of peripherin was found to be associated with ALS (Gros-Louis et al. 2004). This deletion results in the generation of a stop codon in the head domain and thus creates a truncated peripherin species. Ectopic expression of this truncated peripherin leads to a disruption of neurofilament assembly. Moreover, a homozygous peripherin mutation Asp141Tyr which is located in the linker sequence between coil 1a and coil 1b domains was also associated with ALS (Corrado et al. 2011). Functional analysis of the aforementioned mutations revealed that these mutations lead to the formation of aggregates. Another mutation was identified as an Arg133Pro substitution mutation in the first linker sequence of the coil 1 domain, however, functional assays are required to determine its association with aggregate formation (Corrado et al. 2011).

2.1.4.5 EAAT2

The excitatory amino acid glutamate transporter (EAAT2) is a glial glutamate transporter essential for clearing the synaptic cleft from the excess glutamate, in order to keep its level below excitotoxic concentration (Nicholls and Atewell 1990). Glutamate is an important neurotransmitter in the central nervous system. It is required for initiating various signalling cascades by binding to its receptor on the post-synaptic neurons which in turn allows calcium ion influx to initiate intracellular signalling cascades. Clearing the synaptic cleft from glutamate is important for the prevention of excessive activation of the glutamate receptor which otherwise would lead to excitotoxicity. Two isoforms of GLT-1, the murine homologue of EAAT2, are expressed in the CNS: GLT-1, mainly expressed in the astrocytes and GLT-1B, the neuronal splice variant.

The loss of EAAT2 protein has been observed in the motor cortex and spinal cord in some ALS cases and hence negatively impacts the glutamate uptake (Rothstein, J D.; Martin, L J.;Kuncl 1992). Neither a mutation nor a reduction in transcript levels account for this selective loss of EAAT2 protein. It was reported that this loss might be the result of aberrant RNA processing that generates intron seven retention and exon 9

skipping splice variants, which have been seen in some ALS cases (Lin et al. 1998). However, subsequent studies found that these splice variants are also present in the controls and thus are not associated with ALS (Flowers et al. 2001). Another study reported the occurrence of RNA editing in EAAT2 in ALS, which results in an alternative polyadenylation signal in intron 7 (Flomen and Makoff 2011). Nevertheless, the precise process of the selective loss of EAAT2 protein is still under investigation.

2.2 Diseases of upper motor neurons

2.2.1 Hereditary spastic paraplegia

HSP is a genetically and clinically heterogeneous neurodegenerative disease which affects the longest axons of the corticospinal tract and which is characterized by progressive spasticity and weakness in lower limbs (Lo Giudice et al. 2014). HSP can be divided into two groups: pure HSP which is characterized by spastic paraplegia, bladder spasticity and mildly impaired sensations and complicated HSP which is characterized by lower limb spasticity associated with other neurological or non-neurological diseases. There are many genes and loci identified in HSP. Of these is kinesin (see section 2.3.2.1.1 for more details about kinesin structure and function).

There are 15 classes of kinesins and approximately 45 kinesin superfamily genes (Hirokawa et al. 2009). Of relevance to HSP diseases are KIF5A and KIF1A. Mutations in the motor domain of one allele of KIF5A have been found to cause HSP whereas mutations in KIF1A are autosomal recessive. Table 1.8 shows all mutations that have been identified to date in KIF5A and KIF1A.

Table 1.8

Kinesin type	Mutations	Substitution	Location	Inheritance	Ref
KIF5A	N256S	Asparagine to serine at position 256	Located in loop 11 that connects MTs and ATP-binding sites	Autosomal dominant	OMIM, #602821
	R280C	Arginine to cysteine substitution at position 280	Located in the MT binding site		
	Y276C	Tyrosine to cysteine at position 276	nd		
	A361V	Alanine to valine at position 361	Located in the coiled coil domain		
	E251K	Glutamic acid to lysine at position 251	Located in the motor domain		
	R204Q	Arginine to glutamine at position 204	Located in the motor domain		
	A280H	Alanine to histidine at position 280	Located in the motor domain		
	E755K	Glutamic acid to lysine at position 755	Located in the stalk domain		
	G235E	Glycine to lysine at position 235	Located in the motor domain		
KIF1A	A255V	Alanine to valine at position 255	nd	Autosomal recessive	OMIM, #610357
	R350G	Arginine to glycine at position 350	nd		

Table 1.8 - The Table shows all HSP-caused mutations that have been identified to date in two kinesin genes KIF5A and KIF1A. Abbreviations: MT, microtubule; nd, not determined.

2.3 Diseases of lower motor neurons

2.3.1 Distal hereditary motor neuropathies

The distal hereditary motor neuropathies (dHMN) include a group of heterogeneous disorders that share the common feature of distal lower-motor-neuron weakness (Rossor et al. 2012). dHMN is characterized by LMN weakness or degeneration in the ventral horn of the spinal cord and distal muscle wasting and weakness. Figure 1.7 shows an example of a patient with dHMN demonstrating the distal wasting and weakness of the lower limb. Table 1.9 shows all genes and loci that have been identified in dHMN.

Figure 1.7



Figure 1.7 - The Figure demonstrates the distal wasting and weakness of dHMN patient legs [in both the anterior (A) and the posterior (B) compartment of the leg] with a mutation in heat-shock protein B1. Note: adapted from (Rossor et al. 2012).

Table 1.9

dHMN form	Locus	Gene	Inheritance	Phenotype
dHMN type I	—	HSPB1 HSPB8 GARS DYNC1H1	AD	Juvenile onset with distal wasting and weakness
dHMN type II	—	HSPB1 HSPB8 BSCL2 HSPB3 (probable)	AD	Adult onset with distal wasting and weakness
dHMN type III	11q13	Unknown	AR	Slowly progressive wasting and weakness
dHMN type IV	11q13	Unknown	AR	Slowly progressive wasting and weakness with diaphragmatic paralysis
dHMN type V	—	GARS BSCL2	AD	Upper-limb predominance
dHMN type VI	—	IGHMBP2	AR	Spinal muscular atrophy with respiratory distress type 1
dHMN type VII	2q14	DCTN1 TRPV4 Unknown	AD	Adult onset with vocal-cord paralysis
X-linked dHMN	—	ATP7A	X-linked	Distal-onset wasting and weakness
dHMN and pyramidal features	4q34eq35 7q34eq36	SETX* BSCL2 Unknown Unknown	AD	DHMN and pyramidal signs
dHMN from the Jerash region of Jordan	9p21.1ep12	Unknown	AR	DHMN and pyramidal signs originating in the Jerash region of Jordan
Congenital distal spinal muscular atrophy AR	—	TRPV4	AD	Distal weakness at birth and arthrogryphosis

Table 1.9 - The Table shows the causative genes that have been identified so far in dHMN.

Abbreviations: AD, autosomal dominant; AR, autosomal recessive; ATP7A, copper-transporting ATPase 1; BSCL2, Berardinelli-Seip congenital lipodystrophy type 2; DCTN1, P150 subunit of dynactin; DYNC1H1, cytoplasmic dynein heavy chain 1; GARS, glycyl-tRNA synthetase; HSPB1, heat-shock protein B1; HSPB3, heat-shock protein B3; HSPB8, heat-shock protein B8; IGHMBP2, immunoglobulin m binding protein 2; TRPV4, transient receptor vallanoid 4 gene. *dHMN and pyramidal features due to senataxin (SETX) mutations are also referred to as amyotrophic lateral sclerosis type 4. Note: adapted from (Rossor et al. 2012).

2.3.2 SMA

Spinal muscular atrophy (SMA) is an autosomal recessive neurodegenerative disorder characterized by proximal muscle wasting and weakness due to LMN loss in the spinal cord and brainstem (Prior and Russman 2013). SMA is genetically caused by a mutation in the survival motor neuron 1 (*SMN1*) gene. *SMN1* is diminished in patients with SMA. Humans have two almost identical copies of *SMN*: *SMN1* and *SMN2*. *SMN2* however cannot compensate for the lack of *SMN1* protein in patients with SMA due to the absence of alternatively spliced exon 7 in *SMN2*. Thus, *SMN2* only produces a small amount of a functional protein whereas the rest (about 80%) of *SMN2* is unstable.

2.3.2.1 SMA-LED and its molecular genetics

Spinal muscular atrophy with lower extremity predominance (SMA-LED) is an autosomal dominant congenital neurodegenerative disorder characterized by muscle weakness and wasting of the proximal lower limb muscles. SMA-LED is heterogeneous comprising multiple forms due to the presence of many causative mutations in different genes: *TRPV4*, transient receptor potential action channel, superfamily V, member 4; *DYNC1H1*, cytoplasmic dynein heavy chain 1; and *BICD2*, Bicaudal drosophila, homolog 2. SMA-LED which is caused by the aforementioned genes, shows similar symptoms such as early childhood onset and slowly or non-progressive motor neuron degeneration. Each have distinctive features such as vocal cord impairment or upper motor neuron signs. In this thesis, I will focus on SMA-LED which is caused by mutations in *DYNC1H1*. In addition to SMA-LED, mutations in *DYNC1H1* are also known to be associated with other diseases such as Charcot-Marie-Tooth type 2 (CMT2), malformation of cortical development (MCD) and learning disability. Figure 1.8 shows

the structure of *DYNC1H1* and demonstrates the location of all recently reported *DYNC1H1* mutations in human cases with the main phenotypic features. For more details about the structure of *DYNC1H1* see section 2.3.2.1.1.

2.3.2.1.1 Molecular motors

Most intracellular transport in eukaryotic cells is performed by molecular motors. Molecular motors are motor proteins that are involved in transporting cargo (including newly synthesized proteins or mRNAs) to their cellular destination. This directional intracellular transport is more prominent in cell types with a highly polarized structure such as neurons and epithelial cells (Hirokawa et al. 2009). Such intracellular transport is required for the normal function and survival of neurons due to the presence of long axons which requires transporting material from the cell body to the nerve terminals. Cargos such as the membrane bound organelles (e.g. mitochondria, lysosomes, synaptic proteins and endosomes) are transported by fast axonal transport (100-400 mm per day) whereas the cytosolic proteins such as tubulins and neurofilaments are transported at a lower speed, namely 0.1-3 mm per day. There are three types of molecular motor proteins: kinesin, dynein and myosin. Kinesins utilize microtubules as a track to step along and anterogradely transport cargo from the microtubule minus end (points to the cell body) to the microtubule plus end (points to the nerve terminals). The cytoplasmic dynein is involved in retrograde transport along microtubules (from the plus end to the minus end). Myosin walks along actin filaments to drive muscles contraction and to provide short-term transport beneath the plasma membrane. These motor proteins use the chemical energy derived from ATP hydrolysis to generate the force that is required for their motility.

Kinesins

There are 15 classes of kinesins (Figure 1.9A) (Hirokawa et al. 2009). These kinesins can be further grouped into three types based on the location of the motor domain: in the amino terminus (N-kinesins), in the middle of the molecule (M-kinesins) or in the C-terminus (C-kinesins) (Figure 1.9B). N-kinesins are involved in anterograde transport while some C-kinesins are involved in retrograde transport. M-kinesins are involved in

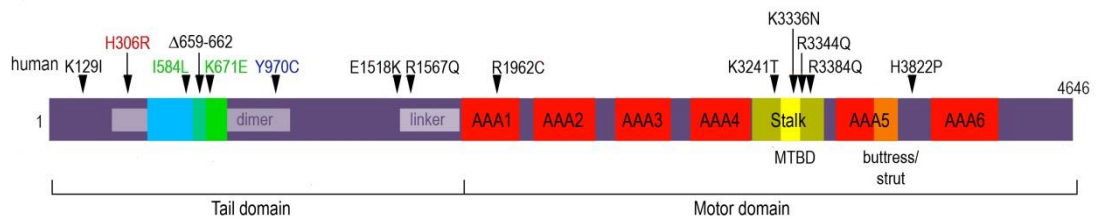
Figure 1.8

Figure 1.8 - The Figure shows a schematic diagram of the human cytoplasmic dynein heavy chain 1. The arrows represent the human mutations. Mutations in black are found in individuals with MCD whereas those in red are found in individuals with SMA-LED or CMT2. Mutations in green cause SMA-LED while mutations highlighted in blue cause SMA-LED with mild cognitive impairment. Note: adapted from with some modifications (Schiavo et al. 2013).

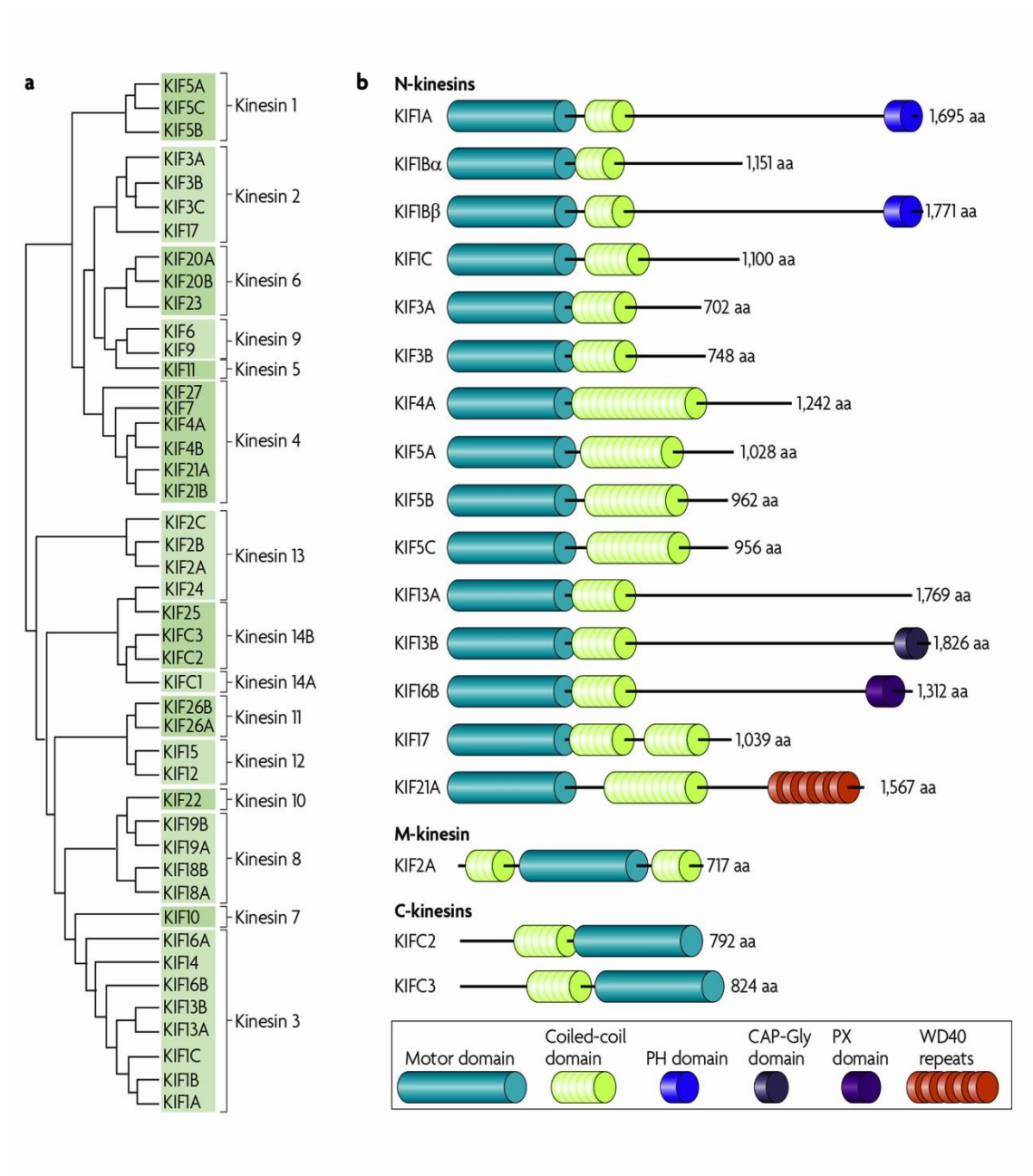
Figure 1.9

Figure 1.9 - The Figure shows a phylogenetic tree of 45 kinesin genes in the mouse genome as well as the domain structure of major mouse kinesins. Note: adapted from (Hirokawa et al. 2009).

depolymerizing microtubules. In neurons, three members of the kinesin superfamily are involved in driving anterograde movement along the axon: kinesin 1, kinesin 2 and kinesin 3 (Moughamian and Holzbaur 2012). Kinesins generally contain a motor domain, a coiled coil domain called stalk and a globular domain called tail (Figure 1.10A). The motor domain is comprised of an ATP binding domain and a microtubule binding site. Some kinesins also contain additional domains: the pleckstrin homology (PH) domain in the KIF1A and KIFB β , the CAP-Gly domain which exist in KIF13B and WD40 repeat found in KIF21A. Kinesins form a dimer by connecting their two heads with a coiled coil stalk. They move along microtubules through repeated cycles of coordinated binding and unbinding of their two heads.

Myosin

Based on genomic analysis, there are 17 classes of myosins. Myosin II is the first member which was identified and purified from skeletal muscles. There are additional myosin II isoforms that are expressed in non-muscle cells. Of relevance to my research, I will focus on non-muscle myosin II due to its role in cell migration and adhesion. Structurally, myosin II is composed of two heavy chains and four light chains. The heavy chain consists of the globular head domain which contains both actin and ATP-binding sites (Figure 1.10B). Adjacent to the head domain is an alpha-helical region called neck, the region where the two light chains can bind: a regulatory light chain and an essential light chain (RLC and ELC, respectively) (Figure 1.10B, ELC, in red and RLC, in blue). RLC is required to regulate myosin II activity and ELC is required to stabilize the structure of the heavy chain. Adjacent to the neck domain is the alpha-helical long tail domain. Myosin II is dimeric in which two tail domains associate to form a coiled-coil structure called bipolar filament. Myosin filaments tether actin filaments through their heads to exert tension by ATP hydrolysis (Vicente-Manzanares et al. 2009). Both the head and the neck represent the N-terminus of myosin II while the tail domain represents the C-terminus. Myosin II plays an important role in cell motility (see section 2.3.2.1.4.4).

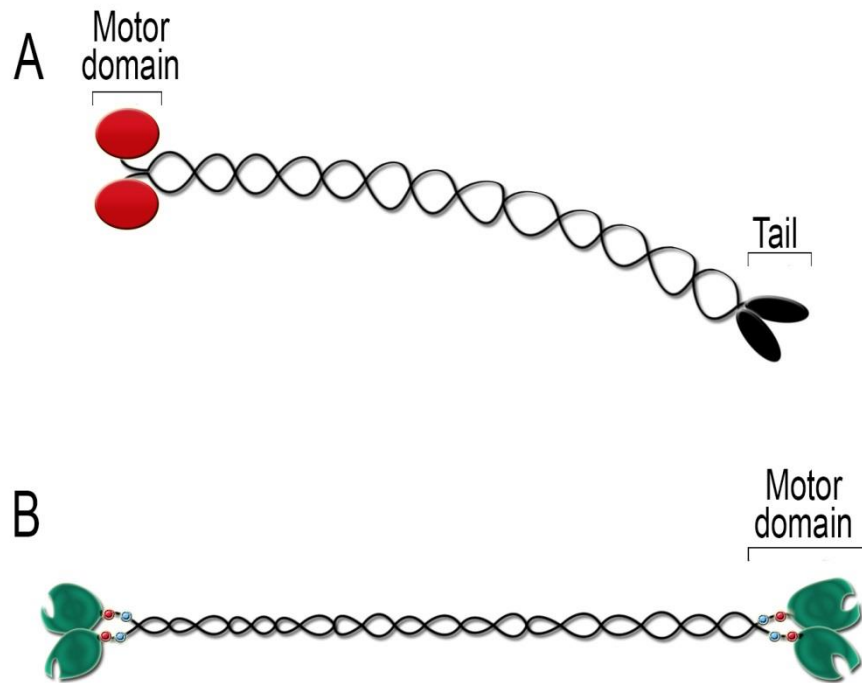
Figure 1.10

Figure 1.10 - Schematic diagram of the motor proteins kinesin, KIF4 (A) and non-muscle myosin II (B). Two light chains bind to the neck namely a regulatory light chain and an essential light chain (RLC and ELC, in blue and red respectively). Note: adapted from (Vallee, Seale, and Tsai 2010; HIROKAWA and NODA 2008).

Dynein

Two families of dynein exist: axonemal dynein and cytoplasmic dynein (Höök and Vallee 2006). Axonemal dynein is located in the axonemes found in flagella and cilia. The axoneme contains a highly conserved cytoskeletal structure and comprises an array of microtubules, two of which are located in the centre of the axoneme and the rest of microtubules form 9 pairs which are arranged in a circle (called the outer doublet) to form a cylinder like structure. The function of axonemal dynein is to connect the outer doublets. It is responsible for the movement of flagella and cilia by forcing the microtubule doublets to slide against each other.

Two forms of cytoplasmic dynein exist: cytoplasmic dynein 1 and cytoplasmic dynein 2 and both function as a complex (Höök and Vallee 2006). Of relevance to SMA-LED, the cytoplasmic dynein 1 complex will be the topic discussed from this point on.

Cytoplasmic dynein 1 is the abundant form and is a large multi-subunit motor complex (about 1.5 MDa). It is involved in many crucial processes such as retrograde transport, cell migration, orientation of the mitotic spindle, nuclear translocation, Golgi maintenance, endocytic trafficking and autophagy. In the nervous system, cytoplasmic dynein 1 is the sole motor protein implicated in the retrograde transport (Schiavo et al. 2013). It transports cargo within the dendrites and axons, carries signalling complexes, misfolded proteins and organelles from the nerve terminus to the soma. Based on similarity in sequence and structural organization, cytoplasmic dynein is related to the AAA superfamily of ATPases. The cytoplasmic dynein 1 complex is composed of two identical subunits of dynein heavy chain 1 (DYNC1H1 referred to as DHC hereafter) (Figure 1.11A). *DYNC1H1* is a large gene composed of 78 exons and encodes an enormous protein which has a mass of approximately 500 kDa. DHC contains two main domains: motor and tail domains. The motor domain is approximately 380 kDa and contains an array of six ATPase catalytic units, which are arranged in a ring shape (Vallee, McKenney, and Ori-McKenney 2012; Carter et al. 2011) (Figure 1.11A, red circles). The site AAA1 is the main site responsible for ATP hydrolysis whereas the role of AAA2 to AAA4 in nucleotide binding and hydrolysis remains unclear. However, they seem to have an impact on the motor activity of dynein. The site AAA3 hydrolyses ATP more slowly than AAA1. Moreover, AAA3 acts as a switch to facilitate microtubule

release. AAA5 and AAA6 do not have their conserved nucleotide binding site and therefore they might only provide a structural role in dynein function. Projecting from AAA1 is the linker which makes contact between AAA1 and AAA4 or AAA5. The linker has a role in linking the chemical and the mechanical cycles of the motor. The truncated-linker motor domain of dynein affects the ATPase rate as well as the motor activity. While the position of the linker tip contacts AAA4 when the motor dynein is in the unprimed state (post power stroke), the linker undergoes a conformational change in the primed state (pre power stroke) in which the linker tip becomes close to AAA2 (Kon, Sutoh, and Kurisu 2011; Burgess et al. 2003). Protruding from AAA4 is a 100 amino acid coiled coil α helical structure called the stalk which contains at its distal end the microtubule binding domain. The stalk interacts with a small coiled coil structure called strut or buttress which is embedded in AAA5. The exact role for the strut is unknown, however it has been believed that it might provide a physical support for the stalk (Kon, Sutoh, and Kurisu 2011).

The two subunits of DHC homodimerize and coil through the tail domains. Similar to the mouse DHC, the dimerization domain lies between amino acids 300 and 1140 of the rat DHC and is homologous to amino acids 302-1142 of the human DHC (Tynan, Gee, and Vallee 2000) (Figure 1.11B). The tail domain contains binding sites for the following cytoplasmic dynein 1 components: intermediate (*DYNC1I1* and *DYNC1I2* referred to as DICs) (Figure 1.11A and B, in blue), light intermediate (*DYNC1LI1* and *DYNC1LI2* referred to as DLICs) (Figure 1.11A and B, in green) and light chains (*DYNLT1*, *DYNLT3*, *DNY1RB2*, *DYNLL1* and *DYNLL2* referred to as DLCs) (Figure 1.11A, in orange) (Pfister et al. 2006). These subunits are part of the dynein complex and are necessary for binding the cargo to the complex. Both DIC and DLIC binding sites are located within the dimerization domain of DHC. The binding sites of the rat DIC and DLIC are distinct but overlapping (amino acids 446-701 and 649-800, respectively, which are homologous to amino acids 448-703 and 651-802 of human DIC and DLIC, respectively) (Tynan, Gee, and Vallee 2000). The cytoplasmic dynein 1 complex also binds accessory proteins (although they do not belong to the complex itself) required for a complete function of dynein either directly through DHC or indirectly through DIC or DLC (Table 1.10) (Schiavo et al. 2013).

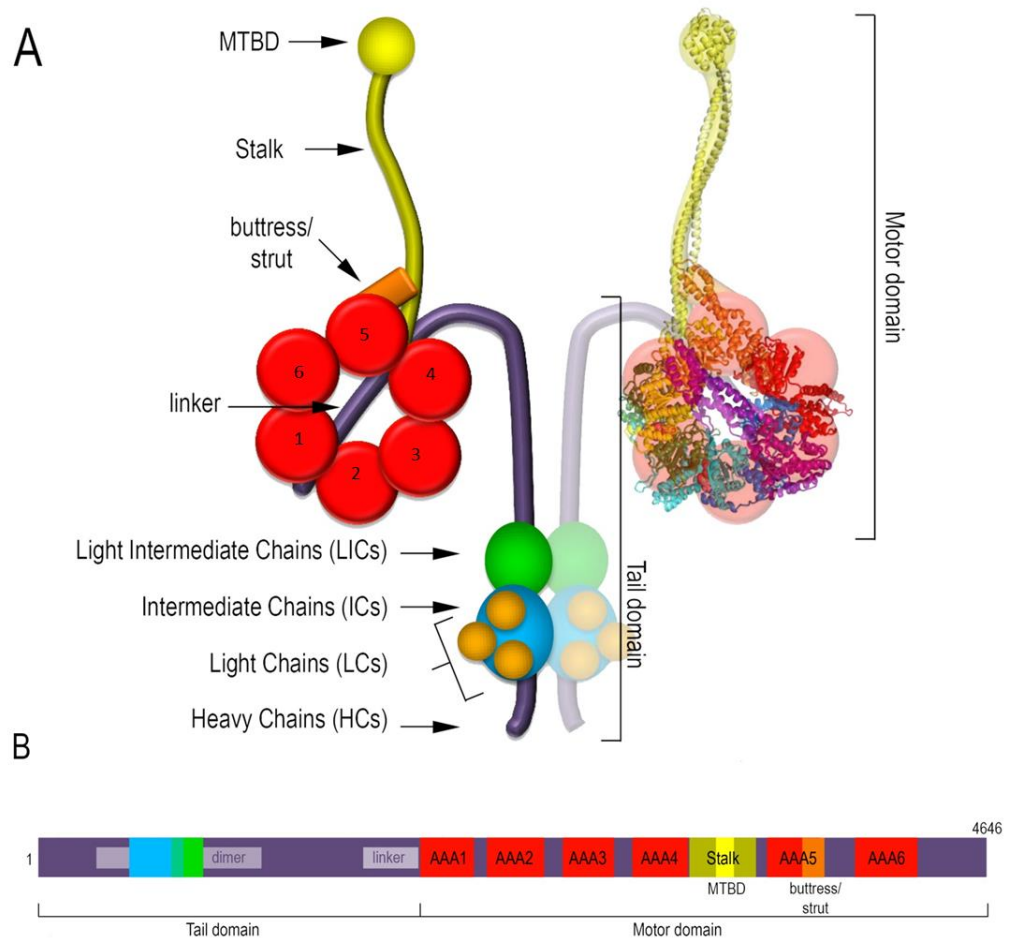
Figure 1.11

Figure 1.11 - The Figure shows a schematic diagram of the human cytoplasmic dynein 1 complex. (A) The cytoplasmic dynein complex includes the heavy chain dimer (HCs) and its associated subunits. (B) The motor domain of the cytoplasmic dynein heavy chain contains (in dark violet) six ATPase domains (in red), the stalk domain which includes the microtubule binding domain (in dark yellow and yellow, respectively) and the buttress (in orange). The tail domain (in dark violet) contains the homodimerization domain and linker (in light violet). It also contains binding sites for intermediate chain (in blue) and light intermediate chain (in light green). The dark green region represents the overlapping region between intermediate chain and light intermediate chain. Note: adapted from (Schiavo et al. 2013).

Table 1.10

Protein	Type of binding	Site/ subunit
LIS1	Direct	DYNC1H1 (AAA3/AAA4 junction) DYNC1H1 (AAA4 arginine finger)
NudE	Indirect	Intermediate chain Light chain – LC8
Dynactin	Indirect	Intermediate chain
Snapin	Indirect	Intermediate chain
Huntingtin (Htt)	Indirect	Intermediate chain
HAP1	Indirect	Dynactin
BICD1	Indirect	Dynactin
BICD1	Indirect	Intermediate chain

Table 1.10 - The Table shows the cytoplasmic dynein 1-interacting partners. Note: adapted from (Schiavo et al. 2013). Abbreviations: LIS1, lissencephaly; NudE, nuclear distribution protein E; HAP1, huntingtin-associated protein 1; BICD1, Bicaudal D.

The cytoplasmic dynein 2 is composed of dynein heavy chain 2 *DYNC2H1* (Höök and Vallee 2006). Dynein 2 plays a role in retrograde intraflagellar transport and is required for the generation and maintenance of cilium and flagellum.

The cytoplasmic dynein 1-interacting partners

While there are several families of kinesins and myosins, which have evolved to maintain different cellular transport, cytoplasmic dynein is the sole minus-end directed motor protein which performs diverse cellular transport similar to that performed by different types of kinesins (Kardon and Vale 2009). Instead, dynein binds to several proteins (different from those that belong to the dynein complex itself) which are required for a complete function of dynein and for adaptation to its cellular function including dynactin, the essential adaptor (Table 1.10). Interestingly, inhibition or loss of function of either dynactin or LIS1 results in similar phenotypes (neurodegenerative

diseases) that are caused by loss of dynein function. A G59S mutation in p150^{Glued} subunit of dynactin impairs binding of dynactin to microtubules and EB1 (a microtubule-plus end binding protein), and is linked to motor neuron disease in humans (Levy et al. 2006). Also, mutations in LIS1 cause lissencephaly which is characterized by a defect in neuronal migration (Mesngon et al. 2006).

The dynactin complex is composed of 11 different subunits and has a molecular weight of 1 MDa (Kardon and Vale 2009) (Figure 1.12). It has been found that dynactin is required for almost all dynein functions in cells. Dynactin is involved in coupling dynein to cargo, mediated by the interaction between the dynactin subunit ARP1 and β III spectrin, the latter being a filamentous protein which coats the cytoplasmic surface of membranes in Golgi and in membranous organelles. Cargo binding can also be performed by the interaction of dynein with specific receptors, either directly, or through dynactin or Bicaudal D. Dynactin also has a role in increasing the processivity of dynein mediated by the dynactin subunit p150. In addition, during cell division in *Saccharomyces cerevisiae*, dynein is known to be localized at the tip of microtubule plus end and then transferred to the cell cortex by binding to a membrane receptor called the cortically localized nuclear migration 1 (NUM1). While dynein stabilizes itself at the cell cortex, it pulls the astral microtubules to translocate the nucleus into the bud neck. Dynactin was shown to be required to transfer dynein to the cell cortex. Loss of dynactin function leads to dynein accumulation at the plus-end tip and depletion of dynein at the cell cortex. In metazoans, the role of dynein and dynactin localization at the tip of microtubules is less clear. Some evidence suggests that it might be involved in cargo loading and transport initiation.

Other dynein interacting partners are also required for the dynein plus end localization: LIS1 and nuclear distribution protein E (NUDE) (Kardon and Vale 2009). In *S. cerevisiae*, the LIS1 and NUDE homologues: Pac1 and Ndl1 are required for targeting dynein to the plus end and deletion of Pac1 or Ndl1 resulted in depletion of dynein at that position as well as at the cell cortex of the bud cell. However, similar to dynactin, studies in the filamentous fungi *Asperillus nidulans* revealed that loss of NudE function results in the accumulation of dynein at the plus tip leading to a suggestion that NudE is required to release dynein from the plus end and therefore to promote the minus

end directed transport. Figure 1.13 shows several proteins that bind to the microtubule plus end and cooperate in targeting dynein to that position. Also, NudE appears to function as an activator of LIS1, as overexpression of Pac1 and NudF, the LIS1 homologue in *S. cerevisiae* and *A. nidulans* respectively, results in the suppression of the phenotype of Ndl1 and NudE loss of function. In metazoans, dynein, LIS1 and NUDE/NUDEL (the NUDE isoform) are involved in the positioning of the nucleus and the microtubule organization centre (MTOC). During neuronal migration, dynein and LIS1-NUDEL are involved in coupling the movements of the centrosome and the nucleus. Inhibition of dynein or LIS1 increased the distance between the nucleus and the centrosome in the leading process (Shu et al. 2004). In migrating fibroblasts, dynein and LIS1 have a role in the reorientation of the centrosome towards the leading edge. While this centrosome positioning is dependent on cortical dynein, the nuclear movement, however, is nuclear dynein dependent (Levy and Holzbaur 2010).

2.3.2.1.2 Cytoplasmic dynein heavy chain mutation in human diseases

Arg399Gly

Arg399Gly is a mutation located in the tail domain of DHC and causes autosomal recessive congenital SMA-LED. This mutation lies within the dimerization domain but located outside the DIC binding region. A ten year old girl has been reported, carrying two alleles of the Arg399Gly mutation. She showed floppiness and joints contractures at birth. She displayed delays in motor development and speech and learning disabilities. Both parents carry one copy of Arg399Gly with the father exhibiting mild changes in the motor function detected by electromyography (EMG).

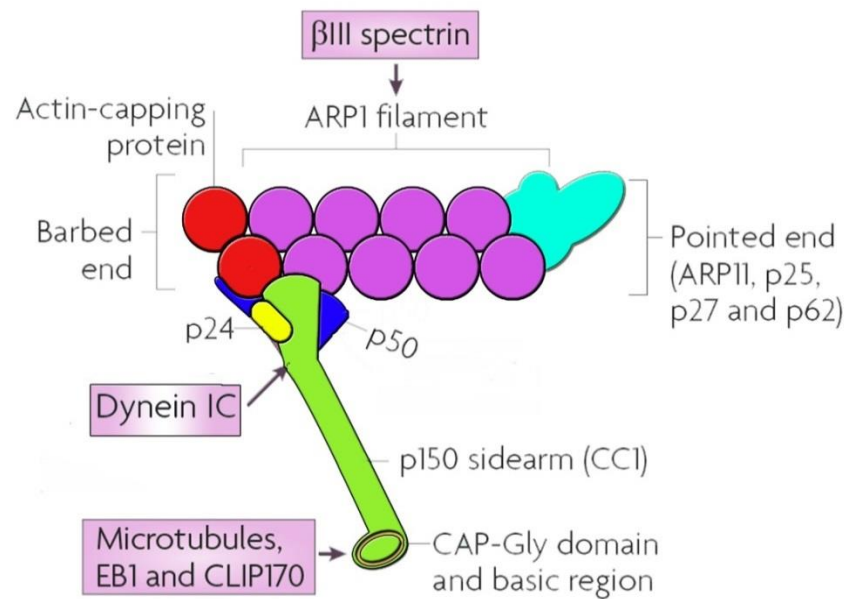
Figure 1.12

Figure 1.12 - The Figure shows a schematic diagram of the dynactin complex. The dynactin complex contains actin-related protein 1 (ARP1) which forms the core of the complex (a short filament coloured in pink). It is involved in linking dynein to cargo through its binding with β III spectrin. At the pointed end of ARP1, there is a subcomplex (coloured in cyan) including ARP11, p25, p27 and p62 which might be involved in the interaction of dynactin with cortical actin. The subcomplex at the barbed end is comprised of a dimer of p150, a tetramer of p50 (also called dynamitin), p24 and the heterodimer actin capping protein. The N-terminus of p150 contains a microtubule binding domain, called a cytoskeleton-associated protein Gly-rich domain (CAP-Gly) as well as a basic region (coloured in yellow). Other proteins can also bind to the CAP-Gly domain including the microtubule plus end-associated proteins end binding 1 (EB1) and CAP-Gly domain-containing linker protein 170 (CLIP170). The binding of dynactin to cytoplasmic dynein is mediated through an interaction between p150 and DIC, the cytoplasmic dynein subunit. Note: adapted from (Kardon and Vale 2009).

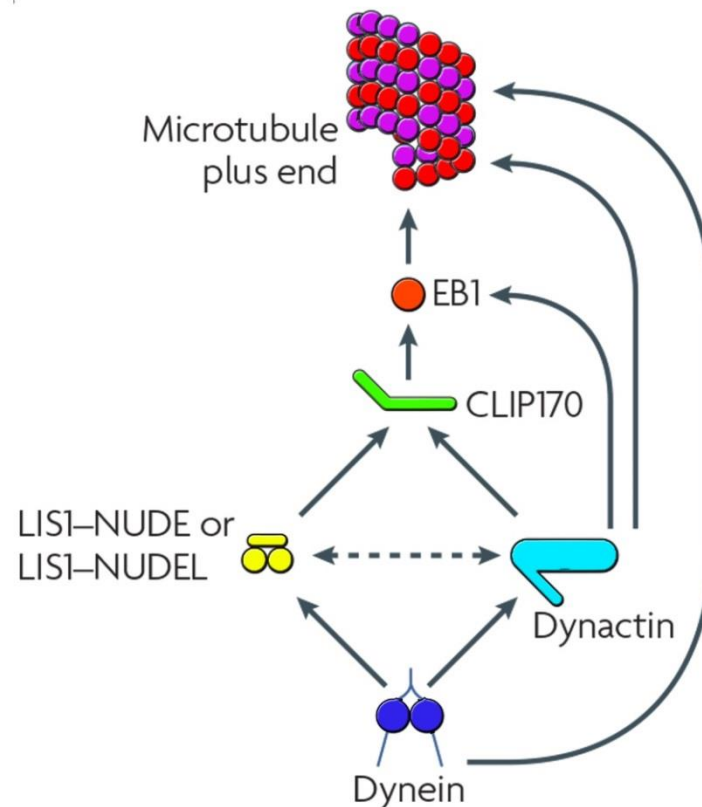
Figure 1.13

Figure 1.13 – Microtubule plus end binding proteins. The Figure shows several proteins including **EB1**, **CLIP-170**, **dynactin** and **LIS1-NUDE** and **LIS1-NUDEL** that bind to the microtubule plus end and cooperate in targeting dynein to that position. **EB1** is required for CLIP170 and dynactin interaction with microtubules. All three can also bind directly to microtubule. CLIP-170 probably mediates LIS1 recruitment to microtubule. Dynein can then be targeted to the plus end through its interaction with LIS-NUDE or LIS1-NUDEL and dynactin. Subsequently, dynein can probe for cargo or for the cell cortex. After cargo loading, the interaction between dynein and the microtubule plus end is released by dynactin and LIS1-NUDE or LIS1-NUDEL. Note: adapted from (Kardon and Vale 2009).

2.3.2.1.3 Cytoplasmic dynein heavy chain mutation in mouse models

***Loa* (Legs at odd angles)**

Loa is a mouse model harbouring a mutation of phenylalanine to tyrosine at position 580 in the tail domain of DHC (Hafezparast et al. 2003). *Loa* exhibits motor neuron dysfunction due to perturbation of neuron-specific functions of cytoplasmic dynein and is inherited in an autosomal dominant fashion. This mouse model was generated using the chemical mutagen *N*-ethyl-*N*-nitrosourea (ENU) which generates T to A point mutations in particular. *Loa* as the name implies exhibits abnormal hindlimb clenching when suspended by the tail reflecting motor dysfunction (Figure 1.14). The heterozygotes have a normal life span whereas the homozygotes die 24 hours after birth, possibly due to lacking the ability to move and feed. Heterozygous *Loa* develop an age-related slowly progressive locomotion deficit manifested by gait abnormality, unusual body twisting, decreased grip strength and rotarod performance deficits. The *Loa* mouse model also shows similar phenotypes to the SMA-LED in human cases: gait abnormality, spinal motor neuron loss (loss of α motor neurons of the anterior horn) and abnormality in cortical neuron migration and development (Hafezparast et al. 2003; Ori-McKenney and Vallee 2011). Importantly, two mutations M581L and I584L in human DHC, which cause SMA-LED, are only 1 and 2 amino acids from the site of the substitution mutation in the *Loa* mouse (Harms et al. 2012; Scoto et al. 2014) (Figure 1.15, I584L). As the *Loa* mutation is located in the tail domain which mediates dimerization with another tail domain of DHC and the association of DHC with DIC, it was predicted that *Loa* mutation affects the integrity of the dynein complex. Indeed, it has been documented that this mutation changes the binding property of DIC to DHC which subsequently affects DIC binding affinity to dynactin (Deng et al. 2010). In addition, the *Loa* mutation affects the performance of cytoplasmic dynein during cellular stress (Hafezparast et al. 2003). Evidence for this came from the observation of impaired Golgi reassembly after nocodazole treatment in MEFs isolated from *Loa* homozygous embryos. Interestingly, the *Loa* mutation impairs the retrograde transport in α -motor neurons. This might explain the slowly progressive neurodegenerative phenotype observed in heterozygous *Loa* (due to reduced constant supply of trophic factors). Also, the abnormal facial neuron migration observed in homozygous *Loa* is

most likely due to a defect in dynein function at the cell cortex for pulling the microtubule organization centre (MTOC) and nucleus in the direction of migration. In addition to the overt motor neuron dysfunction, the *Loa* heterozygous mice exhibit proprioceptive sensory defect, *+/Loa* mutants exhibit a reduction in the number of lumbar dorsal root ganglion neurons (DRG), compared to the wild type, however, this change was not observed in the number of cervical DRG neurons (Chen et al. 2007). Like α -motor neurons, the sensory neurons with longer axons require a significant intracellular trafficking and therefore are most likely to be affected by mutations in DHC. This explains why the hindlimbs are more affected than the forelimbs in mice.

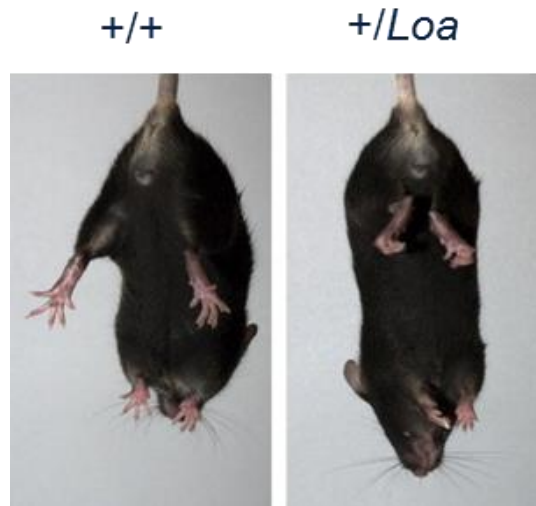
Figure 1.14

Figure 1.14 - The Figure shows the *Loa* mouse model exhibiting hindlimb grasping when the mouse is suspended by the tail compared to the wild type mouse which shows splayed legs.

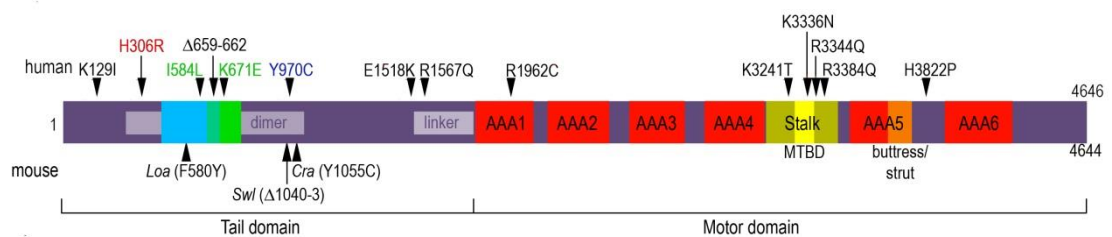
Figure 1.15

Figure 1.15 - The Figure shows a schematic diagram of cytoplasmic dynein heavy chain 1 with mutations. Arrows which are located above the diagram represent the human mutations while those that are located under the diagram represent the mouse mutations. Note: adapted from (Schiavo et al. 2013).

***Cra1* (Cramping-1)**

Cra1 is another mouse model harbouring a mutation in the tail domain of DHC. The *Cra1* mutation is caused by a change in tyrosine to cysteine at position 1055 (Hafezparast et al. 2003) (Figure 1.15). The *Cra1* mouse model exhibits a dominant phenotype of neuronal dysfunction manifested by an age-related progressive locomotor deficit. The homozygous *Cra1* mutant exhibits a severe phenotype manifested by the inability to feed and die within 24 hours after birth. The *Cra1* phenotype was initially interpreted as motor neuron dysfunction (Hafezparast et al. 2003). The heterozygous *Cra1* shows a severe hindlimb clasping at 16 months of age consistent with motor neuron loss in the ventral horn of the spinal cord. However, Dupuis et al reported that the *Cra1* mouse does not show overt motor neuron disease since no motor neuron loss was observed in the aged *Cra1* mice but rather it exhibits proprioceptive sensory neuropathy (Dupuis et al. 2009).

***Swl* (Sprawling)**

The sprawling mouse model exhibits a neuronal dysfunction phenotype and was generated in an irradiation-mutagenesis experiment (Figure 1.15). The phenotype arose from a 9 base pair deletion from exon 12 of cytoplasmic DHC (1040-1043) which results in substitution of four amino acid change (GIVT) with alanine (X.-J. Chen et al. 2007). The DHC mutation in *Swl* mice leads to proprioceptive sensory neuron degeneration without motor neuron involvement.

2.3.2.1.4 Dynein functions

2.3.2.1.4.1 Intracellular trafficking and axonal transport

Cytoplasmic dynein 1 is involved in microtubule-based transport of vesicles, organelles and proteins. Microtubule cytoskeleton is used for long distance intracellular transport. This type of transport is important especially in large polarized cells such as neurons that require transporting materials from soma to nerve termini and vice versa. In such cells it is difficult to rely on diffusion to distribute proteins and organelles, therefore directed transport is essential in neuronal cells. While there are three types of kinesins which drive anterograde motility along the axon, cytoplasmic dynein is the only known motor protein that drives the retrograde transport in neurons.

Cytoplasmic dynein 1 is also involved in driving the inward motility in biosynthetic pathways. For instance, dynein is implicated in transporting vesicles from the endoplasmic reticulum to Golgi.

2.3.2.1.4.2 Degradative pathways

Autophagy is a highly conserved dynamic process and requires autophagosome formation which sequesters some misfolded proteins and dysfunctional organelles for lysosomal degradation (Tanida, Ueno, and Kominami 2004). During autophagy, a part of the cytoplasm is sequestered by autophagosomes to form double-membraned organelles which engulf misfolded proteins and ageing organelles and subsequently fuse with lysosome for degradation. The resulted amino acids can then be recycled to synthesize new proteins. Atg12-conjugation, an autophagy related protein, and LC3-modification, a microtubule associated protein 1 light chain 3, are important for autophagosome formation and dynamicity and they are involved in preautophagosomes and autophagosome formation, respectively. Conjugation of Atg12 with Atg5 necessitates the formation of an autophagosomal precursor, an isolation membrane, in the cytosol, where Atg12/Atg5 localizes to the outer side. This localization of Atg12/Atg5 conjugate is required for the isolation membrane elongation. In addition, another modification is performed on LC3 which is required for autophagosome formation. Immediately after translation, LC3 is cleaved at its C-terminal in order to facilitate the formation of the cytosolic form LC3-I. This cleavage exposes its C-terminal glycine for phospholipid modification (by conjugating to phosphatidylethanolamine) to form the membrane-bound form LC3-II. This conjugation also facilitates its binding to the autophagosome membrane. The modified form LC3-II has been used as a universal marker for autophagy activity since it localizes to both preautophagosomes and autophagosomes during autophagy. It has been thought that the amount of LC3-II correlates with the extent of autophagosome formation as its levels increased during autophagy induction. However, since LC3-II is bound to the inner autophagosomal membrane, it is also subjected to degradation as ultimately all LC3-II-bound autophagosomes are degraded through fusion with autolysosomes (Juhász 2012). Therefore, LC3-II levels depend on both autophagy induction and autophagic degradation activity (autophagy flux).

The removal of misfolded proteins or dysfunctional organelles is a critical process in maintaining the homeostasis of post-mitotic neuronal cells (Hara et al. 2006; Komatsu et al. 2006; Moughamian and Holzbaur 2012). It is thought that autophagy has a protective role against the development of neurodegenerative disorders. Mice lacking either Atg5 or Atg7 develop cytoplasmic inclusions and ultimately motor impairment leading to neurodegeneration. This suggests that the continuous clearance of cytoplasmic inclusions is important for neuronal function.

Cytoplasmic dynein 1 is involved in driving the inward motility in degradative pathways. For instance, dynein is implicated in transporting compartments such as late endosomes and autophagosomes for lysosomal degradation (Moughamian and Holzbaur 2012). During autophagosome formation, slow autophagosome movement through the cytoplasm was observed (Kimura, Noda, and Yoshimori 2008). After completion, autophagosomes undergo rapid movements towards the cell centre and near centrosomes where lysosomes are located. It was documented that this rapid autophagosome movement is dynein-dynactin dependent (Kimura, Noda, and Yoshimori 2008). The inhibition of dynein by microinjecting anti-dynein intermediate chain antibody impaired the rapid movement of autophagosome. In neuronal cells, autophagosomes form at nerve terminus and undergo retrograde transport to the soma for lysosomal degradation. Therefore, microtubule-based and dynein-dependent movement of autophagosomes are important in neurons since clearance of protein aggregates has a protective role against neurodegeneration.

2.3.2.1.4.3 Endocytic pathways

Endosomes are one type of cargo that dynein carries via binding to dynactin. When a ligand binds to its receptor, the whole complex is endocytosed into clathrin-coated vesicles (Doherty and McMahon 2009). Clathrin is then dissociated from the vesicles before the latter start fusing with early endosomes. After fusion, efficient sorting occurs including the uncoupling of the receptor and the ligand. The receptor is then transported back for recycling while the ligand-containing early endosome continues traveling towards the perinuclear region where lysosomes are located for degradation. However, not all receptors are recycled. The transferrin receptor, for example, is

recycled but EGF receptors are mainly degraded in the lysosomes. The transport of the early endosomes to late endosomes is mediated by large vesicles named endosomal carrier vesicles (ECVs).

The movement of ECVs to late endosomes was shown to be microtubule- and dynein-dependent (Aniento et al. 1993). Dynein also has a role in receptor sorting, motility and maturation of early endosomes (Driskell et al. 2007). Using live cell imaging analysis, some early endosomes exhibit short-range motility while others alternate between short and long distance movements. When dynein function was inhibited by microinjecting Hela cells with CC1 [a polypeptide that binds dynactin binding site on dynein intermediate chain (DIC) and therefore preventing dynactin from binding], the long-range rapid movement of endosomes towards the cell centre was rarely observed. In addition, compared with control cells, which showed rapid separation of cargo (i.e. the separation of transferrin receptor from the epidermal growth factor-containing endosomes for receptor recycling), CC1-injected cells exhibited a delay in cargo separation. This experiment suggests that dynein is also implicated in efficient receptor sorting at early endosomes. Inhibition of dynein also slowed the maturation of endosomes indicating that dynein is also involved in early endosome maturation.

Growth factors and their signalling cascades

Brain derived neurotrophic factor

Neurotrophins are a family of four proteins which consists of: the nerve growth factor (NGF), the brain-derived neurotrophic factor (BDNF), neurotrophin 3 (NT3) and neurotrophin 4 (NT4). Neurotrophins can bind to two types of structurally related receptors namely the tropomyosin-related kinase (Trk) receptor and pan-neurotrophin receptor (p57^{NTR}) (Huang and Reichardt 2003). While all the aforementioned neurotrophins can bind to p75^{NTR} receptor, each can bind differentially to Trk receptors: NGF binds to TrkA, BDNF and NT4 bind to TrkB and NT3 binds to TrkC. In relevance to my research, I will focus on TrkB and the signal transduction induced by BDNF binding.

Upon BDNF binding, TrkB is activated by homodimerization and autophosphorylation of key tyrosine residues located in the cytoplasmic C-terminal domain. The active

BDNF-TrkB complex is then endocytosed and transported retrogradely (in a dynein-dependent manner) towards the cell soma for degradation in the lysosomes. As the BDNF/TrkB-containing endosome is transported towards the cell soma, it signals which therefore triggers downstream signalling pathways.

Phosphorylation of some key tyrosine residues located in the cytoplasmic C-terminal domain of the Trk receptor creates binding sites that can be recognized by the effector proteins (Figure 1.16). As a result, this stimulates many downstream signalling pathways including the phosphoinositide-3-kinase/protein kinase B (PI3K/Akt) and the mitogen activated protein kinase. In relevance to my research, I will focus on BDNF-mediated ERK1/2 (the extracellular signal related kinases 1 and 2) activation pathways.

Three signalling pathways are known to mediate ERK1/2 activation upon binding of BDNF to TrkB: PLC- γ 1, Ras-MAP kinase and Crk/Rap1 (Figure 1.16) (Huang and Reichardt 2003). Phosphorylation of Tyr816 on the TrkB receptor creates a binding site for phospholipase C (PLC- γ 1) which is therefore phosphorylated by the Trk receptor kinase. Active PLC- γ 1 hydrolyses phosphatidylinositol 3,4-bisphosphate (PtdIns (4,5)P₂) to generate inositol tris-phosphate (IP₃) and diacylglycerol (DAG), required for the stimulation of protein kinase C (PKC). PKC is required for ERK1/2 activation via MEK1/2 to promote neurite outgrowth in PC12 upon NGF binding (Corbit, Foster, and Rosner 1999). In addition, phosphorylation of Tyr515 creates a binding site for the adaptor protein Shc followed by a recruitment of the adaptor protein Grb2, which forms a complex with the Ras exchange factor SOS. The GEF activity of SOS promotes the dissociation of guanosine diphosphate (GDP) from inactive Ras, so that Ras can bind guanosine triphosphate (GTP) to become active. Active Ras then activates ERK1/2 through a pathway involving sequential activation of Raf and MEK. ERK1/2 activation by the Ras-MAP kinase pathway is transient. Termination of this pathway seems to be mediated through phosphorylation of SOS by active ERK1/2 resulting in the dissociation of the SOS-Grb2 complex.

On the other hand, prolonged activation of ERK1/2 is mediated through a distinct signalling pathway involving the adaptor protein Crk, the guanine nucleotide exchange factor C3G, the small G protein Rap1, and Raf (Huang and Reichardt 2003). Upon

activation of the TrkB receptor, Crk is phosphorylated which results in C3G activation. C3G acts as a guanine nucleotide exchange factor for Rap1. Consequently, Rap1-GTP stimulates Raf which subsequently activates ERK1/2.

Activation of the aforementioned signalling pathways promotes several cellular functions including cell proliferation, survival, axon growth, differentiation and neuroplasticity (Duman and Voleti 2012). This can be mediated by phosphorylating proteins to promote local axonal elongation (Atwal et al. 2000). Alternatively, phosphorylated ERK1/2 translocates to the nucleus where it phosphorylates transcription factors including CREB (cAMP response element-binding) leading to the expression of immediate early genes such as c-Fos (Sheng, Mcfadden, and Greenberg 1990).

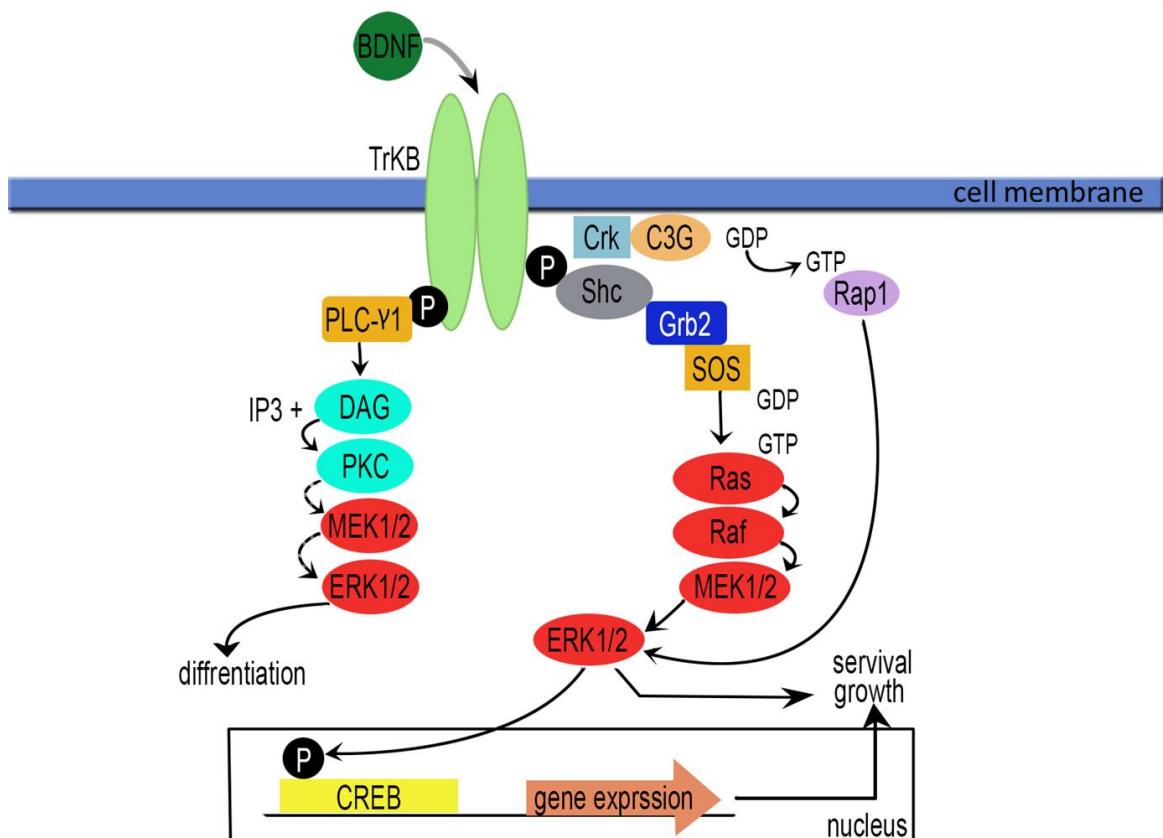
Figure 1.16

Figure 1.16 – Figure showing BDNF/TrkB-mediated ERK1/2 activation signalling pathways. BDNF binding to TrkB receptor induces dimerization and autophosphorylation of the receptor. Phosphorylated tyrosines act as a docking site for adaptor proteins: Crk (CT10 regulator of kinase), the Src homology 2 domain-containing (Shc) adaptor protein, phospholipase C (PLCγ1). Phosphorylation of the tyrosine 816 of TrkB leads to the recruitment of PLCγ1 which hydrolyses phosphatidylinositol 3,4-bisphosphate (PtdIns(4,5)P₂) and diacylglycerol (DAG). The latter is required to activate protein kinase C (PKC) which promotes differentiation and neurite outgrowth through activation of ERK1/2. Phosphorylation of tyrosine 515 of TrkB results in the recruitment of Shc followed by the formation of Grb2/SOS complex (Growth factor receptor-bound protein 2/ Son of sevenless). SOS acts as a guanine exchange factor for Ras which therefore results in transient activation of the mitogen-activated protein kinases (MAPK): Ras, Raf, MEK and ERK. Phosphorylation of TrkB receptor at 515 also promotes the recruitment of Crk and C3G and the activation of Rho GTPase 1 (Rap1) which leads to ERK1/2 activation. ERK1/2 activation promotes several cellular functions including neuronal survival and axon growth either via phosphorylating proteins or activating transcription factors such as CREB. Dotted arrows refer to an ERK1/2 activation by PKC upon TrkA receptor activation (Corbit, Foster, and Rosner 1999). Note: adapted from (Duman and Voleti 2012; Huang and Reichardt 2003).

Epidermal growth factor (EGF) signalling cascade

Epidermal growth factor receptor (EGFR) is a member of ErbB cell surface receptor tyrosine kinases (RTK) which span the cell membrane and endocytose upon binding the ligand EGF (Bazley and Gullick 2005).

Similar to BDNF binding to TrkB receptor, upon binding of EGF to EGFR, this initiates the receptor dimerization and autophosphorylation followed by the internalization of the EGF/EGFR complex (Bazley and Gullick 2005). Phosphorylation of key tyrosine residues of the cytoplasmic C-terminal domain of EGFR results in initiating signalling pathways: the Ras MAPK and PI3K/Akt leading to cell proliferation and survival (Chong and Jänne 2013; Bazley and Gullick 2005). Activation of EGFR results in the recruitment of the adaptor protein Grb2 which forms a complex with SOS. This promotes a transient activation of ERK1/2 signalling pathway involving Ras, Raf, MEK1/2 and ERK1/2. Active ERK1/2 phosphorylates downstream transcription factors including ELK1 which induces the expression of the immediate early genes (IEGs) such as c-Fos by binding to the cis acting element SRE (serum response element) located upstream of the c-Fos promoter (Treisman 1992).

We showed that EGF degradation was delayed in homozygous *Loa* mouse embryonic fibroblasts (MEFs) in comparison to the wild type. This delay caused aberrant ERK1/2 activation and c-Fos expression (Garrett et al. 2014). Moreover, BDNF-induced endocytic trafficking was also impaired in cultured motor neurons isolated from heterozygous *Loa* embryos, resulting in aberrant ERK1/2 activation and c-Fos phosphorylation. In comparison to MEFs where ERK1/2 was not activated during serum starvation, ERK1/2 as well as c-Fos were activated in motor neurons of both wild type and *+/Loa*, however, levels of activation were higher in *+/Loa* (Garrett et al. 2014). This, therefore, indicates that motor neurons are more susceptible to serum starvation-induced stress than MEFs. In addition, compared to ERK1/2 activation levels after stimulation with BDNF, active ERK1/2 was slightly increased in response to starvation whereas c-Fos was massively activated (Garrett et al. 2014). This raised the possibility of implicating other MAP kinases [such as c-Jun N-terminal kinase (JNK) and p38] in c-Fos activation. I contributed to this study by identifying the MAP kinase responsible for c-Fos activation during serum-starvation and/or BDNF stimulation. I

showed that c-Fos activation is ERK1/2 dependent during starvation and after BDNF stimulation. Thus, our study provides evidence for a cell type specific response to serum starvation stress and that the ERK1/2-cFos signalling pathway might be a contributory factor to the pathogenesis of *Dync1h1*-related neurological diseases (Garrett et al. 2014) (the paper is attached).

2.3.2.1.4.4 Axonal pathfinding and growth dynamics

Migration in non-neuronal cells

Cell migration plays important roles during wound healing and development. During cell migration, the cell forms two dynamic and actin filament-based structures named the lamellipodia and lamella (Ponti et al. 2004). The lamellipodium is located 1-3 μm beneath the plasma membrane at the leading edge whereas the lamella is the zone located between the lamellipodium and the nucleus. The lamellipodial region contains a meshwork of actin filaments and actin polymerization in this region provides the force required for protrusion formation (Tojkander, Gateva, and Lappalainen 2012). The lamella, however, is composed of actin filament bundles called traverse arcs. Although both regions contain two distinct actin filament networks that are believed to overlap, the lamellipodial actin filament lies on top of the lamellar actin network (Figure 1.17, in light red and grey, respectively). Each structure has a distinct molecular signature. The lamellipodium contains a high concentration of the actin nucleator Arp2/3, a protein that is responsible for generating free barbed ends of the filaments i.e. exposing certain domain of the F-actin filament so that it can be recognized for polymerization. In contrast, the lamella is enriched with myosin II and tropomyosin. In addition, the lamellipodium and the lamella have two distinct kinetics. The lamellipodium is known to have a fast retrograde flow, whereas the lamella has a slow retrograde flow (Ponti et al. 2004; Medeiros, Burnette, and Forscher 2006). Also, the dynamics of the actin filament network in the lamella, compared to that of the lamellipodium, is less, due to the presence of mature focal adhesions (FAs) (read below about the role of FAs).

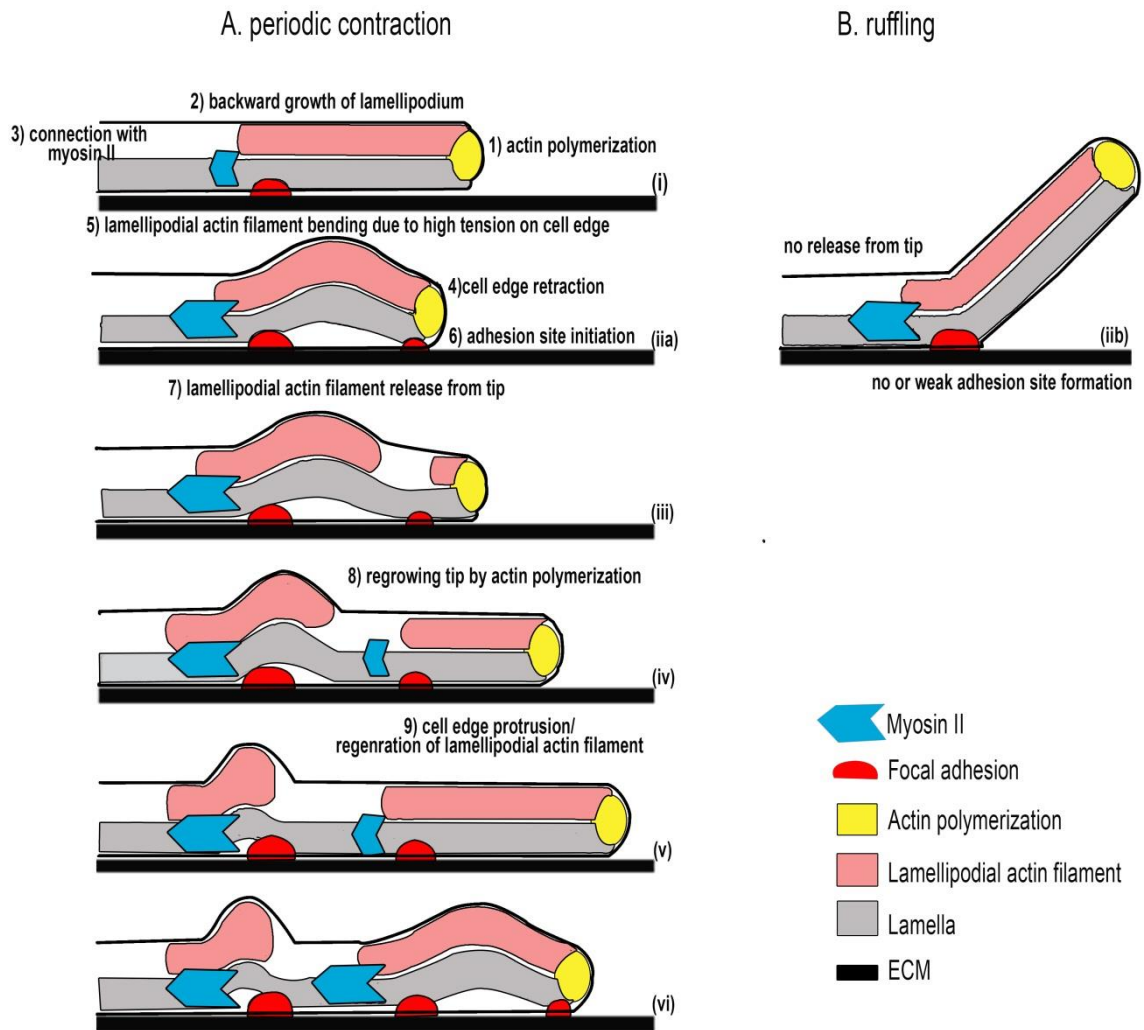
Figure 1.17

Figure 1.17 – Figure depicting the interplay between dynamic actin filaments and myosin II to promote the leading edge advance. (A) In the presence of strong adhesion sites, actin polymerization (yellow) results in growing the lamellipodial actin filament backward towards the myosin II cluster where they connect (i). The actomyosin contractility which is generated by myosin II pulling the actin filament backward causes retraction of the edge (iia). As a result, adhesion sites will form to stabilize the leading edge by bridging the lamellipodial actin filaments to the ECM. This will cause the lamellipodia buckling due to high tension exerted on the leading edge. Continuous pulling by myosin II will release the lamellipodia from the tip (iii). The tip will regrow again through actin polymerization resulting in the formation of new cell protrusions as well as new lamellipodial actin filaments (iv). The new edge protrusion will be further shifted forward (compare v with i). The advance of the leading edge will continue until the lamellipodial actin filaments reach another myosin II cluster which then will cause retraction of the edge (vi). (B) Depicting the leading edge ruffling as a result of weak or no adhesion sites (iib). Note: adapted from (Giannone et al. 2007).

Myosin II has a role in the formation of protrusion and actin filament bundles (stress fibres). No actin filament bundles were formed when myosin II was inhibited (Tojkander, Gateva, and Lappalainen 2012). The formation of cell protrusion depends on the interplay between actin filament dynamics, myosin II-dependant contraction and FA assembly and disassembly. The interaction between the actin filament and the motor protein myosin II generates contractile forces. As a result, these forces cause severing of actin filaments, a process that generates retrograde actin flow. These traction forces generated by actomyosin pull actin filaments away from the leading edge towards the cell centre. This pulling force will also cause the retraction of the leading edge and reduce protrusion formation. FAs are protein cluster bridges between the extracellular matrix (ECM) outside the cell and actin filaments inside the cell. Forces exerted by myosin are applied to (transmitted to) the ECM through focal adhesion connection to the actin filaments. Binding of FAs to actin filament attenuates contractile forces and reduces the retrograde actin flow. This linking breaks the balance between disassembling of the actin filaments (retrograde actin flow) and actin polymerization which as a result establishes protrusion (Dent, Gupton, and Gertler 2011). Actin polymerization will continue to form protrusions, while FAs counter the contractile force and slow the retrograde actin flow. Thus, the balance between the rate of actin polymerization and retrograde flow determines the fate of protrusions (whether to be extended or withdrawn). During protrusion formation, actin polymerization exceeds both retrograde flow and actin depolymerisation whereas during the leading edge retraction, the retrograde flow and actin depolymerisation exceed actin polymerization (Gomez and Letourneau 2014).

The distribution and the dynamics of actin filaments and FAs were mapped in migrating keratinocytes using live cell imaging of cells transfected with GFP-tagged vinculin, a FA marker, or GFP-tagged actin and applying the cell shape normalization technique as reported in Möhl et al (Möhl et al. 2012). Both FAs and actin filaments exhibit a polarized distribution during migration. The FAs are mainly present at the leading edge and on the lateral sides of the cell, being more concentrated in the former. At the rear, there are only a few focal adhesions. The amount of actin flow is negatively correlated with the presence of FAs. At the cell front, there is a large

number of small FAs which slow the centripetal movement of the actin flow, whereas at the back, it increases because of the low number of FAs. As FAs couple the actomyosin network to the substrate, therefore, the differential spatial distribution of FAs within the cell determines the pattern of traction forces that pull the cell towards a certain direction. Actin filaments show a more spread out pattern (criss-crossed) at the cell front due to the high density of FAs which decelerate actin flow. In the region of low FA density i.e. the cell rear, and therefore fast actin flow, the actin network was more compressed forming a narrow band behind the nucleus.

Möhl et al (2012), using their mapping technique, revealed that differential patterns of FAs assembly and disassembly (FA turnover) affects the distribution of both actin flow and traction forces (Figure 1.18A, B and C). At the cell front, the rate of focal adhesion assembly relative to its disassembly is high, resulting in a large number of small FAs (also termed focal complex, FXs) (Figure 1.18A, cell front). As a consequence of the coupling of the actin to the substrate by these FAs, there is reduced actin flow within this region (Figure 1.18B, cell front, and small arrows). However, due to their small size they only provide low traction forces (Figure 1.18C, small red arrows). Nonetheless, the reduced actin flow promotes the formation of protrusion (Figure 1.18B, Cell front, brown arrows). These FAs start to disassemble when they depart the leading edge. This occurs when the cell membrane protrudes and as a consequence new FAs are formed (Figure 1.18A, cell front and small green spots) and the old FAs matured and ultimately disassembled (Figure 1.18A, cell front and large green spots). The FAs that are located to the sides do not disassemble and continue to grow and mature (Figure 1.18A, lateral side of the cell). The turnover of these lateral FAs is low resulting in more matured, large and stable FAs (Figure 1.18A, lateral and dark green spots). This increases the effectiveness of the actin-substrate coupling resulting in higher traction compared to the frontal area (Figure 1.18C, lateral side, large red arrows). Due to the forward migration of the cell, these large FAs will reach the rear part of the cell and ultimately disassembled. At the rear, there is a low number of FAs, due to higher disassembling, resulting in a low actin-substrate coupling and high actin flow (no traction). This high actin flow promotes the retraction of the back of the cell (Figure 1.18B, cell rear, and black large arrows).

Figure 1.18

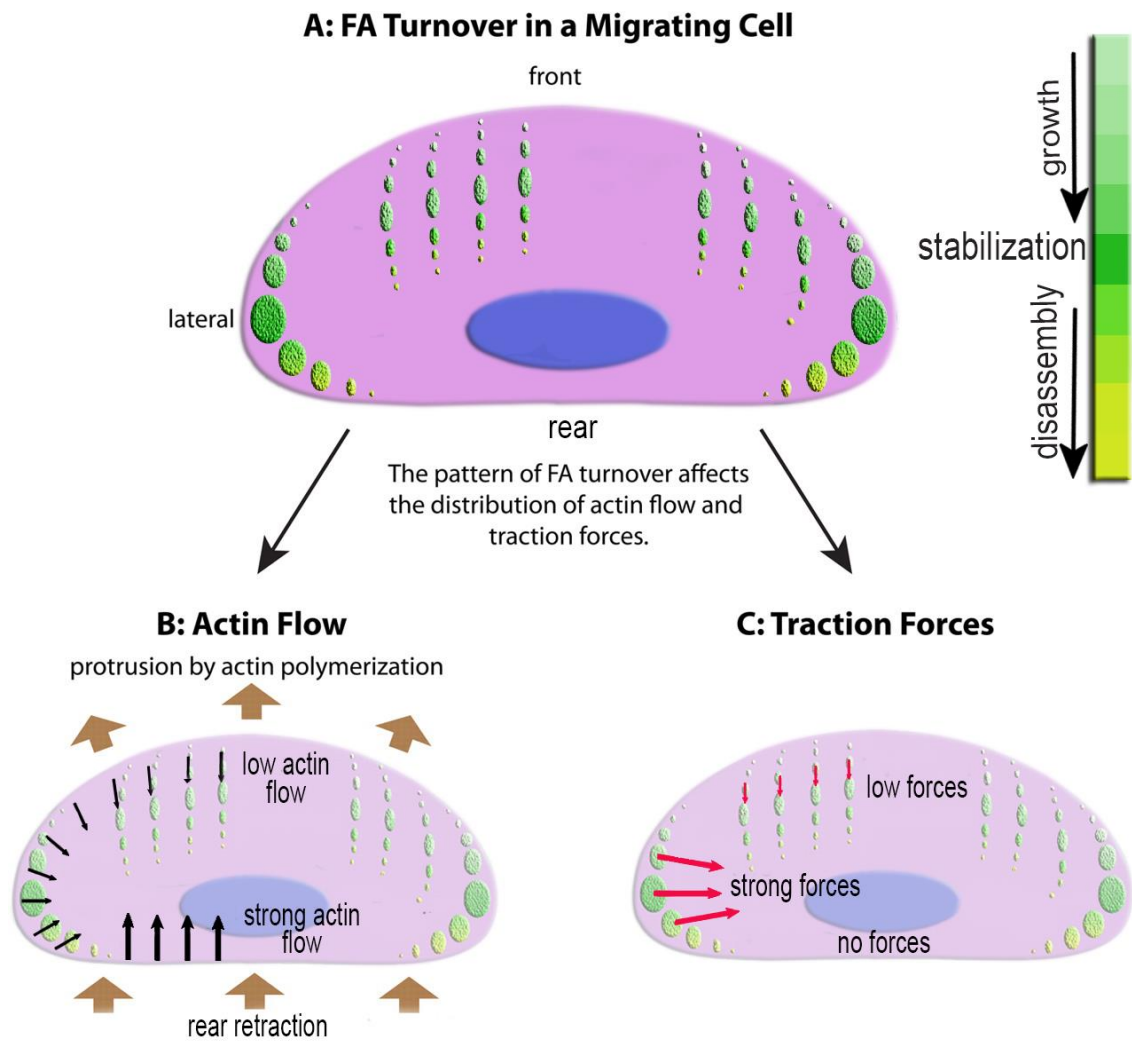


Figure 1.18 – The Figure shows the differential pattern of FA assembly and disassembly (A) and how this affects the distribution of actin flow (B) and traction forces (C). Note: adapted from (Möhl et al 2012).

Several models have been proposed to understand how actin filaments, myosin II and FAs are linked and organized to promote the leading edge advance. In the first model (Giannone et al. 2007), as it has been proposed by Ponti et al (2004) both the lamellipodium and the lamella appear as two distinct but overlapping actin networks (Figure 1.17, light red and gray, respectively). At the cell front, actin polymerization (yellow) results in growing the lamellipodial actin filaments (light red) backward towards the myosin II cluster (blue arrow) (Figure 1.17, i). Myosin II pulls the lamellipodial actin filaments to the back and simultaneously exerts high tension at the leading edge. As a result, nascent adhesions are formed (red). If nascent adhesions are strong, pulling the lamellipodial actin filament by myosin II will buckle the lamellipodial actin filament and retract the edge (Figure 1.17, iia). Continuous pulling results in the release of the lamellipodial actin filaments from the tip (Figure 1.17, iii) and the tip will regrow again and extend backward until it reaches another cluster of myosin to start the cycle again (iv-vi). If nascent adhesions are weak, this will cause detaching the leading edge from the ECM and will cause the membrane to ruffle (iib).

A more recent model was proposed in which both the lamellipodium and the lamella appear as two non-overlapping distinct actin networks (Figure 1.19). When a new protrusion is formed, myosin II appears in the lamellipodia only during the peak of protrusion formation, compressing the meshwork of the lamellipodial actin filaments, transforming it into actin arcs and then pulling it back into the lamella. This process will result in the retraction of the leading edge. As a consequence of this pulling force, nascent adhesions are formed, coupling actin arcs with the ECM. If the coupling is strong, this will slow down the backward movement of actin arcs to the lamella and will allow another new protrusion to form. The new protrusion will be shifted forward compared to the old one and the edge retraction in this cycle will also be shifted further forward compared to the old retraction. If the coupling is weak, this will result in backward slipping of focal adhesions which are still associated with actin arcs but not with the ECM and consequently no new protrusion will be formed.

Figure 1.19

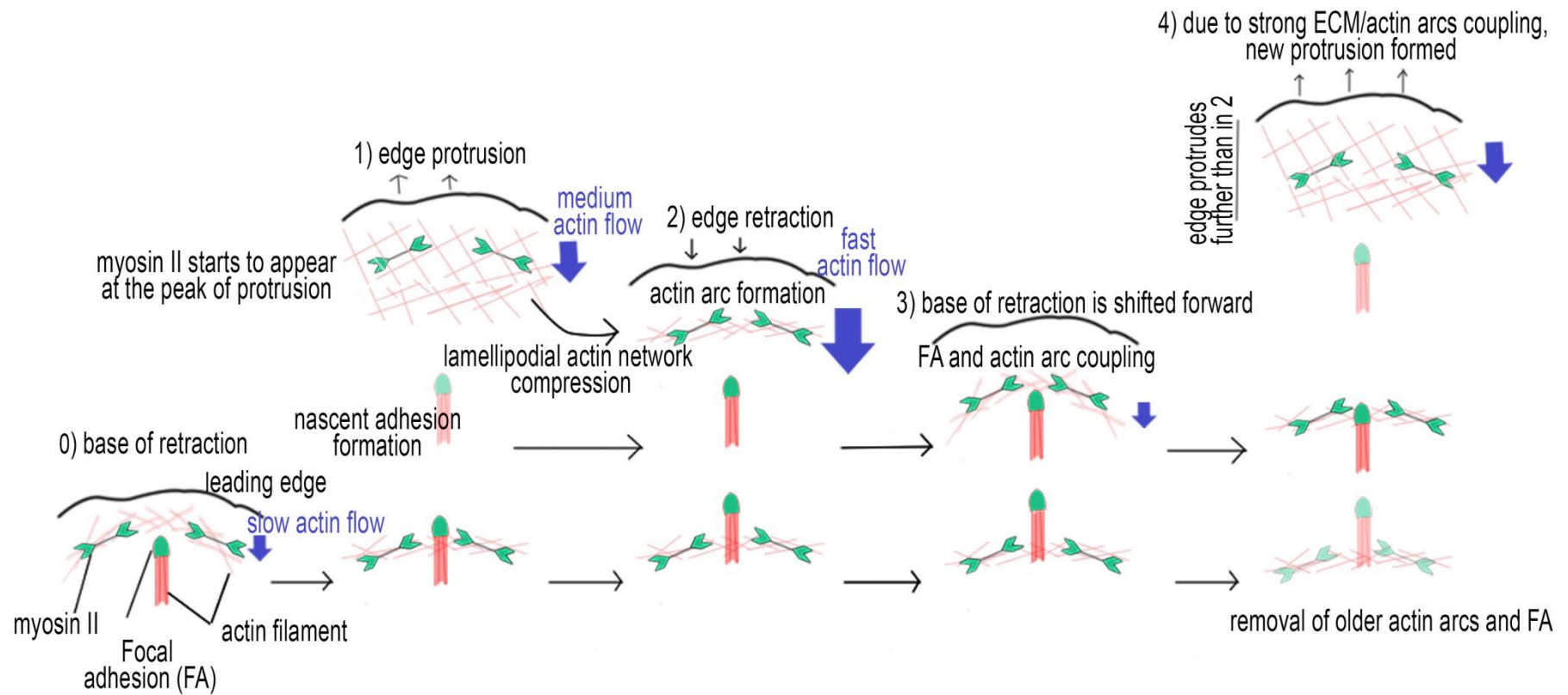


Figure 1.19 – The Figure shows a schematic diagram of the leading edge growth. Step (0) shows the base of an old retraction where focal adhesions link a newly formed actin arcs to the extracellular matrix (ECM). In step 0, actin arcs and ECM coupling is strong. This allows new lamellipodial actin network and new protrusion to form (by actin polarization) which is followed by the formation of nascent adhesions (step 1). In step 1, myosin II starts to appear at the peak of protrusion which results in generation of local network contraction. As a consequence, lamellipodial actin network is compressed and the edge is retracted (step 2). Actin arcs move backward towards the lamella due to the fast retrograde flow (step 2). This movement slows when actin arcs reach and link to focal adhesions (step 3). The base of retraction at this stage is shifted forward compared to the old one (compare 3 and 0). If the actin arcs/ECM coupling is strong, a new lamellipodial actin network is formed and a new protrusion is established (step 4). At this stage, the new protrusion is shifted forward compared to the older protrusion (compare 4 and 1). In cells that showed no leading edge advance, actin arcs which are linked to focal adhesions, slip rearward due to a weak coupling with the ECM.

Migration in neuronal cells

The structure of growth cones

A growth cone is a motile domain located at the distal tip of a growing axon. Based on the cytoskeleton location, the growth cone can be divided into three compartments: 1) The peripheral domain which is an actin-rich region, comprised of polarized actin filament bundles embedded in a criss-crossed, less polarized actin filament network. 2) The central domain contains microtubule bundles that extend from the axonal shaft and extend single microtubules to explore the peripheral domain. 3) The transition zone which represents an interface between the peripheral and the central domain and contains actin arcs (Figure 1.20). The actin filament bundles often extend beyond the lamellipodium to form a finger-like domain called filopodia which has an important role in axonal pathfinding. Abnormal growth cone steering was observed in growth cones lacking filopodia after treatment with cytochalasin B (Bentley and Toroian-Raymond 1986).

The growth cones respond to the environmental guidance cues by remodelling cytoskeletons to move forward and steer. Below is a brief description of the roles of two essential components responsible for growth cone remodelling: actin filaments and microtubules.

The role of actin dynamics in growth cone motility

Two aspects of actin dynamics underlie growth cone movement: 1) actin filament polymerization, depolymerisation and recycling and 2) retrograde actin flow, that is generated by both the interaction of myosin II with actin, and the resistance of the plasma membrane tension against actin polymerization (Gomez and Letourneau 2014; Medeiros, Burnette, and Forscher 2006). The fast retrograde flow in the peripheral domain pushes the actin network (Figure 1.21, in brown) and actin bundles (Figure 1.21, in red) backward (Figure 1.21, step 1). This results in actin arcs formation and therefore translocation into the transition zone (pink area) where retrograde flow is slower (Figure 1.21, step 2). As a consequence of actin network contraction in the transition region, actin bundles exhibit buckling near the proximal end and are

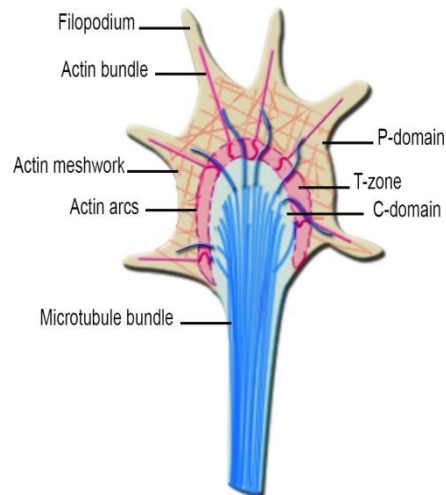
Figure 1.20

Figure 1.20 – The Figure shows the structure of the growth cone. The growth cone is divided into three regions according to the cytoskeleton location: central domain, transition zone and peripheral domain. The peripheral domain contains filopodia, lamellipodia, actin meshwork and bundles and microtubules that are exploring the domain. The transition zone forms a barrier between the P-domain and the C-domain and it includes actin arcs. The central domain contains microtubule bundles. Note: adapted from (Lowery and Vactor 2009).

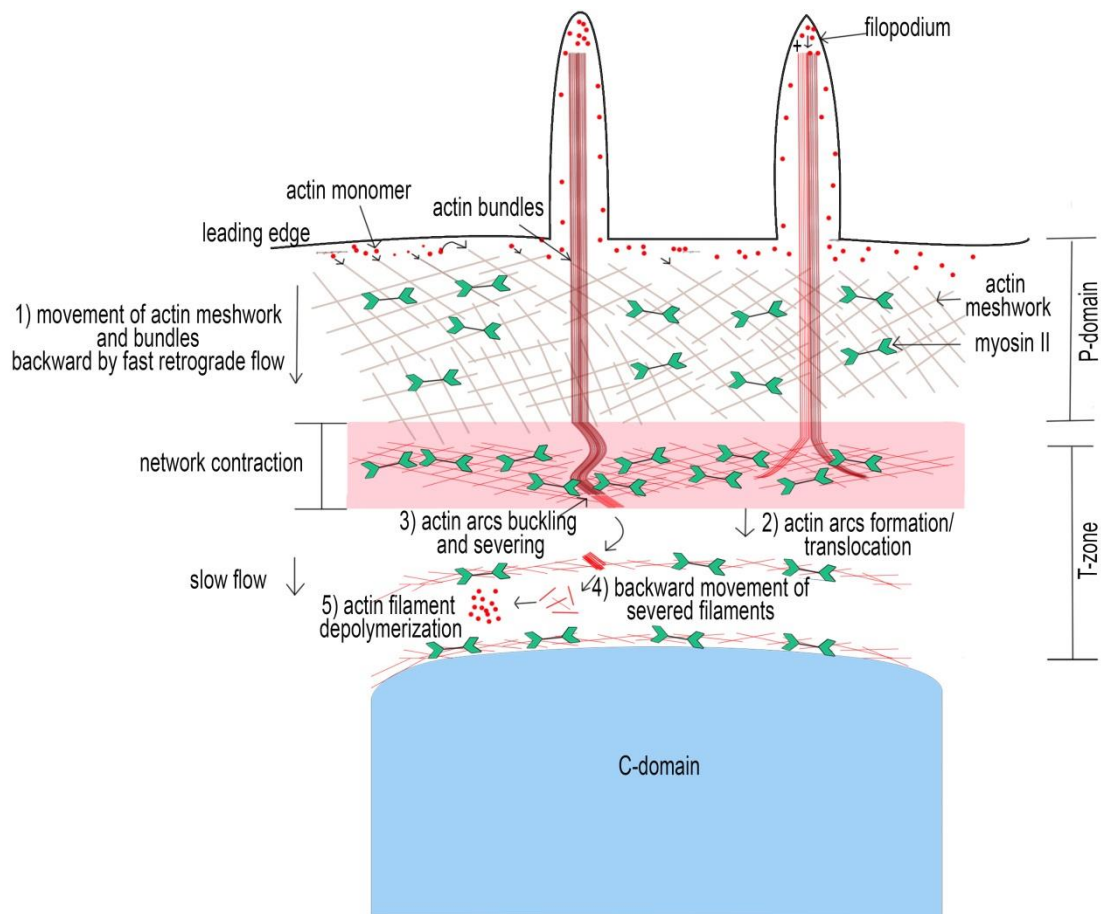
Figure 1.21

Figure 1.21 – The Figure shows a schematic diagram of actin filament dynamics in the growth cone. Fast retrograde flow moves actin meshwork and bundles backward away from the leading edge resulting in the formation of actin arcs in the transition zone. As a result of actin network contraction in the transition zone, actin buckling and severing occurred and ultimately depolymerized. To keep actin meshwork and bundles in the same position in the leading edge, actin bundle recycling is operated. Note: adapted from (Medeiros, Burnette, and Forscher 2006).

ultimately severed (Figure 1.21, step 3). The severed actin filaments keep moving backward by attaching to actin arcs (Figure 1.21, step 4) and ultimately undergo depolymerisation (Figure 1.21, step 5). Since the retrograde flow pushes the actin network and bundles backward away from the leading edge, actin bundle recycling is operated to keep them in the same position.

Microtubules in growth cones

Microtubules (MTs) play a significant role in growth cone motility. Applying low doses of vinblastine, that only interfere with microtubule dynamics, leads to depleting MTs from the P-domain and stops the growth cone translocation (Tanaka, Ho, and Kirschner 1995). The growth cone movement is resumed after washing the drug. MTs are thought to act as guidance sensors recruiting signalling molecules required for growth cone motility. For instance, binding of apCAM-coated beads (a polystyrene bead coated with apCAM, the immunoglobulin superfamily cell adhesion molecule) to the growth cone receptor during the latency phase (the stage when actin filaments weakly couple to the cell adhesions), increases the number of exploratory MTs in the P-domain. Moreover, this increase in exploratory MTs coincides with elevated levels of active Src kinase at adhesion sites (Suter et al. 2004). This accumulation of active Src kinase at adhesion sites is required for strong coupling between apCAM and actin filaments. Inhibition of MT dynamics perturbs active Src kinase accumulation at these sites.

As microtubules usually follow the same trajectories of actin filament bundles in the P-domain of the growth cone, this leads to an assumption that actin bundles might guide MT's advance into the P-domain (Lowery and Vactor 2009). However, another study shows that this actin filament/MT interaction (which is mediated through cross linking proteins) is to inhibit MT penetration into the P-domain (Burnette et al. 2007). In addition, another interaction between MT and actin arcs occurs in the C-domain during engorgement. Actin arcs usually form a barrier between the P-domain and C-domain. During engorgement, actin arcs rearrange and concentrate on the sides of the growth cones to regulate MT advance by capturing them and transporting them into the C-domain. Also, transporting MTs into the C-domain as well as MT consolidation requires actomyosin contractility since inhibition of myosin perturbs these processes (Burnette

et al. 2008). In addition, cytoplasmic dynein and LIS1 are also involved in growth cone neck consolidation. Inhibition of dynein or LIS1 interferes with this process (Vallee, Seale, and Tsai 2010).

The dynamics of MTs in growth cones are also regulated by microtubule associated proteins (MAPs). MAPs are involved in microtubule stability during axonogenesis, mediate microtubule cross linking to actin filaments, regulate MT polymerization and depolymerisation, and facilitate motor protein interaction and transport initiation. An example of MAPs that have an important role in growth cone motility is the family of plus-end tracking proteins (+TIPs) (see section 2.3.2.1.1.). Interestingly, cytoplasmic dynein and LIS1 (a dynein-interacting partner) are both known to be localized at the MT plus end and inhibition of either of them leads to MT depletion in the P-domain due to the inability of MTs to resist the retrograde actin flow (Grabham et al. 2007). This depletion of MTs in the P-domain is not due to changes in MT polymerization, as many MTs are shifted backward at rates consistent with retrograde actin flow. This phenotype can be recovered by inhibition of myosin II, which is known to underlie the retrograde actin flow (Myers et al. 2006). Thus, dynein is required to maintain growing MTs at the leading edge by exerting force on MTs and therefore resisting the retrograde actin flow (Vallee, Seale, and Tsai 2010).

Growth cone dynamics and axon outgrowth

During the stationary phase, in the absence of attractive adhesive substrates (Figure 1.22A), no coupling exists between the substrate and actin filaments and the number of MTs exploring the P-domain is low (Figure 1.22A; B, step 1). MTs appear buckled and cannot penetrate the P-domain. Also, actin filaments move backward due to retrograde actin flow (Figure 1.22B, step 2, red arrow). At this stage, the position of MTs (Figure 1.22B, step 3) is determined by a balance between MT assembly and retrograde transport of MTs (Figure 1.22B, blue arrow) which are linked with actin filaments by cross linking proteins (Figure 1.22B, green). During the latency phase, the growth cone encounters attractive adhesive substrate (Figure 1.22A, green). A weak molecular clutch is formed (Figure 1.22B, step 1) and therefore no change in the rate of retrograde flow (no retrograde flow attenuation) (Figure 1.22B, step 2). Putative signals might be generated to form the adhesion sites and might result in reduced

coupling between MT and actin filaments, possibly by reducing the affinity of cross linking proteins (Figure 1.22B, step 3). This leads to an increase in the number of exploratory MTs towards the adhesion sites (Figure 1.22A; B). During the traction phase, the substrate and actin filaments are strongly coupled by adhesion molecules (Figure 1.22B, step 1) and thus attenuating the retrograde flow (Figure 1.22B, step 2). This allows filopodia and lamellipodia to extend (Figure 1.22A, protrusion formation) followed by rearrangement of actin arcs to the sides of the growth cone. This will clear the corridor for the transportation of the C-domain MTs (Figure 1.22A, engorgement; B, step 3). Finally, MTs located in the new region of the growth cone neck are compressed to form a new axon shaft (Figure 1.22A, consolidation).

Focal adhesion proteins

Focal adhesion kinase (FAK)

FAK: phosphorylation and domain functions

Focal adhesion kinase is a non-receptor tyrosine kinase (FAK) activated as a consequence of integrin activation as well as in response to other stimuli such as growth factors (M D Schaller 2001; Parsons 2003; Hall, Fu, and Schaller 2011). FAK contains six tyrosine residues and autophosphorylates at Tyr397 which is located just upstream of the kinase domain (Figure 1.23, red circles). Phosphorylation at this site results in FAK activation as well as provides binding sites for the Src-homology 2 (SH2)-domain containing proteins including the Src family, phosphoinositide 3-kinase (PI3-kinase), phospholipase C (PLC γ), the GTPase activating protein p120RasGAP and the growth-factor-receptor-bound protein 7 (Grb7). Src binds FAK through two sites: the phosphorylated Tyr397 site and the proline-rich region which is also located upstream the kinase domain (Figure 1.23, red circle and red box, respectively). This recruitment of Src to FAK leads to Src-dependent phosphorylation of several FAK tyrosine sites: Tyr576, Tyr577, Tyr861, and Tyr925 for the maximal activation of FAK. Tyr576 and Tyr577 are both located within the activation loop of the kinase domain (Figure 1.23). Phosphorylation of Tyr576 and Tyr577 is important to enhance the maximal activity of

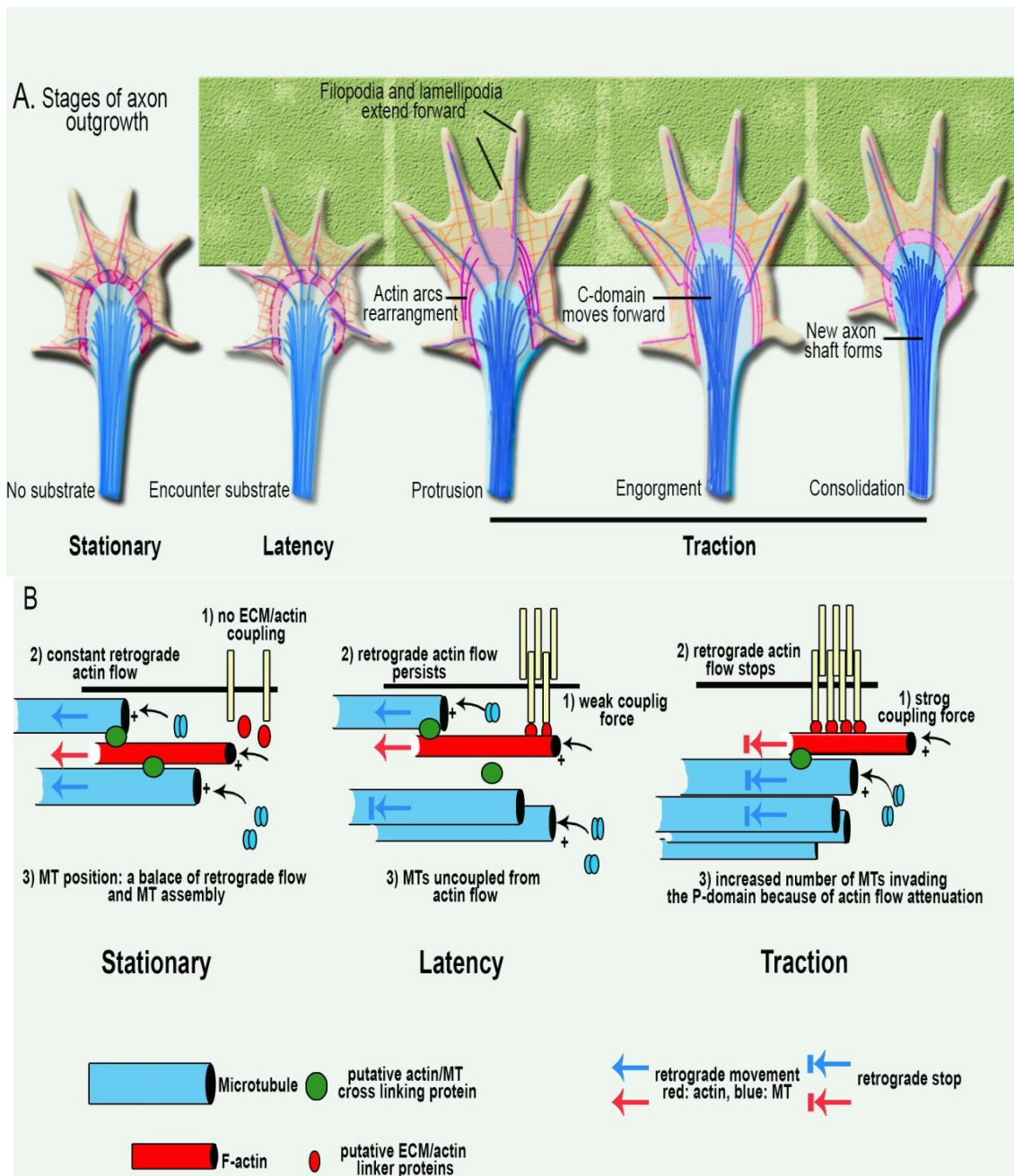
Figure 1.22

Figure 1.22 - The Figure depicts the growth cone dynamics and axon outgrowth summarized into three phases: stationary, latency and traction (A). (B) Schematic diagrams show cross-sections of growth cones which depict the dynamics of as well as the interaction between microtubules and actin filaments at the corresponding phase. Note: adapted from (Lowery and Vactor 2009; Lee and Suter 2008) with modifications.

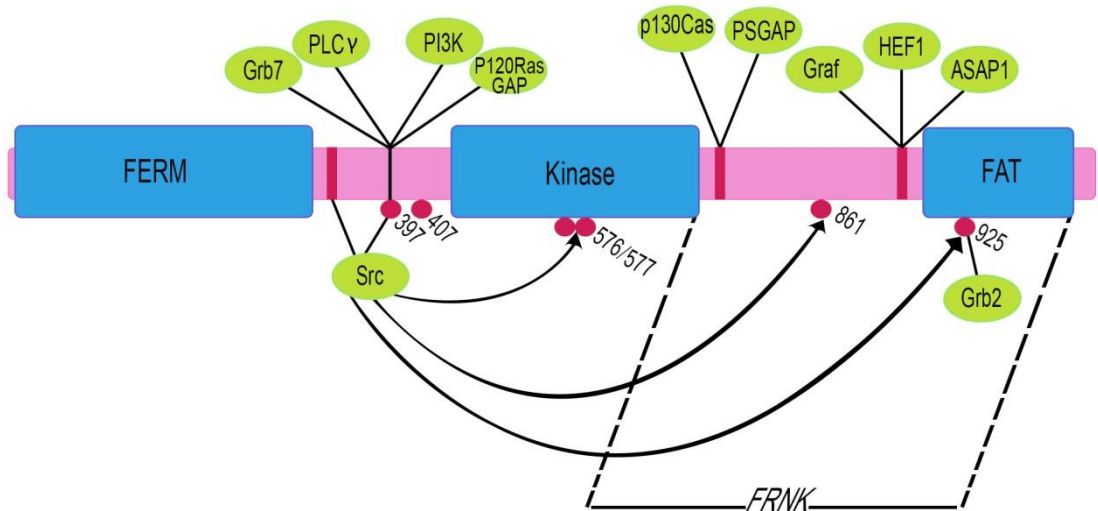
Figure 1.23

Figure 1.23 - The Figure shows FAK functional domains: FAT, kinase and FERM (blue boxes) and six tyrosine phosphorylation sites (red circles). FAK autophosphorylation at tyrosine 397 provides binding sites for Src, PI3K, PLCγ, p120RasGAP and Grb7. Src further phosphorylates FAK at several tyrosine sites, 576, 577, 861 and 925. Src phosphorylation of Tyrosine 925 provides binding site for Grb2. Red boxes represent proline rich regions that provide binding sites for proteins such as Cas and GTPase activating proteins. Image adapted from Hall et al. 2011 and Parsons, J. T. 2002.

the enzyme. Phosphorylation of Tyr925 on FAK provides a binding site for Grb2 which is required for the activation of the Ras/MAPK signalling pathway (Figure 1.23). Also, the binding of Src to FAK results in the formation of FAK/Src complex which facilitates Src phosphorylation of other substrates such as paxillin and p130Cas. Serine phosphorylation at Ser723 is mediated by Cdk5 and is essential for several physiological processes: cytoskeletal reorganization, neuronal migration and centrosome function during mitosis and neuronal migration. The N-terminus of the protein is constituted of a FERM domain which has a regulatory role in FAK function and the deletion of this domain results in elevated FAK catalytic activity. The FERM domain might also facilitate interaction with the cytoplasmic domain of transmembrane proteins including $\beta 3$ integrin, the EGF and PDGF receptors. The C-terminus of the protein consists of a region of no catalytic activity referred to as FRNK (FAK related non kinase) which itself includes a region known as the focal adhesion targeting domain (FAT). It also contains several proline-rich regions that serve as binding sites for SH3 containing proteins: Cas (Crk-associated substrates: p130Cas and Hef1), and GTPase-activating proteins, ASAP1 (a GAP for Arf 1/6), PSGAP and GRAF (a GAP for Rho) (Parsons, J. T. 2003) (Figure 1.23, red boxes). A truncated form of FAK is also expressed consisting only of the FRNK domain, which instils a dominant negative effect by competing with FAK for localisation to FA. FAT is responsible for FAK's localization to FAs as well as providing binding sites for focal adhesion associated proteins. Using deletion analysis, the FAT domain was defined as the region spanning amino acid residues 904-1040 (Hildebrand, Schaller, and Parsons 1995). Two proteins are known to bind the FAK FAT domain: paxillin and talin (Hildebrand, Schaller, and Parsons 1995; H.-C. Chen et al. 1995).

Paxillin binding and regulation of FAK function

It was found that the binding sites of paxillin might potentially reside within the 904-1054 amino acid residues of FAK (Jeffrey *et al.*, 1995). Evidence for which came from in-vitro deletion analysis which showed that a region spanning the amino acids of the FAT domain (929-1023) is implicated in paxillin binding. Also, Jeffrey *et al* (1995) showed that the cFAK (missing the 13 distal amino acids of the C-terminus 1041-1054) prevents paxillin binding but retains normal FAK localization. Thus, this indicates that

paxillin is not essential for FAK localization. However, more recent papers showed that binding of FAK to paxillin is essential for FAK localization to adhesion sites, where it is activated, and for regulating FAK function (Scheswohl et al. 2008; Deramaudt et al. 2014). FAK binding to paxillin is mediated by the two hydrophobic patches: HP1 and HP2 that reside within the FAT domain and are known to bind leucine-rich domains (LD) of paxillin. Scheswohl et al (2008) inhibited two binding sites of paxillin on FAK by introducing triple mutations into the HP1 (Glu949Ala/Lys956Ala/Arg963Ala) and a point mutation into the HP2 (I937A). Consequently, FAK localization to adhesion sites was reduced by 90%, which was completely abolished by introducing an additional mutation at site Glu997 to alanine. Despite this, FAK autophosphorylation as well as phosphorylation of Tyr861 levels were not affected suggesting that the phosphorylation at those two sites is not dependent on paxillin binding. However, phosphorylation of Tyr576 and Tyr577, located within the activation loop, as well as the phosphorylation of paxillin and p130Cas, the downstream targets of FAK, were reduced. Phosphorylation of paxillin and p130Cas was completely abolished by disrupting the two binding sites in HP1 and HP2, whereas it was attenuated when each binding site was disrupted individually. This attenuation suggests that both paxillin binding sites are required for the maximal FAK activation and function. Therefore, this study suggests that the binding of FAK to paxillin is indeed important for FAK localization and phosphorylation at some sites. Similar evidence also supports this, as paxillin binding to FAT domain was disrupted along with FAK targeting to adhesion sites by introducing two mutations located in HP1 and HP2, Ile998Glu and Ile936Glu, respectively (Deramaudt *et al.*, 2014). In terms of phosphorylation, Ile998 and Ile936 mutations affect both the phosphorylation status of FAK as well as the phosphorylation of the FAK downstream substrates, p130Cas and p-paxillin. For example, FAK phosphorylation at Tyr397, Tyr576 and Tyr925 was significantly reduced in FAK^{Ile998/Ile936}-expressing FAK^{-/-} MEFs compared to those expressing the wild type FAK. Furthermore, the phosphorylation of Tyr118 of paxillin was reduced in FAK^{Ile998/Ile936} by 29% compared to the wild type FAK. Similarly, P130Cas phosphorylation at Tyr410 was reduced by 38% in FAK^{Ile998/Ile936} compared to the wild type FAK. The reduced phosphorylation of FAK substrates suggests that FAK-paxillin interaction is required for maximal phosphorylation of downstream substrates. Also,

the reduction of p130Cas phosphorylation might be due to the loss of FAK at adhesion sites where p130Cas phosphorylation normally occurs. Furthermore, altered FAK/paxillin interaction led to defects in cell adhesion and migration. FAK^{Ile998/Ile936}-expressing FAK^{-/-} cells exhibited reduced adhesion on fibronectin coated plates and decreased migration speed by 40% compared to FAK^{-/-} cells expressing the wild type FAK.

FAK's role in cell motility

FAK was shown to regulate signalling pathways involved in cell motility in response to ECM protein stimuli. The autophosphorylation of FAK at Tyr397 as well as FAK/Src complex formation are required to promote cell motility (M D Schaller 2001). FAK^{-/-} fibroblasts exhibit defective cell migration and the re-expression of FAK in FAK^{-/-} fibroblasts enhanced cell migration. Interestingly, if FAK was co-expressed with the Src negative regulator Csk, it reduced the ability of FAK from enhancing cell migration. This suggests that Src is also involved in cell migration in the context of FAK mediated cell migration. Another downstream target of FAK involved in promoting cell migration is p130Cas (Cary et al. 1998). Cells expressing FAK mutant with mutations in the proline rich region (Pro712Ala/Pro715Ala) fail to bind and phosphorylate p130Cas, leading to a defect in cell migration.

Tyrosine phosphorylation of P130Cas by FAK/Src complex creates a binding site for Crk, which results in the formation of p130Cas/Crk complex (Figure 1.24) (Klemke et al. 1998). The formation of this complex leads to Rac activation and subsequently actin polymerization and lamellipodia formation. Rac activation is mediated by the recruitment of P130Cas/Crk to DOCK180, which acts as a guanine nucleotide exchange factor (GEF) when bound to ELMO (Brugnera et al. 2002). Collectively, the above evidence is indicative of a pathway in which FAK activation results in the formation of the FAK/Src complex and consequently responsible for the phosphorylation of p130Cas. This phosphorylation promotes the formation of the p130Cas/Crk complex, which subsequently recruits more proteins (CAS/CRK/DOCK/ELMO) to stimulate Rac activity (Figure 1.24). Furthermore, phosphorylation of paxillin at Tyr31 and Tyr118, another downstream target of FAK/Src, generates a binding site for the SH2-containing protein Crk. Like p130Cas/Crk, the paxillin/Crk complex recruits DOCK180, which

stimulates Rac activity (Vallés, Beuvin, and Boyer 2004). Thus, FAK provides a second pathway to regulate Rac activity through paxillin phosphorylation. However, paxillin phosphorylation is also implicated in recruiting of Csk, the negative regulator of Src. However, the downstream signalling caused by this binding is still unclear (Parsons, J. T. 2003).

In addition to the ECM, FAK is also implicated in cell motility in response to chemoattractants as shown by the inability of FAK^{-/-} cells to migrate in the presence of EGF (Sieg et al. 2000). This phenotype can be rescued by the re-expression of wild type FAK, indicating that EGF is upstream of FAK. This is further supported by co-immunoprecipitation assays, which show that FAK interacts with EGF receptor. The mechanistic role of FAK in cell migration is still being elucidated but significant progress has been made. This includes the understanding of FAK's role in focal adhesion turnover and the recruitment of focal adhesion proteins.

FAK's regulation of focal adhesion turn-over

FAK's role in FA turn-over is evidenced by the fact that FAK^{-/-} MEFs exhibited an increase in the number of FAs compared to control cells (Ilić et al. 1995). Additionally, there are suggestions that FAK performs this function by suppressing Rho activity as shown by the fact that FAK^{-/-} MEFs have constitutively high levels of Rho activity (Ren et al. 2000). This high level of activity decreased to normal levels upon the re-expression of FAK. More specifically FAK is thought to affect Rho activity by its recruitment of GRAF (Figure 1.24), which is known to reduce Rho signalling.

Additionally, FAK regulation of FA turn-over was affected upon disrupting FAK/paxillin interaction. FA turn-over was reduced in FAK^{Ile998/Ile936}- expressing FAK^{-/-} cells compared to cells expressing wild type FAK. In FAK^{Ile998/Ile936}- expressing FAK^{-/-} cells 58% of FAs remained stable, whereas this percentage reduced to 35% in FAK^{-/-} cells expressing wild type FAK.

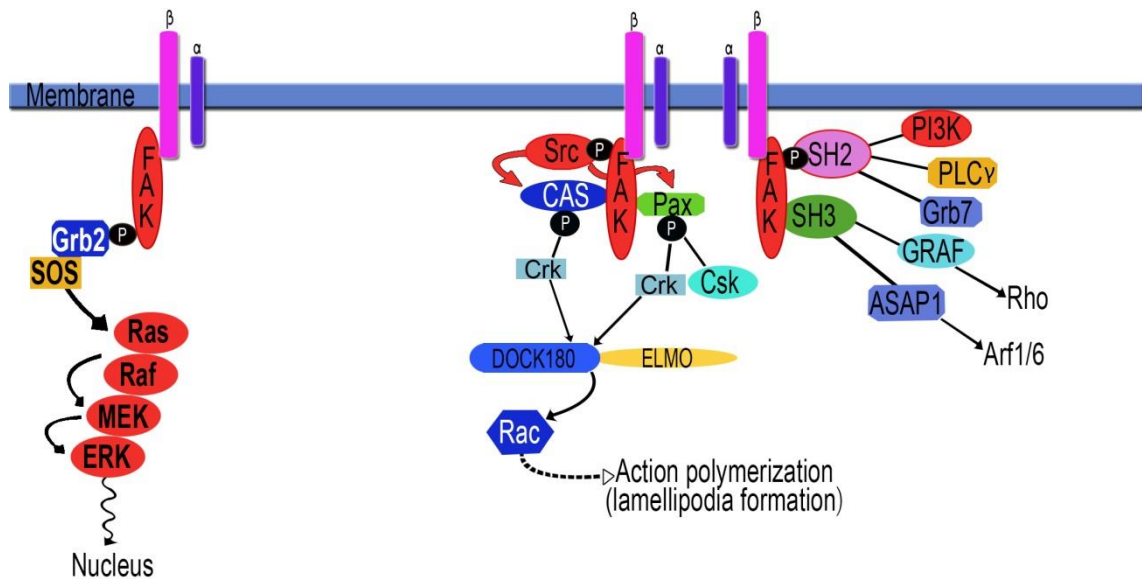
Figure 1.24

Figure 1.24 - The Figure shows multiple signalling pathways that implicate FAK upon integrin activation. Up on integrin activation and clustering, FAK is autophosphorylated at Tyr397 which therefore provides binding sites for the SH2-containing proteins PI3K, PLC γ , Grb2 and Grb7. It also binds the SH3 containing proteins, GRAP and ASAP1 that regulate Rho and Arf families of proteins, respectively. FAK autophosphorylation recruits Src to form the FAK/Src complex, which subsequently phosphorylates the downstream targets Cas and paxillin (red arrows), each of which forms a complex with Crk, DOCK180 and ELMO to activate Rac and lamellipodia formation. FAK is involved in the Ras/MAPK signalling pathway through its binding to Grb2. Image adapted from Parsons, J. T. 2003 with some modification.

FAK and the recruitment of focal adhesion proteins

As mentioned above, FAK is involved in recruiting focal adhesion proteins to adhesion sites. For example, in FAK^{-/-} cells, talin is not localised to nascent focal adhesions thus suggesting the requirement of FAK for its recruitment (Lawson et al. 2012). Similarly, talin was not localized to nascent adhesions when human ovarian carcinoma cells SKOV3.ip1 were transfected with siRNA against FAK. Moreover, expressing the mutant FAK (E1015A), lacking the binding site of talin, in FAK^{-/-} null fibroblasts does not rescue the recruitment of talin to nascent adhesions whereas expressing the wild type FAK retains talin to nascent adhesions. This recruitment of talin by FAK is independent of talin binding to integrin.

Paxillin

Paxillin structure and isoforms

Paxillin is a 62-kDa adaptor protein localized to adhesion sites, where it provides a platform for the recruitment of more proteins. This facilitates actin cytoskeleton anchorage to adhesion sites and the formation of multi-protein complexes for coordinating the signalling pathways at these sites (M D Schaller 2001; Brown and Turner 2004). Three alternative-splice variants of paxillin give rise to α , β and γ isoforms. While paxillin α , β and γ are known to be expressed in humans, in murines only paxillin α and β are expressed (Mazaki et al. 1998). Paxillin α is the main isoform that is ubiquitously expressed, whereas β and γ are generated from a short exon insertion between lysine 277 and phenylalanine 278, located between leucine-rich motifs LD4 and LD5 motifs of paxillin α (Mazaki et al. 1997) (Figure 1.25). In addition, δ is an alternative translation isoform beginning at methionine 132 and thus lacking the first LD motif. Paxillin comprises multiple motifs and domains that are involved in mediating protein-protein interactions. These include five leucine-rich motifs and several proline-rich regions located in the N-terminus, as well as four zinc binding structures, known as LIM domains, which are located in the C-terminus (Figure 1.25 and Table 1.11). The proline-rich region and the tyrosine phosphorylated sites provide binding sites for the SH3- and SH2-containing proteins, respectively. The LIM3 domain and, to a lesser extent, LIM2 are required for targeting paxillin to the adhesion sites. Moreover, the phosphorylation of LIM domain at Ser457 and Ser481 is required for

targeting paxillin to the focal adhesions (Brown, Perrotta, and Turner 1998). LD motifs mediate interactions with cytoskeletal proteins (actopaxin and vinculin), tyrosine and serine/threonine kinases (focal adhesion kinase FAK and the integrin linked kinase ILK) and the GTPase activating proteins (paxillin kinase linker PKL, p21 GTPase-activated kinase PAK). In addition, the LD4 motif is also known to bind a protein complex that contains PAK, the PAK-interacting exchange factor PIX and PKL which is required to stimulate Cdc42 activity and therefore cell polarity (Turner et al. 1999; Brown, West, and Turner 2002). Additional paxillin binding partners are shown in Table 1.11, including their binding region and function.

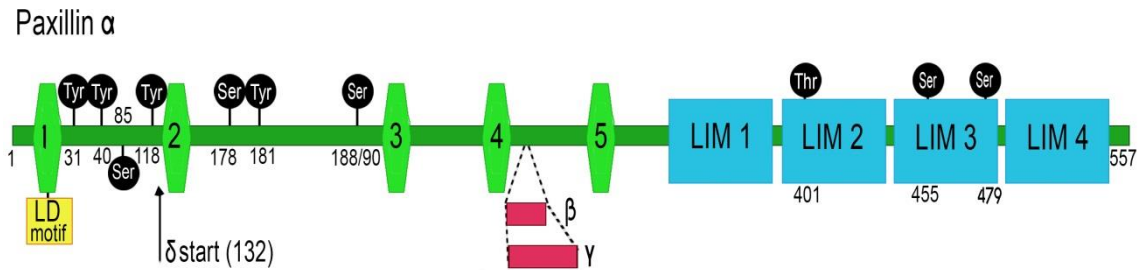
Figure 1.25

Figure 1.25 - The Figure shows the domain structure of paxillin α . Paxillin α is a 557 amino acid protein comprised of five leucine-rich (LD) motifs (consensus sequence LD \times LL \times XL, green boxes) and four zinc binding structures (LIM). The Figure also shows tyrosine, serine and threonine phosphorylation sites, as well as two isoforms β and γ generated from alternative splicing and one alternative translated isoform δ .

Table 1.11 Paxillin binding partners at adhesion sites

Paxillin binding partner	binding region	Function
The integrin-linked kinase (ILK)	LD1	<ul style="list-style-type: none"> - Paxillin/ILK interaction is required for targeting ILK to adhesion sites. - Paxillin/ILK interaction may be important in the regulation of ILK signalling ((Nikolopoulos & Turner 2000).
FAK	LD2 and 4	<ul style="list-style-type: none"> - The binding sites were determined in Turner <i>et al.</i>, 1999. - Paxillin/FAK interaction is important for FAK localization and the regulation of FAK function (Scheswohl <i>et al.</i>, 2008 and Deramaudt <i>et al.</i>, 2014).
Tubulin	LIM2 and 3	<ul style="list-style-type: none"> - Paxillin co-localizes with γ and α-tubulin at MTOC in T lymphoblasts, suggesting a potential role for paxillin in regulating the function of microtubule network (Herreros <i>et al.</i>, 2000). - Mutations in the MT binding sites in LIM2 domain compromised cell spreading and caused cell rounding suggesting uncontrolled focal adhesion turnover (Brown and Turner 2002).
Crk	pTyr31/pTyr118	Recruitment of Crk to the phosphorylated Tyr31 and Tyr118 promotes lamellipodia formation (Lamorte <i>et al.</i> , 2003).
the extracellular signal related kinases (ERK)	The ERK binding site: pTyr118,Sre119,Phe120, Pro121	pTyr118/ERK interaction is important for normal cell spreading (Ishibe <i>et al.</i> , 2003).

Table 1.11 - The Table shows some paxillin binding partners, the binding regions and the known functions of these bindings.

Phosphorylation of Tyr31 and Tyr118 and its role in adhesion dynamics and migration

During migration, paxillin is primarily phosphorylated at Tyr31 and Tyr118 through which it creates binding sites for the SH2-containing proteins. For example, tyrosine phosphorylation results in the recruitment of adaptor proteins like Crk, which in turn recruit CrkL into a complex with paxillin (Schaller and Parsons 1995). The Crk/CrkL complexes then recruit additional signalling molecules such as the guanine exchange factors: C3G and DOCK180 in order to form a complex with paxillin. Consequently, the Crk-Dock180 complex results in the activation of Rac, which promotes lamellipodia extension and enhances migration (M D Schaller 2001; Brown and Turner 2004).

Phosphorylation of paxillin at Tyr31 and Tyr118 is by FAK and FAK related protein kinases Cak β , Pyk2, CadTK and RAFTK. Cak β is thought to compensate for the loss of FAK in FAK^{-/-} fibroblasts, as paxillin phosphorylation levels is only slightly reduced in these cells (Deramaudt et al. 2014; M D Schaller 2001). Moreover, FAK has been shown to phosphorylate paxillin at Tyr118 *in vitro* (Bellis, Miller, and Turner 1995). The *in vitro* assay was performed by incubating immuno-precipitated FAK with truncated paxillin fusion proteins which vary in size, in order to map the site of p-paxillin. These truncated fusion proteins were generated from the original paxillin fusion protein that covers the amino acid sequence from 54 to 313 and contains four tyrosine sites: Tyr76, Tyr88, Tyr118 and Tyr182. FAK was unable to phosphorylate the truncated paxillin that lacks Tyr118. This was further confirmed by incubating FAK with paxillin fusion proteins in which one of the tyrosine residues was mutated to phenylalanine. FAK was able to phosphorylate all the tyrosine paxillin mutants except the Tyr118Phe mutant. Further evidence for the phosphorylation of paxillin by FAK at Tyr118 came from the inhibition of p-FAK (Tyr397) by FAK targeting siRNA which resulted in reduced levels of both p-FAK (Tyr397) and consequently p-paxillin (Li et al. 2009). Moreover, immuno-precipitation of FAK, utilizing GST-paxillin, revealed that the mutant Tyr118Phe did not change the binding ability of paxillin to FAK (Bellis, Miller, and Turner 1995).

Paxillin is also tyrosine-phosphorylated by Src, as Csk^{-/-} fibroblasts which lack the Src negative regulator, show enhanced Src activity, as well as elevated levels of tyrosine phosphorylation of substrates, including paxillin. This was further confirmed by the fact that Src-null fibroblasts showed a remarkable decrease of tyrosine phosphorylation of paxillin (Klinghoffer et al. 1999). Overall, these data indicate that both FAK and Src phosphorylate paxillin. Src, however, phosphorylates paxillin at a much higher rate than FAK. In addition, Src is also responsible for phosphorylating paxillin at Tyr118 upon the stimulation of mIMCD-3 epithelial cells with hepatocyte growth factor (HFG). This phosphorylation of Tyr118 induces the recruitment of inactive ERK to adhesion sites, where it binds directly to paxillin (Table 1.11, the ERK binding site: pTyr118, Ser119, phe120, pro121) (Ishibe et al. 2003). Inhibition of Src by pretreating mIMCD-3 cells with the Src inhibitor PP1, results in a reduction in the phosphorylation levels of Tyr118, as well as ERK/paxillin interaction. MEK and Raf were also found to be associated with paxillin and thus to activate ERK. Subsequently, ERK phosphorylates paxillin at serine/threonine sites, resulting in the recruitment of FAK to adhesion sites and the subsequent activation of FAK, in order to promote cell spreading and adhesion (Liu et al. 2002; Brown and Turner 2004). Interestingly, staining porcine aortic endothelial cells (PAECs) transfected with the phosphomimetic paxillin (Tyr118Glu/Tyr31Glu) shows that tyrosine phosphorylation of paxillin increases the recruitment of p-FAK (Tyr397) to adhesion sites to stimulate adhesion turnover (Zaidel-Bar et al. 2007). Conversely, PAECs transfected with Tyr118Phe or Tyr31Phe mutant paxillin suppressed the recruitment of FAK to adhesion sites. Overall, the data produced by Zaidel-Bar et al. (2007) and Ishibe et al. (2003) are indicative of a pathway in which Src phosphorylates paxillin at Tyr118, leading to the recruitment of inactive ERK and its subsequent activation by MEK. Once ERK is activated and subsequently phosphorylates paxillin, FAK is recruited and then activated, which is required for the recruitment of more proteins involved in cell spreading and adhesion (Figure 1.26).

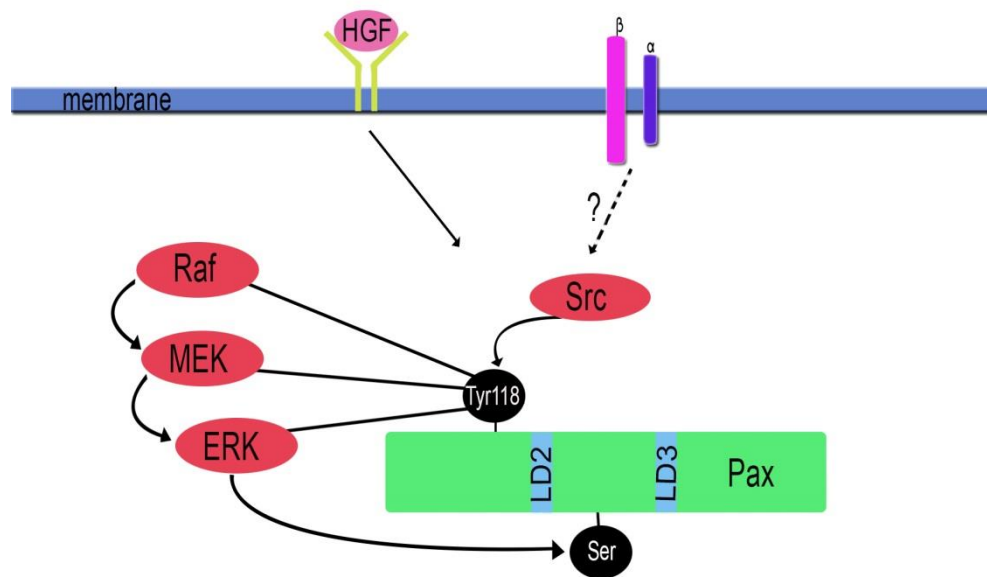
Figure 1.26

Figure 1.26 - The Figure demonstrates a signalling pathway involving Src, ERK, paxillin and FAK upon HGF receptor activation. Binding of HGF to the cell receptor results in the recruitment of paxillin to adhesion sites and in its subsequent phosphorylation at tyrosine 118 by Src. This causes an increase in ERK/paxillin association and the subsequent phosphorylation of paxillin at Ser/Thr, which as a result recruits FAK to adhesion sites.

Tyrosine phosphorylation of paxillin was found to be associated with the assembly and disassembly of adhesion sites (Zaidel-Bar et al., 2007). Focal complexes (FXs, formed at the leading edge where the lamellipodium is located) are considerably more dynamic than FAs (found further back from the leading edge where the lamella is located) and contain high levels of phosphorylated paxillin (pTyr118/ pTyr31), whereas FAs are more stable and contain comparatively lower levels of phosphorylated paxillin. As the cells move forward during migration, FAs, located at the cell front, translocate centripetally towards the cell centre, where they disassemble in the disassembly zone. High levels of tyrosine phosphorylated paxillin were observed in those FAs located in the disassembly zone, whereas levels varied in those located in the assembling front. Also, transfecting porcine aortic endothelial cells (PAECs) with the phosphomimetic paxillin, where tyrosine molecules at Tyr118 and Tyr31 were mutated to glutamic acid (Tyr118Glu/Tyr31Glu), enhanced adhesion dynamics, where cells showed numerous FXs, whereas the level of FAs did not change. Conversely, transfecting cells with the non-phosphorylatable paxillin, where tyrosine residues were mutated to phenylalanine (Tyr118Phe/Tyr31Phe), led to the stabilization of adhesion sites and cells showed more FAs and less FXs. It is noteworthy that the amount of tyrosine-phosphorylated paxillin is negatively regulated by mechanical force, as the ratio of pTyr-paxillin/paxillin increased 1 minute after treatment with the actomyosin-contraction inhibitor H7 [H7, 1-(5-isoquinolinesulfonyl)-2-methylpiperazine].

The role of cytoplasmic dynein 1 and paxillin in focal adhesion turnover

Cytoplasmic dynein 1 has been shown to be involved in regulating the disassembly of focal adhesions (Rosse et al. 2012). This is mediated by the interaction of the DIC subunit of cytoplasmic dynein 1 with the focal adhesion protein, paxillin. This interaction increases during cell migration and therefore facilitates the endocytosis of focal adhesions. Subsequently, DIC is phosphorylated at Ser84 in an aPKC-dependent manner (aPKC, atypical protein kinase C). As a result, DIC no longer interacts with paxillin and subsequently all focal adhesion components are recycled.

3. Research

My research focuses on the elucidation of the underlying molecular and cellular basis of motor neuron cell death in two motor neuron diseases namely amyotrophic lateral sclerosis (ALS) and spinal muscular atrophy with lower extremity predominance (SMA-LED).

The molecular mechanism underlying the degeneration of motor neurons in ALS is still unclear. Several genes have been implicated in ALS. One of them, the gene *TARDBP* encoding the DNA/RNA binding protein TDP-43 is known to underlie ~4% of ALS cases. Interestingly, there have been other genes also implicated in causing defects in RNA splicing in ALS pathogenesis including *EAAT2* and *peripherin*. I hypothesized that TDP-43 might be involved in the RNA splicing of *EAAT2* and *peripherin* which therefore might highlight the RNA splicing mechanism as an underlying cause for ALS pathogenesis. In my results chapter 3, I investigated whether TDP-43 regulates RNA splicing of *EAAT2* and *peripherin* and whether impaired function of TDP-43, caused by ALS-associated mutations, would lead to abnormal RNA splicing mechanisms of *EAAT2* and *peripherin*.

Mutations in the cytoplasmic dynein heavy chain subunit (*DYNC1H1*) have been associated with several neurological disorders including SMA-LED, CMT type2 and learning disability. In this part of my research, I used the *Loa* mouse model of SMA-LED and fibroblasts isolated from human patients *DYNC1H1*^{R399G/R399G} to investigate the impact of mutations in *DYNC1H1* on cellular functions of cytoplasmic dynein including retrograde transport, growth cone movement and axonal elongation. Impaired retrograde transport of growth factor-induced endosomes were observed in heterozygous *Loa* motor neurons resulting in aberrant activation of extracellular-signal-related kinases 1 and 2 and of the immediate early gene *c-Fos*. I investigated the MAP kinases responsible for *c-Fos* activation during starvation as well as during BDNF stimulation (results chapter 4). I also investigated whether autophagy has a role in *c-Fos* activation during the aforementioned conditions. In addition, my research in chapter 5 focused on investigating the role of the mutant forms of cytoplasmic dynein

heavy chain including the *Loa* mouse mutation and the mutant human form DYNC1H1^{R399G/R399G} on cell migration and growth cone motility.

Chapter 2

Materials and Methods

2.1 Genotyping

2.1.1 DNA preparation from mouse tail biopsies

Approximately 0.2 - 0.5 cm of the tail or ear tissue was lysed in 200 µl lysis buffer containing 2 µl Proteinase K (20 mg/ml) at 55°C in a water bath overnight. The samples were vortexed and centrifuged at 13,000 rpm for 10 minutes. The DNA was diluted to 1:50 by adding 4 µl of the supernatant to 200 µl double distilled water. The diluted samples were then vortexed and centrifuged briefly. One or 2 µl of the dilution was used in PCR reaction.

2.1.2 Genotyping TDP-43^{A315T} transgenic mice

To genotype TDP-43^{A315T} transgenic mice, a standard PCR was performed using two sets of primers designed by Jackson laboratory (Table 2.1). One set was used to target and amplify part of the transgene (Figure 2.1A, primers are highlighted in yellow). The other set, which works as an internal positive control, was used to amplify part of the mouse DNA. The size of the transgene amplicon is 400 bp, whereas the control amplicon is 200 bp (Figure 2.1B).

Table 2.1

Primer	Sequence 5'→ 3'
TDP-43 transgene FWD	GGA TGA GCT GCG GGA GTT CT
TDP-43 transgene REV	TGC CCA TCA TAC CCC AAC TG
Internal positive control FWD	CAA ATG TTG CTT GTC TGG TG
Internal positive control REV	GTC AGT CGA GTG CAC AGT TT

Table 2.1 – The genotyping primer sequences for the TDP-43^{A315T} transgenic mouse.

2.1.3 Genotyping SOD1^{G93A} transgenic mice

Biopsies tissues were lysed following the same procedure mentioned in section 2.1.1. Two sets of primers designed by Jackson laboratory were used to genotype SOD1^{G93A} transgenic mice carrying the human G93A mutant form of SOD1 under its own promoter (shown in Table 2.2). One set was used to target and amplify part of the

transgene (Figure 2.2A, highlighted in yellow). The other set, functioning as an internal positive control, was used to amplify part of the mouse DNA. The size of the transgene amplicon is 236 bp, whereas the control amplicon is 324 bp in length (Figure 2.2B).

Figure 2.1

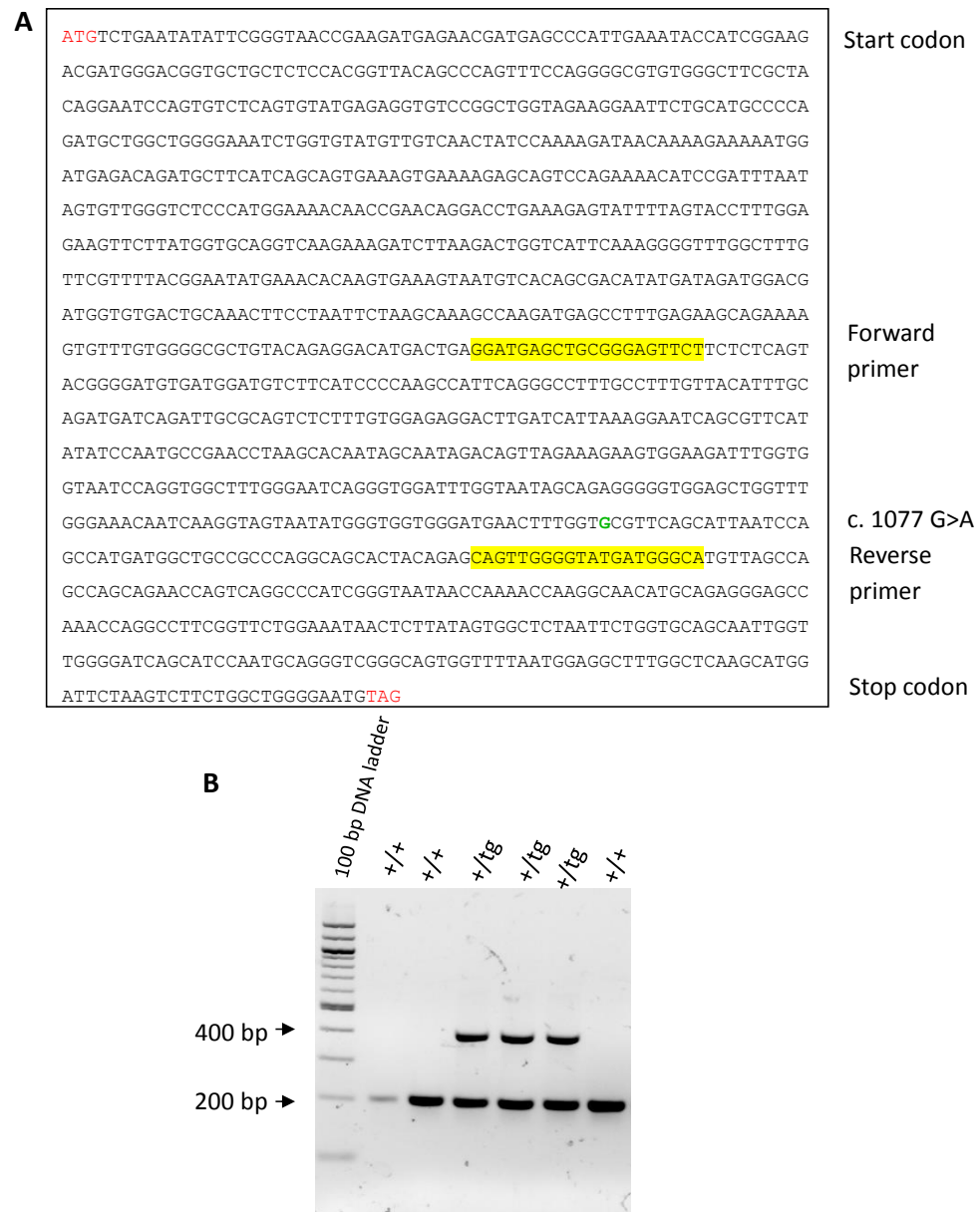


Figure 2.1 – Genotyping the TDP-43^{A315T} transgenic mouse. (A) The human TDP-43 coding sequence (NCBI, NM_007375.3) showing the annealing sites of the genotyping primers highlighted in yellow. The start codon and the stop codon are colored in red. The base pair change (c. 1077 G>A) is colored in green. (B) A 2% agarose gel, stained with 0.01% ethidium bromide, showing PCR product of the human TDP-43 transgene (400 bp) and the internal positive control (200 bp).

Table 2.2

Primer	Sequence 5'→3'
SOD1 transgene FWD	CATCAGCCCTAATCCATCTGA
SOD1 transgene REV	CGCGACTAACAATCAAAGTGA
Internal positive control	CTAGGCCACAGAATTGAAAGATCT
Internal positive control	GTAGGTGGAAATTCTAGCATCATC

Table 2.2 - The genotyping primer sequences for the SOD1^{G93A} transgenic mouse.

2.1.4 Genotyping TDP-43^{F210I} mutant mice

Genotyping the TDP-43^{F210I} mice was performed by multiplex PCR using three primers designed by PhD student Charlotte Chapman. One set of primers was used to amplify a product regardless of the genotype and therefore acting as an internal positive control (outer primers) (Figure 2.3, coloured in black and Figure 2.4, highlighted in yellow). The third primer (inner reverse primer) was designed to be allele specific. This was achieved by introducing a mismatch (the mismatch represents the F210I mutation, 'A' to 'T') between the last base of the 3' end of the primer and the template. A second mismatch was introduced to enhance the specificity, represented by the asterisk at position -2 (Table 2.3). This would hinder the annealing of the last three bases of 3' terminus (at 0, -1, and -2 positions) to the template and therefore creating an overhang. As a result, this overhang would prevent the binding of Taq polymerase to the 3' end. Two PCR products are expected from the multiplex PCR. Using both the outer primers and the inner wild type specific allele primer (Figure 2.3, coloured in red) to amplify the wild type template, two bands were amplified with equal intensity (Figure 2.3A, Table 2.4, and Figure 2.5). When they were used with the heterozygous mutant template, the PCR product of the outer primers was more intense than that amplified by the inner primer (Figure 2.3B, Table 2.4 and Figure 2.5). If the homozygous mutant template was amplified, only one intense band, produced by the outer primers, was observed (Table 2.4). No band was produced by the inner wild type allele specific primer due to the presence of two mutant alleles. When both the outer primers and the inner mutant specific primer were used (Figure 2.3, coloured in green)

to amplify the wild type template, only one intense band was observed, produced by the outer primers (Figure 2.3C, Table 2.4 and Figure 2.5).

Figure 2.2

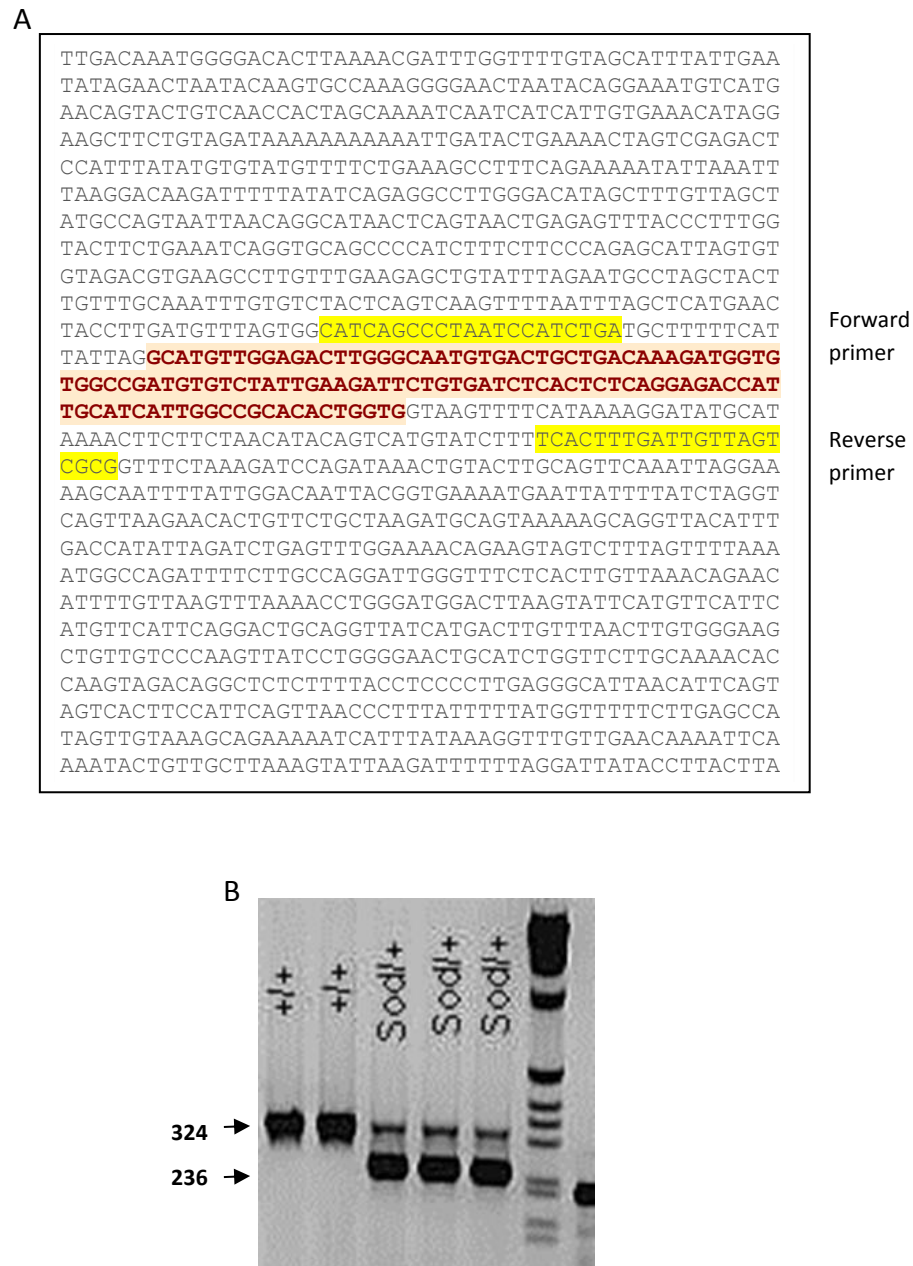


Figure 2.2 – Genotyping the $SOD1^{G93A}$ transgenic mouse. Part of the human *SOD1* gene sequence showing the annealing sites for the genotyping primers as well as gel electrophoresis for genotyping the $SOD1^{G93A}$ transgenic mouse. (A) Is part of the human *SOD1* gene inserted into the mouse genome (Ensemble, ENSG00000142168). The annealing sites of the human *SOD1* transgene primers are highlighted in yellow. The sequences in red bold font represent exons. (B) A 2% agarose gel, stained with 0.01% ethidium bromide, showing the PCR products of human *SOD* transgene (236 bp) and the internal positive control (324 bp).

When the heterozygous mutant template was amplified, one intense band amplified by the outer primers, was observed, as well as a band with lower intensity amplified by the mutant allele specific primer (Figure 2.3D, Table 2.4 and Figure 2.5). If the homozygous mutant template was amplified, two bands with equal intensity would be produced (Table 2.4).

Reaction components

Total reaction is 10 µl: [microzone master mix^{5µl}, outer FWD primer^{1µl}, outer REV primer^{1µl}, inner REV primer^{1µl}, template^{1µl}, water^{1µl}]

Two reactions were set up for each template, including the outer primers: one reaction was set up with the inner wild type allele specific primer and the other with the inner primer for the mutant allele.

PCR cycle

Temperature^{time}: 95°C^{5:00} [94^{0:30}, 60.5^{0:30}, 72^{0:45}]₃₅ 72^{2:00}

Table 2.3

Primer	Sequence 5' → 3'
Wild type specific allele (inner reverse)	TACCACTTCTCCATACTGACAGAA T A
Mutant specific allele (inner reverse)	TACCACTTCTCCATACTGACAGAA T A T
Outer primer (FWD)	GTGTTTACCATCTCCTGTTCTCTCTT
Outer primer (REV)	GACAAATGACCAACAAATATACCTTATC

Table 2.3 - Sequences of genotyping primers of the mutant TDP-43 F210I. The mutation at the 3' terminus of the inner primers are coloured in red whereas the mismatch is coloured in green.

Table 2.4











	+/+	+/TDP-43^{F210I}	TDP-43^{F210I}/TDP-43^{F210I}
Outer primers			
Inner wild type allele			
Outer primers			
Inner mutant allele			

Table 2.4 - The pattern of band intensity expected from the multiplex PCR for genotyping TDP-43^{F210I} mice.

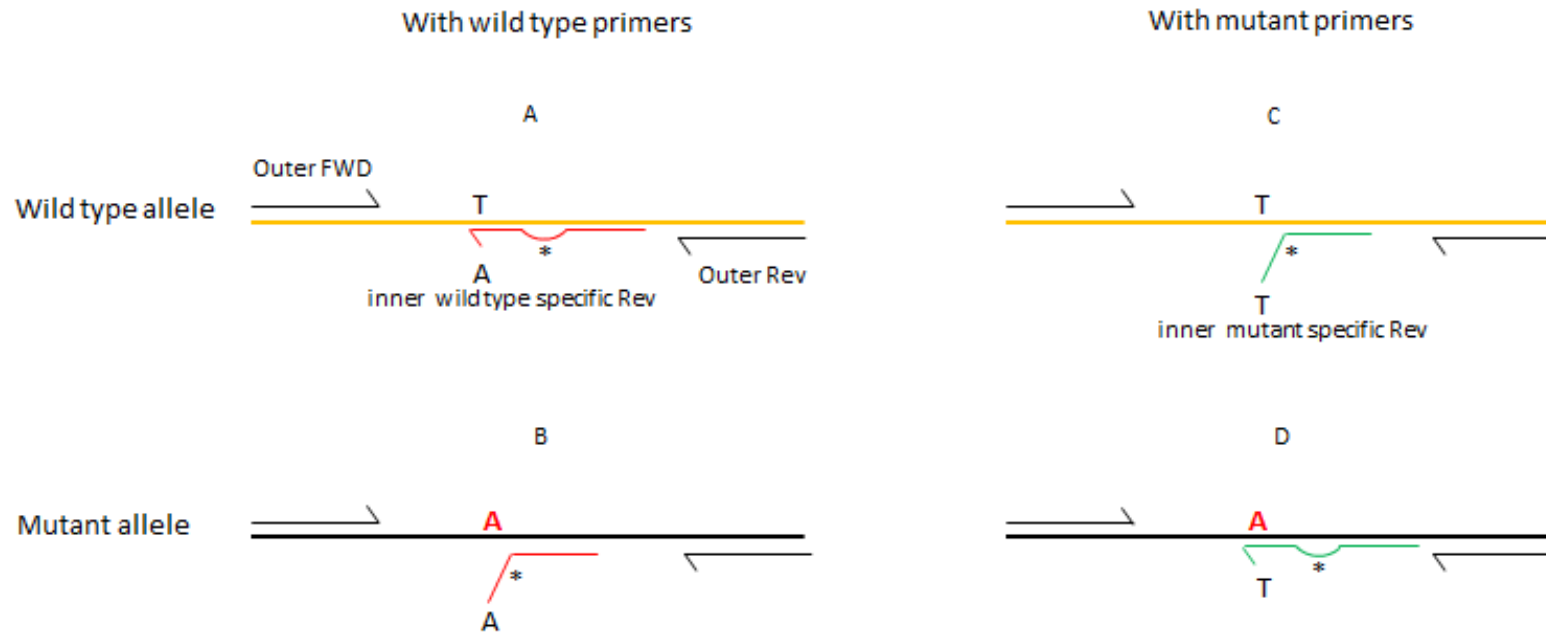
Figure 2.3

Figure 2.3 – Schematic diagram showing genotyping of TDP-43^{F210I} using the multiplex PCR. The outer primers are coloured in black. The inner wild type specific reverse primer is shown in red whereas the inner mutant specific is coloured in green. The asterisk represents the mismatch introduced to enhance the specificity of the inner primer.

Figure 2.4

Figure 2.4 – The sequence of the mouse *Tardbp* gene showing the annealing sites of primers. Sequence is obtained from the *Ensembl databases* (ENSMUSG00000041459). The annealing sites of the outer primers are highlighted in yellow. The inner reverse primer is underlined with the mutation in larger font and bold. The second mismatch is in green.

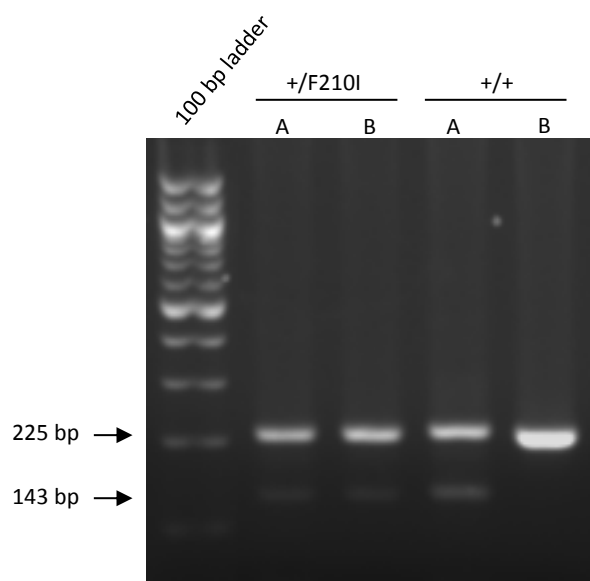
Figure 2.5

Figure 2.5 - Gel electrophoresis showing bands produced from the multiplex PCR using the outer primers and the inner wild type or inner mutant specific primers. Lane A is the multiplex PCR reaction containing the outer primers and the inner wild type specific primer. Lane B is the multiplex reaction containing the outer primers and the inner mutant specific primer. The 225 bp band is the expected size of PCR product amplified by the outer primers whereas the 143 bp band represents the PCR product amplified by the inner primer.

Figure 2.6 - Part of the cytoplasmic dynein heavy chain gene sequence *Dync1h1* showing the primer annealing sites as well as *RsaI* restriction sites. The sequence is obtained from Ensembl databases (ENSMUSG00000018707). Exons are shaded in grey and the primers are highlighted in yellow. *RsaI* restriction sites are colored in red. The mutation T>A that creates the second *RsaI* restriction site is in bold and larger font.

Table 2.6

	672bp	537bp	135bp	24bp
WT	+			+
<i>Loa/Loa</i>		+	+	+
<i>+/Loa</i>	+	+	+	+

Table 2.6 - Expected band sizes produced after *RsaI* restriction digestion of the PCR products of wild type, *+/Loa* and *Loa/Loa*.

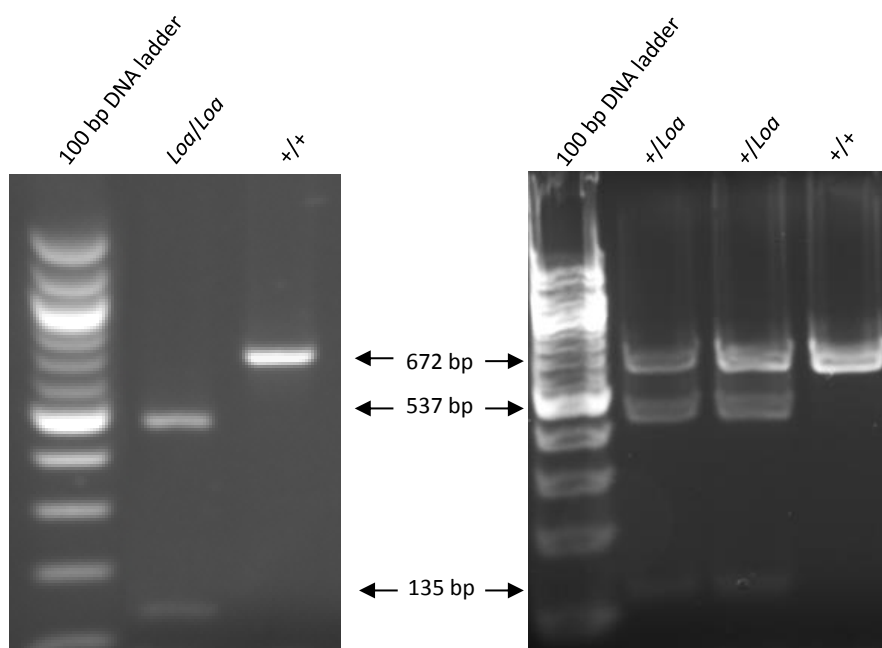
Figure 2.7

Figure 2.7 - Gel electrophoresis of wild type, *+/Loa* and *Loa/Loa* PCR products after digesting with *RsaI*. The left panel shows the expected band sizes in the homozygotes, 537 and 135 bp, and the wild types, a 672 bp band. The right panel shows the results of the restriction digestion of the heterozygotes. Three bands are expected: 672, 537 and 135 bp in length.

2.2 Dissection and cell culture

2.2.1 Isolation and culture of mouse embryonic fibroblasts

Pregnant female mice were sacrificed at 13 days post-coitum (dpc) through cervical dislocation. The uterine horn was dissected out and placed in a petri dish containing DPBS plus 1% penicillin and streptomycin (P/S). Each embryo was separated from its placenta and surrounding membranes and was kept on ice in a separate 15 ml Falcon tube in DPBS supplemented with 1% P/S. The embryo was placed on a 5 cm petri dish that had already been filled with black wax to increase the contrast during dissection under the microscopes. Using autoclaved dissecting instruments, the head was cut away, as well as any dark red visceral tissues. The remaining tissue was washed once with DPBS containing 1% P/S. Using a small amount of DPBS and a razor blade, the tissue was minced until it became pipettable and then transferred into a clean 15 ml falcon tube. The falcon tubes that contained the tissue were wiped with 70% IMS before transferring them to the laminar flow cabinet where they were subsequently left to stand for a few minutes to pellet the minced tissue through gravity. DPBS was removed and replaced with 1 ml of 0.05% trypsin-EDTA containing 100 units per ml DNase. This was done to avoid viscosity due to cell lysis and genomic DNA, which might have prevented efficient pelleting of cells in the subsequent centrifugation steps. The minced tissue was suspended and incubated at 37°C in a water bath for 15 minutes with occasional gentle shakes. The resulting cell suspension should be free of any larger pieces of tissue and should not be too viscous. The suspension was transferred to a universal tube and about 2 volumes of growth medium were added. The tubes were left to stand for a few minutes to pellet any remaining pieces before taking off the supernatant. Then, they were centrifuged at 390 *g* for 5 minutes. The cells were resuspended in MEFs culture medium and plated out in a T25 flask. The passage number should be zero. The medium was changed the following day.

2.2.2 Motor neuron isolation and culture

A pregnant female mouse was sacrificed at 13 dpc by cervical dislocation. The uterine horn was dissected out and placed on ice in a petri dish containing DPBS supplemented with 1% P/S. E13 embryos were removed from the uterine horn. The head and tail of

the embryo were removed and snap frozen in liquid nitrogen for further analyses and genotyping respectively. The body was placed on its sternum, with the dorsal side uppermost, on a 5 cm petri dish filled with black wax. The embryo was stabilised using its limbs. The spinal cord was clearly visible. Skin overlying the spinal cord was removed. The spinal cord was first separated from the right side of the body by inserting fine tweezers in between the cord and the body. Using curved tweezers to stabilise the body on its side, fine straight tweezers were used to separate the spinal cord from the vertebrae and to simultaneously remove the dorsal root ganglia. At the same time, the meninges were severed from the side of the spinal cord, as this would eventually facilitate removing it. The ventral side was oriented uppermost to remove any remaining dorsal root ganglia with a scalpel. The meninges were easily removed from the spinal cord by pulling them off, starting from the top of the spinal cord, where they could be easily visualized, all the way down. The ventral root containing the motor neurons was transferred to a 15 ml falcon tube containing fresh DPBS with antibiotics (P/S) and kept on ice.

Under the laminar flow cabinet, DPBS was removed from the spinal tissue (by pipetting using a 1 ml pipette and without using a pump) and replaced with 1ml HBSS, 1% P/S and 0.025% trypsin (10 μ l of 2.5% w/v stock). The samples were incubated in water bath at 37°C for 10 minutes with occasional agitation. The solution was then removed (using a 1 ml pipette) and 1 ml of complete L-15 media with 0.4% BSA (Sigma, A9056) and 100 μ g DNaseI (Sigma, DN25) were added (Table 2.7). The tissue was dissociated by pipetting 16 times and then allowed to settle for 2 minutes before the supernatant containing the cells was collected and transferred to a fresh tube. One millilitre complete L-15 media with 0.4% BSA and 20 μ g DNase were added to the pellet and triturated a further 16 times and then allowed to settle. Subsequently, the supernatant was removed and added to the previous collection. A 900 μ l complete L-15 media was added to the remaining tissue and a final dissociation carried out before the removal of the supernatant and disposal of the remaining pellet. The collected supernatants were spun through a 1 ml of 4% BSA cushion at room temperature for 5 minutes at 390 *g*. The supernatant was discarded and the pellet was resuspended in 600 μ l motor neuron culture medium (Table 2.7). For live cell imaging, 300 μ l of the suspension was

added per chamber (Lab-Tek II chamber slides, Fisher Scientific, #155379). For immunocytochemistry and imaging the growth cones of motor neurons, 50 μ l of the suspension was added per well of a 24-well plate containing coverslips. Coverslips and live cell imaging chambers were coated with either 0.1 mg/ml poly-D-lysine (Sigma, P7280) or coated with poly-L-ornithine/Laminin (Sigma, P4538/L2020, respectively; 50 μ g/ml for each). For biochemical analysis, a 100 μ l per well of a 24-well plate was added. Motor neuron culture media were added to reach a final volume of 1 ml in the live cell imaging chambers and 0.5 ml per well of a 24-well plate. Media were supplemented with 0.1 ng/ml GDNF, 0.5 ng/ml CNTF, 0.1 ng/ml BDNF. Cells were incubated at 37°C in a humidified 5% CO₂ incubator.

After 24 hours, half of the medium was removed and replaced with fresh medium containing 14 μ M of cytosine β -D-arabinofuranoside hydrochloride (AraC) in order to obtain a final concentration of 7 μ M. The cells were left to mature for at least 1 week before carrying out biochemical experiments and for two days before conducting immunocytochemistry or live cell imaging.

2.2.3 Cell assay

To measure solely the serum deprivation effect, motor neurons were starved for two hours in serum-free neurobasal media supplemented with serum-free B27, and growth factors; GDNF, CNTF and BDNF. To test their response to BDNF stimulation, motor neurons were first serum starved for two hours, without the addition of growth factors, followed by stimulation with 5 ng/ml BDNF.

2.3 Biochemistry

2.3.1 Preparation of lysates from tissues

All materials required for preparing lysates from tissues as well as the homogenization process were kept and performed in cold condition. Centrifugation steps were all performed in a refrigerated microcentrifuge. With regard to homogenizing brain tissue, the brain was placed in a glass Dounce homogenizer and the pestle, which tightly fitted within the shaft of the homogenizer, was used for homogenising the brain. The amount of the lysis buffer required for homogenizing the tissue was added

in relation to the tissue weight. For example, for each a 100 mg of tissue, 1 ml of a lysis buffer was added. The brain was homogenized in a lysis buffer composed of DPBS, 1% Triton X-100, 1x phosphatase inhibitor cocktail 2 and 3 (Sigma, P0044), and 1x protease inhibitor cocktail (Roche, 11836170001) and was ice-cold prior to homogenization. The brain was first homogenized using the tight pestle followed by a further homogenization using a 21-gauge needle. The homogenate was then transferred to a

Table 2.7

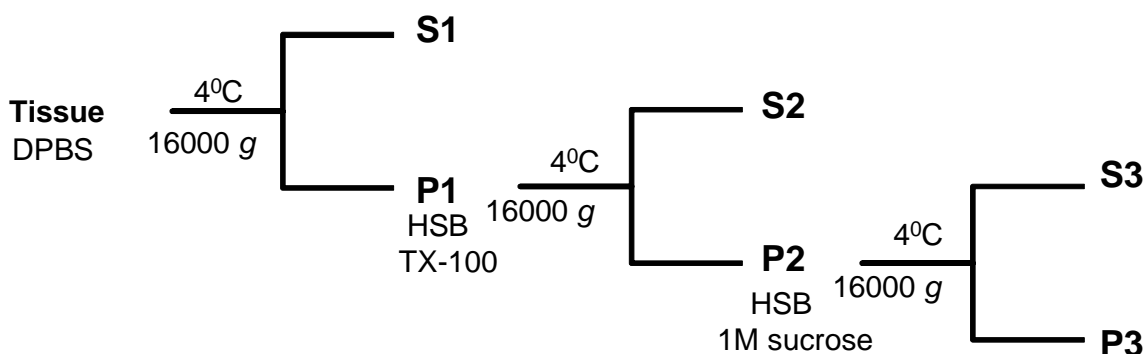
motor neuron culture medium	working concentration	complete L-15 medium	working concentration
Neurobasal medium (Gibco, 21103-049)	_____	L-15 medium (Sigma, L1518)	_____
B27 serum-free supplement (Gibco, 17504-044)	1x	Glucose	1%
Glutamine (Gibco, Cat.no.25030)	500 μ M	penicillin/streptomycin	1%
B-mercaptoethanol (Fisher Scientific)	0.1%	progesterone (Sigma, P8783)	20nM
Horse serum (Sigma, H1270)	2%	Horse serum (Sigma, H1270)	2%
penicillin/streptomycin (Gibco, 15070-063)	1%	Insulin (Sigma, I6634)	5 μ g/ml
BDNF (Invitrogen, 10908-010)	0.1 ng/ml	Putrescine (Sigma, P5780)	100 mM/ml
GDNF (R&D system, 512-GF)	0.1 ng/ml	Conalbumin (Sigma, C7786)	100 μ g/ml
CNTF (Gibco, PHC7015)	0.5 ng/ml	Sodium selenite (Sigma, S5261)	30 nM/ml
Cytosine β -D-arabinofuranoside hydrochloride (Sigma, C6645)	7 μ M	_____	_____

Table 2.7 – The components of motor neuron culture medium as well as complete L-15 medium.

fresh cold 1.5 ml Eppendorf tube and centrifuged at 13,000 rpm for 10 min. Then, the supernatant was transferred into a fresh cold tube and quantified for protein concentration. Both supernatant and the pellet were stored in -80°C for long term storage.

2.3.2 Neurofilament extraction

With regard to homogenizing lumbar spinal cord, three mouse lumbar spinal cords (LSCs) were pooled to facilitate homogenization as it is a small tissue and to avoid tissue loss. Considering that the spinal cord is a tough tissue, the tissue was subjected to sequential homogenization in order to obtain a high yield of proteins (Figure 2.8). This was conducted based on a protocol described by Xiao et al (2008) with some modifications. LSCs were placed in the glass Dounce homogenizer and homogenised 20 times in DPBS, supplemented with phosphatase and protease inhibitors, using the tight pestle. A further homogenization was carried out using a 21-gauge needle. Subsequently, the homogenate was centrifuged at 13,000 rpm for 10 minutes by which two fractions were obtained: supernatant 1 and pellet 1 (referred to as S1 and P1, respectively). S1 was transferred to a fresh Eppendorf tube and kept on ice while P1 was subjected to a further homogenization. P1 was re-homogenized in a high salt buffer (HSB) (750 mM NaCl, 5 mM EDTA, 50 mM Tris, pH 7.5), 1x of phosphatase inhibitor cocktails 2 and 3, 1x of protease inhibitors, and 1% Triton X-100 using the 21-gauge needle. The addition of Triton X-100 facilitates the lysis of any remaining unlysed cells as well as the myelin sheaths from axons, whereas HSB precipitates neurofilaments. The homogenate was centrifuged at 13,000 rpm for 10 minutes and two fractions were obtained: supernatant 2 and pellet 2 (referred to as S2 and P2, respectively). S2 was transferred to a fresh Eppendorf tube and kept on ice while P2 was processed with further homogenization. Lastly, P2 was re-homogenized in HSB buffer containing 1M sucrose (to remove myelin) using the 21-gauge needle. After centrifugation, two fractions were obtained: supernatant 3 (S3) and pellet 3 (P3). S3 was collected and kept on ice while P3 was washed with DPBS and pelleted again by centrifugation. The supernatant was discarded and P3 was dissolved in DPBS containing 2% SDS.

Figure 2.8**Figure 2.8** - Sequential extraction of neurofilaments from mouse lumbar spinal cords.

2.3.3 Preparation of lysates from cell culture

Motor neurons, cultured in a 24-well plate, were washed with warm PBS twice to remove any remaining media. A 50 μ l of RIPA buffer, supplemented with 1X phosphatase inhibitor cocktails 2 and 3, and 1X protease inhibitors cocktail, was used to lyse motor neurons which were incubated on ice for 15 minutes. The lysate was collected into a fresh tube and centrifuged at 1000 g for 10 minutes to pellet the nuclei. Supernatants were collected and stored in -80°C until being processed.

With regard to lysing human and mouse fibroblasts, cells were harvested by trypsinization and washed twice with ice-cold DPBS without Mg^{+2} and Ca^{+2} . Cells were centrifuged at low speed (2000 rpm) using the refrigerated microcentrifuge and freezed in -80°C prior to homogenization. Cells were resuspended in a homogenization buffer consisting of DPBS without Mg^{+2} and Ca^{+2} and supplemented with 1X phosphatase inhibitor cocktails 2 and 3, and 1X protease inhibitors cocktail. Using the glass homogenizer, cells were homogenized using the tight pestle followed by centrifugation at 13,200 rpm for 5 minutes. The clarified homogenate was transferred to a fresh cold tube and quantified for protein concentration.

2.3.4 Determination of protein concentration

Protein concentrations of tissue lysates were determined using bicinchoninic acid assay (BCA) (Thermo scientific, 23227). The assay was conducted following the manufacturer's protocol.

2.3.5 SDS-PAGE electrophoresis

Depending on the molecular weight of the target proteins (Table 2.8), 10% and 12% homogeneous standard SDS-PAGE as well as 4-12% gradient gels were used. The 12% gel was used to resolve proteins with small molecular weights such as LC3 I and LC3 II, 14 and 16 kDa respectively, whereas the 4-12% gradient gels were used to resolve protein complexes. The 10% homogeneous standard SDS-PAGE was prepared in the laboratory whereas the gradient 4-12% (Life technology, NP0323BOX) and the 12% homogeneous standard gels (Life technology, NP0343BOX) were precast gels.

2.3.6 Immunoblotting and analysis

All membranes were blocked in 5% skimmed milk for at least two and a half hours at room temperature (unless specified, Table 2.9) with constant agitation. To prepare the blocking solution, milk was dissolved in PBS containing 0.05% Tween-20 (PBS-T) and mixed properly either by a magnetic bar or by rotating. For detecting phospho-proteins, membranes were blocked in TBS containing 0.1% Tween-20 and 5% BSA. All primary antibodies were diluted (at the recommended dilution by the manufacturer) in PBS containing 0.2% Tween-20, 5% BSA and 0.1% sodium azide, unless specified in Table 2.9. The antibodies were applied on the membrane with the protein side facing up to ensure optimal binding. The membrane was incubated with the primary antibody overnight at 4°C with constant agitation. A short incubation for one hour at room temperature was performed for abundant proteins. Subsequently, the membranes were washed in PBS-T once for 15 minutes and three times for 5 minutes. The washing was performed in a big box (five times the size of the membrane) containing enough washing reagent to ensure a complete removal of excess antibodies. The membrane was incubated with secondary antibodies, 1:10,000 in PBS-T containing 0.05% skimmed milk, for 45 minutes at room temperature with constant agitation. Subsequently, the membrane was subjected to further washes with PBS-T (1 x 15 minutes and 3 x 5 minutes). Afterwards, either substrate of the horse radish phosphatase (HRP) or alkaline phosphatase (AP) was applied evenly on the membrane, with the protein side facing up. The membrane was then placed in between transparency sheets to avoid drying and was placed in a film cassette. Films were

Table 2.8

Protein name (protein symbol)		Size (kDa)	Gel percentage	Running buffer /running time	Amount protein loaded
Stress-activated protein kinase/Jun-amino-terminal kinase (p-SAPK/ JNK)		JNK: 48	Bis-Tris precast 12%	MES SDS running buffer/50 min at 200 volt	15 µl of MN lysate
Microtubule-associated protein light chain 3A (MAP1LC3A)		LC3 I: 14 LC3 II: 16	Bis-Tris precast 12%	MES SDS running buffer/50 min at 200 volt	15 µl of MN lysate
p38 mitogen-activated protein kinases (p38α, β, γ, δ)		41, 41, 42 and 42 respectively	Bis-Tris precast 12%	MES SDS running buffer/50 min at 200 volt	15 µl of MN lysate
Glutamate transporter-1	(GLT-1)	62	Tris-glycine 10%	SDS running buffer/75 minutes at 140 volt	1 µg of mouse brain
	(GLT-1B)	60	Tris-glycine 10%	SDS running buffer/75 minutes at 140 volt	30 µg of mouse brain
Peripherin (Prph)		58	Tris-glycine 10%	SDS running buffer/90 minutes at 140 volt	20 µg of SC lysate
Paxillin (Pxn)		62	Tris-glycine 10%	SDS running buffer/90 minutes at 140 volt	15 µg of MEF lysate
Cytoplasmic dynein intermediate chain subunit (DYNC111)		68	Tris-glycine 10%	SDS running buffer/90 minutes at 140 volt	15 µg of MEF lysate

Table 2.8 - Proteins of interest for immunoblotting. Table provides information about the size of the proteins, the percentage of SDS PAGE for protein detection and the amount of protein loaded.

subsequently developed using automated X-ray developers. Films were scanned using an Epson Perfection 4990 photo scanner and quantified using TotalLab TL100 image analysis software. GraphPad prism 5 was used for statistical analysis.

2.3.7 Immuno-precipitation

Protein A-Sepharose 4B beads (Invitrogen, 101041) were washed three times by adding 1 ml ice cold DPBS and centrifuged at 400 *g* for 2 minutes at 4°C before being incubated with the primary antibody (PA). Also, tubes with a narrow conical bottom were used to facilitate removing the washing buffer without disturbing the beads as well as using a 200 µl tip to remove the buffer that is in a close proximity with the beads. Subsequently, the beads were blocked in 3% BSA/DPBS for 1 hour followed by one wash with DPBS. The homogenate was cleared by incubation with the beads for 2 hour at 4°C with agitation followed by centrifugation for 2 minutes at 400 *g* to collect the homogenate. The beads were incubated with either 1.5 µg of PA or IgG (negative control) for two hours at 4°C with shaking after which the beads were washed three times with DPBS to remove unbound antibody. Then, a 100 µl of cleared homogenate was incubated with either PA-linked or IgG-linked beads overnight at 4°C with agitation. Next day, the supernatant was aspirated and kept as a control and the beads were washed 6 x 10 minutes with DPBS on a rotator at 4°C followed by one wash with water for 10 minutes. Finally, the interaction between the beads and the protein complex-linked antibodies were released by adding 1x SDS sample buffer followed by boiling the sample at 95°C for 5 minutes. The samples were centrifuged at 16000 *g* for 5 minutes to collect the supernatant using a fine loading gel pipette tip. The samples were kept in -20°C for short term storage prior to western blotting.

2.3.8 Immunocytochemistry

Coverslips for immunofluorescence were cleaned with 70% ethanol and flamed to remove any dust that might cause artifacts. Under a fume cupboard, 22 mm² coverslips were placed in a 6-well plate and 13 mm round coverslips in a 24-well plate. Coverslips were then coated (unless stated) with 10 µg/ml collagen type I by adding 200 µl to the

22 mm² coverslips or 50 µl to the 13 mm coverslips. Collagen was either allowed to air dry in a tissue culture hood at room temperature or baked at 60°C without the lid followed by UV sterilization. For coating with poly-D-lysine, 100 µg/ml of poly-D-lysine was added to the coverslips and incubated at 37°C for two hours. The excess solution was removed and wells were washed twice with double distilled water followed by air drying in the tissue culture hood without the lid. Fibroblast cells at a density of 5×10^5 and 3×10^5 were seeded onto 22 mm² and 13 mm coverslips, respectively. Seeding cells at this density was enough to obtain cells at 50% confluence. All reagents used in this procedure were added at 1 ml/22 mm² and 0.5 ml/13 mm coverslips. For fixing cells, growth medium was removed and cells were washed three times with warm PBS. Cells were fixed with 4% paraformaldehyde diluted in PBS for 10-20 minutes at room temperature. The fixative solution was removed and cells were washed three times in PBS. Cells were then permeabilized with 0.1% Triton X-100 in PBS for 5 minutes to ensure a complete penetration of antibodies when applied. The permeabilizing solution was removed and cells were washed three times with PBS. Cells were blocked with 3% BSA in PBS for 20 minutes followed by further three washes with PBS. A humidified chamber was constructed to prevent cells from drying out and to be exposed to the light. To create the humidified chamber, a large box was wrapped with aluminium foil while ensuring that the lid could be removed. Paper towels were soaked in water and placed inside the box. The cells were incubated with primary antibodies for 1 hour and with secondary antibodies for 30 minutes at room temperature and were placed in the humidified chamber (Table 2.10). Following the application of antibodies, the cells were washed three times with PBS. To stain with DAPI, cells were incubated with DAPI diluted in water at the ratio of 1: 80,000 for 5 minutes followed by three washes in double distilled water. For slide preparation, approximately 10 µl of mounting medium (Invitrogen, P36930) was placed onto the slide ensuring that no air bubbles were introduced. Using a tip-curved tool, the coverslip was removed from the 6-well plate and the excess liquid was removed by blotting the edge of the coverslip on a white paper towel. The edge of the coverslip was rested on the slide with the cell side facing towards the slide and gradually released so that it dropped onto the mounting medium.

Table 2.9

primary antibody	dilution/incubation buffer	incubation time/temp	blocking time/ buffer	secondary antibody
Peripherin (abcam, AB1530)	1:500/PBS-T + 5% BSA	O/N 4°C	O/N, PBS-T + 5% BSA	Anti-Rabbit IgG antibody/AP (Sigma, A3812)
Per61 (abcam, Ab4646)	1:500/PBS-T + 5% BSA	O/N 4°C	O/N, PBS-T + 5% BSA	Anti-Rabbit IgG antibody/AP (Sigma, A3812)
GLT-1 (Tocris, 2063)	1:500/PBS-T + 5% BSA	O/N 4°C	2 h/PBS-T + 5% skimmed milk	Anti-Rat IgG/AP (Sigma, A8438)
GLT-1B (Thermo scientific, MA1-46011)	1:200/PBS-T + 5% BSA	O/N 4°C	O/N, PBS-T + 5% skimmed milk	Anti-Mouse IgG/AP (Sigma, A3562)
LC3A (Cell signalling, D50G8)	1:500/PBS-T + 5% BSA	O/N 4°C	2 h, 30 min/ PBS-T + 5% skimmed milk	Anti-Rabbit IgG antibody/HRP- conjugated (G E Healthcare ,NA934VS)
pJNK (Cell signalling, 9251)	1:1000/PBS-T + 5% BSA	O/N 4°C	2 h, 30 min/ PBS-T + 5% skimmed milk	Anti-Rabbit IgG antibody/HRP- conjugated (G E Healthcare ,NA934VS)
c-Fos (Santa Cruz Biotechnology, sc- 52)	1:400/PBS-T + 5% BSA	O/N 4°C	2 h, 30 min/ PBS-T + 5% skimmed milk	Anti-Rabbit IgG antibody/HRP- conjugated (G E Healthcare ,NA934VS)
Phospho-p38 MAPK (Thr180/Tyr182)	1:1000/PBS-T + 5% BSA	O/N 4°C	2 h, 30 min/ PBS-T + 5% skimmed milk	Anti-Rabbit IgG antibody/HRP- conjugated (G E Healthcare ,NA934VS)
Alpha-tubulin (Upstate, 05-829)	1:1000/PBS-T + 5% BSA	60 min R/T	1 h/PBS-T + 5% skimmed milk	Anti-Rabbit IgG antibody/HRP- conjugated (G E Healthcare ,NA934VS)
Beta-actin (Sigma, A5316)	1:1500/PBS-T + 5% BSA	60 min R/T	1 h/PBS-T + 5% skimmed milk	Anti-Mouse IgG antibody/HRP (Dako, P0260)
cytoplasmic dynein intermediate chain (gift from Kevin Pfister)	1:1000/PBS-T + 5% BSA	60 min R/T	2 h, 30 min/ PBS-T + 5% skimmed milk	Anti-Mouse IgG antibody/HRP (Dako, P0260)
p-Paxillin (Invitrogen)	1:1000/TBS-T containing 3% BSA	2 h R/T	O/N, TBS-T + 5% BSA	Anti-Rabbit IgG antibody/AP (Sigma, A3812)
Paxillin (BD Transduction laboratory, cat no 610051)	1:1000/PBS-T + 5% BSA	60 min R/T	O/N, TBS-T + 5% BSA	Anti-Mouse IgG antibody/HRP (Dako, P0260)

Table 2.9 – Antibodies for immunoblotting. Abbreviation: *HRP* Horse radish peroxidase, *AP* Alkaline phosphatase, *O/N* overnight, *R/T* room temperature, *BSA* Bovine serum albumin, *PBS-T* PBS containing 0.2% Tween-20, *TBS-T* TBS containing 0.1% Tween-20.

Table 2.10

primary antibody	dilution/incubation buffer	Incubation time/temp	secondary antibody
Paxillin (BD Transduction laboratory, cat no 610051)	1:100/PBS + 3% BSA	1 h R/T	Anti-Mouse IgG antibody/Alexa fluor 488 (Molecular Probes, A11001)
cytoplasmic dynein light intermediate chain (gift from Kevin pfister)	1:100/PBS + 3% BSA	1 h R/T	Anti-Rabbit IgG antibody/Alexa fluor 546 (Molecular Probes, A11035)
Alpha-tubulin-1A chain/FITC-conjugated (Sigma, F2168)	1:500/PBS + 3% BSA	1 h R/T	_____

Table 2.10 - Antibodies for immunocytochemistry. Abbreviation: *O/N* overnight, *R/T* room temperature, *BSA* Bovine serum albumin.

2.3.9 Cell spreading assay

In order to perform spreading assay on mouse embryonic fibroblasts (MEFs), cells were first treated with trypsin and then deactivated by adding complete MEF's medium. Subsequently, the cells were pelleted in order to remove the trypsin, then washed once in DPBS to remove any remaining trypsin residues and at last resuspended in complete medium. The cells were subsequently placed into an incubation shaker at 37°C for 45 minutes in order to ensure recovery from the trypsin treatment. MEFs were plated onto 22 mm² coverslips, pre-coated with collagen. Cells were incubated at 37°C for 50-60 minutes until the cell population had reached its maximum spread. The

cells were either fixed in 4% paraformaldehyde for immunocytochemistry or lysed for immunoblotting.

2.3.10 Wound healing/scratch assay

For IP and western blotting, MEF cells were plated in a 10 cm petri dish in order to obtain a confluent monolayer after 24 hours. The cells were treated either with 30 µg/ml mitomycin C for one hour or with 10 µg/ml for two hours to inhibit cell proliferation as previously described (Menon et al. 2009). Subsequently, the cells were washed with warm DPBS to remove any remaining residue of mitomycin C. The monolayer was extensively scratched, using a 10 µl pipette tip. The medium was changed to remove floating cells. Cells were then incubated at 37°C for the following time points: 6, 11, 13 hours and then collected by trypsinization, followed by three consecutive washes with cold DPBS. The cells were then stored at -80°C prior to lysing.

In order to capture images of the cells using a phase contrast microscope (Zeiss, Axiovert 25) and monitoring cell motility, cells were plated on a 6-well plate to obtain a cell monolayer after 24 hours followed by treatment with 10 µg/ml of mitomycin C for two hours. Subsequently, one scratch was performed onto the monolayer using a 10 µl pipette tip. Cells were captured at pre-migration (time 0) and during migration at the following time points 13, 15, 17, 19, 21 and 23 hours. In order to ensure that the plate was always placed in the same position for image capturing after each incubation time point, the following method was devised: at first masking tape was applied around the plate (Figure 2.9A). On this tape, lines could be drawn matching the lines drawn on each side of the plate itself (Figure 2.9A middle and bottom panel, red arrow). Five images were captured from each well (one scratch), each from a different position. After capturing the image from the first position, number 1 on the plate matched number 1 on the masking tape. The plate was then moved upward, thus number 2 on the plate matched number 1 on the masking tape on both sides of the plate (Figure 2.9A, middle panel). Images of the cells were captured with a camera (Canon G3), mounted using an adaptor (Carl Zeiss, 426126), through a 5x objective, which combined with 4x optical zoom to give a total magnification of 20x. For statistical analysis, the time points, 13, 15, 17, 19, 21 and 23 hours were allocated ratio values by

dividing the scratch area at each time point by the scratch area at time point 0 (fold change of wound area in Figure 5.7). The mean of ratio values (five values for each time point corresponding to the five images captured at different regions from one scratch) were compared between wild type and mutant samples using unpaired t-test.

Figure 2.9



Figure 2.9 - Setting up the microscope stage for capturing an image with the plate being in the same position. The masking tape surrounding the plate was marked every half a centimetre matching those marks on the side of the plate (red arrow). Capturing an image in the first position of the well, was achieved by matching the first line on the masking tape with the first line on both sides of the plate. The next position was determined by aligning the second line on the plate (middle panel, number 2 coloured in yellow) with the first line on the masking tape (middle panel, number 1 coloured in green).

2.3.11 RNA extraction and cDNA preparation

RNA was extracted using a column based method (Qiagen, 74134). The tissue (lumbar spinal cord or brain) was homogenized in RLT Plus lysis buffer containing 1% beta mercaptoethanol. The tissue was first homogenized in a glass homogenizer using the tight pastel followed by a further homogenization using a 21 gage needle. Total homogenate was spun for 3 minutes at maximum speed. This is important for discarding all cell debris that might block the column. The supernatant was used to isolate RNAs following the manufacturer's instructions. RNA integrity was determined by running a 0.8% agarose gel containing 0.1% ethidium bromide. A 100 ng of total RNAs were loaded in 6 X 7 cm agarose gel. The gel was run at 11 volt/cm for 20 minutes. The quality of total RNAs was examined by the presence of two intensive bands representative of the ribosomal RNAs 28S and 18S (Figure 2.10). The 28S rRNA band should be twice as intense as the 18S rRNA. The smearing represents mRNAs.

cDNA was generated using the Promega reverse transcription system. In brief, about 0.5-1 µg of total RNAs were used for reverse transcription reaction using random hexamer primers. The reaction was incubated at 42°C for 1 hour to synthesize cDNAs followed by a further incubation at 95°C for 5 minutes to deactivate the enzyme. One to two µl of cDNA was used in polymerase chain reaction (PCR) to amplify the target mRNAs (Table 2.11).

Table 2.11

Gene symbol	FWD primer sequences (5'-3')	REV primer sequences (5'-3')	annealing temp / elongation time
Prph	CTTGCCACCCGGCCTAGTT	ACCATGGGGTCATTCTTGAG	58.1°C/2 min
Per56/58	TGCCTGAGATGGAGCCTCTCCAG GA	GCATGCAGAGCAGGACTGGATA CGA	62°C/30 Sec
Per61/58	TCCCGCCTAGAACTGGAGCGCA AG	TGGCGGCGTCCGACAGGTCAGC AT	69°C/30 Sec
Per61	AGAGGAGTGGTATAAGTCGAAA GTGCC	TGACGTCGAGACTCGTTCAT	62°C/30 Sec
GLT-1	AGAGAGGCTGCCCCGTAAAT	ACAAAAGGAAGCTGGCAAGA	63.8°C/2:30 min
GLT-1B	TTAGAGGGGTGAGGTGGATG	AACAATATGCCCAAGCAGGT	63.8°C/2 min

Table 2.11 – The primer sequences for mRNAs of interest. The FWD primer of per61 was adapted from (Swarup et al. 2011) with some modifications.

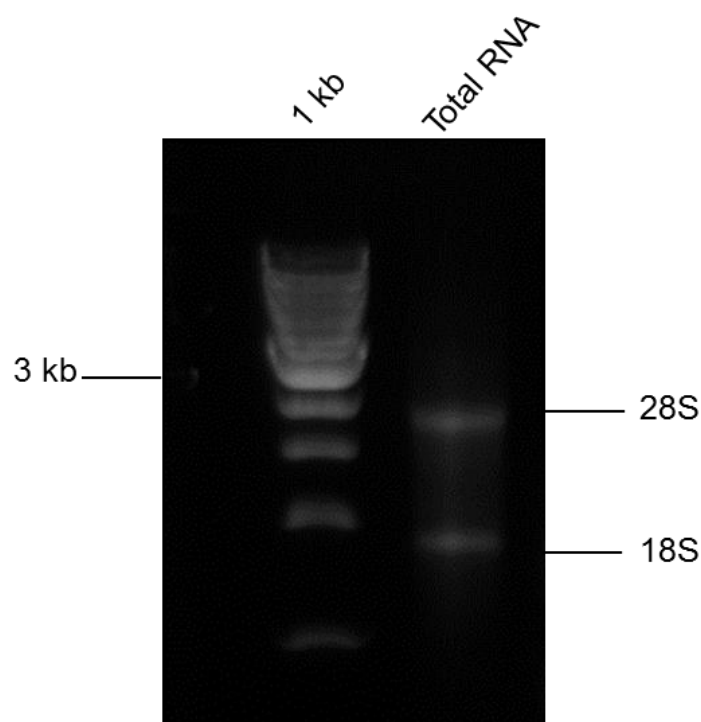
Figure 2.10

Figure 2.10 – Gel electrophoresis of purified total RNA using a column based method. Total RNA was extracted from brain tissue. Around 100 ng of total RNA was analysed on a 0.8% non-denaturing DNA agarose gel stained with ethidium bromide to determine the yield and the integrity. Two distinct bands were observed representing ribosomal RNA; 28S and 18S. 28S and 18S are just under 2 kb and 1 kb, respectively. The smearing represents mRNAs.

2.4 Cloning and transfection

2.4.1 Transformation of the chemically competent cells DH5 alpha

Plasmids were first propagated into the chemically competent bacteria strain DH5a. A 50 µl of competent cells was thawed on ice. A 2 µl of a plasmid suspension was added into the 50 µl competent cells, mixed by gentle flicking a few time and incubated on ice for 30 min. A heat shock was applied on the mixture by the incubation at 42°C for 40 seconds following by two-minute incubation on ice. The pre-warmed recovery medium, either super optimal broth (S.O.B) or lysogeny *broth* (LB), was then added to the cells followed by incubation at 37°C for 1 hour with agitation. The transformation mixture was then plated onto LB agar plates containing the selection marker (Table 2.12) and spread using a sterilised spreader. The plates were kept on the bench for a

few minutes (10-15 min) for the agar to absorb the mixture then inverted and incubated at 37°C overnight. For miniprep isolation of the plasmids, LB broth containing a 100 µg /ml ampicillin was inoculated with a single colony and incubated in a shaker at 37°C overnight.

Table 2.12

Antibiotic	Stock concentration	Working concentration	
		High copy plasmid (relaxed)	Low copy plasmid (stringent)
Ampicillin	50 mg/ml	50 µg/ml	20 µg/ml
Kanamycin	40 mg/ml	50 µg/ml	10 µg/ml

Table 2.12 - Antibiotics and their recommended concentration according to the type of plasmids.

2.4.2 Miniprep isolation of plasmid DNA

Plasmid DNA was isolated using a column based method (Promega miniprep kit, A1223) according to the manufacturer's instructions. In sterilised conditions, a 5 ml of LB medium was added into a clean 10 ml bottle containing an appropriate selective antibiotic (Table 2.12). The medium was inoculated using an inoculating loop either from a single colony from a bacterial culture plate or directly from the bacterial glycerol stock. The culture was incubated at 37°C overnight with vigorous shaking at 300 rpm. A 3 ml of the bacterial culture was used for plasmid isolation. For processing a total of 3 ml of culture, 1.5 ml of the bacterial culture was centrifuged at 13,000 rpm for 30 seconds and the supernatant was discarded. An additional 1.5 ml of the bacterial culture was added to the same tube that contained the pellet from the first centrifugation and subjected to the same centrifugation conditions. From this point onwards the manufacturer's instruction were followed aside from the plasmid DNA being eluted in 30 µl double distilled water by centrifugation at 13,000 rpm. The plasmid DNA concentration was estimated using a nanodrop spectrophotometer. The plasmid DNA was highly purified if, the 260/230 and 260/280 ratios were between 1.8-2.

2.4.3 Midiprep isolation of plasmid DNA

Plasmid DNA was isolated using the Invitrogen midiprep kit (K2100-04) following the manufacturer's instructions. To prepare a 100 ml bacterial culture, a 5 ml LB medium was inoculated with a single colony from a freshly streaked plate and incubated at 37°C for 8 hours with shaking. After 8 hours, the culture was sufficiently cloudy to perform a 1/1000 dilution in a final volume of 100 ml. The culture was incubated at 37°C with shaking at 300 rpm. Twenty five millilitres (if high copy plasmid) or 75 ml (if low copy plasmid) of bacterial cells were harvested by centrifugation at room temperature at 3760 *g* for 15 minutes. Subsequently, the manufacturer's instructions were followed. After pelleting the plasmid DNA by adding a 100% isopropanol, the pellet was washed with 70% ethanol without disturbing the pellet. The tube was centrifuged again and ethanol was discarded. The pellet was dried and resuspended in an appropriate volume of double distilled water to achieve a sufficient concentration or a sufficient volume of the plasmid DNA depending on requirements (100 µl to achieve a higher concentration or 200 µl for a higher volume). The plasmid DNA concentration was measured using a nanodrop spectrophotometer. A high purification of plasmid was always obtained using this kit ($260/230$ and $260/280 > 1.9$).

2.4.4 Transfecting mammalian cells by electroporation

For the transfection of MEFs using the electroporation-based Neon Transfection system (Invitrogen, MPK10025), cells were grown in a T75 flask until confluent. Following the manufacture's protocol, cells were harvested by trypsinization and counted (using a haemocytometer) in order to obtain the recommended cell density of 5×10^6 cells/ml. Cells were washed with warm DPBS (37°C) without Mg^{+2} and Ca^{+2} before re-suspending in Re-suspension buffer R. Using a 100 µl tip (provided with the kit), approximately 5×10^5 cells were pipetted and mixed with 5-7 µg plasmid DNA. A pulse was then applied using the electroporation parameters that are shown in Table 2.13. According to the manufacture's instruction, the tip can be used up to three times. Therefore, the same tip was used to electroporate more cells (15×10^5 cells in total) and the cells were added into a T25 flask containing a recovery medium (a cell culture medium without antibiotics). After 24 hours, the recovery medium was

replaced with their growing medium. For live-cell imaging applications, cells were imaged 48-hour after electroporation and the medium was replaced with live-cell imaging medium (life technologies, A14291DJ).

Table 2.13

Cell type	Pulse voltage (v)	Pulse width (ms)	Pulse number
MEFs	1,650	20	1

Table 2.13 - Electroporation parameters for transfecting MEFs with plasmid DNA.

2.4.5 Replacing EGFP with m-Cherry in TRIP-Syn-G-W lentivirus plasmid and EB1 cloning

My aim was to replace EGFP which is already found in a 2nd generation lentivirus plasmid (p.TRIP-Syn-G-W), which contains the neuron specific synapsin promoter, with m-Cherry in order to create fusion proteins. This plasmid was a kind gift from Dr Piotr Michalak (UCL Institute of Neurology). M-Cherry was amplified from the m-Cherry- α -tubulin-IRES plasmid (Add gene, 21043). The *NheI* restriction site was found in the 5' end of both plasmids. However, no compatible site was found for the 3' end of m-Cherry. Therefore, I created an *SpeI* restriction site, which was already present in the lentivirus plasmid downstream of EGFP, for subcloning m-Cherry because it is not within the m-Cherry sequence or in any of my proteins of interest. To achieve this, I designed a primer to amplify m-Cherry and simultaneously create the *SpeI* restriction site (Figure 2.11A and Table 2.14). Also I designed primers to create the *SpeI* restriction site upstream the proteins of interest as well as remove the start codon (Figure 2.11B and Table 2.14). I also included the linker sequence in the m-Cherry- α -tubulin-IRES plasmid in between m-Cherry and alpha tubulin (Figure 2.11A). The reverse primer included the entire linker sequence and the *SpeI* restriction site was inserted at the 5' end of the reverse primer (Figure 2.11A). I also ensured that the Kozak sequence is also included and therefore the translation will be initiated at the start codon of m-Cherry.

As I aimed to clone End-binding protein 1 (EB1) downstream of m-Cherry, I designed primers to PCR amplify EB1 from the mouse brain cDNA (Table 2.14). As this protein

will be in fusion with m-Cherry, there is no need for a start codon. Therefore, the start codon was deleted by designing the primer to include nucleotides located just after the start codon and adding the *SpeI* restriction site at the 5' end of the forward primer (Figure 2.11B). The reverse primer was designed from the 3' UTR. The *BstB1* restriction site was also added to the 5' end of the reverse primer as this site is already found downstream the *SpeI* restriction site in the TRIP-Syn-G-W lentivirus plasmid (Figure 2.11B).

After PCR amplification, m-Cherry or EB1 was blunt-end ligated into pBluescript II SK(+). The blunt end ligation was conducted according to the manufacturer's protocol (New England Biolabs, M0367). The m-Cherry coding sequence was restricted out from pBluescript II SK(+) using *NheI* and *SpeI* and was sticky-end ligated into the TRIP-Syn-G-W lentivirus plasmid after excising EGFP out with the same enzymes. The sticky-end ligation was conducted according to the manufacturer's protocol (New England Biolabs, M0370). Subsequently, EB1 was subcloned into the TRIP-Syn-m-Cherry lentivirus plasmid downstream of m-Cherry (Figure 2.12). The next stage will be the packaging of p.TRIP-Syn-m-Cherry-EB1 lentivirus using HEK293 cells. Subsequently, the virus will be used to transduce the recombinant lentiviral construct into motor neurons to visualise the microtubule plus ends by conducting live-cell imaging.

Table 2.14

Primers	FWD primer sequence 5'-3'	REV primer sequence 5'-3'
m-Cherry	AGTGAACCGTCAGATCCGCT	TATA ACTAGT TCGAGATCTGAGTCCGGA
EB1	TATA ACTAGT GCAGTGAATGTGTAC TCTACG	TTAAT TCGAA GATTAATAAAAAGGGAGTA T

Table 2.14 - Primers for cloning m-Cherry and EB1 into the TRIP-Syn-G-W lentivirus plasmid. Bold letters represent the restriction sites for the enzymes *SpeI* and *BstB1*, ACTAGT and TTCGAA, respectively.

Figure 2.11

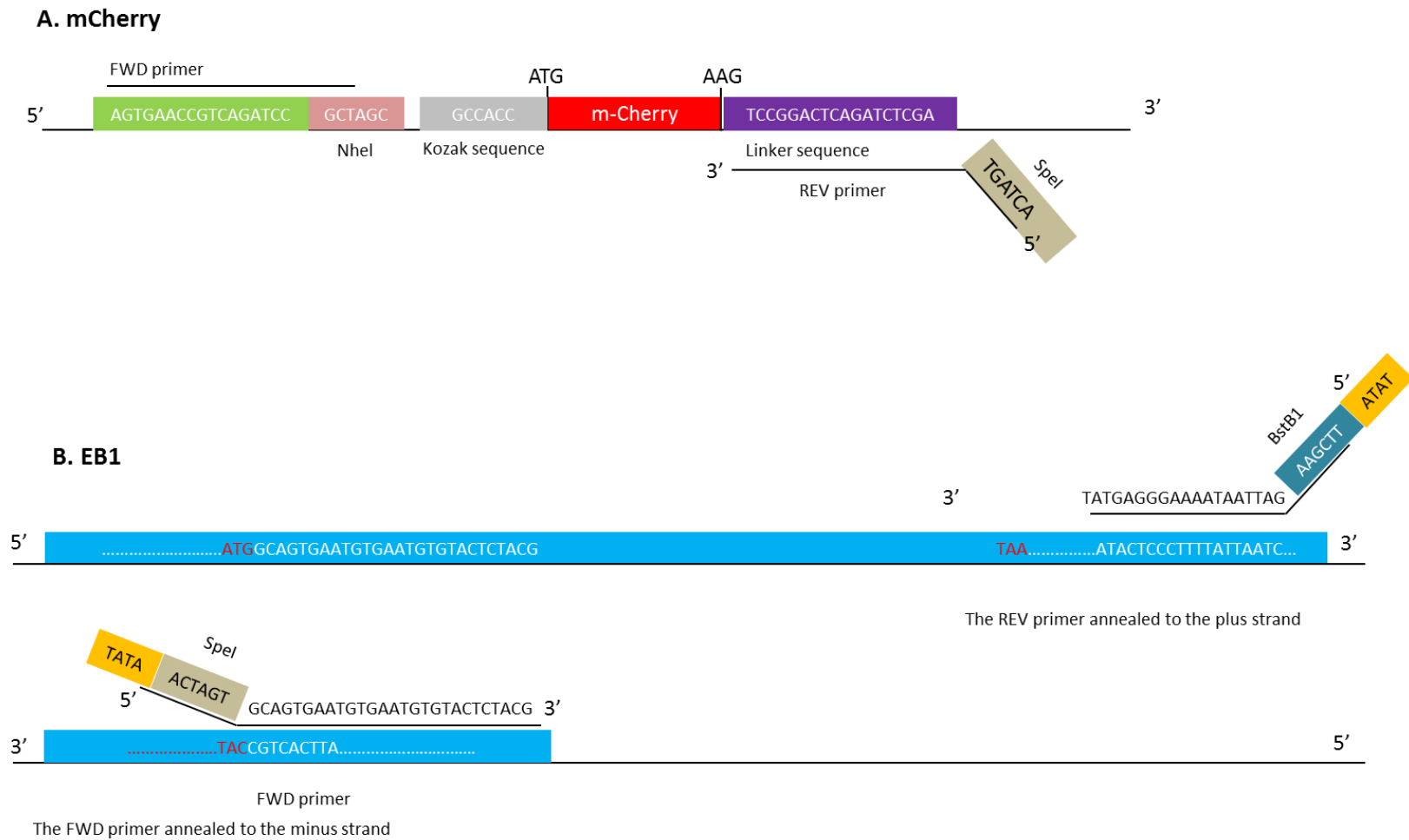
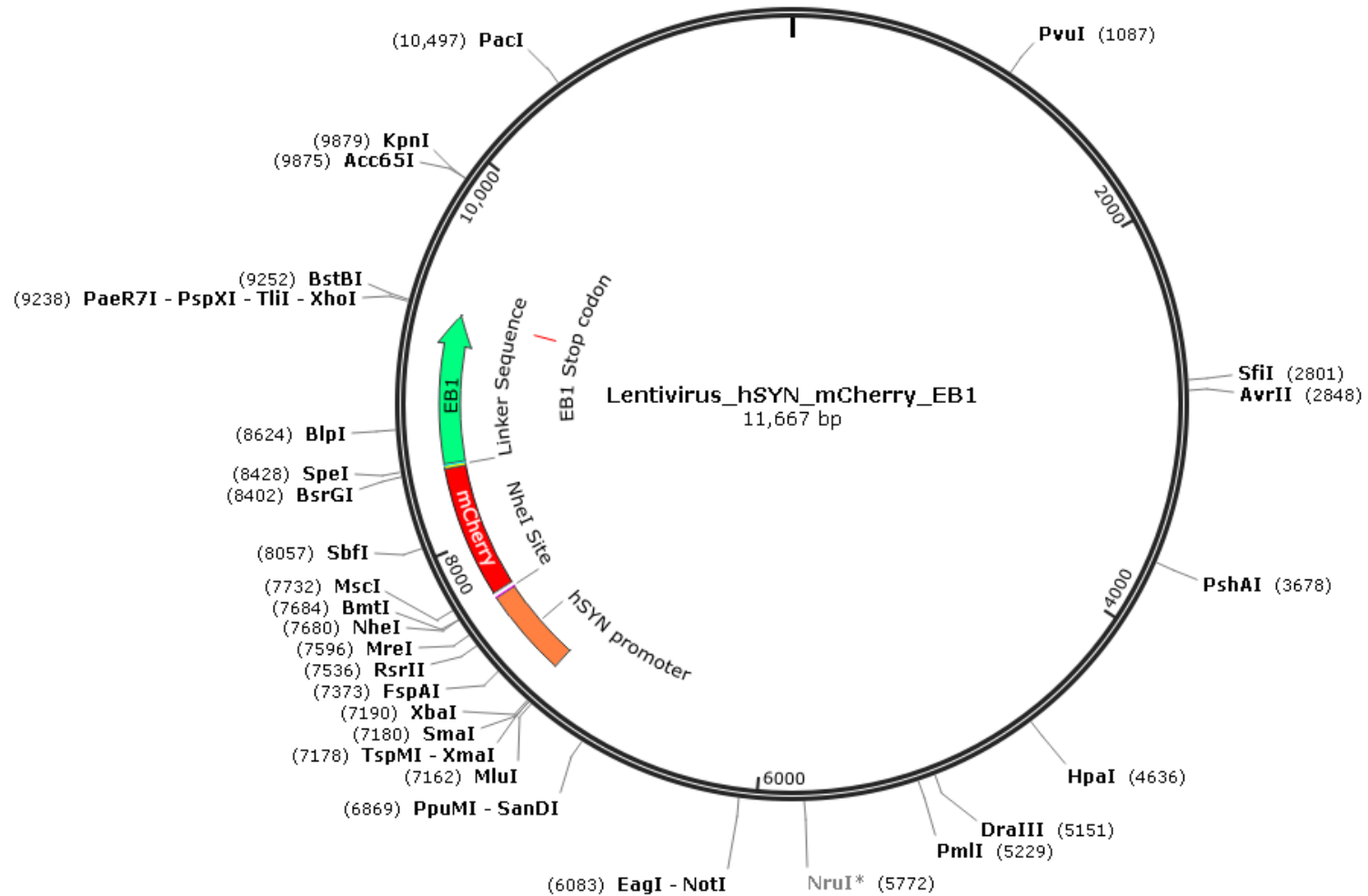


Figure 2.11 - Designing m-Cherry and EB1 primers for cloning into the TRIP-Syn-G-W lentivirus plasmid.

Figure 2.12

Figure 2.12 - A vector map of the 2nd generation TRIP-Syn-m-Cherry-EB1 lentivirus plasmid.

2.4.6 AdEasy mCherry- α -tubulin plasmid purification, isolation from HEK293 and preparation of high titre viral stock

The AdEasy mCherry- α -tubulin plasmid (Add gene, 26767) was propagated into the chemically competent bacteria strain DH5 α followed by purification using a Qiagen kit (27104) according to the manufacturer's instructions. This kit enables purification of large plasmids as the size of pAdEasy mCherry- α -tubulin is approximately 30 kb. Prior to transfection into HEK293, the plasmid was linearized by restriction digestion using the restriction enzyme *PacI* followed by purification with phenol/chloroform/isoamyl alcohol. Briefly, one volume of phenol/chloroform/isoamyl alcohol was added to a 200 μ l of the digestion mixture containing 8 μ g of plasmid. The mixture was gently vortexed for 2 minutes followed by centrifugation at 13000 rpm for 10 minutes. The upper phase, which contains the plasmids, was transferred into a 1.5 ml transparent Eppendorf tube to facilitate visualizing the small pellet at the end of the process. A 1/10 volume of 3 M sodium acetate (pH 5.2) was added and mixed well by vortexing the mixture slightly. Subsequently, two volumes of 100% cold ethanol were added followed by a slight vortexing and centrifugation at 4°C at 13000 rpm for 10 minutes. The pellet was small but easy to visualize. The supernatant was removed and the pellet was washed with 70 % ethanol followed by centrifugation at 13000 rpm for 1 minute. The pellet was air dried and then suspended in either a complete culture medium, if peqFECT transfection reagent was used (cat no 13-8099, Peqlab), or in jetPRIM buffer (cat no 114-01), if Polyplus transfection reagent was used. The suspension was then incubated for 10 minutes at room temperature. The mixture was added dropwise into HEK293 cells, which are grown one day before transfection in a T25 flask 50% -70% confluent. The flask was gently rocked to ensure a good mixing between the medium and the reagent. The medium was replaced after four hours when Polyplus reagent was used. No medium change is required when using peqFECT reagent. The cells were incubated with the virus for upto three weeks. Subsequently, the virus was extracted by applying four freeze-thaw-vortex cycles (Figure 2.13). After centrifugation to pellet cell debris, the supernatant, which contains the virus, was collected. This supernatant was used to infect HEK293 grown in two T75 flasks (first round). Supernatants, containing virus, from the first round was used to infect four T75 flasks (second round).

Supernatants from the second round were used to infect HEK293 in eight flasks (third round). After three rounds of viral amplifications, supernatants were pooled and filtered through a 0.45 μm syringe filter. Around 25 ml were centrifuged for two and a half hours at 47000 g at 4°C to pellet the virus. A visible pellet was observed and the supernatant was removed. The pellet was resuspended in 200 μl PBS, aliquotted into 20 μl and stored in -80°C.

2.5 Image acquisition and microscopy analysis

Live cell images of m-Cherry microtubules in MEFs were taken every 5 seconds for a period of 10 minutes using a spinning disk confocal microscope. M-Cherry-microtubules were captured with a 60X oil objective using a TRITC filter (561m) with an exposure time of 300 ms. Live cell images of RFP-EB1 in MEFs were taken every 2 seconds for a 2 minute duration using personal DeltaVision (widefield deconvolution microscope) with a 100X oil objective and a TRITC filter (ex. 555/28, em. 617/73). The exposure time was 0.5 seconds at 50% transmission. Table 2.15 shows microscopes and parameters used to capture fixed-cell images.

Table 2.15

Proteins of interest/Cell type	Microscope	Objective	Filter set	Exposure time	Transmission
Paxillin/MEFs and human fibroblasts	DeltaVision Core	40X	Fitc (ex. 490/20, em. 528/38)	0.25 Sec	50%
DLIC/MEFs	DeltaVision Core	40X	Tritc (ex. 555/28, em. 617/73)	0.5 Sec	100%
Microtubules/MNs	DeltaVision Core	100X	Fitc (ex. 490/20, em. 528/38)	0.25 Sec	50%

Table 2.15 – Microscopes and parameters for fixed-cell images.

2.6 Measuring the pixel intensity of adhesion sites

In order to measure the pixel intensity of adhesion sites, an algorithm was generated in collaboration with Dr Constantino Reyes Aldasoro. The leading edge of cells that were subjected to the spreading assay was first defined. This was performed by

measuring the average intensity of pixels from the cell centre to the cell periphery. Given the centre of the cell as the start point, the intensity increases, and then decreases due to the presence of a dark ring (Figure 2.14A and B, white arrow and cyan ring, respectively). The pixel intensity increases again at the cell periphery, after the dark ring (Figure 2.14C). This ring acts as the cut off by which the algorithm recognizes the beginning of the cell periphery, measuring objects (adhesion sites) beyond it and towards the cell edge (Figure 2.14D, red circles).

Figure 2.13

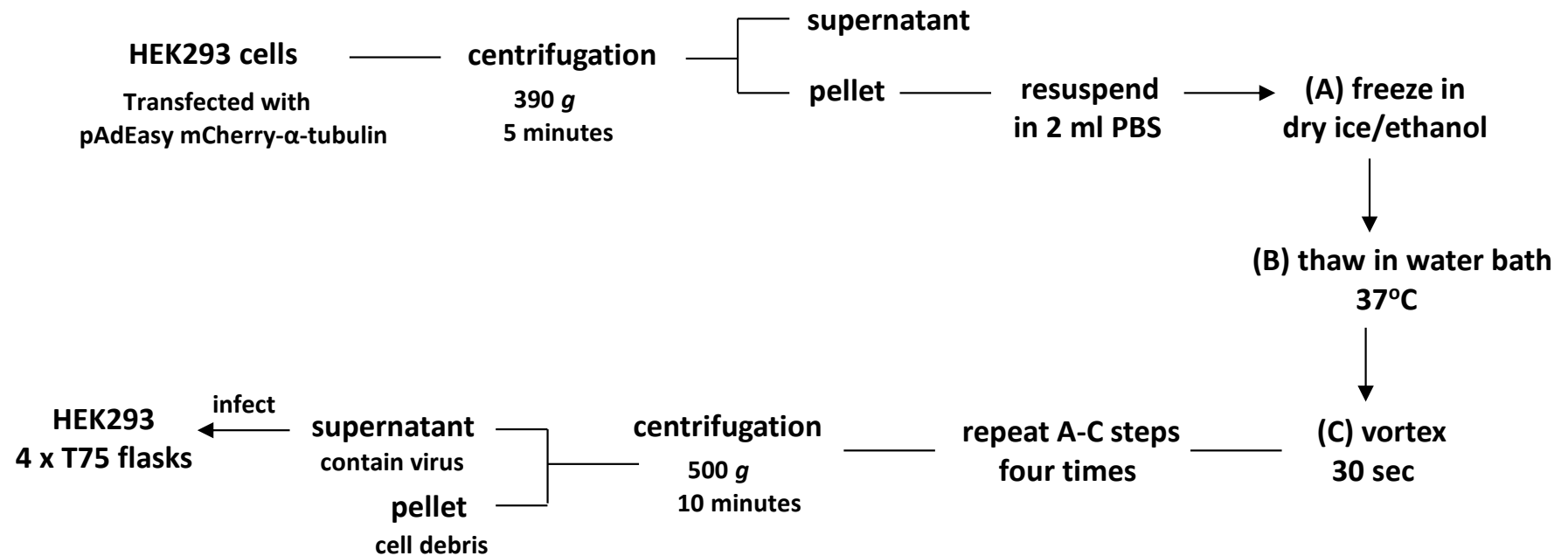


Figure 2.13 - Freeze-thaw-vortex cycles for virus extraction.

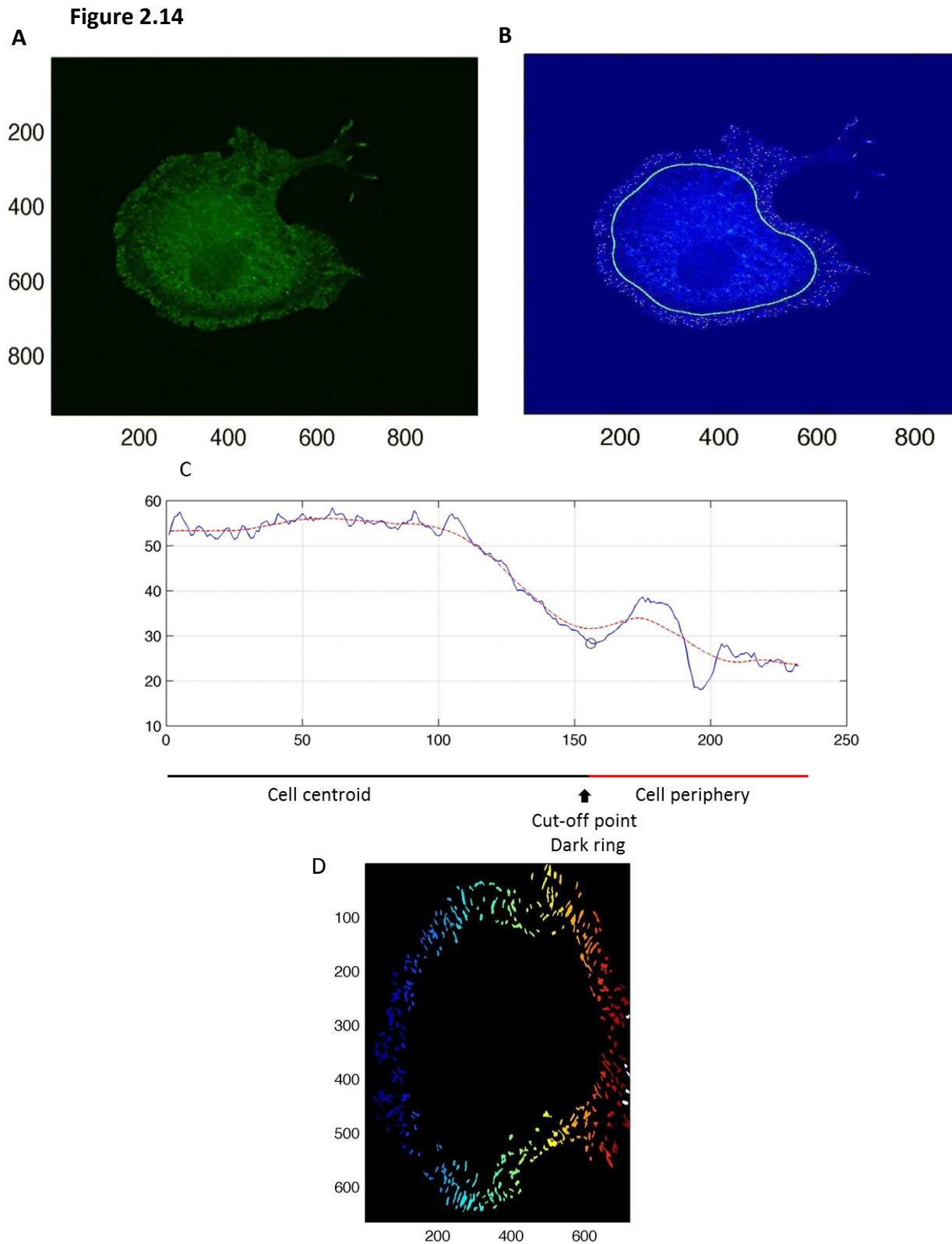


Figure 2.14 – High throughput focal adhesion quantification. The Figure demonstrates how the algorithm defined the leading edge for focal adhesion quantification. (A) Shows a cell subjected to the spreading assay. (B) Shows a cyan ring that represents the dark region between the cell centre and cell periphery. (C) Demonstrates the pixel intensity from the cell centre to the cell periphery. (D) Shows focal adhesions recognized by the algorithm.

Chapter 3

Aberrant expression of peripherin and GLT-1B in TDP-43 mouse models

3.1 Introduction

The molecular basis underlying the degeneration of motor neurons in ALS is still unclear. TDP-43, an RNA/DNA binding protein, is involved in RNA processing and has been implicated in ALS. Nuclear loss as well as cytoplasmic ubiquitin-positive inclusions of TDP-43 are some of the hallmarks of ALS and FTLD. Aberrant RNA splicing of peripherin and EAAT2 (excitatory amino acid glutamate transporter 2) have also been implicated in the pathogenesis of ALS (Lin et al. 1998; Robertson et al. 2003). Abnormal expression of the peripherin splice variant per61 was found in the SOD1 mouse models of ALS and was found to have a toxic effect on motor neurons (Robertson et al. 2003). Moreover, aberrant RNA splicing as well as the loss of EAAT2 protein have been reported in some ALS cases (Lin et al. 1998). In this chapter, I investigated whether: 1) TDP-43 regulates splicing of peripherin and GLT-1 (the murine homologue of EAAT2) RNAs. 2) Impaired function of TDP-43 caused by ALS-associated mutations would lead to abnormal splicing of peripherin and GLT-1 RNAs. To answer these questions, I utilized two mouse models of TDP-43 as a tool to study the effect of TDP-43 dysfunction on peripherin and GLT-1 expression levels: The first was TDP-43^{A315T} transgenic mouse model harbouring a mutation located in the C-terminal region of TDP-43. This mouse model recapitulates key features of ALS and FTLD. The second mouse model was an ENU-mutated TDP-43^{+/^{F210I}} mouse strain harbouring a missense mutation in the RNA recognition motif 2 (RRM2).

3.2 Investigating the expression of the peripherin splice variant per61 in TDP-43^{A315T} and SOD1^{G93A} transgenic mice

Three alternatively spliced variants are produced from peripherin mRNA called: per58, per56 and per61. Per61 was reported as an aberrant splice variant of peripherin and was found in lumbar spinal cords (LSC) of SOD1^{G37R} transgenic mice (Robertson et al. 2003). Here, I asked whether peripherin is abnormally spliced in two ALS mouse models: TDP-43^{A315T} and SOD1^{G93A}. To answer this question, reverse transcription-PCR (RT-PCR) analysis of total RNA, which was isolated from lumbar spinal cords (LSCs) of symptomatic SOD1^{G93A} and TDP-43^{A315T} transgenic mice was performed using previously published primers (Landon et al. 2000). These primers are peripherin isoform specific i.e. each set of primers can detect two different isoforms: one set can detect per58 and per61 while the other set detect per58 and per56. All three peripherin isoforms (per58, per56 and per61) were detected in TDP-43^{A315T} and SOD1^{G93A} transgenic mice (Figure 3.1A, per58 and per61 represented by the 268 bp and 364 bp bands, respectively, and 3.1B, per58 and per56 represented by 240 bp and 178 bp bands, respectively). Interestingly, the band representing per61 was also present in the samples isolated from the wild type mice (Figure 3.1A, a 364 bp band). The presence of per61 in all genotypes was further confirmed using a per61-specific primer set. This eliminated any possibility of artifacts arising from non specific PCR amplification of this splice variant. Indeed, the expected 201 bp band was detected, which is the result of intron 4 retention in per61, in all genotypes (Figure 3.1C). Since per61 arises from intron 4 retention, it was important to check for genomic DNA (gDNA) contamination to ensure that the resultant band would be amplified from per61 cDNA and not from gDNA. To ensure that the RNA extracts were not contaminated with gDNA, a primer set spanning intron 7 in the *Dync1h1* gene, which is known to be spliced out during RNA processing was utilized. No genomic DNA contamination was observed in any of the samples (Figure 3.2).

Figure 3.1

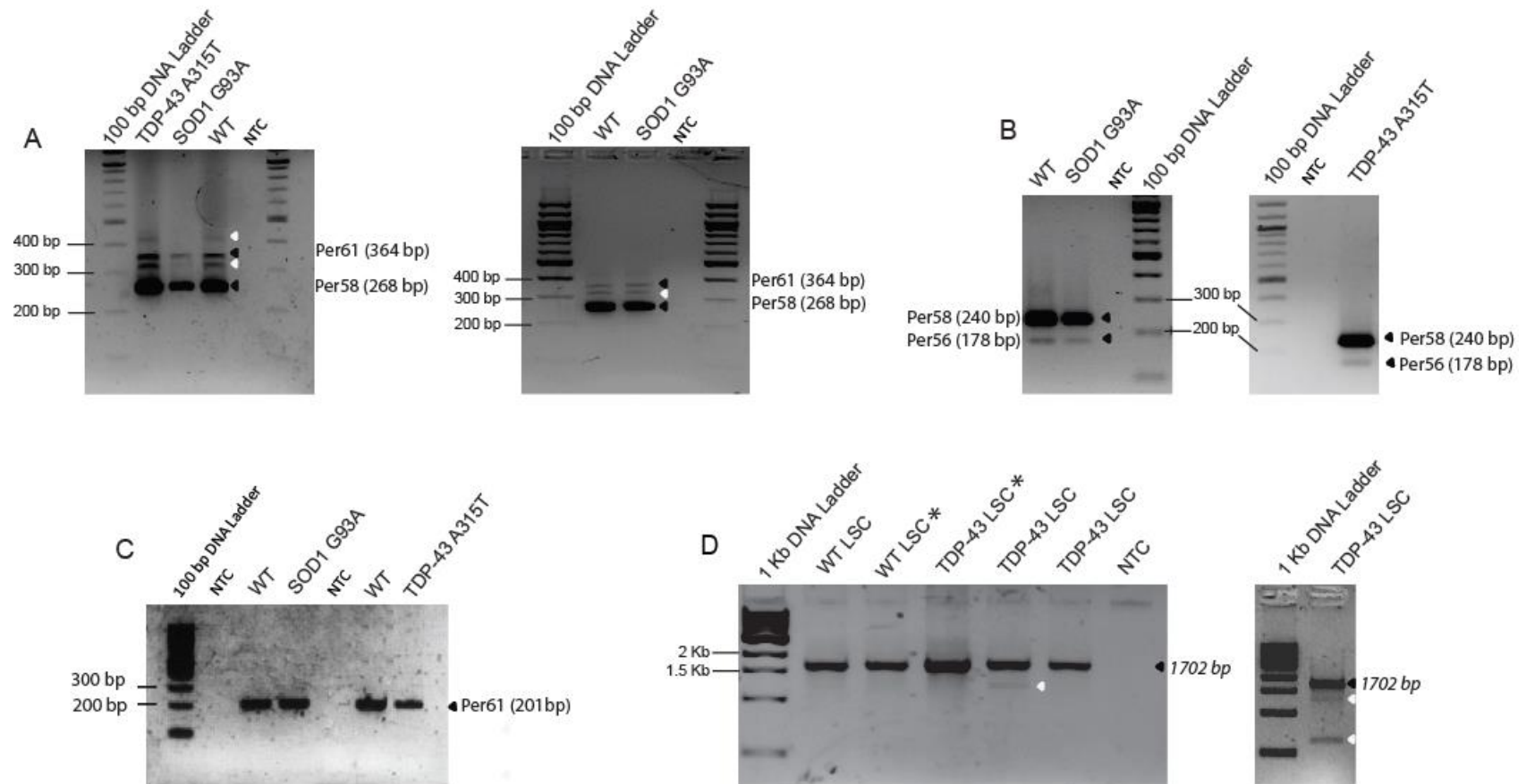


Figure 3.1 – Expression of per61 in SOD1^{G93A}, TDP-43^{A315T} and wild type mice at RNA level. Expression of all known peripherin isoforms including per61 in SOD1^{G93A}, TDP-43^{A315T} symptomatic transgenic and wild type mice using RT-PCR. (A) Detection of both the major form per58, represented by 240 bp, and the minor form per61, represented by 364 bp PCR products, in all genotypes using Landon et al (2000) isoform specific primers. Other unknown amplicons were also amplified (white arrowheads). (B) The 58/56 primer set amplified the major and minor forms, per58 and per56 represented by 240 bp and 178 bp PCR products, respectively. In order to obtain a good separation between peripherin splice variants due to their close sizes, PCR products were run in 2% agarose gel mixed with 1% NuSieve agarose gel in the ratio of a 2:1, respectively (Lonza, 50080). (C) The presence of per61 transcript in all genotypes represented by the 201 bp PCR product from intron 4 inclusion. (D) RT-PCR products of the entire coding sequence of peripherin (1702 bp, black arrowheads). White arrowheads represent unknown bands lacking reproducibility. Asterisks indicate that two pooled LSCs were used to produce the data. NTC represent non-template negative control.

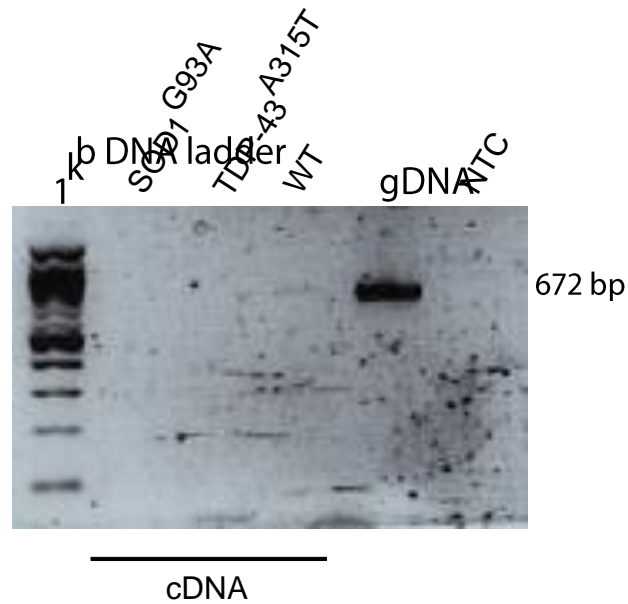
Figure 3.2

Figure 3.2 – DNA contamination test performed on cDNA samples. A DNA contamination test was performed on cDNA samples prepared from LSCs of SOD1^{G93A}, TDP-43^{A315T} symptomatic transgenic and wild type mice. Only one band was amplified from mouse genomic DNA using an intron primer spanning intron 7 in the *Dync1h1* gene. The other cDNA lanes: SOD1^{G93A}, TDP-43^{A315T} and wild type did not contain this band because intron 7 was spliced out and therefore it confirmed the absence of gDNA in these samples. NTC represents non-template negative control.

In addition, I tested for the presence of novel alternative splice variants by designing primers which would amplify the entire coding sequence of peripherin. My primer set was able to detect just the major peripherin isoform per58, but not 56 or 61. Moreover, an amplicon in two out of four TDP-43 mutants in the 1-1.5 kb region was observed (white arrowheads in Figure 3.1D). Another band was observed at a size just above 0.5kb (white arrowhead in Figure 3.1D). However, these two bands lacked reproducibility. Collectively, these results indicate that per61 is not an aberrant splice variant of peripherin and that the presence of this isoform in the wild type LSC suggests a physiological role that per61 may play in peripherin filament formation.

The presence of per61 was further examined at protein level. I performed sequential extraction of neurofilaments from LSC samples isolated from wild type and symptomatic SOD1^{G93A} and TDP-43^{A315T} transgenic mice. Low and high salt buffers were used, with the latter containing a nonionic detergent (Triton X-100) for separating neurofilaments, as described in the materials and methods chapter (section 2.3.2). Three supernatants and one pellet (the final pellet) were obtained from this preparation. Supernatants and the pellet were analysed in 10% and 12% polyacrylamide gels, respectively, using SDS-PAGE. The pellet (containing all filamentous neurofilaments) was examined for the presence of per61, using a specific antibody raised against an antigen corresponding to the retained intron 4 (Cogli et al. 2012). In agreement with the data from RT-PCR analysis of the peripherin splice variant (Figure 3.1), per61 was detected in all three genotypes SOD1^{G93A}, TDP-43^{A315T} and wild type (Figure 3.3).

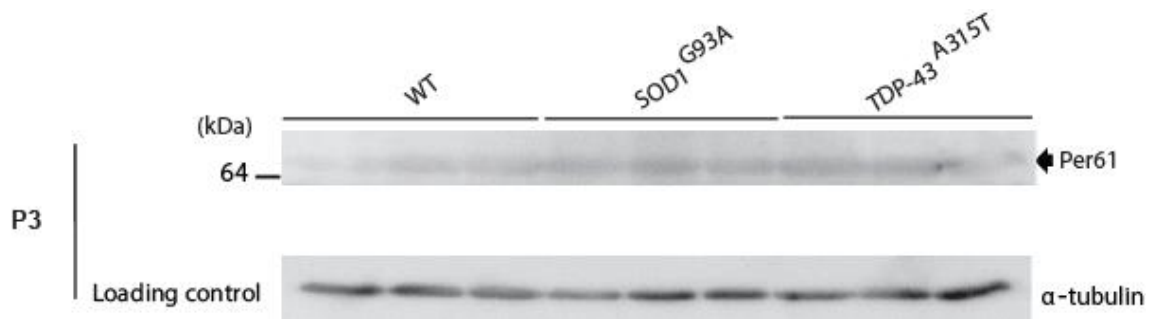
Figure 3.3

Figure 3.3 – Expression of per61 at protein level. Detection of per61 in the pelleted neurofilaments (P3) of LSCs of SOD1^{G93A} and TDP-43^{A315T} transgenic and wild type mice. Alpha-tubulin was used as the loading control.

3.3 Investigating the expression of peripherin isoforms: per58, per56 and per45 in TDP-43^{A315T} and SOD1^{G93A} symptomatic mice

Peripherin levels in all three supernatants (S1, S2 and S3) and the final pellet (P3) that were obtained from neurofilament preparation (described in the materials and methods chapter, section 2.3.2) were examined. Using a polyclonal anti-peripherin antibody, I observed per58, per45 and per61 in S1 obtained from wild type and symptomatic SOD1^{G93A} and TDP-43^{A315T} samples (Figure 3.4A). All peripherin isoforms in S1 are most likely non-filamentous forms and therefore unmodified forms since only DPBS was used in homogenization. Approximately a three fold increase in per45 levels in TDP-43^{A315T} compared to the wild type was observed in the S1 fraction (Figure 3.4A and C, p -values = 0.08; n = 6; representing the number of mice used to produce the data from two independent experiments). In the TX-100 soluble fraction S2, two proteins were separated from the filaments: per58 and an unknown polypeptide, 50 kDa in size, represented by a grey arrow in Figure 3.4B. This polypeptide might represent unidentified peripherin species which was also observed in other studies (referred to as 50 kDa polypeptide from this point onward) (McLean et al. 2008; McLean et al. 2010). No change in per58 was observed between the three genotypes.

In fraction S3, after adding sucrose to remove myelin from the extracts as well as applying a mechanical force, more peripherin isoforms were separated from filamentous peripherin and their levels increased compared to S2. Although they required a better separation (by running the samples on a higher percentage gel e.g. 12% as well as increasing the running time), the major isoform per58 and the minor isoform per56 were both identified in this fraction as well as the 50 kDa polypeptide (Figure 3.5A). Densitometry analysis of these polypeptides in western blots revealed that there was a change in peripherin solubility in SOD1^{G93A} and TDP-43^{A315T} mice in comparison with the wild type (Figure 3.5B). In SOD1^{G93A}, per56 and the 50 kDa polypeptide exhibited a significantly lower solubility (Figure 3.5B left panel, P = 0.009 and 0.03, respectively) compared to the wild type in this fraction. Per58 also showed a lower solubility, but this difference was not statistically significant (Figure 3.5B, p = 0.1). No difference was observed in per58 solubility between TDP-43^{A315T} and wild type in this fraction. However, per56 and the 50 kDa polypeptides showed a significant

increase in solubility by approximately two and ten fold, respectively (Figure 3.5B, right panel, $p = 0.02$ and $= 0.003$, respectively). Peripherin levels in the TX-100-insoluble fraction were also analysed to determine any changes in the ratios of polymerized forms of peripherin in the three genotypes. Samples were run on a 12% SDS-PAGE; however, the running time was not sufficient to obtain a better separation between the two isoforms per58 and per56. Nonetheless, there was no change in the ratios between peripherin isoforms in all genotypes: SOD1^{G93A}, TDP-43^{A315T} transgenic and wild type mice (Figure 3.6).

In summary, these data suggest that overexpressing TDP-43^{A315T} reduces the stability of the peripherin filament network. Conversely, the stability of the peripherin filament network is enhanced in the SOD1^{G93A} transgenic mice. In addition, as per45 isoform is an alternatively translated product initiated from the third ATG of per58 transcript, these data suggest a potential role for TDP-43 in the alternative translation initiation of per45.

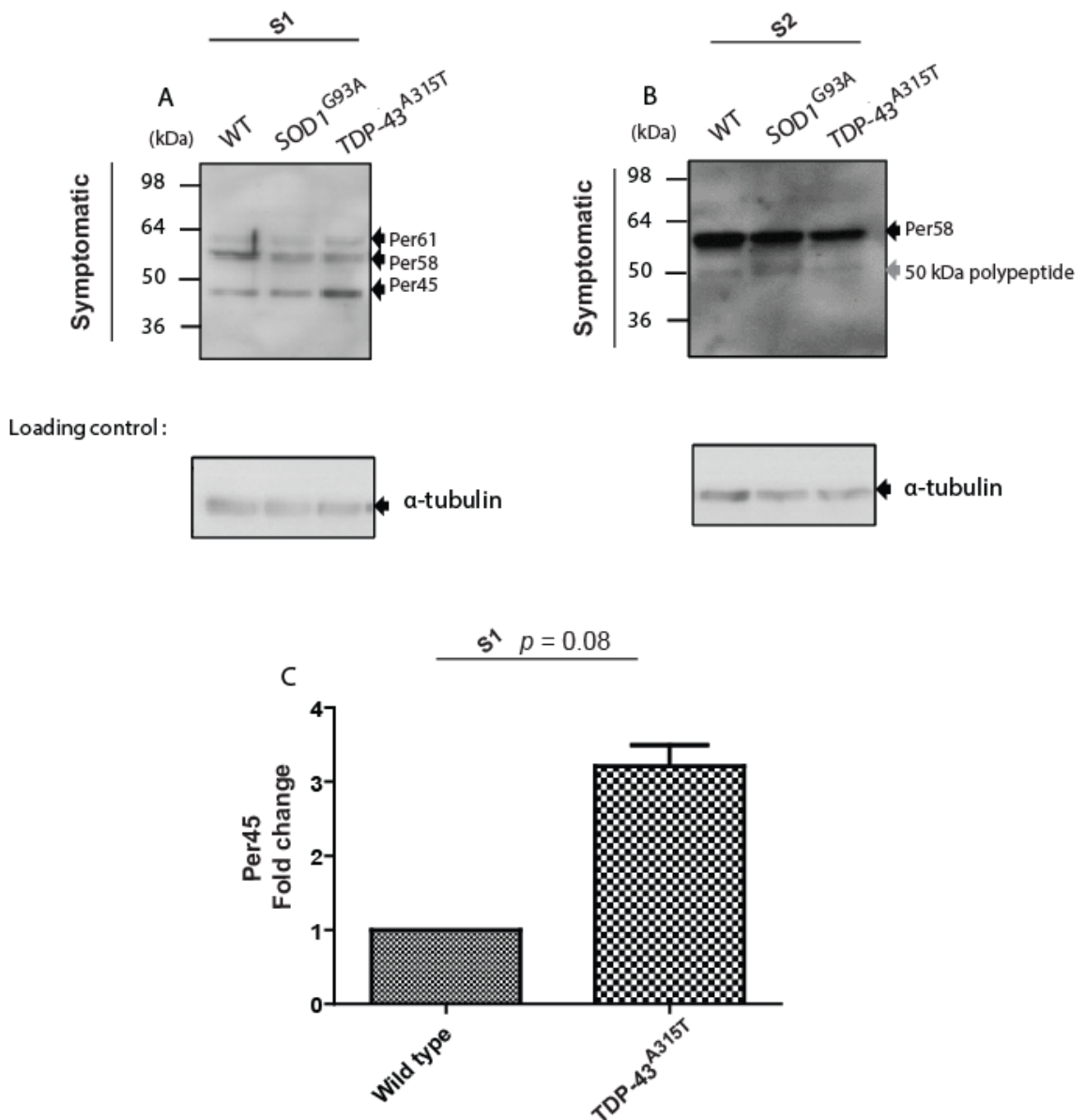
Figure 3.4

Figure 3.4 – Up-regulation of per45 in symptomatic TDP-43^{A315T} transgenic mice. (A) Western blot analysis of S1 (TX-100-untreated) showing an increase in the intensity of per45 in TDP-43^{A315T}. (B) Western blot of S2 (TX-100-treated) showing no change in proteins separated from the neurofilaments: per58 and a 50 kDa polypeptide. SDS-PAGE percentage in A and B is 10%. (C) Quantification of per45 in A. The quantification revealed a tendency towards up-regulation of per45 (unpaired *t*-test; *p*-values = 0.08; *n* = 6, where *n* represents the number of mice used to produce the data). Data represent the mean of two independent experiments +SEM, pooled lumbar spinal cords from three mice for each genotype in one experiment. Alpha tubulin is used as a loading control and the intensity of per45 is normalized against it.

Figure 3.5

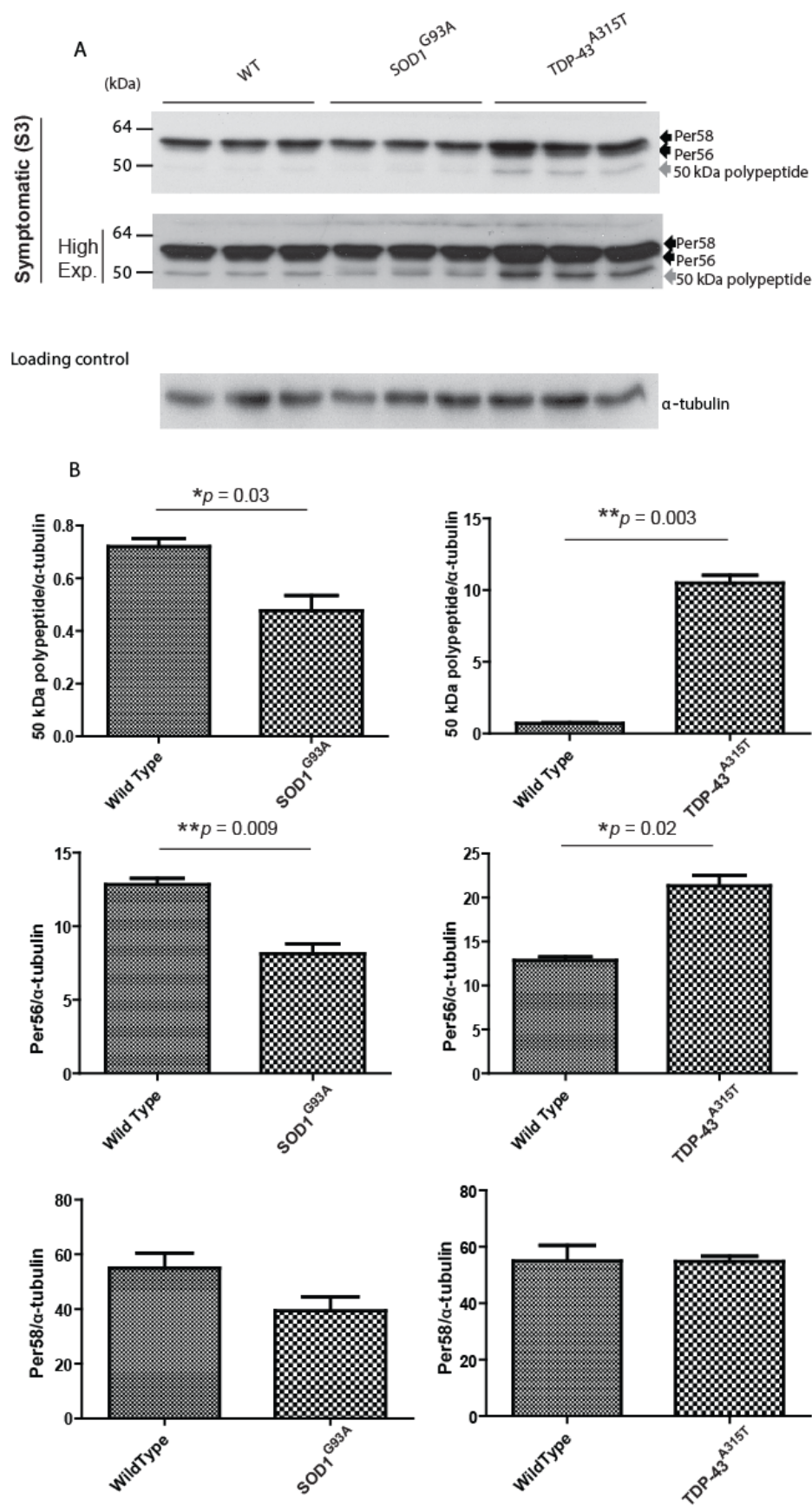


Figure 3.5 – Change in stability of per56 and the 50 kDa polypeptide in S3 obtained from the SOD1^{G93A} and TDP-43^{A315T} transgenic mice. (A) Western blot analysis revealed an increase in the intensity of per56 and the 50 kDa polypeptides in TDP-43^{A315T} and that the intensities of both were reduced in SOD1^{G93A}. SDS-PAGE percentage is 10%. (B) Quantifications of per58, per56 and the 50 kDa polypeptides in A. Unpaired *t*-test; $p = 0.03$ and 0.009 for the 50 kDa polypeptides and per56 obtained from the SOD1 transgenic mice respectively, $p = 0.003$ and 0.02 for the 50 kDa polypeptides and per56 obtained from the TDP-43^{A315T} transgenic mice respectively. The data represent the mean of three replicates of the same biological sample from one experiment (pooled lumbar spinal cords from three mice for each genotype) +SEM. Alpha tubulin is used as a loading control.

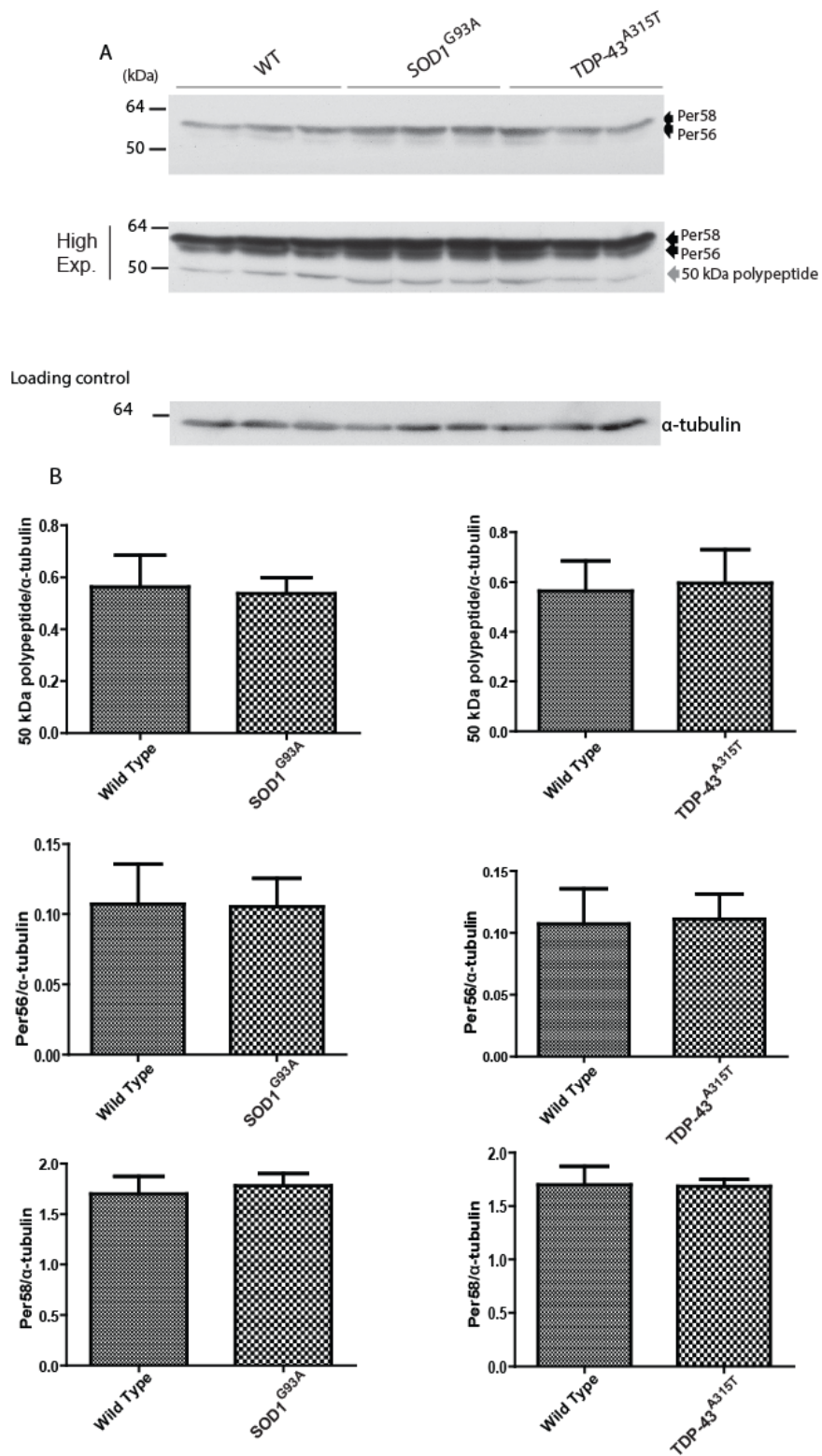
Figure 3.6

Figure 3.6 – No change in the stoichiometric ratio between peripherin isoforms in P3. (A) Western blot analysis performed on the TX-100 insoluble fraction P3. SDS-PAGE percentage is 12%. (B) Quantifications of per58, per56 and the 50 kDa polypeptides in A. Unpaired *t*-test, the data are produced from the mean

of three replicates of the same biological sample from one experiment (pooled lumbar spinal cords from three mice for each genotype) +SEM. Alpha tubulin is used as a loading control.

3.4 Increased expression of per45 and reduced stability of the 50 kDa polypeptide in non-symptomatic TDP-43^{A315T}

Per45 levels were also examined in TDP-43^{A315T} at 60 days of age, a non-symptomatic stage. Neurofilaments were extracted from LSCs of TDP-43^{A315T} transgenic and wild type mice as previously described in Materials and Methods chapter (section 2.3.2). All supernatants: S1, S2 and S3 and the final pellet P3 were analysed in 10% polyacrylamide gels using SDS-PAGE. All known peripherin isoforms were resolved: per58, per56, per61 and per45. However, per56 was barely observed in S3 at low exposure (Figure 3.7A). Due to the short run time of the SDS-PAGE, the two isoforms per58 and per56 were not completely separated (Figure 3.7A). A tendency towards increased levels of per45 was observed in S1 isolated from TDP-43^{A315T} supporting a possible role for TDP-43 in the alternative translation initiation site in per58 transcript (Figure 3.7A and B). Furthermore, a tendency towards increased solubility of the 50 kDa polypeptide was observed in S3 of TDP-43^{A315T}, suggesting that this polypeptide dissociates more easily from the neurofilaments in LSCs isolated from TDP-43^{A315T} mice.

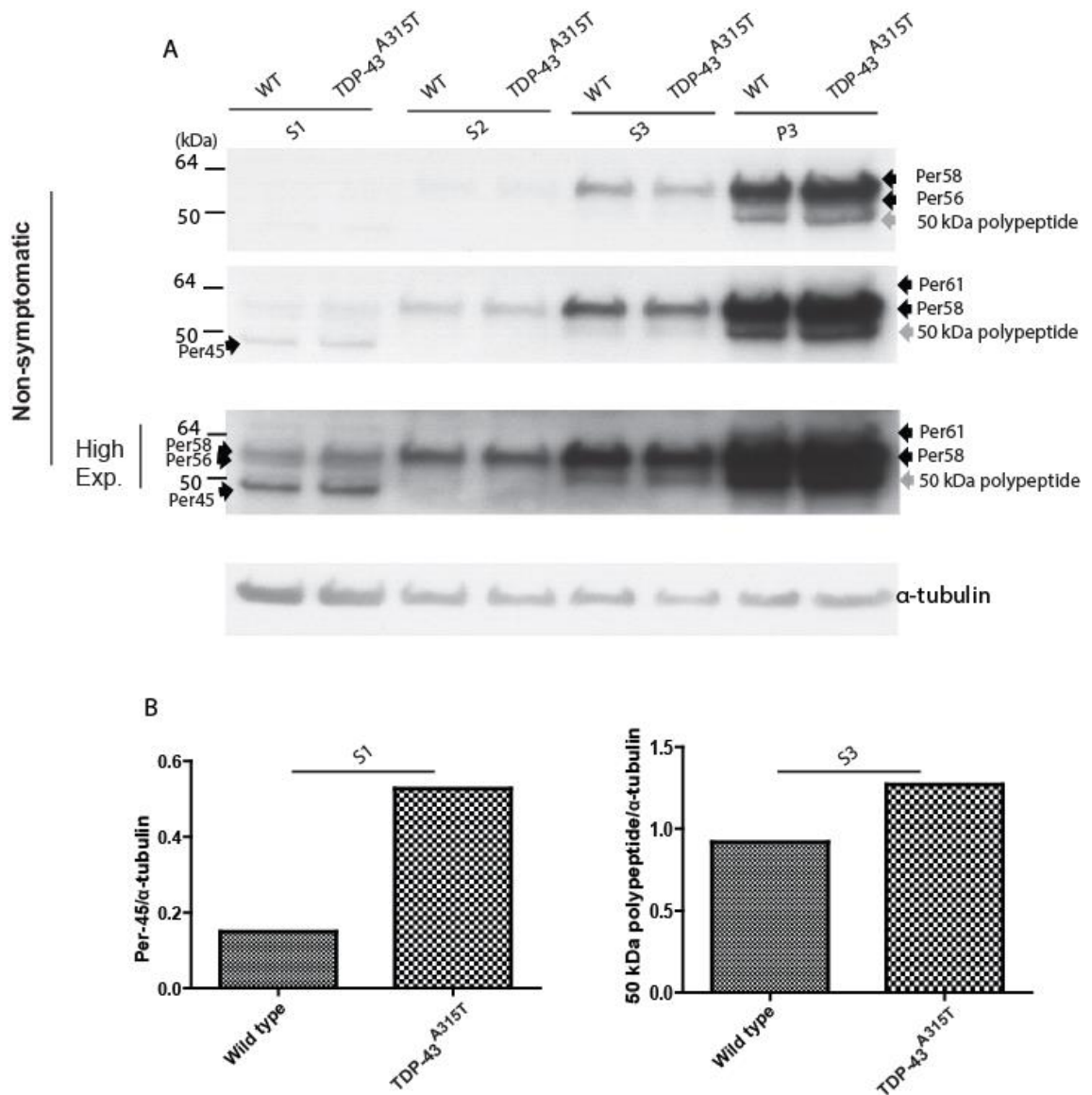
Figure 3.7

Figure 3.7 – Per45 expression level in non-symptomatic TDP-43^{A315T} mice. (A) Western blot analysis performed on S1, S2, S3 and P3. Per45 (in S1) showed a trend towards up-regulation. The level of the 50 kDa polypeptide was increased in S3. SDS-PAGE percentage is 10%. (B) Quantifications of per45 (left panel) and the 50 kDa polypeptides (right panel). The data are produced from one experiment (pooled lumbar spinal cords from three mice for each genotype). Alpha tubulin is used as a loading control.

3.5 Significant down-regulation of the neuron-specific isoform of GLT-1 (GLT-1B) in both symptomatic and non-symptomatic TDP-43^{A315T} transgenic mice

I investigated whether A315T mutation in TDP-43 affects the RNA processing of GLT-1, the rodent homologue of EAAT2. I first examined the presence of novel splice variants in samples isolated from brain tissue of TDP-43^{A315T} and SOD1^{G93A} transgenic mice. This was achieved by performing reverse RT-PCR using primers which amplify the entire coding sequence of GLT-1 as well as the neuron-specific splice variant GLT-1B. Novel splice variants were not observed in either GLT-1 or GLT-1B (Figure 3.8A and 3.9A, respectively). Moreover, western blot analysis of GLT-1 on brain lysates from symptomatic transgenic TDP-43^{A315T} and wild type mice showed no significant change in the level of GLT-1 between TDP-43^{A315T} transgenic and wild type mice, neither in the dimer nor the monomer forms (Figure 3.8B and C; $p = 0.7858$ and 0.8033 for the dimer and the monomer GLT-1 respectively). The analysis of the levels of GLT-1B in brain tissues, however, revealed a significant reduction in GLT-1B expression in both non-symptomatic (Figure 3.9B; $p = 0.004$) and symptomatic transgenic TDP-43^{A315T} mice when compared to that in wild type mice (Figure 6C; $p = 0.03$). Thus, these results indicate that overexpression of A315T mutant form of TDP-43 selectively results in reduced expression of GLT-1B in neurons.

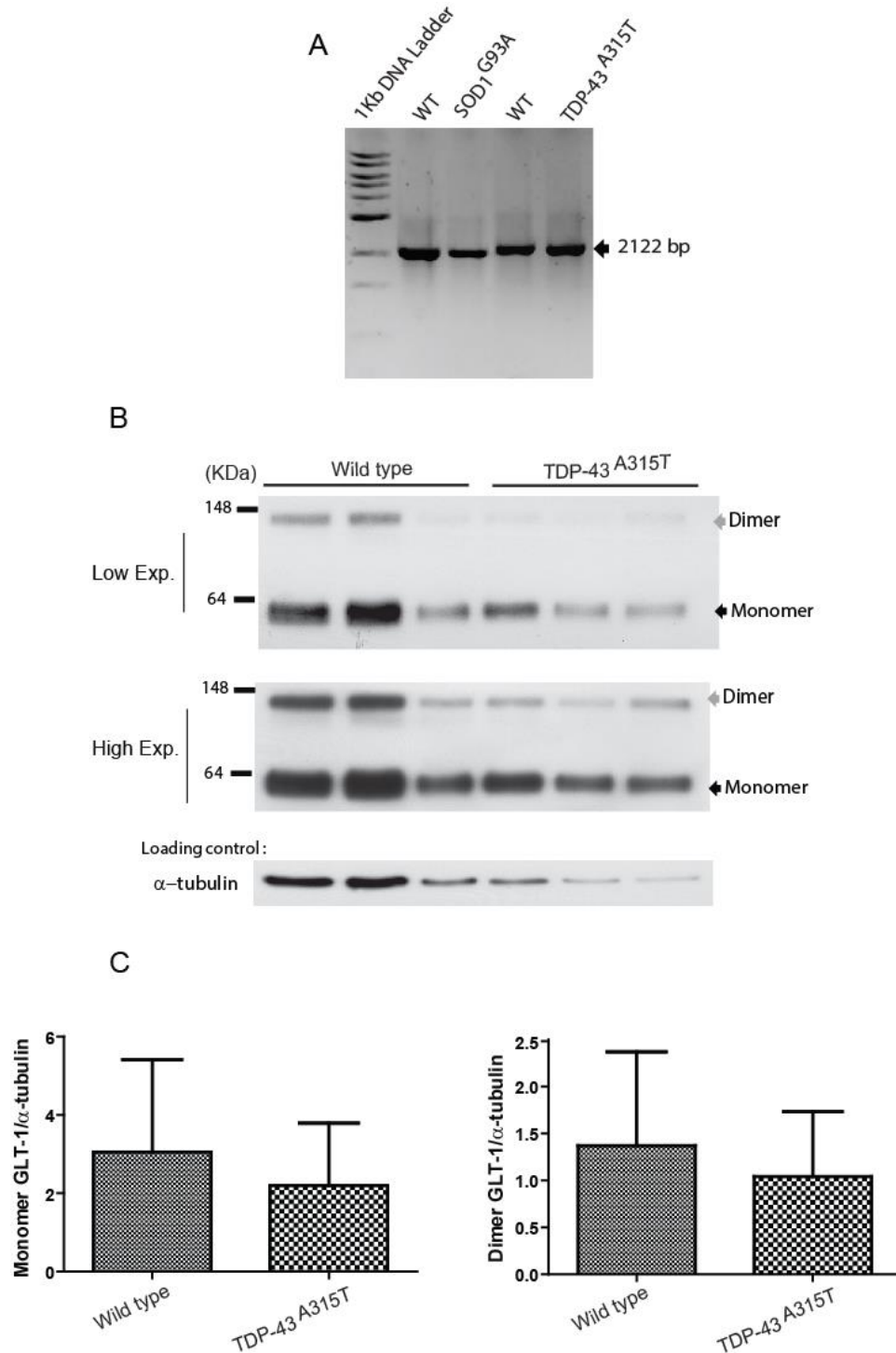
Figure 3.8

Figure 3.8 – GLT-1 expression level in TDP-43^{A315T} transgenic mice. (A) RT-PCR showing no novel splice variants in GLT-1 from TDP-43^{A315T}, SOD1^{G93A} and wild type mice. SDS-PAGE percentage is 10%. (B) Western blot analysis showing a trend towards down-regulation of GLT-1 protein levels in TDP-43^{A315T} mice. (C) Quantification of GLT-1 in B. Unpaired *t*-test; *p* = 0.7858 and 0.8033 for the dimer and the monomer GLT-1 respectively. Data represent the mean from two independent experiments with six independent mice for each genotype TDP-43^{A315T} and wild type (+SEM). Alpha tubulin is used as a loading control, as well as for the normalization of the signal intensity from GLT-1 protein.

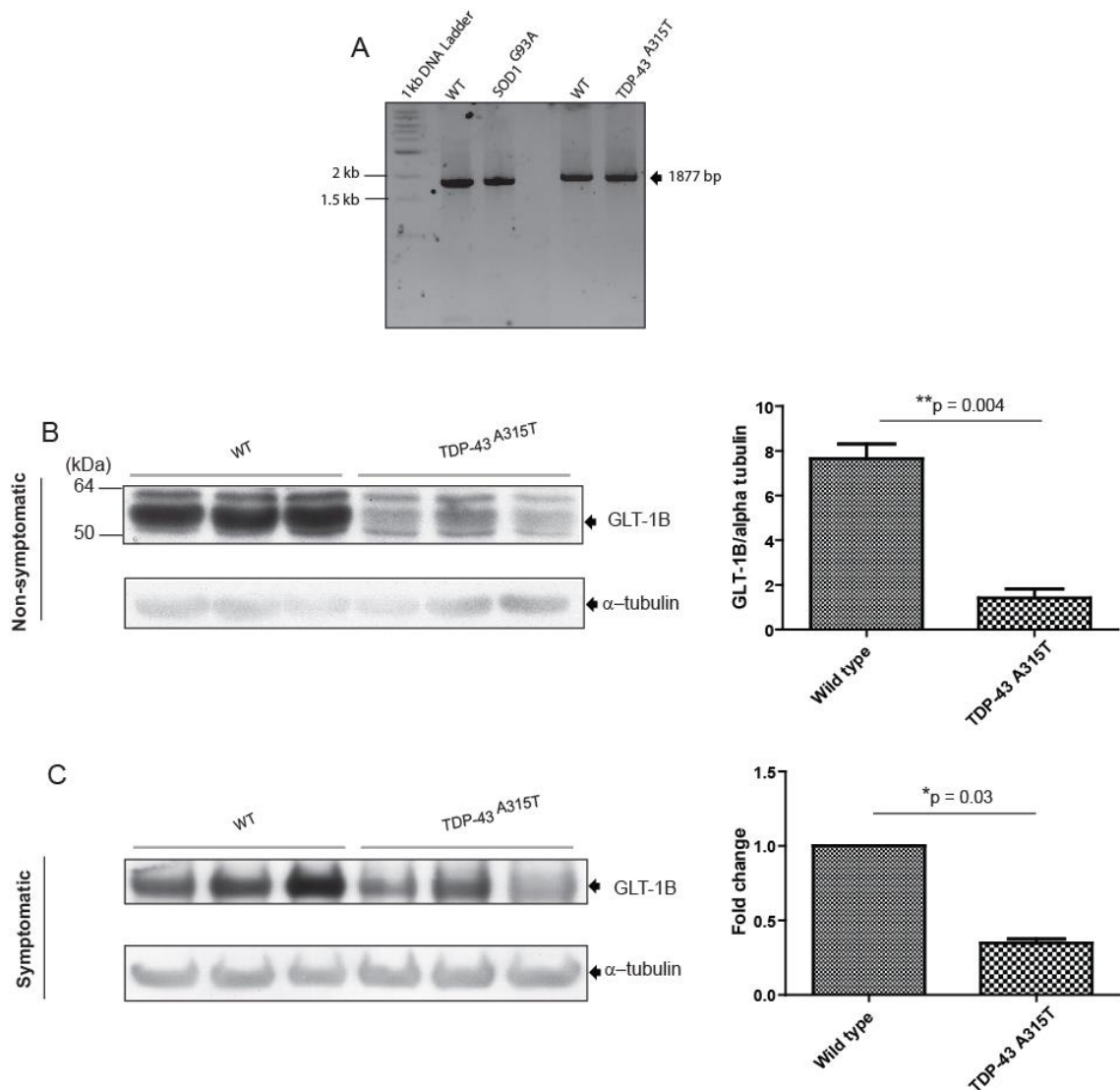
Figure 3.9

Figure 3.9 – GLT-1B expression level in TDP-43^{A315T} transgenic mice. (A) RT-PCR, performed on RNA samples extracted from brain tissues of symptomatic transgenic TDP-43^{A315T}, SOD1^{G93A} and wild type mice, showing no novel splice variants in GLT-1B. (B) Immunoblotting of brain lysate obtained from non-symptomatic TDP-43^{A315T} and wild type mice revealing a significant down-regulation of GLT-1B in non-symptomatic TDP-43^{A315T} mice (left panel). Quantification of GLT-1B protein (right panel). (C) Immunoblotting analysis of brain lysate obtained from symptomatic TDP-43^{A315T} and wild type mice showing a significant down-regulation of GLT-1B in symptomatic TDP-43^{A315T} mice (left panel). Quantification of GLT-1B protein (right panel). SDS-PAGE percentage in B and C is 10%. Unpaired *t*-test; *p* = 0.004 and 0.03 for non-symptomatic and symptomatic mice. Data are shown as the mean of three independent mice for each genotype from one experiment (+SEM). Alpha tubulin is used as a loading control and GLT-1B band intensity is normalized against the α-tubulin signal.

3.6 Analysis of the neuron-expressed GLT-1B in the TDP-43^{+F210I} mouse strain

In a series of tail suspension tests, I noticed that the heterozygotes TDP-43^{+F210I} exhibited abnormal hindlimb clenching at 11 months of age. Thus, given the importance of RRM1 and RRM2 of TDP-43 in binding to its mRNAs targets for regulation of RNA splicing (E Buratti and Baralle 2001), I investigated the level of GLT-1B protein in TDP-43^{+F210I} mice, harbouring the F210I mutation in the RRM2 motif. Western blot analysis on brain lysates showed increased intensity in GLT-1B signal in TDP-43^{+F210I} when compared to that in the wild type mice, suggestive of a potential up-regulation of this isoform in the mutant mice (Figure 3.10). Other unknown bands were also detected which were also up-regulated (Figure 3.10, grey arrows).

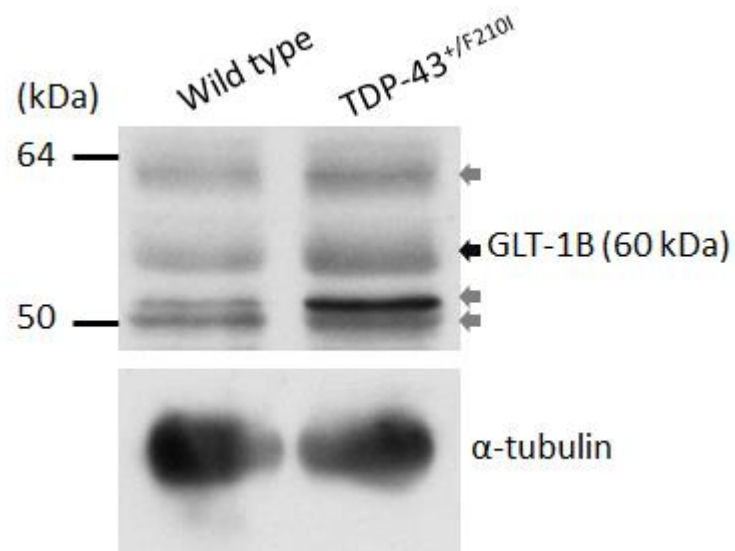
Figure 3.10

Figure 3.10 – Increased levels of GLT-1B in TDP-43^{+/F210I} mouse model. Immunoblotting of brain lysate showing increased levels of GLT-1B protein in the TDP-43^{+/F210I} mutant compared to that in the wild type mice (black arrow). Other unknown bands were also up-regulated (grey arrows). Data are produced from one mouse for each genotype. The intensity of bands from GLT-1B is normalised against those from α -tubulin.

3.7 Chapter 3 summary

Data from this chapter has shown that per61 is present in the wild type mice suggesting a role for this isoform in the assembly of peripherin filament network. Also, my data show that overexpression of TDP-43^{A315T} induces up-regulation of the alternative translated isoform per45, suggesting a possible role for TDP-43 in alternative translation. In addition, overexpression of TDP-43^{A315T} leads to the instability of the filament network as was observed by the increased solubility of per56 and the 50 kDa polypeptide. The converse was observed in the SOD1^{G93A} mutant. Moreover, the reduction of GLT-1B expression in the brain tissue isolated from TDP-43^{A315T} mice suggests impaired RNA processing of GLT-1B, which might exacerbate the disease progression. Collectively, these data show that the expression of peripherin and EAAT2 is regulated by TDP-43 and that aberrant expressions of these two genes caused by TDP-43 mutations could have a role in the pathology of ALS.

Chapter 4

Investigating the impact of the *Loa* mutation on MAP kinase signalling and autophagy during endocytic trafficking and nutrient deprivation

4.1 Introduction

Mutations in *DYNC1H1* result in cytoplasmic dynein dysfunction and defective axonal transport in motor neurons (Hafezparast et al 2003). In a recent study in Hafezparast Laboratory, PhD student Caroline Garrett showed that the *Loa* mutation in *DYNC1H1* impairs BDNF-induced trafficking of endosomes along motor neuron axons (Garrett et al. 2014). Subsequently, she investigated whether this impaired trafficking negatively impacted on the MAP kinases ERK1/2 signalling cascade. To this end, motor neurons were serum starved for two hours followed by stimulation with BDNF. Surprisingly, there was a massive induction of c-Fos activation (a downstream target of MAPKs) upon starvation, which continued during stimulation with BDNF in both wild type and *+Loa* motor neurons (Figure 4.1A). Interestingly, the c-Fos induction was found to be higher in *+Loa* than in the wild type motor neurons during starvation, as well as after the addition of BDNF. This led to two questions: first, ‘which MAP kinases are responsible for the induction of c-Fos upon serum starvation?’ and second, ‘why is this induction more pronounced in *+Loa* than in wild type motor neurons?’. Analysis of ERK1/2 MAP kinases, however, showed that, compared to BDNF stimulation, serum deprivation only slightly increased the active phospho-ERK1/2 levels in the motor neurons. This increase in phospho-ERK1/2 was observed in both genotypes, but more so in the *+Loa* motor neurons (Figure 4.1B) (Garrett et al 2014). My contribution to this study started at this point, and it aimed to:

- 1) Identify the kinases responsible for c-Fos activation in motor neurons upon serum starvation and/or BDNF stimulation.
- 2) Determine whether autophagy has a role in the higher levels of c-Fos induction in *+Loa* motor neurons compared to those in wild type neurons.

Addressing these aims will be the topic of my research in this chapter.

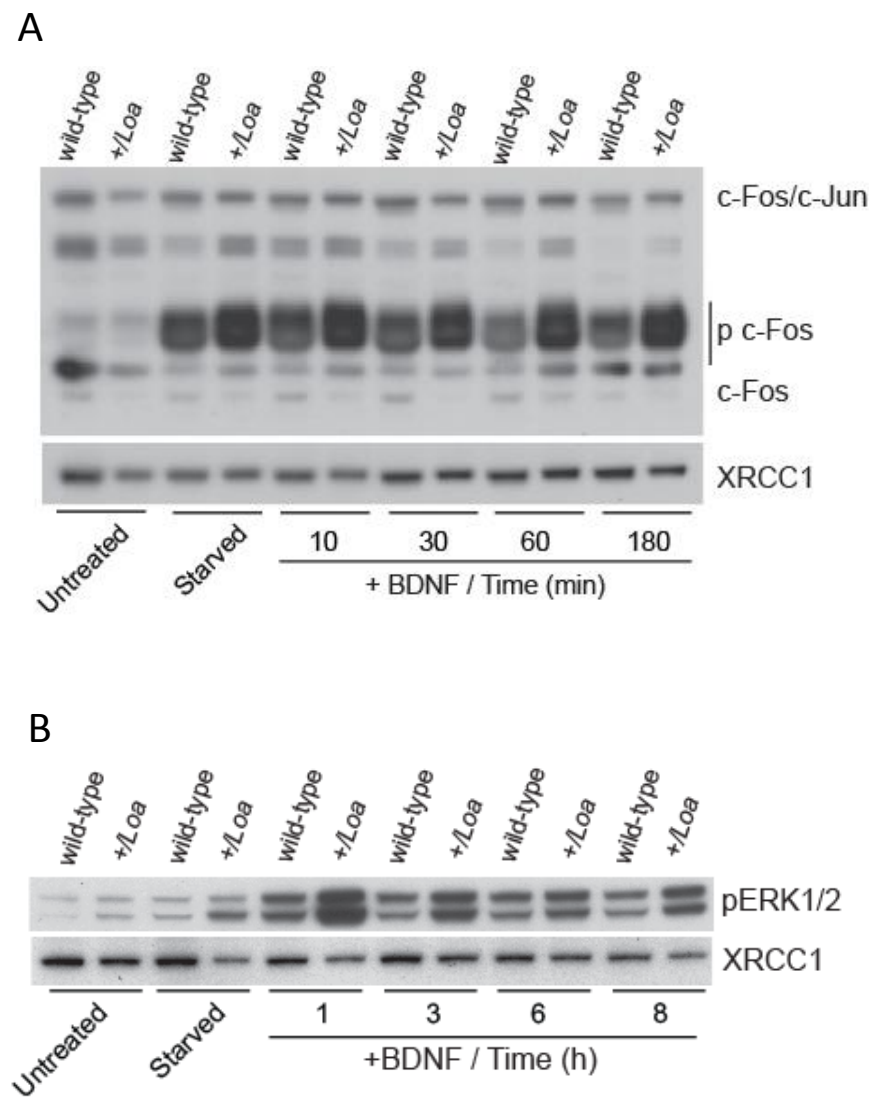
Figure 4.1

Figure 4.1 – Levels of pc-Fos (A) and pERK1/2 (B) in motor neurons, following serum starvation and BDNF-stimulation (Garrett et al. 2014).

4.2 Increased JNK activity in cultured motor neurons after BDNF stimulation without a significant difference between wild type and *Loa* heterozygotes

Three MAP kinases are known to activate c-Fos during biological stress or binding mitogens to cell receptors: ERK1/2, JNK and p38. We first asked whether JNK is the MAP kinase underlying c-Fos phosphorylation during starvation in motor neurons. Wild type and *+Loa* motor neurons at 7 days in vitro were serum-starved for two hours followed by stimulation with 5 ng/ml of BDNF. Motor neurons were then lysed at 1, 3, 6, and 8-hour incubation time point and subjected to a western blot for analysis of JNK activity. Using an anti-phospho-specific antibody that recognises two phosphorylated sites of JNK (Thr183 and Tyr185), two bands were detected, representing p54 and p46 isoforms of JNK. p54 was used to quantify active JNK (Figure 4.2A, top panel). There was no significant difference in the amount of p54 between the two genotypes in the control versus starved neurons (Figure 4.2B, comparison of non-starved and starved). However, when starved motor neurons were treated with BDNF, active JNK levels were increased up to 6 hours and started to decline at 8 hours post BDNF, possibly as a consequence of BDNF depletion (Figure 4.2B, post BDNF). Also, there was no difference in JNK activation between wild type and *+Loa* after BDNF application (Figure 4.2B, compare blue and red lines respectively at time points 1, 3, 6, and 8 hours). Thus, these data suggest JNK involvement in c-Fos induction in the presence of survival factors.

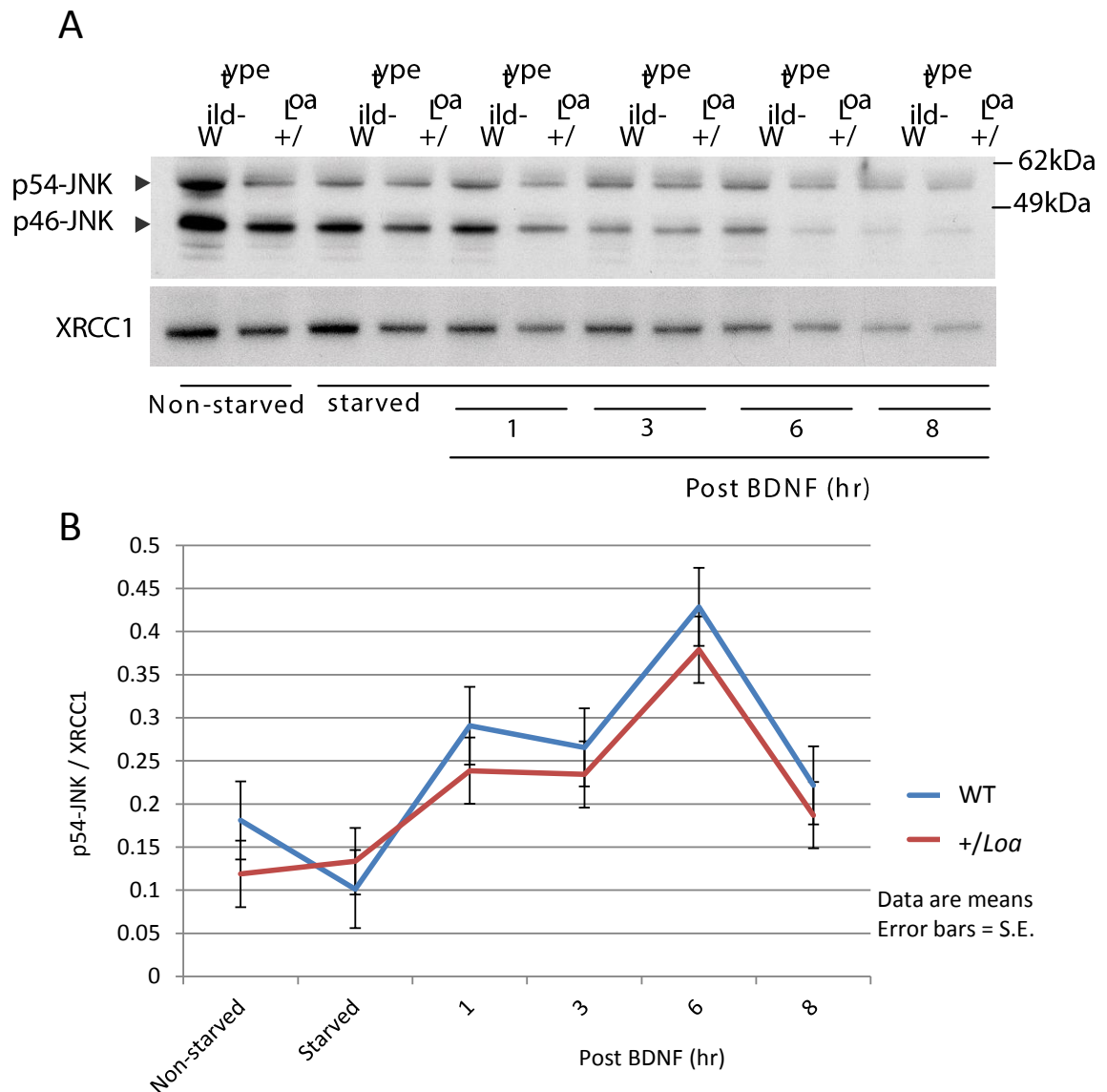
Figure 4.2

Figure 4.2 – Increased active JNK levels in BDNF-stimulated motor neurons. (A) Western blot was performed for analysing JNK activity in non-starved and starved motor neurons, as well as in starved and BDNF stimulated motor neurons at the indicated time points (top panel). The intensity of bands from JNK were normalised against those from XRCC1. (B) p54-JNK was used for measuring the levels of active JNK. Data (at each time point) are representative of three independent cultures, six replicates from each culture corresponding to the following time points: non-starved, starved, 1, 3, 6 and 8 hours.

4.3 Aberrant p38 activation in +/-*Loa* starved motor neurons

Next, I examined activation of p38 to determine whether it contributes to the serum starvation-mediated c-Fos induction. Wild type and +/-*Loa* motor neurons at 7 days in vitro were serum-starved for two hours, followed by stimulation with 5 ng/ml of BDNF and western blot analysis at 1, 3, 6, and 8 hour time points. Using an anti-phospho-p38 antibody, a 62 kDa band was detected, representing a dimeric phosphorylated form of p38 (Figure 4.3A, top panel) (Diskin et al. 2007; Rothweiler et al. 2011). I also used an antibody that detects total p38 (Figure 4.3A, middle panel). P38 expression was normalized against XRCC1 as a nuclear marker, since p38 translocates into the nucleus to phosphorylate transcription factors.

In untreated motor neurons, we found that both the monomer and the dimer forms of p38 were up-regulated in +/-*Loa* compared to the wild type. During starvation, an increase in both the monomer and the dimer levels was observed which declined when starved motor neurons were treated with BDNF (Figure 4.3B and C). This reduction lasted for approximately 6 hours in the presence of BDNF and then started to increase again at the 8-hour time point, possibly due to BDNF depletion. These data indicate that starvation activates p38 and that activation is abnormal in +/-*Loa* motor neurons.

Figure 4.3

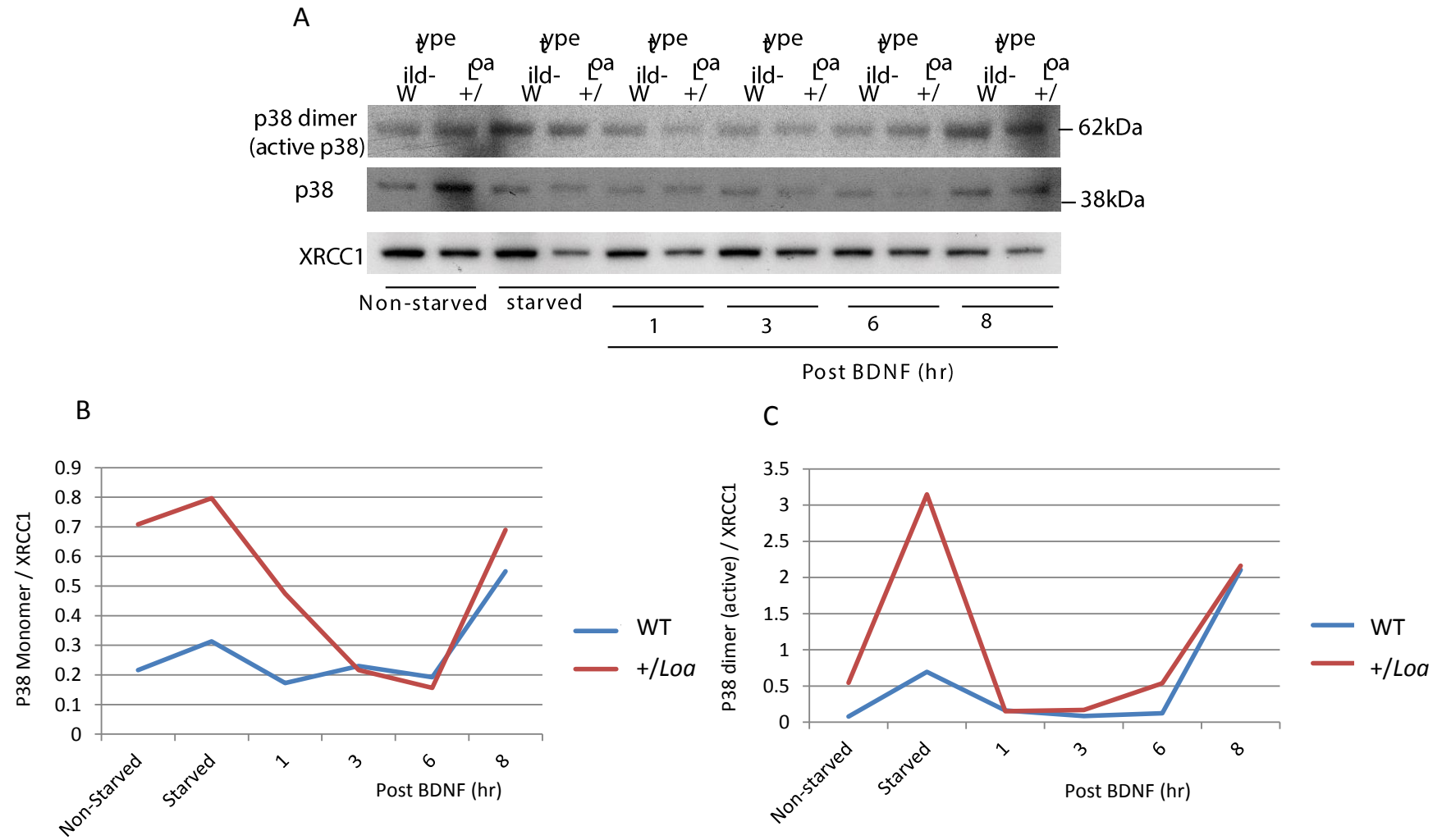


Figure 4.3 – Increased levels of active p38 in +/-*Loa* during serum-starvation. (A) Immunoblotting showed increased levels of active p38 in starved motor neurons which were reduced after stimulation with BDNF. P38 band intensity was normalized against XRCC1. (B and C) Quantification of p38 monomer and dimer. Data represent one experiment.

4.4 C-Fos induction is ERK1/2-dependent

To determine the exact contribution of the MAP kinases JNK and ERK1/2 in c-Fos induction during starvation and after BDNF application, wild type motor neurons (at 7 days in vitro) were treated with U0126 (a selective inhibitor of MEK1/2 which is upstream of ERK1/2) or with SP600125 (a selective inhibitor of JNK) (Figure 4.4). In comparison to motor neurons with no inhibitors, the inhibition of ERK1/2 attenuated c-Fos induction during starvation and after treatment with BDNF, while JNK inhibition increased c-Fos induction. These results indicate that c-Fos induction during starvation and after treatment with BDNF is at least partly ERK1/2-dependent and that JNK activation has an inhibitory role in inducing c-Fos under these conditions.

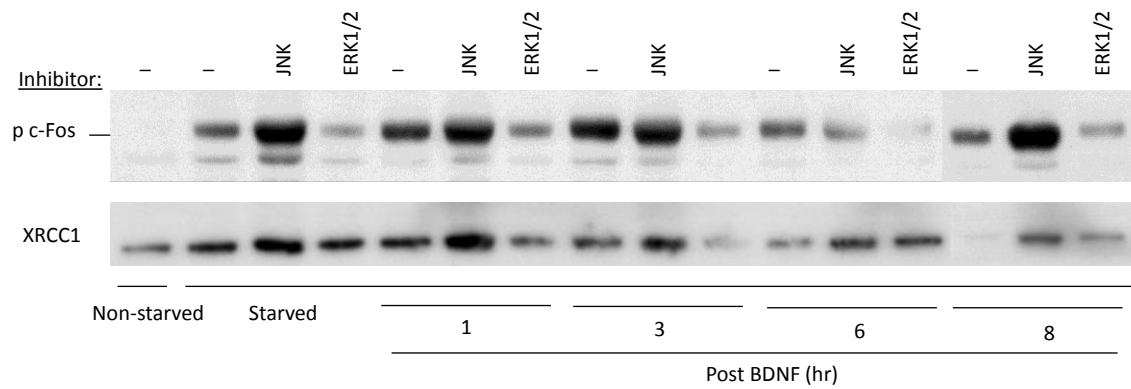
Figure 4.4

Figure 4.4 – c-Fos activation is ERK1/2 dependent. Western blot showing levels of c-Fos induction in starved wild type motor neurons and in those stimulated with BDNF after starvation: without inhibition (represented by a minus sign), treated with JNK inhibitor SP600125 or with ERK1/2 inhibitor U0126 at the indicated time points. pERK1/2 inhibition attenuated c-Fos induction, but inhibition of JNK enhanced phospho-c-Fos levels. XRCC1 was used as a loading control and c-Fos staining intensity was normalized against XRCC1 signal.

4.5 Altered levels of LC3-II in *Loa* heterozygous motor neurons during starvation and stimulation with BDNF

Nutrient deprivation induces autophagy. The significant increase in phospho-c-Fos in *+/Loa* motor neurons following serum starvation led to the question whether this activates autophagy in motor neurons. Moreover, I asked whether the higher levels of p-c-Fos in *+/Loa* motor neurons has an impact on this process and whether this process is impaired in *+/Loa* neurons as a consequence of higher levels of p-c-Fos.

Autophagy was examined by measuring the levels of the autophagy marker LC3-II (microtubule-associated protein 1 light chain 3-II). Using anti LC3 antibody, two bands were detected: LC3-I and LC3-II (16 and 18 kDa, respectively). Although the molecular weight of LC3-II is higher than LC3-I, LC3-II migrates faster due to phospholipid modifications (by conjugating to phosphatidylethanolamine), which increases its hydrophobicity.

Wild type and *+/Loa* motor neurons at 7 days in vitro were serum-starved for two hours followed by stimulation with 5 ng/ml of BDNF. Motor neurons were then lysed at 10, 30, 60, and 180-minute incubation time points and subjected to a western blot for analysis of LC3-II levels. In untreated motor neurons, a slight reduction in LC3-II levels was observed in *+/Loa* compared to the wild type (Figure 4.5A and B, Non-starved). Starvation induced autophagy and hence, LC3-II levels were increased in the motor neurons (Figure 4.5A and B, compare non-starved with starved). However, LC3-II levels were lower in starved *+/Loa* compared to the wild type motor neurons (Figure 4.5A and B). A drop in LC3-II levels was observed in both genotypes when starved motor neurons were stimulated with BDNF for 10 minutes (Figure 4.5A and B, 10 min post BDNF). This was followed by a gradual increase in LC3-II levels in both genotypes at later time points: 30, 60, and 180 min. However, the levels of LC3-II in *+/Loa* was higher than those in wild type at 10, 30 and 60 min post BDNF, but not at 180 min. At this point LC3-II levels in the wild type were increased compared to those in *+/Loa*. These data indicate that starvation fails to induce autophagy in serum starved *+/Loa* motor neurons. Furthermore, the accumulation of LC3-II in *+/Loa* after stimulation

with BDNF might reflect a delayed response to BDNF as a result of impaired endocytic trafficking.

Figure 4.5

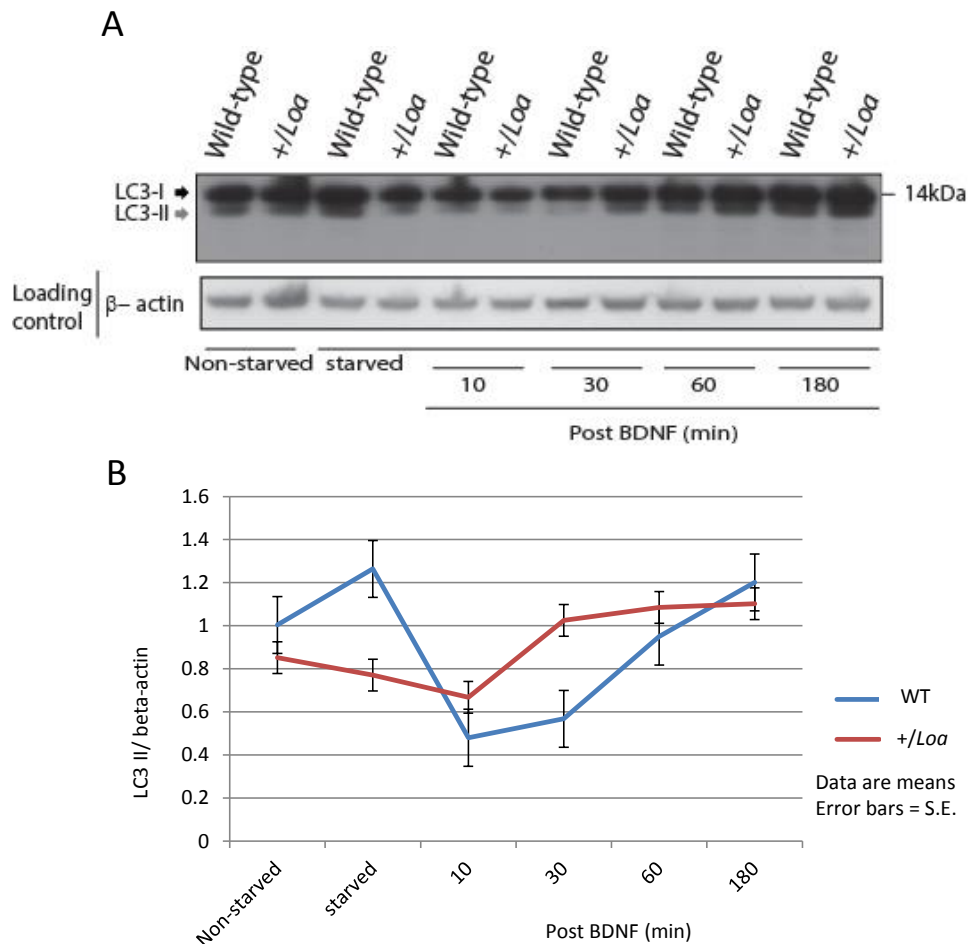


Figure 4.5 - LC3-II levels in non-starved, starved and BDNF-stimulated motor neurons. (A) Western blot showing reduced LC3-II levels in +/-Loa motor neurons during starvation, which increased gradually after stimulation with BDNF. (B) Quantification of LC3-II levels in A. Data (at each time point) are means of two independent cultures, six replicates from each culture corresponding to the following time points: non-starved, starved, 10, 30, 60 and 180 minutes. The intensity of bands from LC3-II were normalised against those from β-actin.

4.6 Reduced levels of LC3-II in *Loa* heterozygous motor neurons after bafilomycin A1 treatment

Autophagy is a dynamic process in which eventually all materials, including LC3-II, in the autophagolysosome will be degraded. LC3-II levels increased upon autophagy activation (autophagy induction) whereas levels reduced when degraded upon fusion of autophagosomes with the lysosomes (autophagy flux). To further define this measurement and rule out the latter, I used bafilomycin A1 to block autophagosome-lysosome fusion and therefore to prevent degradation of autophagosomes. Wild type and *+/-Loa* motor neurons at 7 days in vitro were serum-starved for two hours followed by stimulation with 5 ng/ml of BDNF. Motor neurons were then lysed at 1, 3, 6, and 8-hour incubation time points and subjected to a western blot for analysis of LC3-II levels. The motor neurons were incubated in 2 μ M bafilomycin A1 during serum starvation as well as during stimulation with BDNF.

In non-starved samples, LC3-II levels were lower in *+/-Loa* motor neurons, compared to the wild type (Figure 4.6A and B). During starvation, LC3-II levels increased in both genotypes, but to a lesser extent in *+/-Loa* (Figure 4.6A and B, compare non-starved with starved). When starved motor neurons were stimulated with BDNF, a drop in LC3-II levels was observed in both genotypes at 1 hour post-BDNF, which increased again slowly at later time points (Figure 4.6A and B, compare time points 3, 6, and 8 hr). However, LC3-II levels in *+/-Loa* were always lower compared to the wild type. Collectively, using bafilomycin A1 revealed that changes in LC3-II levels in *+/-Loa* followed the same pattern as those in wild type motor neurons, but to a lower extent. These data indicate reduced autophagic activity in starved and in starved and BDNF stimulated *+/-Loa* motor neurons.

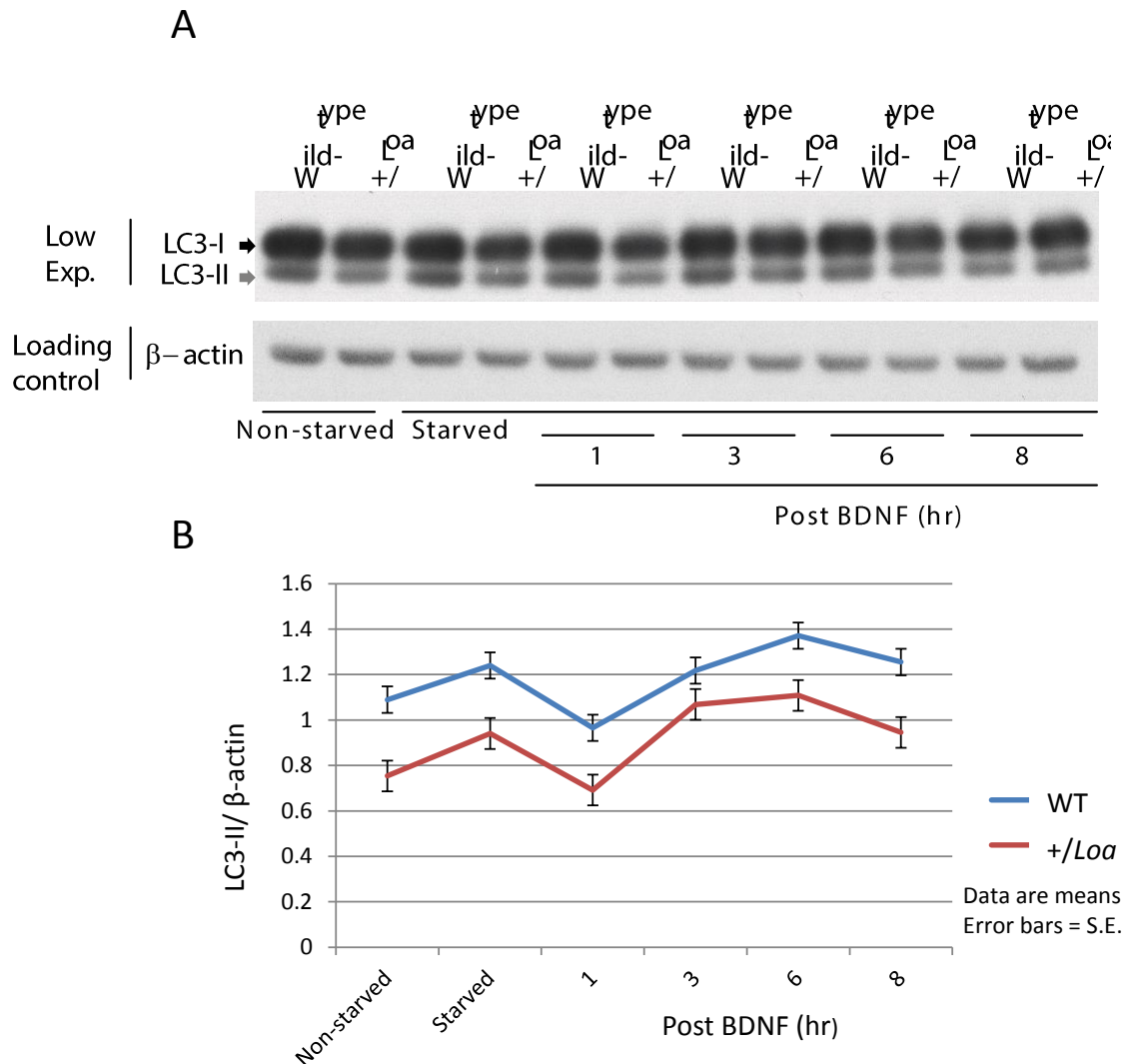
Figure 4.6

Figure 4.6 - LC3-II levels after bafilomycin A1 treatment. (A) Western blot showing reduced levels of LC3-II in *Loa* heterozygous motor neurons in non-starved, starved and BDNF-stimulated motor neurons. (B) Quantification of LC3-II in A. Data (at each time point) are means of two independent cultures, six replicates from each culture corresponding to the following time points: non-starved, starved, 1, 3, 6 and 8 hours. β-actin was used as a loading control and LC3-II staining intensity was normalized against β-actin signal.

4.7 Chapter 4 summary

Data from this chapter has shown that c-Fos activation is ERK1/2 dependent during starvation as well as after BDNF stimulation. Data also suggest that active p38 is implicated in c-Fos activation during starvation. In addition, the activation of autophagy is reduced in heterozygous *Loa* motor neurons. Autophagy is required to assist cells in dealing with serum-starvation by degrading and recycling damaged and/or old organelles to provide amino acids for the synthesis of new proteins. Therefore, the impaired activation of autophagy in *Loa* motor neurons is an indication that cytoplasmic dynein might be a contributing factor to autophagy induction/formation. This impaired autophagy might exacerbate the cellular stress leading to neurodegeneration.

Chapter 5

Investigating the Impact of Mutations in Cytoplasmic Dynein on Growth Cone Remodelling and Axonal Outgrowth

5.1 Introduction

Cytoplasmic dynein is a motor protein involved in a wide variety of functions including microtubule-dependent retrograde transport, growth cone movement and axonal elongation. Mutations in the DHC subunit of cytoplasmic dynein have been associated with neurodegenerative disorders: spinal muscular atrophy with lower extremity predominance (SMA-LED), Charcot Marie Tooth type 2 and learning disability. Children with SMA-LED exhibit contracture of the lower limb, walking delay, waddling walk and difficulty in climbing stairs. The *Loa* mouse strain, harbouring the Phe580Tyr mutation in DHC, exhibits some phenotypes with similarities to the human SMA-LED disease including progressive limb weakness and a waddling gait. The *Loa* mutation is also known to cause neurodegeneration and defective neuronal migration resembling that of human diseases. Although the precise mechanisms causing the defects in neuronal migration and neurodegeneration are yet to be identified, using multiple tools, we will be able to identify the intracellular events that contribute to the disease.

In this chapter, I present my data concerning my attempt to understand the molecular mechanisms underlying the defects in neuronal migration caused by mutations in DHC. To this end, I utilized the *Loa* mouse strain and human fibroblasts harbouring an Arg399Gly substitution mutation in DHC, which causes SMA-LED. Focusing on two essential elements required for cell migration: microtubules and focal adhesions, I hypothesized that the *Loa* mutation affects microtubule stability in the growth cone either by perturbing the binding of cytoplasmic dynein to the microtubule plus end, or by perturbing its anchoring to the cell cortex. I also hypothesized that *Loa* mutation affects focal adhesion disassembly. To verify this, I utilized fixed and live-cell microscopy to analyse microtubule stability and focal adhesion disassembly. I also used immuno-precipitation and immunoblotting to determine the effects of DHC mutations on the interactions between dynein intermediate chain and paxillin as well as on the level of paxillin phosphorylation during cell migration.

5.2 Aberrant focal adhesions in *Loa/Loa* MEFs

Cytoplasmic dynein was shown to be involved in regulating focal adhesion dynamics and migration (Rosse et al. 2012). To determine whether the *Loa* mutation affects focal adhesion dynamics, the spreading assay was conducted on MEFs, which were then fixed at the stage of the highest lamellipodia formation, followed by immuno-staining of MEFs against the focal adhesion protein paxillin and the dynein light intermediate chain subunit of cytoplasmic dynein (DLIC). These assays revealed that the adhesion sites located at the cell periphery were small, punctate and less distinct in *Loa/Loa* cells compared to those in the wild type which exhibited long and rod-shaped adhesions (Figure 5.1A, compare paxillin stain in wild type and *Loa/Loa*). Moreover, the intensity of DLIC at the cell periphery was reduced in the *Loa/Loa* cells compared to the wild type cells where DLIC was accumulated at the leading edge (Figure 5.1A). Focal adhesions were quantified for the number, size, eccentricity and ratios of major/minor axes (Figure 5.1B) (materials and methods chapter, section 2.6). The eccentricity was defined with 1 being the maximum and 0 being the minimum, where 0 represents a circle and 1 represents a straight line. The ratio of major/minor axes represents the ratio between the length and the width of the focal adhesions.

Interestingly, the average size of focal adhesions was significantly reduced in *Loa/Loa* cells compared to the wild type as seen in Figure 5.1B, I ($p = 0.004$, $n = 2048$ and 2793 focal adhesions in wild type and *Loa/Loa*, respectively). Consistent with this, quantification of the major/minor axes ratios showed a significant reduction in the *Loa/Loa* cells as seen in Figure 5.1B, II ($p = 0.01$, $n = 2048$ and 2793 focal adhesions in wild type and *Loa/Loa*, respectively). Also, a trend was observed towards an increase in the number of focal adhesions in *Loa/Loa* cells compared to the wild type as shown in Figure 5.1B, III ($n = 14$ and 18 cells in wild type and *Loa/Loa*, respectively). The aforementioned trend in the difference in focal adhesion numbers was also observed when the lamellipodia size was taken into account (Figure 5.1B, IV). No difference was observed in the eccentricity of focal adhesions in both wild type and *Loa/Loa* (Figure 5.1B, V).

The aberrant focal adhesions that were observed in *Loa/Loa* MEFs prompted me to examine focal adhesions (point contacts) in growth cones of motor neurons.

Therefore, motor neurons were cultured from E13 embryos of wild type and *+/Loa*.

Motor neurons were fixed at day one of culture with 4% paraformaldehyde and stained with antibodies against paxillin and F-actin (Figure 5.2). No difference in point contacts was observed between wild type and *+/Loa* growth cones. Thus, these data suggest focal adhesion impairment in *Loa/Loa* MEFs.

I also investigated focal adhesions in human fibroblasts obtained from patients with SMA-LED which harbour the Arg399Gly mutation in *DYNC1H1*, using the spreading assay described above for MEFs. Cells were then immunostained for paxillin (Figure 5.3). While wild type cells showed lamellipodia formations which were enriched in small adhesions (Figure 5.3, white solid arrows), *DYNC1H1*^{R399G/R399G} cells lacked lamellipodia (Figure 5.3, yellow arrows) which were barely observed in some cells (Figure 5.3, yellow solid arrows). These data indicate impaired lamellipodia formation in *DYNC1H1*^{R399G/R399G} fibroblasts.

Figure 5.1

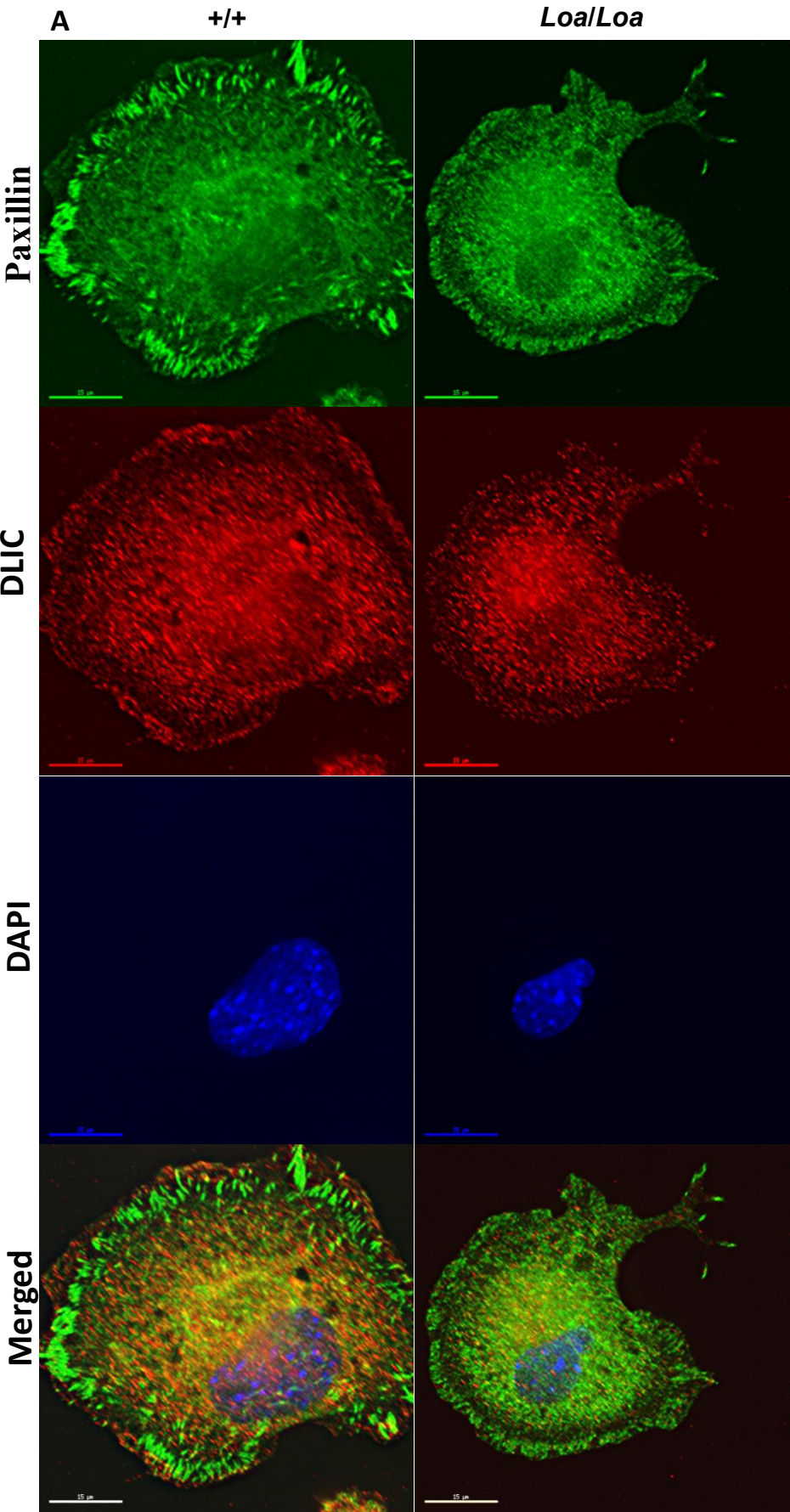


Figure 5.1

B

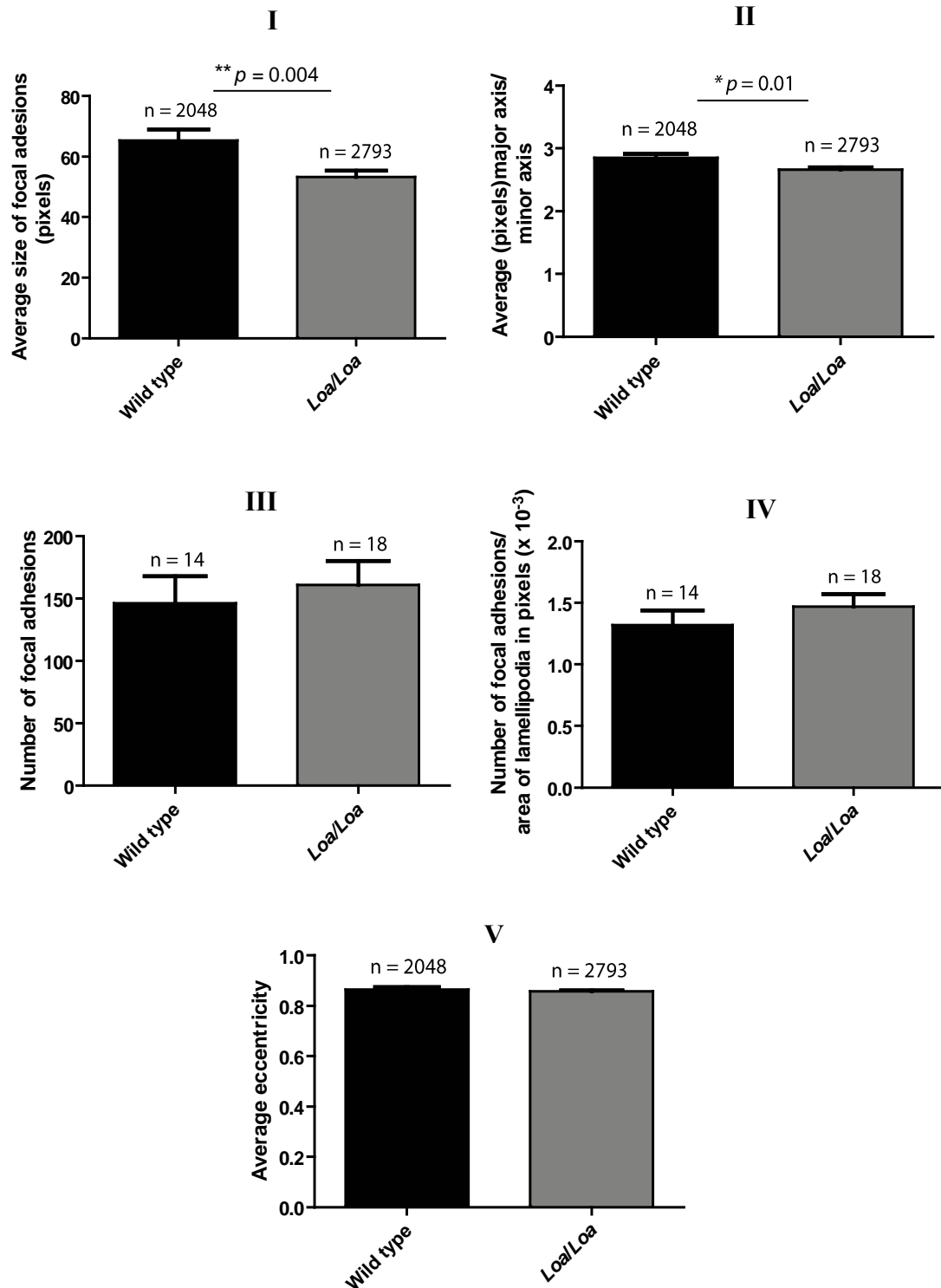


Figure 5.1 – Aberrant focal adhesions in *Loa/Loa* MEFs. (A) MEFs were subjected to a spreading assay and immunostained against the focal adhesion protein paxillin and cytoplasmic dynein subunit DLIC. Scale bar is 15 μ m. Images were captured using the DeltaVision Core microscope at 40x magnification. (B) The numbers, size, eccentricity (circle = 0, ellipse = $0 < X < 1$ and straight line = 1, where X represents focal adhesions) and the ratios of major/minor axes of focal adhesions were quantified. Data are shown

as mean +SEM. In I, II and V, n represents the number of focal adhesions whereas in III and IV, n represents the cell number.

Figure 5.2

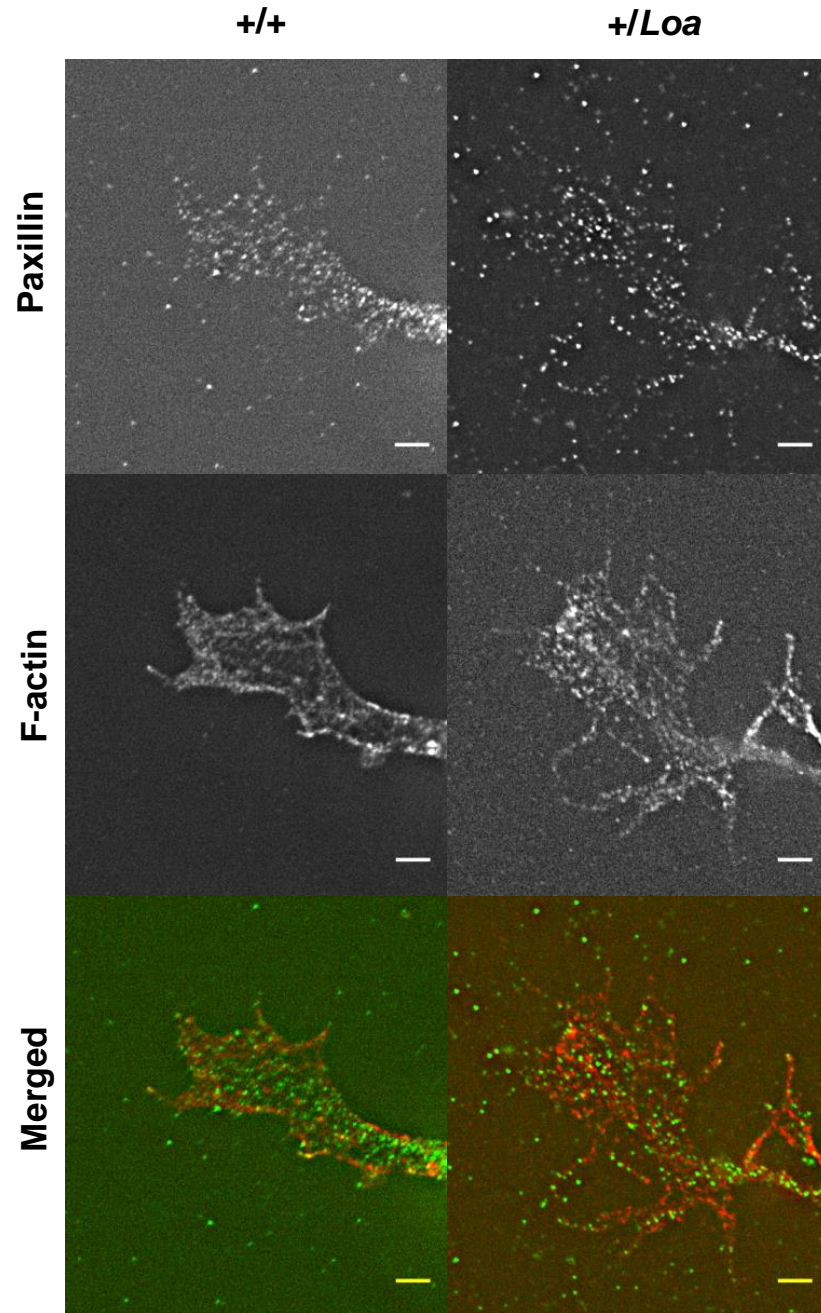


Figure 5.2 – Analysis of point contacts in growth cones of +/Loa versus wild type motor neurons. Two day old primary motor neurons were fixed with 4% paraformaldehyde and immunostained against the point contact protein paxillin, and F-actin. Merged images showed paxillin in green and F-actin in red. Scale bar is 5 μ m. Images were captured using the DeltaVision Core microscope at 100x magnification.

Figure 5.3

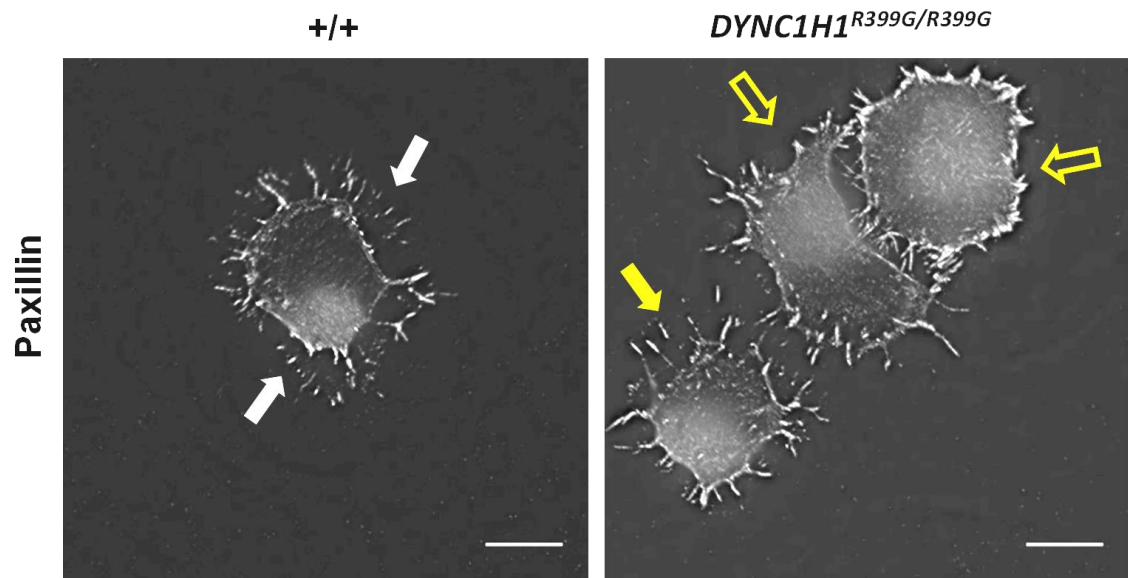


Figure 5.3 – Impaired lamellipodia formation in *DYNC1H1*^{R399G/R399G} human fibroblasts. White solid arrows point to lamellipodia in wild type. Yellow arrows point to *DYNC1H1*^{R399G/R399G} cells that are lacking lamellipodia. Yellow solid arrow points to a *DYNC1H1*^{R399G/R399G} cell with a barely observable lamellipodia. Scale bar is 5 μ m. Images were captured using the DeltaVision Core microscope at 40x magnification.

5.3 The immuno-precipitation of paxillin with dynein intermediate chain

The aberrant focal adhesions in *Loa/Loa* MEFs prompted me to investigate whether the *Loa* mutation affects the interaction between dynein intermediate chain (DIC) and paxillin. To achieve this, a scratch assay on confluent MEFs was performed to stimulate cell migration. Cells were extensively wounded after mitomycin C treatment, and homogenised 6 hours later, followed by immuno-precipitation (IP) with anti-DIC antibody and detection for paxillin.

In non-migrating cells, no paxillin was observed in the IP samples either in wild type or *Loa/Loa* MEFs (Figure 5.4A). A faint band with a size similar to paxillin appeared in the IP samples at longer exposure. A band of similar intensity was also observed in the wild type IgG negative-control which was treated in a similar manner as the IP samples. However, this faint band did not appear when the IP samples were re-run (Figure 5.4B). Furthermore, paxillin was detected in the post-IP samples, where no DIC was observed, indicating that most DIC was immuno-precipitated.

During cell migration, no interaction was observed between paxillin and DIC either (Figure 5.4C). No band was detected in a region which previously had shown to contain a band with similar size to paxillin in non-migratory cells. These results show that the faint band could not be paxillin and it is more likely to be either a non-specific binding or a spillover from adjacent lanes. Furthermore, the results indicate that no interaction between DIC and paxillin was detected in MEFs.

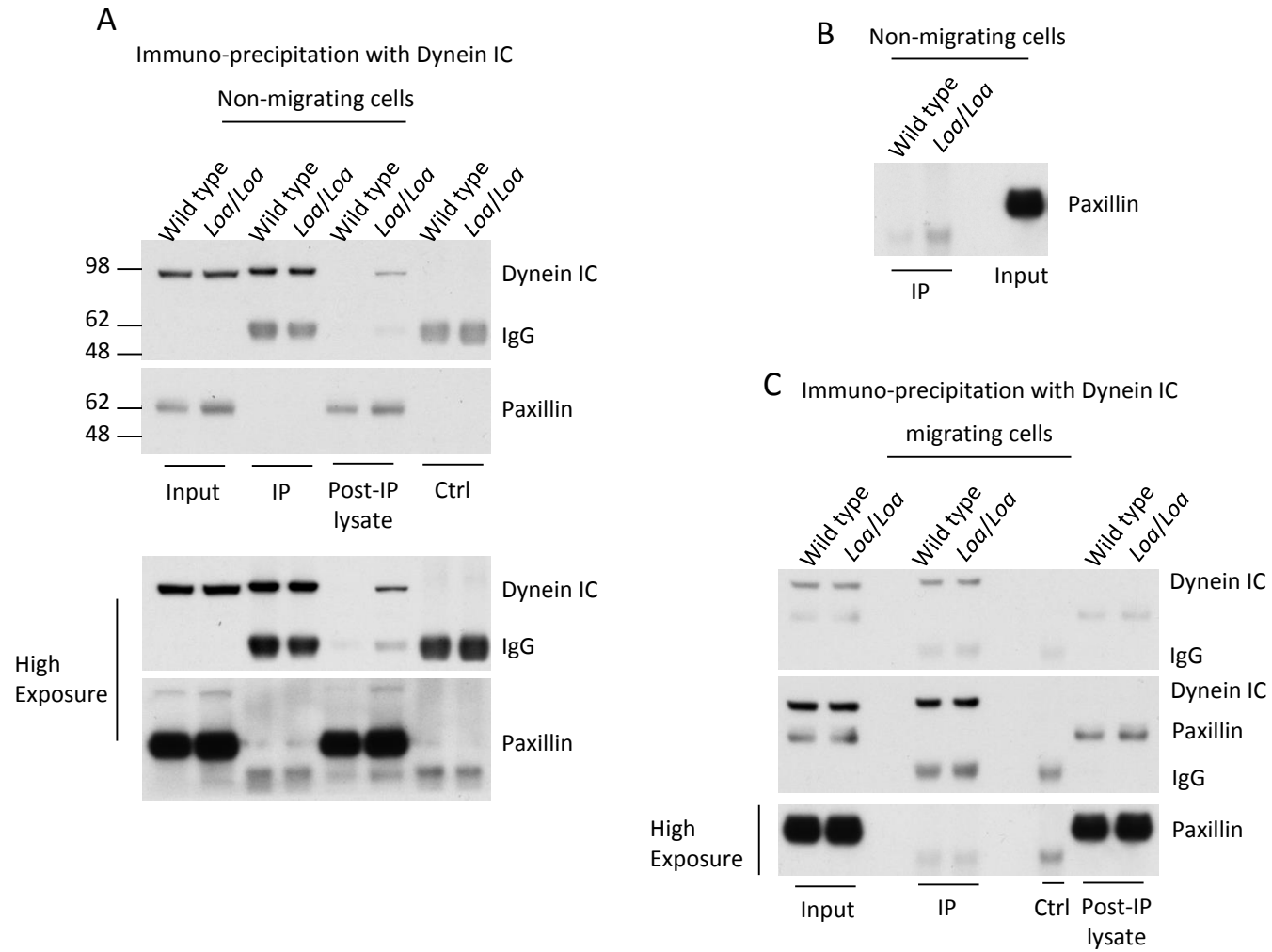
Figure 5.4

Figure 5.4 – Immuno-precipitation of paxillin with dynein intermediate chain in migrating and non-migrating cells. (A) A monolayer of confluent MEFs was harvested and subjected to immuno-precipitation. Dynein IC was immuno-precipitated followed by immunoblotting for dynein IC and paxillin detection. (B) A second run of a western blot of non-migrating samples was performed. (C) Immuno-precipitation of dynein IC in migrating MEFs. A confluent monolayer of MEFs was extensively scratched using a 10 μ l tip. Dynein IC was immuno-precipitated and subjected to immunoblotting for paxillin and dynein IC detection. Samples were run on a 12% precast polyacrylamide gel.

5.4 Reduced paxillin phosphorylation at Tyr118 in *Loa/Loa* MEFs

Cell migration requires dynamic focal adhesions which are regulated by paxillin phosphorylation (Introduction, page 109) (Zaidel-Bar et al. 2007). High levels of paxillin phosphorylation at Tyr118 were observed during focal adhesion disassembly (Zaidel-Bar et al. 2007). Therefore, in my experiment, increasing the number of focal adhesions in *Loa/Loa* MEFs suggests reduced levels of focal adhesion disassembly (Figure 5.1B, III). This prompted me to examine the level of paxillin phosphorylation. To achieve this, MEFs were plated on 10 cm culture plates and grown to a confluent monolayer. Cells were then treated with 10 µg mitomycin C before extensive scratching was performed to stimulate migration. Subsequently, cells were incubated at 37°C and collected at different time points: 6, 11, and 13 hours, followed by western blot analysis of paxillin phosphorylation using an anti phospho-antibody that recognises Tyr118. Paxillin phosphorylation levels were reduced in *Loa/Loa* MEFs compared to their levels in wild type in mitomycin C-untreated, mitomycin C-treated and across all the time points (Figure 5.5A and B). Consistent with the involvement of paxillin in cell division, the Tyr118 phosphorylation levels were reduced after mitomycin C treatment (Figure 5.5B and C). However, levels increased during migration consistent with the fact that Tyr118 phosphorylation is required during migration. Levels of Tyr118 phosphorylation were also determined after wound closure when levels were reduced to those in the mitomycin C-treated sample (Figure 5.5B and C). This indicates that cells did not recover from mitomycin C treatment and that wound closure was the result of cell migration. Collectively, these data show impaired paxillin phosphorylation at Tyr118 in *Loa/Loa* MEFs. Moreover, the data suggest impaired cell migration in *Loa/Loa* MEFs as a result of reduced levels of Tyr118 phosphorylation of paxillin.

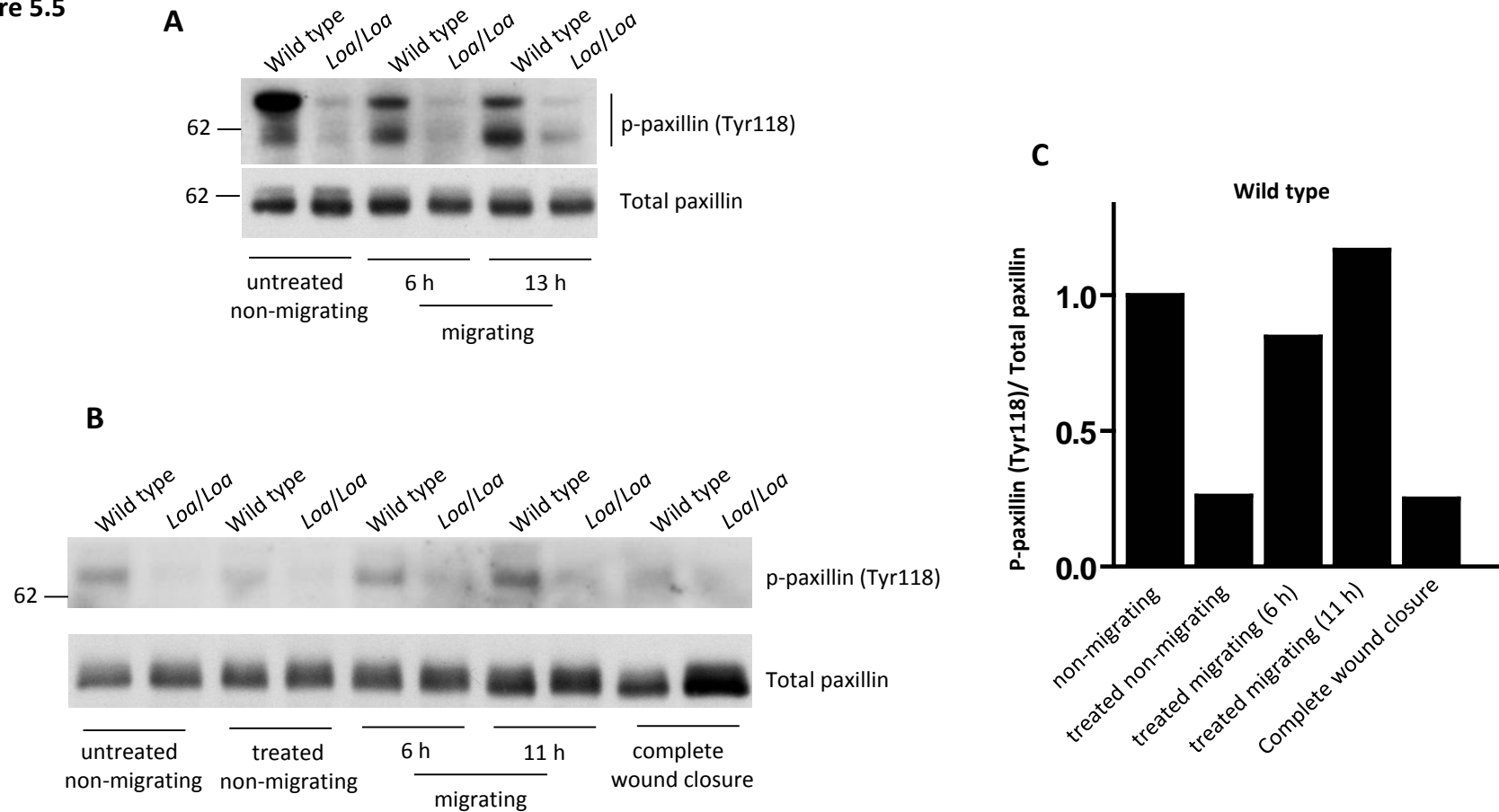
Figure 5.5

Figure 5.5 – Reduced levels of paxillin phosphorylation Tyr118 (p-paxillin) in *Loa/Loa* MEFs. (A and B) Immunoblotting of p-paxillin (Tyr118) in wild type and *Loa/Loa* MEFs. (C) Quantification of p-paxillin in B. Due to the reduced signal intensity of p-paxillin in *Loa/Loa* MEFs, quantification was only performed on p-paxillin in wild type MEFs. Total paxillin was used as a loading control for p-paxillin.

Next, I investigated the level of paxillin phosphorylation at Tyr118 in *DYNC1H1*^{R399G} human fibroblasts. The same protocol which was used on MEFs was implemented here. The level of paxillin phosphorylation was again determined by a western blot using an anti phospho-antibody to Tyr118. In mitomycin C-untreated samples, Tyr118 phosphorylation levels were reduced in *DYNC1H1*^{+ / R399G} and could barely be observed in *DYNC1H1*^{R399G / R399G} compared to the wild type (Figure 5.6). In mitomycin C-treated samples, the levels of Tyr118 phosphorylation were abolished in all genotypes. Cells were stimulated for migration by introducing extensive scratches onto the cell monolayer followed by incubation for 6 hours at 37°C. While the level of Tyr118 phosphorylation was detected neither in *DYNC1H1*^{+ / R399G} nor in *DYNC1H1*^{R399G / R399G}, a faint band was observed in wild type at 6 hours post-migration (Figure 5.6, white arrow).

Figure 5.6

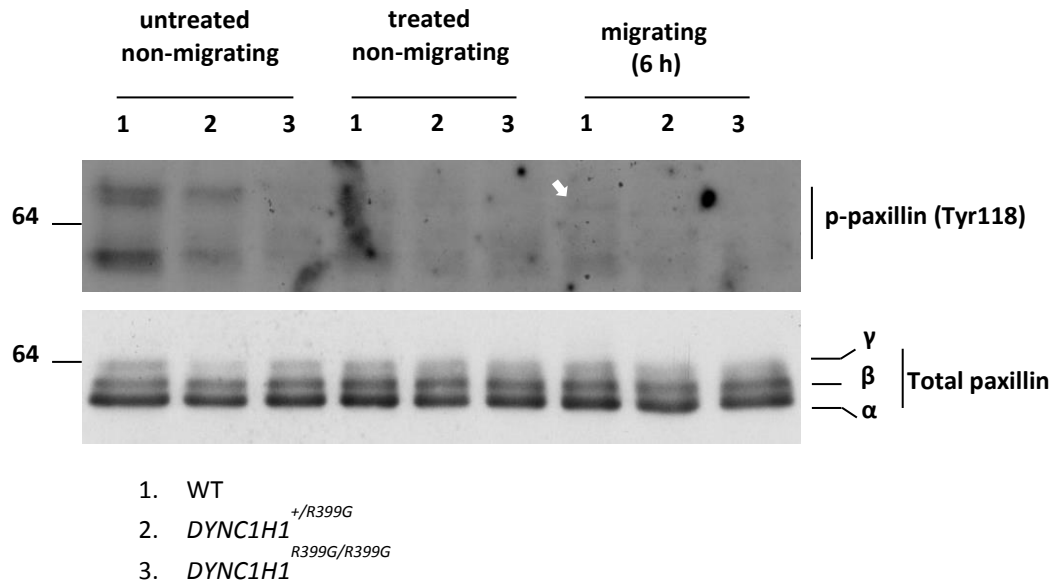


Figure 5.6 - Reduced levels of p-paxillin in *DYNC1H1*^{*R399G*} human fibroblasts. Immunoblotting of p-paxillin (Tyr118) in wild type and *DYNC1H1*^{*R399G*} human fibroblasts. The white arrow refers to a faint band corresponding to Tyr118 phosphorylation observed in wild type fibroblasts after 6 hours migration. Total paxillin was used as a loading control for p-paxillin.

5.5 *Loa/Loa* MEFs exhibit migration defects

The reduced levels of phosphorylated paxillin at Tyr118 in *Loa/Loa* MEFs prompted me to examine migration competency of these cells. To achieve this, MEFs were grown on a 6-well plate and a confluent monolayer was obtained 24 hours after plating. Cells were then treated with 10 µg mitomycin C before introducing the scratch, using a 10 µl pipette tip. Cells were imaged at pre-migration (time 0) and during migration at 13, 15, 17, 19, 21 and 23 hours post scratch (Figure 5.7A). Using image J, the speed of wound closure was measured by quantifying changes in wound size at the indicated time points. *Loa/Loa* MEFs exhibited a delayed wound closure in comparison to the wild type (Figure 5.7A). This delay was statistically significant at time points 19, 21 and 23 ($p = 0.01, 0.02, \text{ and } 0.02$, respectively) (Figure 5.7B).

Figure 5.7

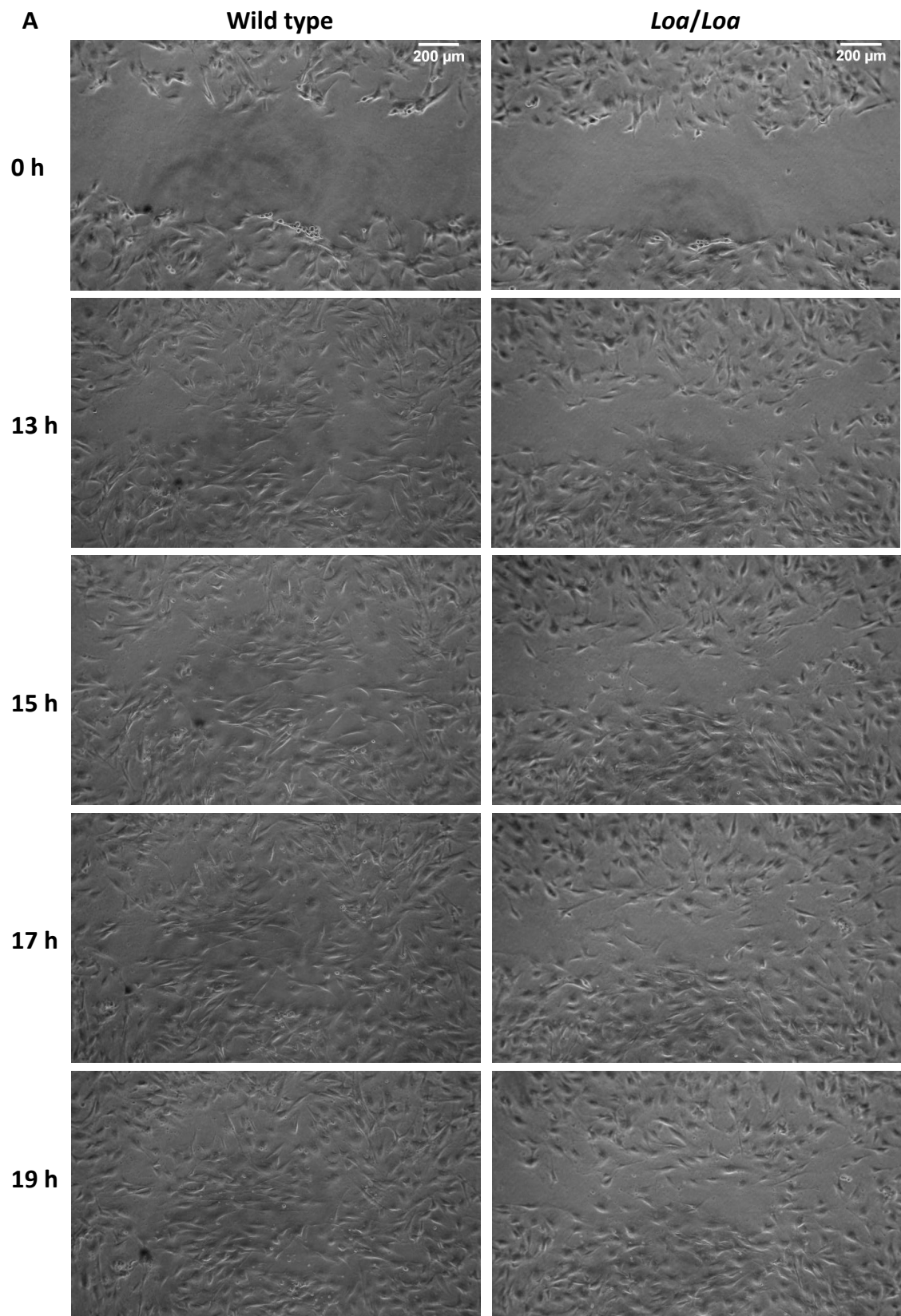


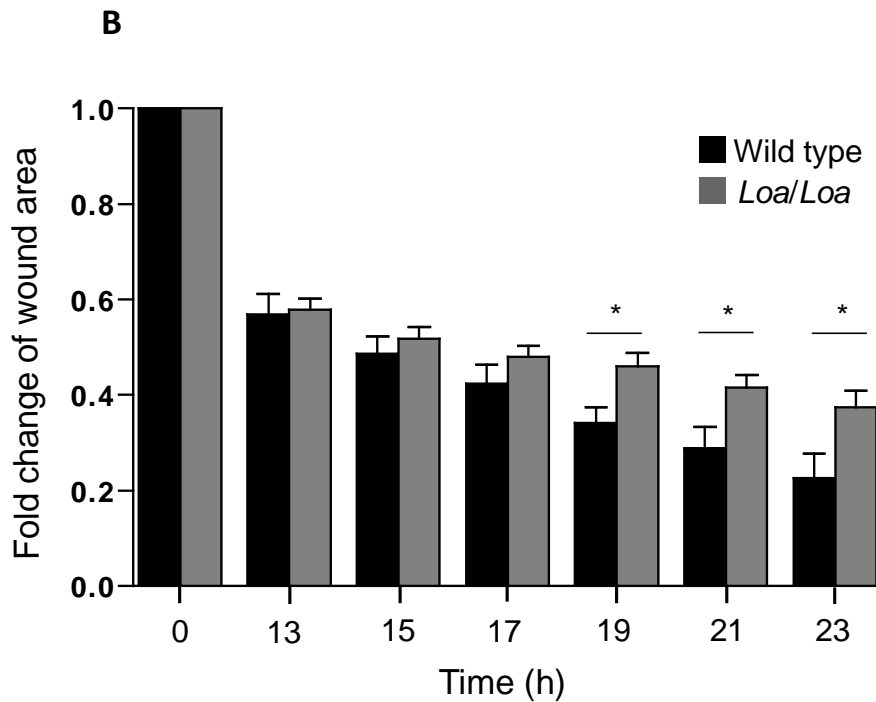
Figure 5.7

Figure 5.7 – Migration is defect in *Loaf/Loaf* MEFs. Figure showing the rate of wound closure from the wound healing assay performed on both wild type and *Loaf/Loaf* MEFs. (A) The wound healing assay performed on MEFs. Cells were imaged at pre-migration (time 0) and during migration at the following time points: 13, 15, 17, 19, 21 and 23 hours. Wound area was measured using image J at each indicated time points. Images were acquired at 20x magnification. The scale bar represents 200 μ m. (B) Histograms representing the average area of the scratch wound at time points: 13, 15, 17, 19, 21 and 23 hours relative to the original scratch area at time point 0. All quantitative data are shown as mean +SEM. Unpaired t-test; * P = 0.01, 0.02, and 0.02 for time points: 19, 21 and 23 hours, respectively. Data are produced from two independent experiments (five readings, corresponding to five different regions from one scratch, were obtained from each time point in one experiment).

5.6 Abnormal microtubule cytoskeleton in growth cones of *+/-Loa* motor neurons

The increased number of focal adhesions that was observed in *Loa/Loa* MEFs (Figure 5.1) suggests a delay in focal adhesion disassembly. A role for microtubules is known to promote focal adhesion disassembly in non-neuronal cells. However, in neuronal cells, microtubules are required to stabilise point contacts in growth cones. Therefore, I investigated microtubule organization in the growth cones. To achieve this, primary motor neurons (MNs) were cultured from E13 embryos on coverslips coated with poly-D-lysine (0.1 mg/ml) and fixed at day one with 4% paraformaldehyde. MNs were then stained with antibodies against microtubules, F-actin and dynein light intermediate chain (DLIC). In the wild type growth cones, microtubules extended their filaments reaching the peripheral domain of the growth cone whereas in the *+/-Loa* growth cones, microtubule cytoskeleton appeared abnormal and depleted from the peripheral domain (Figure 5.8, white arrows). These data suggest that the *Loa* mutation affects microtubule stability in the growth cones of motor neurons.

Figure 5.8

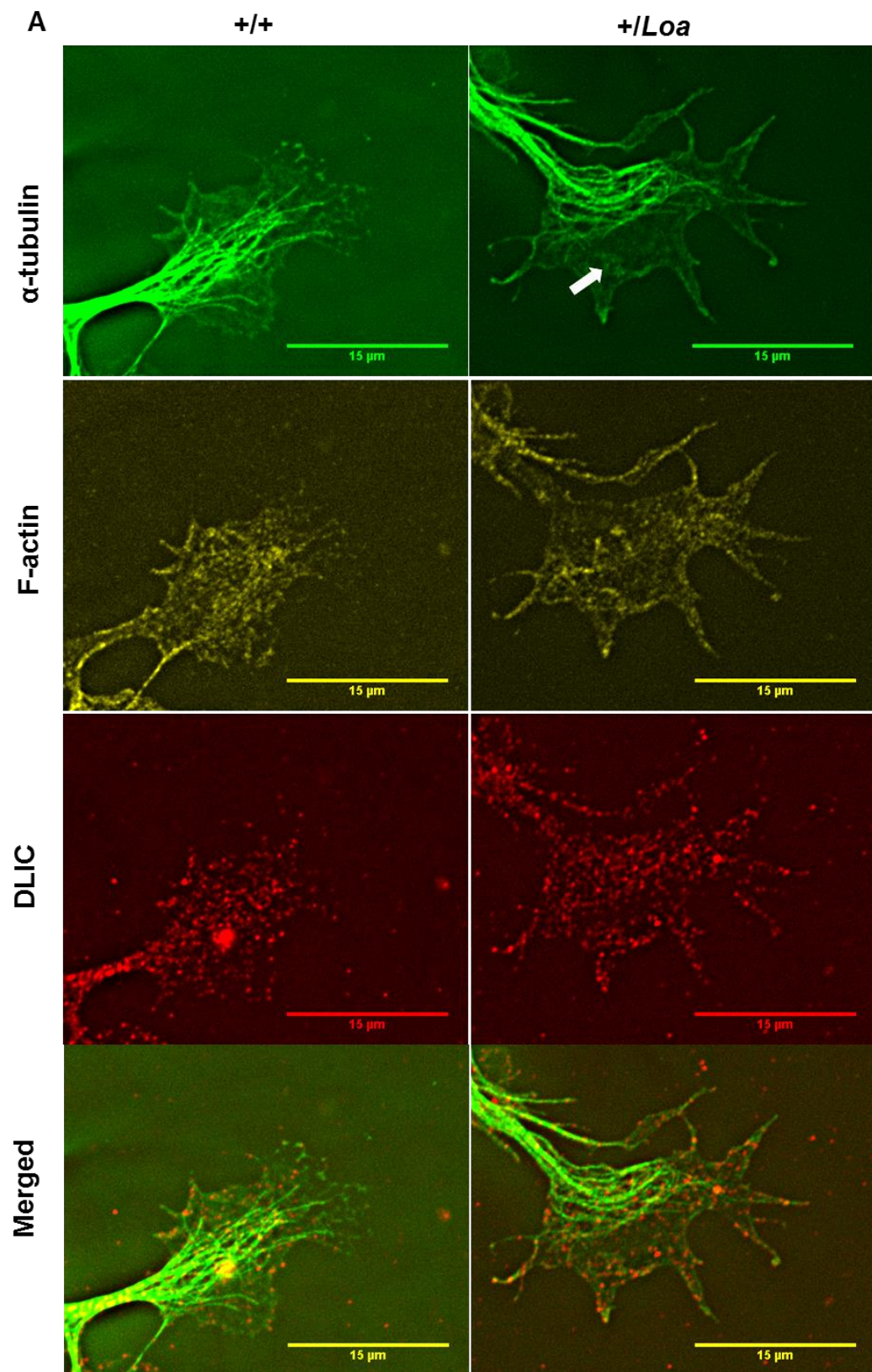


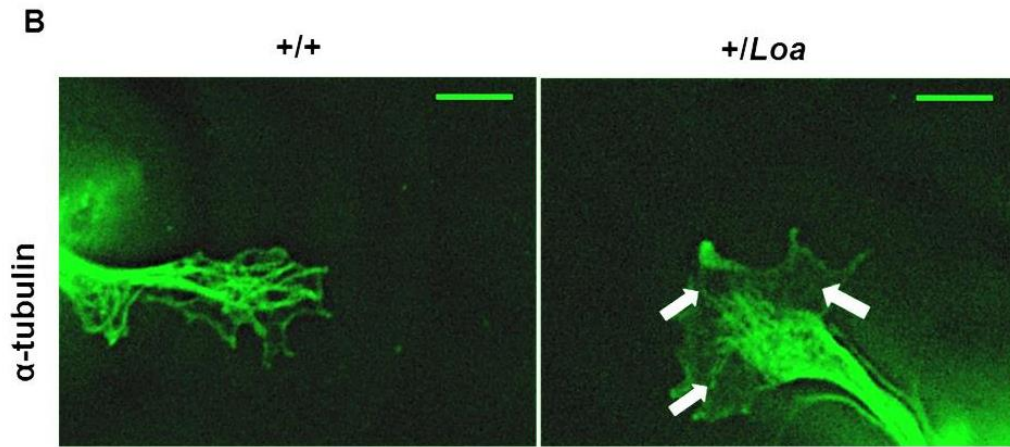
Figure 5.8

Figure 5.8 – Microtubule depletion in the P-domain of *+/Loa* growth cones of motor neurons. (A) Immuno-staining of growth cones against microtubules (green), F-actin (red) and dynein light intermediate chain (DLIC, yellow). Scale bar is 15 μ m. (B) Immuno-staining of microtubules in growth cones. White arrows showing microtubule depletion in the P-domain of growth cone. Scale bar is 5 μ m. Images were captured using DeltaVision Core microscope at a 100x magnification.

5.7 Live cell imaging of m-Cherry-microtubules in MEFs

To gain further insight into the microtubule stability in *Loa* cells, MEFs (wild type and *Loa/Loa*) were grown in a live-cell imaging chamber coated with 10 µg/ml collagen. Cells were grown until 50% confluent to stimulate migration and lamellipodia formation. At 50% confluency, cells were infected with the pAdEasy mCherry- α -tubulin adenovirus and subjected to time-lapse imaging 48 hours post-infection. Although it was difficult to obtain quantitative data, microtubules were scattered and less clustered along the leading edge in *Loa/Loa* MEFs compared to those in the wild type (Figure 5.9) (movies are attached). Thus, these data suggest abnormal microtubule bundling in *Loa/Loa* MEFs.

Figure 5.9

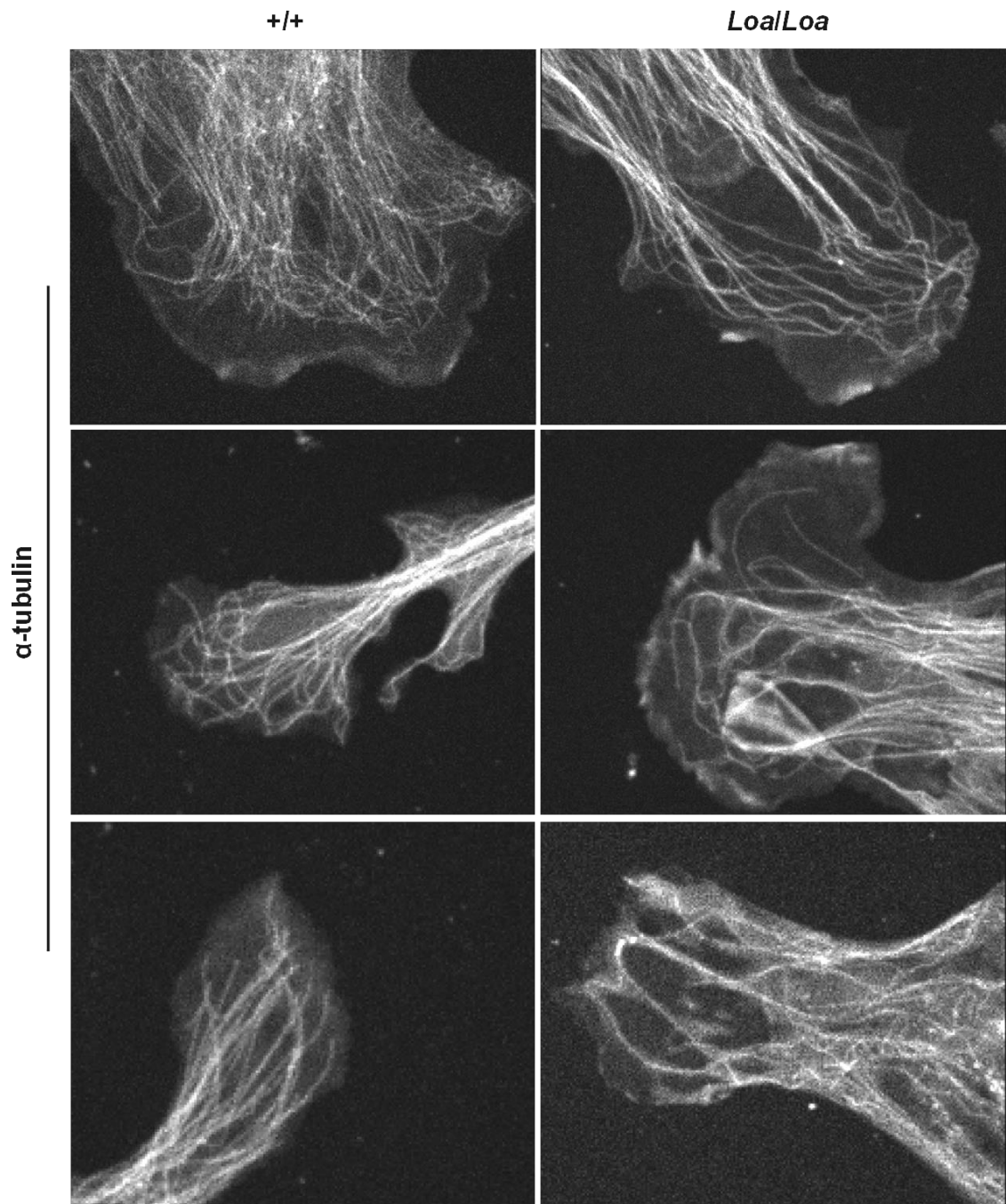


Figure 5.9 – Abnormal microtubule bundling in *Loa/Loa* MEFs. Figure showing representative time-lapse images of mCherry-tagged microtubules from wild type and *Loa/Loa* MEFs. Time-lapse images were taken every 5 seconds for a period of 10 minutes using a spinning disk confocal microscope (60x objective) equipped with an environmental chamber.

5.8 Analysis of microtubule dynamic instability in lamellipodia of wild type and *Loa/Loa* MEFs

The abnormal microtubule bundling observed in Figure 5.9 as well as microtubule depletion in the P-domain of growth cones of *+/Loa* motor neurons (Figure 5.8) prompted me to examine the microtubule dynamic instability in mutant versus wild type cells. Due to the difficulty in obtaining quantitative data from fluorescently labelled microtubules (Figure 5.9), only the microtubule plus ends were labelled. EB1 is known to be localized at the plus end of microtubules and was therefore used to label the tip of the microtubules. To achieve this, MEFs were grown in a live-cell imaging chamber to a density of 75% confluency, followed by transfection with RFP-tagged human EB1 using electroporation (Add gene, 39323). Forty eight hours after transfection, the confluent monolayer was scratched to stimulate cell migration. Subsequently, time-lapse imaging was initiated two hours after wounding, at the stage when most cells start pointing towards the scratch and form lamellipodia (Figure 5.10A) (movies are attached). To analyse the time-lapse images, the online Matlab-based software u-track (<http://lccb.hms.harvard.edu/software.html>) (Applegate et al. 2011) was used. This software enables tracking of thousands of microtubules in a very short time. Also, it offers an extensive list of parameters about microtubule dynamics. However, the most useful parameters for analysing microtubule dynamics in lamellipodia are the speed, lifetime and length of microtubule growth tracks. There was no significant difference in the aforementioned parameters between wild type and *Loa/Loa* lamellipodia of MEFs (Figure 5.10B).

In addition, in order to determine microtubule stability in growth cones of motor neurons, I cloned mCherry-tagged EB1 into the T-Syn-G-W lentivirus plasmid as described in the Materials and Methods chapter (see section 2.4.5).

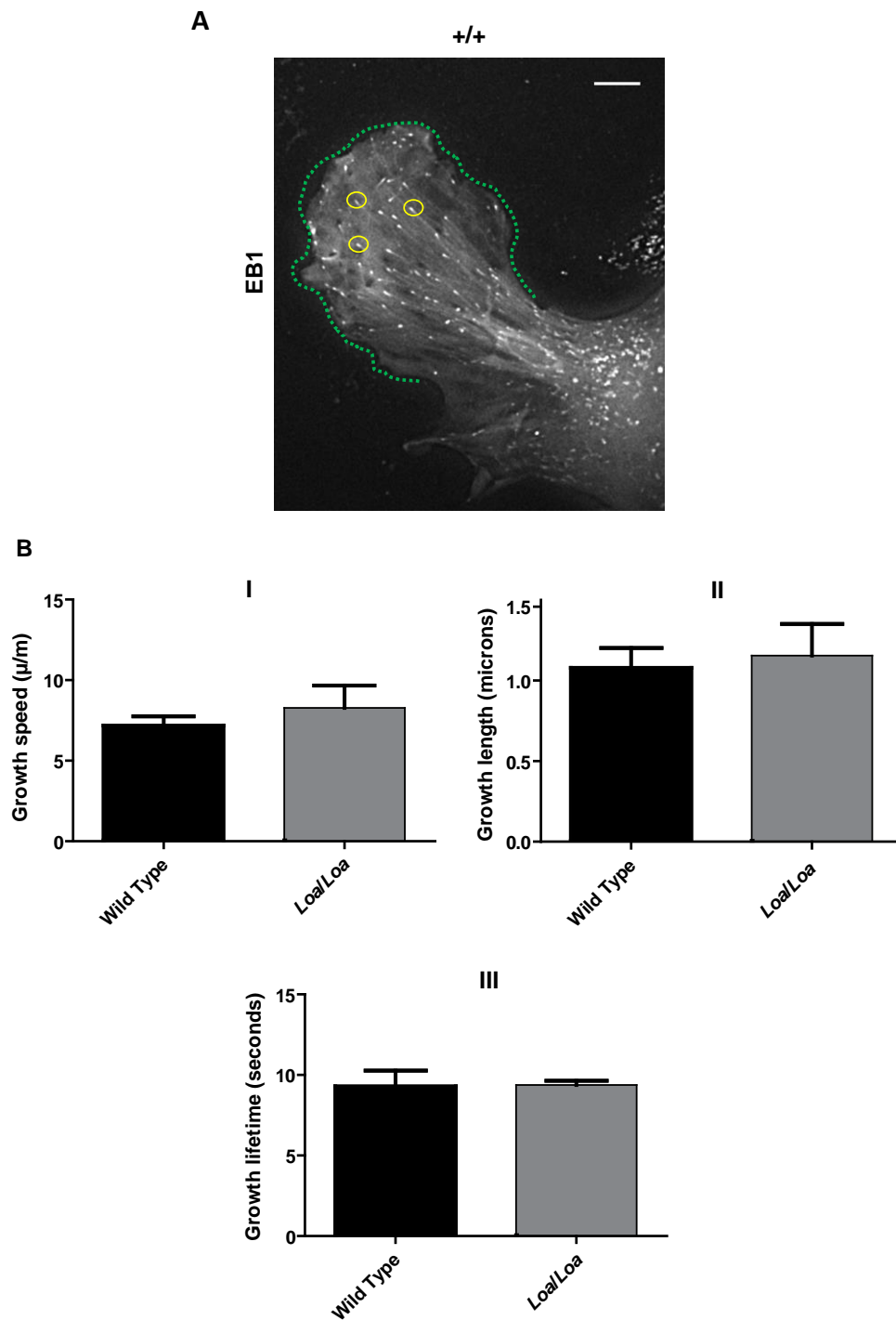
Figure 5.10

Figure 5.10 – Figure showing analysis of microtubule dynamic instability in lamellipodia of wide type and *Loa/Loa* MEFs. (A) A representative time-lapse image of RFP-tagged EB1 in a cell protrusion (surrounded by green dotted line) of wild type MEFs. Some EB1 are circled in yellow. Time-lapse images were taken every 2 seconds for 2 minutes at a 100x magnification using personal DeltaVision equipped with an environmental chamber. Scale bar is 10 μm. (B) The speed, lifetime and length of microtubule growth tracks were quantified (I, II and III respectively). All quantitative data are shown as mean +SEM.

Unpaired t-test; $p = 0.467, 0.358$ and 0.731 for the speed, lifetime and length of microtubule growth track respectively. $N = 5$ for wild type and 7 for *Loa/Loa*, where N represents the cell number; the number of microtubule growth tracks from each cell ranges from 200 to 500 tracks.

5.8 Chapter 5 summary

My data from this chapter indicate a link between mutations in DHC and a defective cell migration in both the *Loa* MEFs and human fibroblasts isolated from patients with SMA-LED. The underlying molecular mechanisms in the motility of growth cones is analogous to that in the fibroblasts, as they both utilize filopodia/lamellipodia dynamics and similar signalling cascades and cytoskeleton remodelling for pathfinding and motility. As point contact formation and stabilisation of microtubules in membrane protrusions at the growth cone play a central role in axonal outgrowth, my data suggest that the molecular pathogenesis of SMA-LED caused by mutations in DHC involves impaired growth cone development and axonal pathfinding.

Chapter 6

Discussion

6.1 Investigating the effect of TDP-43 mutation A315T on RNA metabolism of peripherin and GLT-1 and their roles in ALS pathology (Chapter 3)

6.1.1 GLT-1 expression in Prp-TDP-43^{A315T} transgenic mouse model (Figure 3.8 and 3.9)

In the study presented in chapter 3, I used the mouse model Prp-TDP-43^{A315T} generated by Wegorzewska et al (2009), which overexpresses the TDP-43 transgene under the mouse prion promoter in order to drive the expression of TDP-43 exclusively in the CNS. Due to the lack of a mouse model which overexpresses a similar level of wild type TDP-43, the contribution of TDP-43 overexpression to the observed phenotype cannot be excluded. However, it should be noted that Stallings et al (2010) generated a mouse model overexpressing wild type TDP-43 to a level almost similar to that shown in Wegorzewska's mouse model TDP-43^{A315T} (3-4 fold normalized to TDP-43 endogenous level) under the regulation of the same promoter which, however, did not exhibit a motor phenotype. Despite this, the selective loss of some populations of neurons e.g. layer 5 cortical neurons and motor neurons strongly suggests that the phenotype observed in Wegorzewska's mouse model is related to the TDP-43 mutation A315T and therefore to the altered function of TDP-43 (Wegorzewska et al. 2009). Interestingly, my experiments also showed that the levels of neuron specific GLT-1B significantly decreased while the astrocyte specific isoform GLT-1 showed only a trend towards down-regulation. However, the reduced protein level of GLT-1B cannot be due to neuronal cell loss, since the same phenotype was observed in non-symptomatic TDP-43^{A315T} mice when no neuron loss was observed (Wegorzewska et al. 2009). The fact that these reduced GLT-1B levels were observed in non-symptomatic TDP-43^{A315T} and not only in symptomatic TDP-43^{A315T} further confirmed that they must be a cause for the symptoms rather than an additional symptom itself. Thus, based on GLT-1B results, A315T mutation causes the loss of function property in TDP-43 in this mPrp- TDP-43^{A315T} mouse model.

The mechanism through which overexpression of TDP-43^{A315T} causes a reduced level of GLT-1B protein remains unidentified. However, I suggest several mechanisms that might be causing this altered level of GLT-1B protein. Several studies have reported splicing dysregulation in ALS patients with TDP-43 proteinopathy as well as in TDP-43

mouse models (Arnold et al. 2013; Highley et al. 2014). Also, Wegorzewska et al (2009) reported that the nuclear loss of TDP-43 was occasionally observed in neurons of TDP-43^{A315T} mice expressing late stage symptoms whereas in non-symptomatic TDP-43^{A315T} mice, the nuclear loss of TDP-43 was not observed. This raised the possibility that, in my experiments, the reduced level of GLT-1B protein in both non-symptomatic and symptomatic mice is likely due to splicing deficiency of this neuronal specific splice variant which is caused by A315T mutation and not by nuclear loss of TDP-43.

Moreover, the reduced level of GLT-1B protein might arise from other RNA-binding functions of TDP-43. Indeed, TDP-43 was shown to bind the 3'UTR region of the human neurofilament light (hNFL) mRNA, stabilising the hNFL mRNA levels and therefore preventing it from degradation (Strong et al. 2007). Evidence for this came from co-transfecting HEK293 cells with TDP-43 and full length hNFL mRNA (including the 3'UTR region) resulting in the stabilization of the hNFL mRNA levels in comparison to those cells that were transfected with full length hNFL alone in which hNFL mRNA levels were reduced. Moreover, the level of hNFL mRNA (in cells co-transfected with TDP-43 and hNFL-3'UTR) remained high up to 24 hours after being treated with actinomycin which acts to halt new mRNA synthesis. In addition, iCLIP experiments, performed on cytoplasmic and nuclear fractions of the human brain, revealed TDP-43 binding to the 3'UTR of numerous mRNAs in the cytoplasmic fraction compared to the nuclear fraction, despite its minor level in the cytoplasm (Tollervey et al. 2011). This suggests that TDP-43 might play a role in stabilizing and transporting mRNA. TDP-43 has also been shown to bind the 3'UTR of EAAT2 and that the level of binding is reduced in FTLD patients with TDP-43-positive inclusions (Tollervey et al. 2011). Therefore, it is plausible that the A315T mutation might also affect the binding of TDP-43 to the 3'UTR of GLT-1B mRNA, which in turn might affect the stability of GLT-1B mRNA.

In addition, TDP-43 has been shown to be present in axon terminals and co-purify with proteins involved in axonal transport of RNA (Freibaum et al. 2010; Fallini et al. 2012; Narayanan et al. 2013). Hence, it is possible that TDP-43 is involved in transporting GLT-1B mRNA to the synaptic terminals for local translation, where GLT-1B is required for glutamate clearance and thus for the prevention of excitotoxicity. Therefore, it is

possible that the A315T mutation might affect the transport of GLT-1B mRNA to synaptic terminals, which as a result might provoke excitotoxicity.

Despite these reports which showed the effect of TDP-43 mutations on RNA splicing, stabilization and axonal transport, I cannot exclude the possibility that the reduced level of GLT-1B protein might be caused at the translational level. To answer this question, a real time quantitative PCR can be performed. If GLT-1B cDNA levels are reduced, this will confirm that reduced protein levels of GLT1B are due to aberrant RNA processing. If they are not reduced, this could be an indication that the phenotype might be caused at translational level.

Given the multifunctional roles for TDP-43, the reduced level of GLT-1B protein is unlikely to be the sole contributor of A315T mutation to ALS. However, it is likely to be an important contributor to ALS in which a defect in GLT-1B might exacerbate disease progression. Indeed, elevated levels of glutamate were found in the cerebrospinal fluid (CSF) of some patients with sALS, which was attributed to abnormal glutamate transport (Rothstein et al. 1995). Moreover, the mechanism by which riluzole acts to prolong the life expectancy is by blocking the glutamate release from the pre-synaptic terminals (Fumagalli et al. 2008). Also, riluzole enhances the activity of glutamate transporters and thus increasing the glutamate uptake from the synaptic cleft.

6.1.2 GLT-1B expression in the TDP-43^{+/F210I} mutant mouse (Figure 3.10)

My experiment showed that the level of GLT-1B proteins is increased in the heterozygous F210I mutant TDP-43 mouse. These data was produced from one mouse. I observed abnormal hindlimb clenching in two TDP-43^{+/F210I} mutants at 11 month of age, of which one exhibited more severe clenching than the other. Further experiments are required to confirm this increased level of GLT-1B.

6.1.3 Per61 expression in SOD1^{G93A}, Prp-TDP-43^{A315T} transgenic and wild type mice (Figure 3.1 and 3.3)

I also analysed the effect of overexpression of A315T mutation on peripherin expression, by first investigating the presence of any novel splice variants. Using a primer set to amplify the entire coding sequence, I was not able to detect any novel

splice variants. However, I found that per61 was expressed at both RNA and protein levels in SOD1^{G93A}, TDP-43^{A315T} and wild type. This contradicts previous studies in which the abnormal expression of per61 polypeptide was found in the TX-100 insoluble fraction of SOD1^{G93A} and at the RNA level in SOD1^{G37R} mice (McLean et al, 2010; Robertson et al, 2003). Per61 was first identified in wild type LSC tissue at RNA level by Landon et al (2000), who were the first group designing primers for specific amplification of per61. Therefore, Landon et al's study further confirmed that per61 is normally expressed in wild type tissue. However, Robertson et al (2003) reported the presence of per61 at RNA level in LSC SOD1^{G37R} only but not in wild type, using the same primer set designed by Landon et al (2000). I further confirmed the normal expression of per61 using another primer set that amplifies only per61. My experiment also showed the presence of per61 protein in TX-100 insoluble fraction that contains polymerized filamentous peripherin, in all genotypes: SOD1^{G93A}, TDP-43^{A315T} and wild type (Figure 3.3). From this, I can conclude that per61 contributes in forming filamentous peripherin and that per61 expression is not associated with and does not play a pathological role in ALS, but rather it has a physiological relevance to the formation of peripherin neurofilaments.

6.1.4 Per45 expression in Prp-TDP-43^{A315T} transgenic mouse model (Figure 3.4)

In eukaryotes, protein synthesis is initiated through a process called “the ribosome-scanning mechanism of translation” (Touriol et al. 2003). This process involves the recruitment of the 40 S ribosomal subunit which recognizes the 5'-end cap structure of mRNA. Subsequently, using its ATP-dependent linear scanning, the 40 S ribosomal subunit reads through the sequence until it encounters an initiation codon in a Kozak consensus sequence. If the first codon is suboptimal, the 40 S ribosomal subunit reads through without recognizing it through a process called “leaky scanning”. Translation can also be initiated through a mechanism in which the 40 S ribosomal subunit recognizes *cis*-acting elements called internal ribosome entry site (IRES). This mechanism requires IRES trans-acting factors (ITAF) which stimulate translation of some mRNAs. Interestingly, using in vitro translation systems, the heterogeneous nuclear ribonucleoprotein A1 (hnRNPA1) was also found to be required for the

stimulation of the alternative translation (thorough IRES-dependent manner) of four isoforms of the human fibroblast growth factor 2 (FGF2) mRNA (Bonnal et al. 2005). Importantly, when hnRNPA1 was incubated with the whole nuclear extract of HeLa cells, it had no stimulatory effect on the alternative translation of FGF2 mRNA. However, this stimulatory effect was observed when the nuclear extract was fractionated to separate those proteins that have an inhibitory effect on the FGF2 alternative translation.

Although the sequence surrounding the ATG codon, which generates per45, is suboptimal for the ribosomal scanning mechanism (TTCTCCATGG) in comparison to the ATG start codon in per58 (GCCAGCATGA), *cis* and/or *trans* factors might influence the efficiency of this internal translation initiation. Given the structural similarity between TDP-43 and hnRNPs, it is not surprising that TDP-43 might also play a similar role in alternative translation as hnRNPA1 in stimulating the translation expression of FGF2 isoforms. Indeed, in my experiments, the amount of soluble per45 increased in the cytosolic fraction S1 obtained from prp-TDP-43^{A315T} transgenic mice (Figure 3.4) when compared with non-transgenic wild type and SOD1^{G93A} transgenic mice. This indicates that the third ATG is highly selected in prp-TDP-43^{A315T} transgenic mice. A recent study has shown that hnRNPU, hnRNPA2 and hnRNPA1 are TDP-43 interactors. Mild overexpression of any of these hnRNPs inhibits the neurotoxicity induced by overexpression of nuclear TDP-43^{WT}, suggesting that the hnRNPs are negative regulators of TDP-43 (Suzuki et al. 2014). Therefore, it is possible that, either the A315T mutation in TDP-43 might affect its interaction with hnRNPA1, or overexpression of TDP-43 might overcome the inhibitory effect of hnRNPA1. In either case, the outcome would be the elevation of per45 expression. Thus, alterations in the level of TDP-43 expression or a direct mutation in TDP-43 may result in aberrant ribosomal scanning. This would result in a shift in the preference of the start codon and causes a change in the stoichiometry of peripherin isoforms. These aberrant changes may have pathological consequences, i.e. abnormal cytoskeletal stability or assembly. Indeed, my experiments showed abnormal stability of peripherin in the prp-TDP-43^{A315T} transgenic mouse model, which might be the result of a change in the

stoichiometric contribution of per45 in the filament network formation of peripherin (Figure 3.5).

Interestingly, despite the low expression of per58 in the cortex, hippocampus, olfactory bulb and cerebellum, per45 was found to be highly expressed in these regions (McLean et al. 2008). Further experiments are required to determine the level of per45 expression in these regions in TDP-43^{A315T} transgenic mice, which might be relevant to some aspects of the neuropathology of mutant TDP-43.

6.1.5 The 50 kDa polypeptide (Figure 3.5)

My data and those reported by other groups (McLean et al. 2008), have shown the presence of an as yet unidentified 50 kDa polypeptide detected by anti-peripherin antibody. My experiments showed the presence of this polypeptide in all fractions (S2, S3 and P3) apart from the cytosolic fraction (S1). More importantly, my experiments showed increased levels of the soluble 50 kDa polypeptide in fraction S3 TDP-43^{A315T} transgenic mice. Further experiments are required to determine the identity of this polypeptide and its role in peripherin filament network.

6.2 Investigating the signalling cascade underlying c-Fos activation during starvation and BDNF stimulation (Chapter 4, Figure 4.2, 4.3 and 4.4)

The aim of the study presented in chapter 4 was to investigate which MAP kinases were implicated in transmitting the signal responsible for inducing c-Fos phosphorylation in serum-starved primary motor neurons. In order to pursue this question, activation of MAP kinases: JNK, ERK1/2 and p38 was analysed in motor neurons using immunoblotting. Our group had shown increased levels of active pERK1/2 in motor neurons during starvation, which remained higher in +/-*Loa* motor neurons after the addition of BDNF (Garrett et al 2014). My experiment showed that starvation induces p38 activation whereas JNK is activated by BDNF stimulation. However, the elevated level of pc-Fos during starvation and after BDNF stimulation is at least partly resulted from ERK1/2 activation and not from the stress activated protein kinase JNK. Evidence for this conclusion came from the experiment where the inhibition of JNK in fact led to increased pc-Fos levels, whereas treating motor neurons with the ERK1/2 inhibitor, reduced pc-Fos levels, thus indicating that pc-Foc levels is

ERK1/2 dependent (Figure 4.4). Perhaps, it remains to be shown whether increasing the concentration of ERK1/2 inhibitor completely abolishes c-Fos activation or whether another kinase is involved.

C-Fos induction in motor neurons is increased by both starvation and in response to BDNF stimulation (Garrett et al 2014). My data show that p38 activation is only increased in starvation, but not in response to BDNF. This suggests that BDNF inhibits p38 activation because the addition of BDNF to starved cells counteracts the activating effect of starvation until BDNF begins to disappear from the media at 8 hours, at which point p38 activity increases again. However, an experiment should be set up in which motor neurons are starved for a longer duration in the absence of BDNF, in order to confirm the likely inhibitory effect of BDNF on p38 activity and to prove that the reduced p38 activity was not caused by a longer starvation period. My data also suggest that active p38 is responsible for c-Fos induction during starvation. Therefore, further experiments, using a selective p38 inhibitor, are required to establish the role of p38 in c-Fos induction, during serum starvation or in response to BDNF.

Garrett et al showed that impaired trafficking of signalling endosomes in *Loa* results in higher levels of pERK1/2 in both motor neurons and MEFs without a significant impact on pc-Fos levels in *Loa* MEFs (Garrett et al 2014). However, in motor neurons, ERK1/2 was activated during starvation and consequently led to c-Fos induction and phosphorylation. The level of both pERK1/2 and p-c-Fos were strikingly up-regulated in *+Loa* motor neurons. These data indicate that motor neurons are equipped with a stress response machinery involving ERK1/2 and its downstream effector c-Fos. This, therefore, might act as a protective mechanism against cellular stress.

It has been shown that in response to glutamate excitotoxicity, BDNF transiently activates ERK1/2 to promote cell survival (Almeida et al. 2005). Moreover, persistent activation of ERK1/2 in cortical neurons in response to glutamate-induced oxidative stress causes cell death (Stanciu et al. 2000). Therefore, the persistent ERK1/2 activation in *+Loa* motor neurons, which is caused by impaired endocytic trafficking, is likely to contribute to neuronal death by making them more prone to physiological insults.

Mitchell et al (2012) showed that activation of ERK1/2 in cortical neurons upon BDNF stimulation leads to phosphorylation of dynein intermediate chain (DIC) (Mitchell et al. 2012). Interestingly, Hafezparast laboratory previously showed that the amount of DIC phosphorylation is reduced in the brain tissue isolated from homozygous *Loa* embryos (Deng et al 2010). It is, therefore, possible that the increased affinity of DHC to DIC, as a result of the *Loa* mutation, causes conformational changes in DIC, which might impede its phosphorylation site from being phosphorylated by ERK1/2. As a consequence, this might lead to impaired dynein-mediated endocytic transport and consequently results in persistent ERK1/2 activation.

Collectively, these data indicate that in serum-starved motor neurons, active JNK was reduced, while the levels of active p38 and pERK1/2 increase. When starved motor neurons were treated with BDNF, the active p38 levels declined over the course of 6 hours and increased again after 8 hours. However, the levels of active JNK and pERK1/2 increase after BDNF stimulation and decline after 8 hours, the time point when p38 activity increases again. These changes in the activation of MAP kinases might be related to the amount of BDNF in the media, which reduces over time. Based on these observations, I propose a model for the involvement of MAP Kinases in c-Fos induction upon starvation and stimulation with BDNF (Figure 6.1). According to this model, starvation induces activation of p38 and ERK1/2. C-Fos is phosphorylated through an ERK1/2-dependent pathway and possibly by active p38. Upon activation of TrkB receptor by BDNF and endocytosis of ligand-receptor, active p38 is suppressed, while both JNK and ERK1/2 are initiated. However, phosphorylation of c-Fos is ERK1/2-dependent.

Figure 6.1

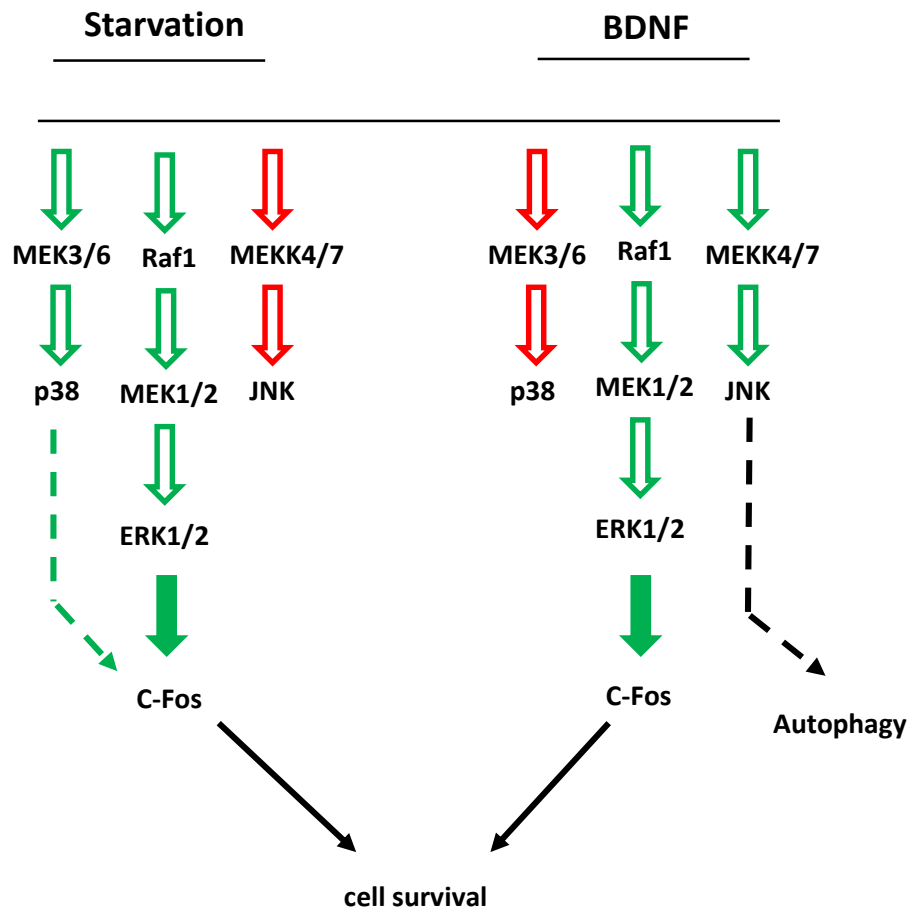


Figure 6.1 – Proposed model of signalling pathways underlying c-Fos activation in motor neurons upon serum starvation or stimulation with BDNF. Red arrows represent suppressed pathways, while green arrows represent active pathways. During starvation, p38 and ERK1/2 are activated but not JNK. C-fos induction is ERK1/2 dependent and possibly by active p38. Solid green arrows indicate experimentally confirmed c-Fos induction by pERK1/2, while dotted green arrow indicates a potential c-Fos induction by active p38. Dotted black arrow indicates a potential signalling pathway in mediating autophagy. When starved cells are stimulated with BDNF, ERK1/2 and JNK are activated, whereas the p38 pathway is suppressed. Note: the MAP kinase pathways are adapted from (Roux and Blenis 2004).

6.2.1 Autophagy during starvation (Chapter 4, Figure 4.5 and 4.6)

Autophagy was activated in wild type motor neurons upon nutrient deprivation. However, starvation failed to induce autophagy in *+/-Loa* as evidenced by down-regulation of LC3-II in *+/-Loa* compared to those in untreated motor neurons (Figure 4.5). To further verify this phenotype, the autophagosome fusion with lysosome was blocked by treatment with bafilomycin A1. Bafilomycin A1 was used to facilitate the analysis by looking at LC3-II accumulation in a more defined temporospatial phase. Reduced levels of LC3-II can reflect either reduced generation of autophagosomes or increased clearance. Therefore, blocking the phagosome-lysosome fusion will rule out autophagy clearance as a cause for the phenotype (reduced LC3-II levels). In my experiment, In the presence of bafilomycin A1, changes in LC3-II levels in *+/-Loa* followed the same pattern as those in wild type motor neurons. The level of LC3-II in *+/-Loa* motor neurons increased during starvation, but to a lower extent compared to that in starved wild type motor neurons (Figure 4.6, starved). This leads me to believe that the lower LC3-II levels in *+/-Loa* are likely due to reduced autophagy induction/formation in *+/-Loa*.

6.2.3 Autophagy in the absence of bafilomycin A1 (Chapter, Figure 4.5)

When starved motor neurons were treated with BDNF, the level of LC3-II dropped after 10 minutes in both genotypes, but a more pronounced decrease was seen in wild type motor neurons. Subsequently, LC3-II levels gradually increased at time points 30, 60 and 180 minutes. One possible reason is that the drop in LC3-II levels might be resulted from binding of BDNF to TrkB receptor, which induces the MAP kinase signalling cascade. However, due to the absence of vital nutrients autophagy is reinitiated, leading to increased LC3-II levels at time points 30, 60 and 180 minutes. Levels of LC3-II during these time points remained higher in *+/-Loa* motor neurons in comparison to wild type except for the 180-minute time point, when LC3-II levels in wild type was higher. To explain these results, it is noteworthy to know that BDNF activates autophagy in primary cortical neurons (A. Chen et al. 2013). Therefore, the increased LC3-II levels in *+/-Loa* are likely due to impaired endocytic trafficking of BDNF-containing endosomes and therefore a delay in degradation of BDNF. As a

consequence, BDNF continues triggering autophagy, which results in increased LC3-II levels, while in the wild type, due to efficient endocytic trafficking, BDNF degrades faster which results in less LC3-II levels than those in the *+/-Loa*. The reactivation of autophagy that is observed in the wild type after three hours, is most likely due to BDNF depletion. This might also be related to the efficiency of endocytic trafficking in wild type which results in faster depletion of BDNF compared to *+/-Loa* where autophagy is still activated at three hours by BDNF.

6.2.4 Autophagy in the presence of bafilomycin A1 (Chapter4, Figure 4.6)

Next, I investigated LC3-II levels in BDNF-stimulated motor neurons after bafilomycin A1 treatment (Figure 4.6). Consistent with the results observed at 10 min post BDNF in the absence of bafilomycin A1 (Figure 4.5), the drop in LC3-II levels was also observed at 1 hour post BDNF in both wild type and *+/-Loa*. At later time points 3 and 6 hours, increased levels of LC3-II was observed in both genotypes consistent with stimulation of autophagy by BDNF (A. Chen et al. 2013). However, since bafilomycin A1 inhibits acidification of lysosomes which is important to mediate fusion with organelles for hydrolysis, the degradation of BDNF-containing endosomes are therefore inhibited. This will eliminate any changes in LC3-II that resulted from endocytic trafficking. Consistent with the fact that bafilomycin A1 inhibits endosome degradation and that endosomes will keep signalling in both genotypes, I expected that LC3-II levels will exhibit a similar pattern in both genotypes. Indeed, my experiment showed that the changes in LC3-II levels in *+/-Loa* followed the same pattern as those in wild type motor neurons but was to a lower extent. This is consistent with LC3-II levels in *+/-Loa* starved motor neurons in Figure 4.5 (Figure 4.5), Thus, the reduced levels of LC3-II observed in *+/-Loa* motor neurons during starvation and stimulation with BDNF in the presence of bafilomycin further indicates abnormal autophagy induction/formation in *+/-Loa*.

6.3 Focal adhesions in *Loa/Loa* MEFs (Figure 5.1)

My experiment showed abnormal focal adhesions in spreading *Loa/Loa* MEFs (Figure 5.1). Although it is not statistically significant, the *Loa/Loa* MEFs also showed an increase in the number of focal adhesions compared to the wild type MEFs. It should be noted that focal adhesion kinase-null fibroblasts (FAK^{-/-}) exhibit a similar phenotype following the spreading assay, i.e. they contain numerous small punctate adhesions (Ilić et al. 1995). Therefore, it is plausible that an impaired FAK pathway is the main cause for the focal adhesion abnormalities in the *Loa/Loa* MEFs and the increase in their number is a result of deficient focal adhesion disassembly.

6.4 Immuno-precipitation of paxillin with dynein intermediate chain (Figure 5.4)

Cytoplasmic dynein has been shown to be involved in regulating focal adhesion disassembly via the interaction of dynein intermediate chain 1/2 with paxillin (Rosse et al. 2012). This was shown by immuno-precipitating DIC followed by detection of paxillin. However, although the DIC antibody that I used in my experiment is able to detect all DIC isoforms, I could not detect this interaction. This is likely due to the cell type as Rosse et al used normal rat kidney cells (NRK) whereas I used fibroblasts. Another possibility is that DIC is an abundant protein involved in various intracellular events and it might be a small population of DIC that interacts with paxillin. Therefore, it would be useful to conduct immuno-precipitation using an anti paxillin antibody to detect DIC.

6.5 Paxillin phosphorylation in *Loa/Loa* MEFs and in DYNC1H1^{R399G} human fibroblasts (Figure 5.5 and 5.6)

Tyr118 phosphorylation of paxillin was found to be associated with focal adhesion assembly and disassembly which is required to promote cell migration (Zaidel-Bar et al., 2007). It is also known that Tyr118 phosphorylation of paxillin is mediated by FAK and Src (Li et al. 2009; Bellis, Miller, and Turner 1995; Klinghoffer et al. 1999). My experiments showed that Tyr118 phosphorylation of paxillin was reduced in the *Loa/Loa* MEFs which therefore provided another evidence for implicating FAK and/or Src in focal adhesion abnormality in the *Loa/Loa* MEFs. This reduction in paxillin

phosphorylation might explain the increase in the number of focal adhesions as a result of the delayed focal adhesion disassembly. As the Tyr118 phosphorylated paxillin is required to stimulate focal adhesion assembly and disassembly during migration, reduced phosphorylation levels would lead to a defect in migration. Indeed, *Loa/Loa* MEFs exhibited migration deficits as proven by delayed wound closure (Figure 5.7).

My experiments also showed that Tyr118 phosphorylation of paxillin is reduced in mitomycin C-untreated *DYNC1H1*^{R399G/R399G} human fibroblasts (Figure 5.6). However, when cells were treated with mitomycin C and stimulated for migration, Tyr118 phosphorylation was barely seen in wild type after 6 hours post migration, while none was observed *DYNC1H1*^{+ /R399G} nor *DYNC1H1*^{R399G/R399G}. Due to the reduced signal intensity of Tyr118 phosphorylation in wild type, this experiment should be repeated where cells should be incubated for a longer period to stimulate their migration. It is likely that the defect in lamellipodia formation in *DYNC1H1*^{R399G/R399G} cells following the spreading assay is caused by the low level of Tyr118 phosphorylation (Figure 5.3). Indeed, Tyr118 and/or Tyr31 phosphorylation of paxillin was found to be required for the creation of binding sites for SH2-containing proteins (such as Crk) which is thought to be involved in Rac activation that is required to promote lamellipodia extensions (Zaidel-Bar et al. 2007; M D Schaller 2001; Brown and Turner 2004) (Introduction page 106).

6.6 Microtubule stability in +/-*Loa* growth cones (Figure 5.8)

The role of microtubules during cell migration is important for several processes including transporting vesicles to the leading edge of migrating cells and regulating focal adhesion disassembly. It should be noted that focal adhesions are usually covered with actin filament arrays that cannot be easily penetrated by microtubules alone. In growth cones of neurons, microtubule advancement to the P-domain is encountered by actin arcs and the retrograde actin flow. So, how do microtubules target focal adhesions as well as reach the cell cortex? One proposed mechanism is that the advancement of microtubules to focal adhesions as well as to the cell cortex is probably guided by actin stress fibres (Palazzo and Gundersen 2002). Moreover, live-

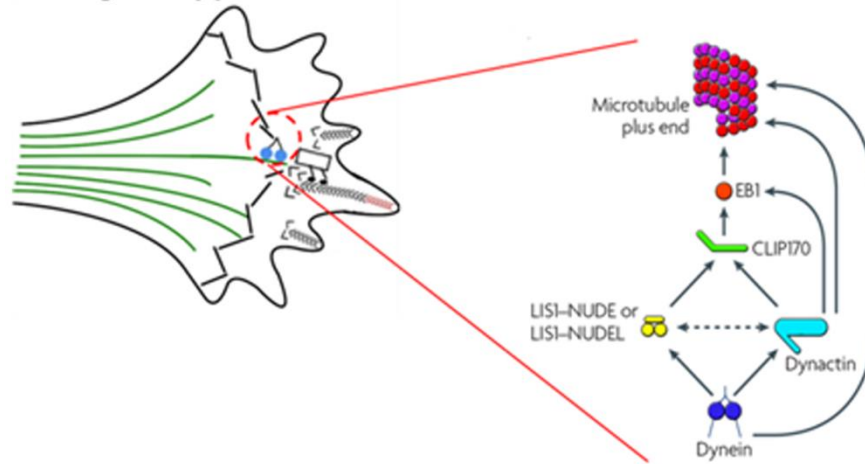
cell imaging of microtubule dynamics at the cell cortex revealed that microtubules experience buckling as a result of being compressively loaded. Those microtubules were shown to be reinforced by the cytoskeletal actin network to attenuate their buckling and therefore to sustain the compressive forces (Brangwynne et al. 2006). This interaction between actin filaments and microtubules is mediated by cross-linking proteins which probably involves cytoplasmic dynein. In addition to its role in transporting cargo towards the nucleus, cytoplasmic dynein is involved in linking microtubules to the cell cortex which in turn facilitates transporting cargo from the cell centre to the periphery and vice versa. This requires dynein to stabilize itself by interacting with cortical proteins in order to exert a pulling force to hold microtubules and therefore to control microtubule growth and dynamics (Laan et al. 2012). Furthermore, inhibition of dynein or its binding partner LIS1 blocks microtubule transition from the C-domain into the P-domain which in turn results in aberrant growth cone development (Grabham et al. 2007). Thus, the invasion of microtubules into the P-domain is mediated by cytoplasmic dynein, located on the tip of microtubules, by exerting tension on the microtubules. Moreover, the binding of dynein to its regulatory proteins, such as LIS1, contributes to this force production. Interestingly, my experiment showed a similar phenotype to dynein or LIS1 inhibition. Microtubules were almost completely depleted from the P-domain of the *+/-Loa* growth cones (Figure 5.8).

How does the *Loa* mutation affect microtubule stability in the P-domain of growth cones? The mechanism through which the *Loa* mutation causes microtubule depletion in the P-domain remains unidentified. However, I suggest several mechanisms that might be causing this abnormal phenotype. First, it is possible that the *Loa* mutation might affect dynein binding to its regulatory proteins located at the tip of microtubules which therefore affect dynein stability and the force production required to exert tension on microtubules (Figure 6.2, 1). Also, dynein anchorage to the cell cortex might be affected by the *Loa* mutation, which is required for holding microtubules as well as for controlling microtubule growth and dynamics in the growth cones (Figure 6.2, 2). In addition, the establishment of point contacts prevents the retrograde flow of actin, hence promoting the advancement of microtubules to the P-domain. This results in

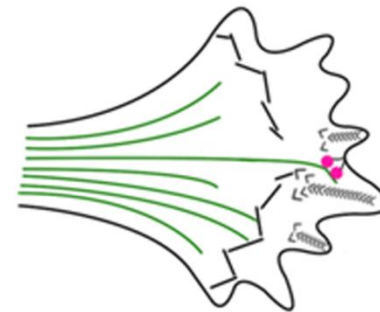
increased levels of active Src kinase at point contacts which therefore promote a strong coupling between point contacts and actin filament. It is therefore possible that the *Loa* mutation might affect point contact formation (Figure 6.2, 3) or it could be a downstream effect of impaired microtubule invasion to the P-domain caused by instability of cytoplasmic dynein at the tip of microtubules (Figure 6.2, 1). Although I could not detect a difference in point contacts between the wild type and *+/Loa* growth cones when immunostained against paxillin (Figure 5.2), further experiments are required to investigate point contacts and paxillin phosphorylation levels in the *Loa/Loa* growth cones.

It was shown by live-cell imaging that in non-neuronal cells, microtubules target focal adhesions at the cell periphery for disassembling focal adhesions (Kaverina, Krylyshkina, and Small 1999). This disassembly is important for limiting adhesions at the cell front and to promote trailing back of the cell during cell migration. Two mechanisms were proposed by which microtubules might promote focal adhesion disassembly (Palazzo and Gundersen 2002): 1) Microtubules might transport factors to or away from focal adhesions. In this regard, the cytoplasmic dynein, located at the microtubule plus tip, may interact with those factors and transport them away from focal adhesion which results in promoting focal adhesion turn-over. 2) Focal adhesion disassembly can be mediated by inhibition of GEF-H1 (a Rho guanine exchange factor) and suppression of its nucleotide exchange activity through binding to microtubules. It is known that active Rho increases cell contractility which therefore promotes focal adhesion formation (Chrzanowska-wodnicka and Burridge 1996). It was also observed that binding of GEF-H1 to microtubules inhibits its Rho-GTP exchange activity (Krendel, Zenke, and Bokoch 2002). Interestingly, Meiri et al have shown that this binding happens in a cytoplasmic dynein-dependent manner. Lfc (the murine homologue of GEF-H1) is located on microtubules through its binding to Tctex1, the DLC subunit of cytoplasmic dynein (Meiri et al. 2012). Through this binding, Tctex1 represses Lfc nucleotide exchange activity. It is possible that the increased binding affinity between DIC and Tctex1 (Deng et al. 2010), which is caused by the *Loa* mutation, might lead to conformational changes which might impede the Lfc binding site.

Figure 6.2 1) *Loa* mutation might affect dynein binding to its regulatory proteins



2) Dynein anchorage to the cell cortex might be affected



3) *Loa* mutation might affect point contact formation

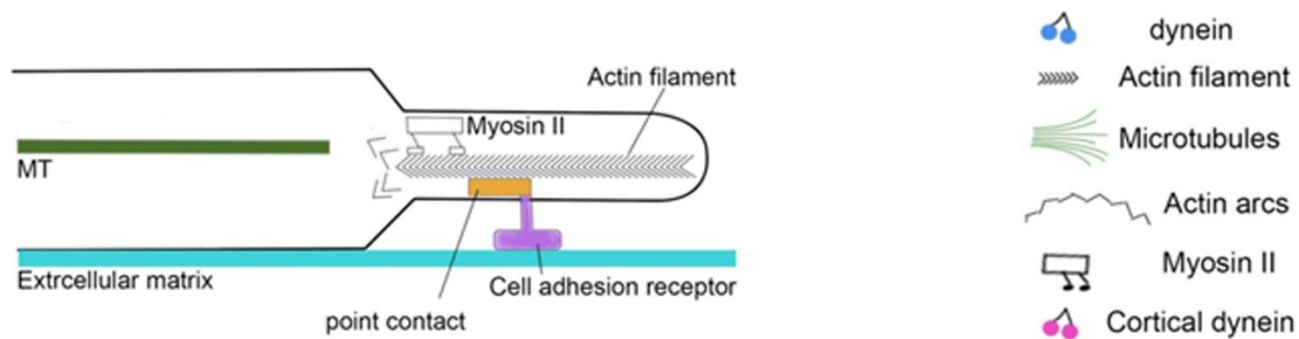


Figure 6.2 – Possible mechanisms underlying the effects the *Loa* mutation has on microtubule stability in the P-domain of growth cones.

6.7 Conclusion

The data presented in this thesis have advanced our understanding of the roles of mutant forms of TDP-43 and cytoplasmic dynein in ALS and SMA-LED respectively which therefore may help us to identify potential causal pathways leading to neurodegeneration. Our understanding may bring us closer to finding a cure for these types of neurological diseases or to developing treatments which at least would be able to slow down these diseases.

My data provide novel insights into the mechanisms underlying the neurotoxic effects of mutations in TDP-43 in the pathology of ALS. The data show for the first time a novel role of TDP-43 in alternative translation. The ALS-associated mutation A315T in TDP-43 affects the expression level of the alternative translated isoform of peripherin per45 leading to a change in the stability of the peripherin network. Further experiments are required to investigate this role in human tissue from patients with ALS and to further investigate other alternative translated isoforms with neurological functions. Moreover, the analysis of expression levels of the glutamate transporter isoforms reveals a significant down-regulation of the neuronal isoform GLT-1B. As a result, this might lead to excitotoxicity due to increased glutamate levels and ultimately to neurodegeneration.

My data also provide further understanding of the role of cytoplasmic dynein in endocytic trafficking and signalling. The data show that the induction of c-Fos upon serum starvation and/or growth factor stimulation is ERK1/2 dependent. Moreover, activation of autophagy is reduced in mouse motor neurons with a mutation in the cytoplasmic dynein heavy chain subunit (*Dync1h1*^{+/*Phe580Tyr*}) suggesting a role for dynein in this process.

In addition, the data suggest a novel pathway underlying the molecular pathogenesis of SMA-LED, caused by mutations in the cytoplasmic dynein heavy chain subunit, which is likely to involve growth cone development and axonal pathfinding.

References

- Aguirre, T, L Van Den Bosch, K Goetschalckx, P Tilkin, G Mathijs, J J Cassiman, and W Robberecht. 1998. "Increased Sensitivity of Fibroblasts from Amyotrophic Lateral Sclerosis Patients to Oxidative Stress." *Annals of Neurology* 43 (4) (April): 452–7.
- AK, Afifi, FP Aleu, J Goodgold, and B MacKay. 1966. "Ultrastructure of Atrophic Muscle in Amyotrophic Lateral Sclerosis." *Neurology* 16 (5): 475–81.
- Al-Chalabi, Ammar, Peter M Andersen, Peter Nilsson, Barry Chioza, Jörgen L Andersson, Carsten Russ, Christopher E Shaw, John F Powell, and P Nigel Leigh. 1999. "Deletions of the Heavy Neurofilament Subunit Tail in Amyotrophic Lateral Sclerosis." *Human Molecular Genetics* 8 (February): 157–64.
- Almeida, R D, B J Manadas, C V Melo, J R Gomes, C S Mendes, M M Grãos, R F Carvalho, a P Carvalho, and C B Duarte. 2005. "Neuroprotection by BDNF against Glutamate-Induced Apoptotic Cell Death Is Mediated by ERK and PI3-Kinase Pathways." *Cell Death and Differentiation* 12 (October): 1329–43.
- Aniento, F, N Emans, G Griffiths, and J Gruenberg. 1993. "Cytoplasmic Dynein-Dependent Vesicular Transport from Early to Late Endosomes." *The Journal of Cell Biology* 123 (6 Pt 1) (December): 1373–87.
- Applegate, Kathryn T, Sebastien Besson, Alexandre Matov, Maria H Bagonis, Khuloud Jaqaman, and Gaudenz Danuser. 2011. "plusTipTracker: Quantitative Image Analysis Software for the Measurement of Microtubule Dynamics." *Journal of Structural Biology* 176 (2) (November): 168–84. doi:10.1016/j.jsb.2011.07.009. <http://www.pubmedcentral.nih.gov/articlerender.fcgi?artid=3298692&tool=pmcentrez&rendertype=abstract>.
- Arnold, Eveline S, Shuo-Chien Ling, Stephanie C Huelga, Clotilde Lagier-Tourenne, Magdalini Polymenidou, Dara Ditsworth, Holly B Kordasiewicz, et al. 2013. "ALS-Linked TDP-43 Mutations Produce Aberrant RNA Splicing and Adult-Onset Motor Neuron Disease without Aggregation or Loss of Nuclear TDP-43." *Proceedings of the National Academy of Sciences of the United States of America* 110 (8) (February 19): E736–45.
- Atwal, Jasvinder K, Bernard Massie, Freda D Miller, and David R Kaplan. 2000. "The TrkB-Shc Site Signals Neuronal Survival and Local Axon Growth via MEK and PI3-Kinase." *Neuron* 27 (8): 265–277.
- Ayala, Youhna M, Laura De Conti, S Eréndira Avendaño-Vázquez, Ashish Dhir, Maurizio Romano, Andrea D'Ambrogio, James Tollervey, et al. 2011. "TDP-43 Regulates Its mRNA Levels through a Negative Feedback Loop." *The EMBO Journal* 30 (2) (January 19): 277–88.

- Ayala, Youhna M, Paola Zago, Andrea D'Ambrogio, Ya-Fei Xu, Leonard Petrucelli, Emanuele Buratti, and Francisco E Baralle. 2008. "Structural Determinants of the Cellular Localization and Shuttling of TDP-43." *Journal of Cell Science* 121 (Pt 22) (November 15): 3778–85.
- Barber, Siân C, and Pamela J Shaw. 2010. "Oxidative Stress in ALS: Key Role in Motor Neuron Injury and Therapeutic Target." *Free Radical Biology & Medicine* 48 (5) (March 1): 629–41.
- Bazley, L a, and W J Gullick. 2005. "The Epidermal Growth Factor Receptor Family." *Endocrine-Related Cancer* 12 (July): S17–27.
- Bellis, Susan L, John T Miller, and Christopher E Turner. 1995. "Characterization of Tyrosine Phosphorylation of Paxillin in Vitro by Focal Adhesion Kinase.pdf." *The Journal of Biological Chemistry* 270 (29): 17437–17441.
- Bentley, David, and Alma Toroian-Raymond. 1986. "Disoriented Pathfinding by Pioneer Neurone Growth Cones Deprived of Filopodia by Cytochalasin Treatment." *Letters to Nature* 323: 712–715.
- Bhatnagar, Subhash. 2001. *Neuroscience for the Study of Communicative Disorders*. Second Edi.
- Bonnal, Sophie, Frédéric Pileur, Cécile Orsini, Fabienne Parker, Françoise Pujol, Anne-Catherine Prats, and Stéphan Vagner. 2005. "Heterogeneous Nuclear Ribonucleoprotein A1 Is a Novel Internal Ribosome Entry Site Trans-Acting Factor That Modulates Alternative Initiation of Translation of the Fibroblast Growth Factor 2 mRNA." *The Journal of Biological Chemistry* 280 (6) (February 11): 4144–53.
- Borchelt, D R, P C Wong, M W Becher, C a Pardo, M K Lee, Z S Xu, G Thinakaran, et al. 1998. "Axonal Transport of Mutant Superoxide Dismutase 1 and Focal Axonal Abnormalities in the Proximal Axons of Transgenic Mice." *Neurobiology of Disease* 5 (1) (July): 27–35.
- Bradley, Lloyd J, Jan-Willem Taanman, Constantinos Kallis, and Richard W Orrell. 2009. "Increased Sensitivity of Myoblasts to Oxidative Stress in Amyotrophic Lateral Sclerosis Peripheral Tissues." *Experimental Neurology* 218 (1) (July): 92–7.
- Brangwynne, Clifford P, Frederick C MacKintosh, Sanjay Kumar, Nicholas a Geisse, Jennifer Talbot, L Mahadevan, Kevin K Parker, Donald E Ingber, and David a Weitz. 2006. "Microtubules Can Bear Enhanced Compressive Loads in Living Cells because of Lateral Reinforcement." *The Journal of Cell Biology* 173 (5) (June 5): 733–41.
- Brown, Michael C, Joseph A Perrotta, and Christopher E Turner. 1998. "Serine and Threonine Phosphorylation of the Paxillin LIM Domains Regulates Paxillin Focal

Adhesion Localization and Cell Adhesion to Fibronectin." *Molecular Biology of the Cell* 9 (7): 1803–1816.

Brown, Michael C, and Christopher E Turner. 2004. "Paxillin: Adapting to Change." *Physiological Reviews* 84 (October): 1315–39.

Brown, Michael C, Kip A West, and Christopher E Turner. 2002. "Paxillin-Dependent Paxillin Kinase Linker and p21- Activated Kinase Localization to Focal Adhesions Involves a Multistep Activation Pathway" 13 (May): 1550–1565.

Brugnera, Enrico, Lisa Haney, Cynthia Grimsley, Mingjian Lu, Scott F Walk, Annie-Carole Tosello-Tramont, Ian G Macara, Hiten Madhani, Gerald R Fink, and Kodimangalam S Ravichandran. 2002. "Unconventional Rac-GEF Activity Is Mediated through the Dock180-ELMO Complex." *Nature Cell Biology* 4 (August): 574–82.

Bucci, Cecilia, Oddmund Bakke, and Cinzia Progida. 2012. "Charcot-Marie-Tooth Disease and Intracellular Traffic." *Progress in Neurobiology* 99 (3) (December): 191–225. doi:10.1016/j.pneurobio.2012.03.003.

Buratti, E, and F E Baralle. 2001. "Characterization and Functional Implications of the RNA Binding Properties of Nuclear Factor TDP-43, a Novel Splicing Regulator of CFTR Exon 9." *The Journal of Biological Chemistry* 276 (39) (September 28): 36337–43.

Buratti, Emanuele, Antonia Brindisi, Maurizio Giombi, Sergio Tisminetzky, Youhna M Ayala, and Francisco E Baralle. 2005. "TDP-43 Binds Heterogeneous Nuclear Ribonucleoprotein A/B through Its C-Terminal Tail: An Important Region for the Inhibition of Cystic Fibrosis Transmembrane Conductance Regulator Exon 9 Splicing." *The Journal of Biological Chemistry* 280 (45) (November 11): 37572–84.

Burgess, Stan A, Matt L Walker, Hitoshi Sakakibara, Peter J Knight, and Kazuhiro Oiwa. 2003. "Dynein Structure and Power Stroke." *Nature* 421 (2): 715–718.

Burnette, Dylan T, Lin Ji, Andrew W Schaefer, Nelson a Medeiros, Gaudenz Danuser, and Paul Forscher. 2008. "Myosin II Activity Facilitates Microtubule Bundling in the Neuronal Growth Cone Neck." *Developmental Cell* 15 (1) (July): 163–9.

Burnette, Dylan T, Andrew W Schaefer, Lin Ji, Gaudenz Danuser, and Paul Forscher. 2007. "Filopodial Actin Bundles Are Not Necessary for Microtubule Advance into the Peripheral Domain of Aplysia Neuronal Growth Cones." *Nature Cell Biology* 9 (12) (December): 1360–9.

Caccamo, Antonella, Smita Majumder, and Salvatore Oddo. 2012. "Cognitive Decline Typical of Frontotemporal Lobar Degeneration in Transgenic Mice Expressing the 25-kDa C-Terminal Fragment of TDP-43." *The American Journal of Pathology* 180 (1) (January): 293–302.

- Cannon, Ashley, Baoli Yang, Joshua Knight, Ian M Farnham, Yongjie Zhang, Charles a Wuertzer, Simon D'Alton, et al. 2012. "Neuronal Sensitivity to TDP-43 Overexpression Is Dependent on Timing of Induction." *Acta Neuropathologica* 123 (6) (June): 807–23.
- Carlson, Neil R. 2012. *Physiology of Behavior*. 11TH Inter. U.S.A.: Pearson Education.
- Carter, Andrew P, Carol Cho, Lan Jin, and Ronald D Vale. 2011. "Crystal Structure of the Dynein Motor Domain." *Science* 331 (6021): 1159–1165.
- Cary, Leslie A, Dong Cho Han, Thomas R Polte, Steven K Hanks, and Jun-lin Guan. 1998. "Identification of p130Cas as a Mediator of Focal Adhesion Kinase-Promoted Cell Migration." *The Journal of Cell Biology* 140 (1): 211–221.
- Cervenakova, L, I I Protas, A Hirano, V I Votiakov, M K Nedzved, N D Kolomiets, I Taller, et al. 2000. "Progressive Muscular Atrophy Variant of Familial Amyotrophic Lateral Sclerosis (PMA/ALS)." *Journal of the Neurological Sciences* 177 (2) (August 15): 124–30.
- Chen, Ai, Li-Jing Xiong, Yu Tong, and Meng Mao. 2013. "Neuroprotective Effect of Brain-Derived Neurotrophic Factor Mediated by Autophagy through the PI3K/Akt/mTOR Pathway." *Molecular Medicine Reports* 8 (4) (October): 1011–1016.
- Chen, Hong-Chen, PaulA Appeddu, J Thomas Parsons, Jeffrey D Hildebrand, Michael D Schaller, and Jun-lin Guan. 1995. "Interaction of Focal Adhesion Kinase with Cytoskeletal Protein Talin." *The Journal of Biological Chemistry* 270 (28): 16995–16999.
- Chen, Sheng, Pavani Sayana, Xiaojie Zhang, and Weidong Le. 2013. "Genetics of Amyotrophic Lateral Sclerosis: An Update." *Molecular Neurodegeneration* 8 (1) (January): 28.
- Chen, Xiang-Jun, Eleni N Levedakou, Kathleen J Millen, Robert L Wollmann, Betty Soliven, and Brian Popko. 2007. "Proprioceptive Sensory Neuropathy in Mice with a Mutation in the Cytoplasmic Dynein Heavy Chain 1 Gene." *The Journal of Neuroscience : The Official Journal of the Society for Neuroscience* 27 (52) (December 26): 14515–24.
- Chong, Curtis R, and Pasi a Jänne. 2013. "The Quest to Overcome Resistance to EGFR-Targeted Therapies in Cancer." *Nature Medicine* 19 (11) (November): 1389–400.
- Chrzanowska-wodnicka, Magdalena, and Keith Burridge. 1996. "Rho-Stimulated Contractility Drives the Formation of Stress Fibers and Focal Adhesions." *The Journal of Cell Biology* 133 (6): 1403–1415.
- Cogli, Laura, Cinzia Progidà, Claire L Thomas, Bradley Spencer-Dene, Claudia Donno, Giampietro Schiavo, and Cecilia Bucci. 2012. "Charcot-Marie-Tooth Type 2B

- Disease-Causing RAB7A Mutant Proteins Show Altered Interaction with the Neuronal Intermediate Filament Peripherin." *Acta Neuropathologica* 125 (2) (November 23): 257–272.
- Colombrita, Claudia, Eleonora Zennaro, Claudia Fallini, Markus Weber, Andreas Sommacal, Emanuele Buratti, Vincenzo Silani, and Antonia Ratti. 2009. "TDP-43 Is Recruited to Stress Granules in Conditions of Oxidative Insult." *Journal of Neurochemistry* 111 (4) (November): 1051–61.
- Corbit, Kevin C, David A Foster, and Marsha Rich Rosner. 1999. "Protein Kinase C ζ Mediates Neurogenic but Not Mitogenic Activation of Mitogen-Activated Protein Kinase in Neuronal Cells." *Molecular and Cellular Biology* 19 (6): 4209–4218.
- Corbo, M, and a P Hays. 1992. "Peripherin and Neurofilament Protein Coexist in Spinal Spheroids of Motor Neuron Disease." *Journal of Neuropathology and Experimental Neurology* 51 (5) (September): 531–7.
- Corrado, Lucia, Yari Carlomagno, Luca Falasco, Simona Mellone, Michela Godi, Emanuela Cova, Cristina Cereda, Lucia Testa, Letizia Mazzini, and Sandra D'Alfonso. 2011. "A Novel Peripherin Gene (PRPH) Mutation Identified in One Sporadic Amyotrophic Lateral Sclerosis Patient." *Neurobiology of Aging* 32 (3) (March): 552.e1–6.
- Cox, Laura E, Laura Ferraiuolo, Emily F Goodall, Paul R Heath, Adrian Higginbottom, Heather Mortiboys, Hannah C Hollinger, et al. 2010. "Mutations in CHMP2B in Lower Motor Neuron Predominant Amyotrophic Lateral Sclerosis (ALS)." *PloS One* 5 (3) (January): e9872.
- D'Alton, Simon, Marcelle Altshuler, Ashley Cannon, Dennis W Dickson, Leonard Petrucelli, and Jada Lewis. 2014. "Divergent Phenotypes in Mutant TDP-43 Transgenic Mice Highlight Potential Confounds in TDP-43 Transgenic Modeling." *PloS One* 9 (1) (January): e86513.
- D'Ambrogio, Andrea, Emanuele Buratti, Cristiana Stuari, Corrado Guarnaccia, Maurizio Romano, Youhna M Ayala, and Francisco E Baralle. 2009. "Functional Mapping of the Interaction between TDP-43 and hnRNP A2 in Vivo." *Nucleic Acids Research* 37 (12) (July): 4116–26.
- Dal Canto, Mauro C, and Mark E Gurney. 1994. "Short Communication Development of Central Nervous System Pathology in a Murine Transgenic Model of Human Amyotrophic Lateral Sclerosis." *American Journal of Pathology* 145 (6): 1271–1279.
- Deng, Wenhan, Caroline Garrett, Benjamin Dombert, Violetta Soura, Gareth Banks, Elizabeth M C Fisher, Marcel P van der Brug, and Majid Hafezparast. 2010. "Neurodegenerative Mutation in Cytoplasmic Dynein Alters Its Organization and

- Dynein-Dynactin and Dynein-Kinesin Interactions." *The Journal of Biological Chemistry* 285 (51) (December 17): 39922–34.
- Dent, Erik W, Stephanie L Gupton, and Frank B Gertler. 2011. "The Growth Cone Cytoskeleton in Axon Outgrowth and Guidance." *Cold Spring Harbor Perspectives in Biology* 3 (3) (March): 1–39.
- Deramaudt, Thérèse B, Denis Dujardin, Fanny Noulet, Sophie Martin, Romain Vauchelles, Ken Takeda, and Philippe Rondé. 2014. "Altering FAK-Paxillin Interactions Reduces Adhesion, Migration and Invasion Processes." *PloS One* 9 (3) (January): e92059.
- Diskin, Ron, Mario Lebediker, David Engelberg, and Oded Livnah. 2007. "Structures of p38alpha Active Mutants Reveal Conformational Changes in L16 Loop That Induce Autophosphorylation and Activation." *Journal of Molecular Biology* 365 (1) (January 5): 66–76.
- Doherty, Gary J, and Harvey T McMahon. 2009. "Mechanisms of Endocytosis." *Annual Review of Biochemistry* 78 (January): 857–902.
- Driskell, Owen J, Aleksandr Mironov, Victoria J Allan, and Philip G Woodman. 2007. "Dynein Is Required for Receptor Sorting and the Morphogenesis of Early Endosomes." *Nature Cell Biology* 9 (1) (January): 113–20.
- Duman, Ronald S, and Bhavya Voleti. 2012. "Signaling Pathways Underlying the Pathophysiology and Treatment of Depression: Novel Mechanisms for Rapid-Acting Agents." *Trends in Neurosciences* 35 (1) (January): 47–56.
- Dupuis, Luc, Anissa Fergani, Kerstin E Braunstein, Judith Eschbach, Nathalie Holl, Frédérique Rene, Jose-Luis Gonzalez De Aguilar, et al. 2009. "Mice with a Mutation in the Dynein Heavy Chain 1 Gene Display Sensory Neuropathy but Lack Motor Neuron Disease." *Experimental Neurology* 215 (1) (January): 146–52.
- Eriksson, Krister S, Shengwen Zhang, Ling Lin, Roxanne C Larivière, Jean-Pierre Julien, and Emmanuel Mignot. 2008. "The Type III Neurofilament Peripherin Is Expressed in the Tuberomammillary Neurons of the Mouse." *BMC Neuroscience* 9 (January): 26.
- Ferguson, Toby a, and Lauren B Elman. 2007. "Clinical Presentation and Diagnosis of Amyotrophic Lateral Sclerosis." *NeuroRehabilitation* 22 (6) (January): 409–16.
- Fischer, Lindsey R, Anissa Igoudjil, Jordi Magrané, Yingjie Li, Jason M Hansen, Giovanni Manfredi, and Jonathan D Glass. 2011. "SOD1 Targeted to the Mitochondrial Intermembrane Space Prevents Motor Neuropathy in the Sod1 Knockout Mouse." *Brain : A Journal of Neurology* 134 (Pt 1) (January): 196–209.

- Flomen, Rachel, and Andrew Makoff. 2011. "Increased RNA Editing in EAAT2 Pre-mRNA from Amyotrophic Lateral Sclerosis Patients: Involvement of a Cryptic Polyadenylation Site." *Neuroscience Letters* 497 (2) (June 22): 139–43.
- Flowers, J M, J F Powell, P N Leigh, P Andersen, and C E Shaw. 2001. "Intron 7 Retention and Exon 9 Skipping EAAT2 mRNA Variants Are Not Associated with Amyotrophic Lateral Sclerosis." *Annals of Neurology* 49 (5) (May): 643–9.
- Foran, Emily, and Davide Trotti. 2009. "Glutamate Transporters and the Excitotoxic Path to Motor Neuron Degeneration in Amyotrophic Lateral Sclerosis." *Antioxidants & Redox Signaling* 11 (7) (July): 1587–602.
- Fumagalli, Elena, Marcella Funicello, Thomas Rauen, Marco Gobbi, and Tiziana Mennini. 2008. "Riluzole Enhances the Activity of Glutamate Transporters GLAST, GLT1 and EAAC1." *European Journal of Pharmacology* 578 (2-3) (January 14): 171–6.
- Garrett, Caroline A, Muruj Barri, Anna Kuta, Violetta Soura, Wenhan Deng, Elizabeth M C Fisher, Giampietro Schiavo, and Majid Hafezparast. 2014. "DYNC1H1 Mutation Alters Transport Kinetics and ERK1/2-cFos Signalling in a Mouse Model of Distal Spinal Muscular Atrophy." *Brain : A Journal of Neurology* 137 (7) (July): 1883–93.
- Gendron, T F, K a Josephs, and L Petrucelli. 2010. "Review: Transactive Response DNA-Binding Protein 43 (TDP-43): Mechanisms of Neurodegeneration." *Neuropathology and Applied Neurobiology* 36 (2) (April): 97–112.
- Giannone, Grégory, Benjamin J Dubin-Thaler, Olivier Rossier, Yunfei Cai, Oleg Chaga, Guoying Jiang, William Beaver, et al. 2007. "Lamellipodial Actin Mechanically Links Myosin Activity with Adhesion-Site Formation." *Cell* 128 (3) (February 9): 561–75.
- Goldman, Robert D, Boris Grin, Melissa G Mendez, and Edward R Kuczmarski. 2011. "Intermediate Filaments: Versatile Building Blocks of Cell Structure." *Current Opinion in Cell Biology* 20 (1): 28–34.
- Gomez, Timothy M, and Paul C Letourneau. 2014. "Actin Dynamics in Growth Cone Motility and Navigation." *Journal of Neurochemistry* 129 (2) (April): 221–34.
- Grabham, Peter W, Garrett E Seale, Malika Bennecib, Daniel J Goldberg, and Richard B Vallee. 2007. "Cytoplasmic Dynein and LIS1 Are Required for Microtubule Advance during Growth Cone Remodeling and Fast Axonal Outgrowth." *The Journal of Neuroscience : The Official Journal of the Society for Neuroscience* 27 (21) (May 23): 5823–34.
- Gros-Louis, François, Roxanne Larivière, Geneviève Gowing, Sandra Laurent, William Camu, Jean-Pierre Bouchard, Vincent Meininger, Guy a Rouleau, and Jean-Pierre Julien. 2004. "A Frameshift Deletion in Peripherin Gene Associated with

Amyotrophic Lateral Sclerosis." *The Journal of Biological Chemistry* 279 (44) (October 29): 45951–6.

Gurney, M E, H Pu, a Y Chiu, M C Dal Canto, C Y Polchow, D D Alexander, J Caliendo, A Hentati, Y W Kwon, and H X Deng. 1994. "Motor Neuron Degeneration in Mice That Express a Human Cu,Zn Superoxide Dismutase Mutation." *Science (New York, N.Y.)* 264 (5166) (June 17): 1772–5.

Hafezparast, Majid, Rainer Klocke, Christiana Ruhrberg, Andreas Marquardt, Azlina Ahmad-Annuar, Samantha Bowen, Giovanna Lalli, et al. 2003. "Mutations in Dynein Link Motor Neuron Degeneration to Defects in Retrograde Transport." *Science (New York, N.Y.)* 300 (5620) (May 2): 808–12.

Hall, Jessica E, Wei Fu, and Michael D Schaller. 2011. "Focal Adhesion Kinase: Exploring Fak Structure to Gain Insight into Function." *International Review of Cell and Molecular Biology* 288 (January): 185–225.

Hara, Taichi, Kenji Nakamura, Makoto Matsui, Akitsugu Yamamoto, Yohko Nakahara, Rika Suzuki-Migishima, Minesuke Yokoyama, et al. 2006. "Suppression of Basal Autophagy in Neural Cells Causes Neurodegenerative Disease in Mice." *Nature* 441 (7095) (June 15): 885–9.

Harms, M B, K M Ori-McKenney, M Scoto, E P Tuck, S Bell, D Ma, S Masi, et al. 2012. "Mutations in the Tail Domain of DYNC1H1 Cause Dominant Spinal Muscular Atrophy." *Neurology* 78 (22) (May 29): 1714–20.

Highley, J Robin, Janine Kirby, Joeri a Jansweijer, Philip S Webb, Channa a Hewamadduma, Paul R Heath, Adrian Higginbottom, et al. 2014. "Loss of Nuclear TDP-43 in ALS Causes Altered Expression of Splicing Machinery and Widespread Dysregulation of RNA Splicing in Motor Neurons." *Neuropathology and Applied Neurobiology* 40 (6) (April 18): 670–85.

Hildebrand, Jeffrey D, Michael D Schaller, and J Thomas Parsons. 1995. "Paxillin , a Tyrosine Phosphorylated Focal Adhesion- Associated Protein Binds to the Carboxyl Terminal Domain of Focal Adhesion Kinase." *Molecular Biology of the Cell* 6 (June): 637–647.

HIROKAWA, NOBUTAKA, and YASUKO NODA. 2008. "Intracellular Transport and Kinesin Superfamily Proteins , KIFs : Structure , Function , and Dynamics." *Physiological Reviews* 88 (3): 1089–1118.

Hirokawa, Nobutaka, Yasuko Noda, Yosuke Tanaka, and Shinsuke Niwa. 2009. "Kinesin Superfamily Motor Proteins and Intracellular Transport." *Nature Reviews. Molecular Cell Biology* 10 (10) (October): 682–96.

Höök, Peter, and Richard B Vallee. 2006. "The Dynein Family at a Glance." *Journal of Cell Science* 119 (Pt 21) (November 1): 4369–71.

- Huang, Eric J, and Louis F Reichardt. 2003. "Trk Receptors: Roles in Neuronal Signal Transduction." *Annual Review of Biochemistry* 72 (January): 609–42.
- Igaz, Lionel M, Linda K Kwong, Edward B Lee, Alice Chen-plotkin, Eric Swanson, Travis Unger, Joe Malunda, et al. 2011. "Dysregulation of the ALS-Associated Gene TDP-43 Leads to Neuronal Death and Degeneration in Mice." *The Journal of Clinical Investigation* 121 (2).
- Iguchi, Yohei, Masahisa Katsuno, Jun-ichi Niwa, Shinnosuke Takagi, Shinsuke Ishigaki, Kensuke Ikenaka, Kaori Kawai, et al. 2013. "Loss of TDP-43 Causes Age-Dependent Progressive Motor Neuron Degeneration." *Brain : A Journal of Neurology* 136 (5): 1371–1382.
- Ikenaka, Kensuke, Masahisa Katsuno, Kaori Kawai, Shinsuke Ishigaki, Fumiaki Tanaka, and Gen Sobue. 2012. "Disruption of Axonal Transport in Motor Neuron Diseases." *International Journal of Molecular Sciences* 13 (1) (January): 1225–38.
- Ilić, D, Y Furuta, S Kanazawa, N Takeda, K Sobue, N Nakatsuji, S Nomura, J Fujimoto, M Okada, and T Yamamoto. 1995. "Reduced Cell Motility and Enhanced Focal Adhesion Contact Formation in Cells from FAK-Deficient Mice." *Nature* 377 (6549) (October 12): 539–44.
- Ishibe, Shuta, Dominique Joly, Xiaolei Zhu, Lloyd G Cantley, and New Haven. 2003. "Association Mediates Hepatocyte Growth Factor-Stimulated Epithelial Morphogenesis." *Molecular Cell* 12: 1275–1285.
- Janssens, Jonathan, Hans Wils, Gernot Kleinberger, Geert Joris, Ivy Cuijt, Chantal Ceuterick-de Groote, Christine Van Broeckhoven, and Samir Kumar-Singh. 2013. "Overexpression of ALS-Associated p.M337V Human TDP-43 in Mice Worsens Disease Features Compared to Wild-Type Human TDP-43 Mice." *Molecular Neurobiology* 48 (1) (August): 22–35.
- Joyce, Peter I, Pietro Fratta, Elizabeth M C Fisher, and Abraham Acevedo-Arozena. 2011. "SOD1 and TDP-43 Animal Models of Amyotrophic Lateral Sclerosis: Recent Advances in Understanding Disease toward the Development of Clinical Treatments." *Mammalian Genome : Official Journal of the International Mammalian Genome Society* 22 (7-8) (August): 420–48.
- Juhasz, Gabor. 2012. "Interpretation of Bafilomycin, pH Neutralizing or Protease Inhibitor Treatments in Autophagic Flux Experiments." *Autophagy* 8 (12): 1875–1876.
- Julien, Jean-Pierre, and Jasna Kriz. 2006. "Transgenic Mouse Models of Amyotrophic Lateral Sclerosis." *Biochimica et Biophysica Acta* 1762 (11-12): 1013–24.
- Kabashi, Edor, Paul N Valdmanis, Patrick Dion, Dan Spiegelman, Brendan J McConkey, Christine Vande Velde, Jean-Pierre Bouchard, et al. 2008. "TARDBP Mutations in Individuals with Sporadic and Familial Amyotrophic Lateral

- Sclerosis." *Nature Genetics* 40 (5) (May): 572–4. doi:10.1038/ng.132.
<http://www.ncbi.nlm.nih.gov/pubmed/18372902>.
- Kardon, Julia R, and Ronald D Vale. 2009. "Regulators of the Cytoplasmic Dynein Motor." *Nature Reviews. Molecular Cell Biology* 10 (12) (December): 854–65.
- Katsuno, Masahisa, Fumiaki Tanaka, Hiroaki Adachi, Haruhiko Banno, Keisuke Suzuki, Hirohisa Watanabe, and Gen Sobue. 2012. "Pathogenesis and Therapy of Spinal and Bulbar Muscular Atrophy (SBMA)." *Progress in Neurobiology* 99 (3) (December): 246–56.
- Kaverina, Irina, Olga Krylyshkina, and J Victor Small. 1999. "Microtubule Targeting of Substrate Contacts Promotes Their Relaxation." *The Journal of Cell Biology* 146 (5): 1033–1043.
- Keifer, Orion P, Deirdre M O'Connor, and Nicholas M Boulis. 2014. "Gene and Protein Therapies Utilizing VEGF for ALS." *Pharmacology & Therapeutics* 141 (3) (March): 261–71.
- Kiernan, Mc, Ak Lethlean, and Pw Blum. 1999. "Monomelic Amyotrophy: Non Progressive Atrophy of the Upper Limb." *Journal of Clinical Neuroscience : Official Journal of the Neurosurgical Society of Australasia* 6 (4) (July): 353–355.
- Kimura, Shunsuke, Takeshi Noda, and Tamotsu Yoshimori. 2008. "Dynein-Dependent Movement of Autophagosomes Mediates Efficient Encounters with Lysosomes." *Cell Structure and Function* 33 (1) (January): 109–22.
- Kinsley, Lisa, and Teepu Siddique. 2012. *Amyotrophic Lateral Sclerosis Overview*.
<http://www.ncbi.nlm.nih.gov/books/NBK1450/>.
- Klemke, R L, J Leng, R Molander, P C Brooks, K Vuori, and D a Cheresh. 1998. "CAS/Crk Coupling Serves as a 'Molecular Switch' for Induction of Cell Migration." *The Journal of Cell Biology* 140 (4) (February 23): 961–72.
- Klinghoffer, R a, C Sachsenmaier, J a Cooper, and P Soriano. 1999. "Src Family Kinases Are Required for Integrin but Not PDGFR Signal Transduction." *The EMBO Journal* 18 (9) (May 4): 2459–71.
- Komatsu, Masaaki, Satoshi Waguri, Tomoki Chiba, Shigeo Murata, Jun-ichi Iwata, Isei Tanida, Takashi Ueno, et al. 2006. "Loss of Autophagy in the Central Nervous System Causes Neurodegeneration in Mice." *Nature* 441 (7095) (June 15): 880–4.
- Kon, Takahide, Kazuo Sutoh, and Genji Kurisu. 2011. "X-Ray Structure of a Functional Full-Length Dynein Motor Domain." *Nature Structural & Molecular Biology* 18 (6) (June): 638–42.

- Kraemer, Brian C, Theresa Schuck, Jeanna M Wheeler, Linda C Robinson, John Q Trojanowski, Virginia M Y Lee, and Gerard D Schellenberg. 2010. "Loss of Murine TDP-43 Disrupts Motor Function and Plays an Essential Role in Embryogenesis." *Acta Neuropathologica* 119 (4) (April): 409–19.
- Krendel, Mira, Frank T Zenke, and Gary M Bokoch. 2002. "Nucleotide Exchange Factor GEF-H1 Mediates Cross-Talk between Microtubules and the Actin Cytoskeleton." *Nature Cell Biology* 4 (3): 294–301.
- Laan, Liedewij, Nenad Pavin, Julien Husson, Guillaume Romet-Lemonne, Martijn van Duijn, Magdalena Preciado López, Ronald D Vale, Frank Jülicher, Samara L Reck-Peterson, and Marileen Dogterom. 2012. "Cortical Dynein Controls Microtubule Dynamics to Generate Pulling Forces That Position Microtubule Asters." *Cell* 148 (3) (February 3): 502–14.
- Lagier-Tourenne, Clotilde, Magdalini Polymenidou, and Don W Cleveland. 2010. "TDP-43 and FUS/TLS: Emerging Roles in RNA Processing and Neurodegeneration." *Human Molecular Genetics* 19 (R1) (April 15): R46–64.
- Landon, Françoise, Marguerite Lemonnier, Richard Benarous, Claude Huc, Marc Fisman, François Gros Portier, and Marie-Madeleine Portier. 1989. "Multiple mRNAs Encode Peripherin: A Neural Intermediate Filament Protein." *The EMBO Journal* 8 (6): 1719–1726.
- Landon, Françoise., Annie Wolff, and Beatrice de Nechaud. 2000. "Original Article Mouse Peripherin Isoforms." *Biology of the Cell* 92: 397–407.
- Lattante, Serena, Guy a Rouleau, and Edor Kabashi. 2013. "TARDBP and FUS Mutations Associated with Amyotrophic Lateral Sclerosis: Summary and Update." *Human Mutation* 34 (6) (June): 812–26. doi:10.1002/humu.22319. <http://www.ncbi.nlm.nih.gov/pubmed/23559573>.
- Lawson, Christine, Ssang-Taek Lim, Sean Uryu, Xiao Lei Chen, David a Calderwood, and David D Schlaepfer. 2012. "FAK Promotes Recruitment of Talin to Nascent Adhesions to Control Cell Motility." *The Journal of Cell Biology* 196 (2) (January 23): 223–32.
- Lee, Aih Cheun, and Daniel M Suter. 2008. "Quantitative Analysis of Microtubule Dynamics during Adhesion-Mediated Growth Cone Guidance." *Developmental Neurobiology* 68 (12): 1363–1377.
- Levanon, Ditsa, Judy Lieman-hurwitz, Naomi Dafni, Levana Sherman, and Yael Bernstein. 1985. "Architecture and Anatomy of the Chromosomal Locus in Human Chromosome 21 Encoding the Cu / Zn Superoxide Dismutase K B . ORI-." *The EMBO Journal* 4 (1): 77–84.
- Levy, Jennifer R, and Erika L F Holzbaur. 2010. "Dynein Drives Nuclear Rotation during Forward Progression of Motile Fibroblasts" 121 (Pt 19): 1–18.

- Levy, Jennifer R, Charlotte J Sumner, Juliane P Caviston, Mariko K Tokito, Srikanth Ranganathan, Lee a Ligon, Karen E Wallace, et al. 2006. "A Motor Neuron Disease-Associated Mutation in p150Glued Perturbs Dynactin Function and Induces Protein Aggregation." *The Journal of Cell Biology* 172 (5) (February 27): 733–45.
- Li, Dan, Jian Ding, Xiaozhong Wang, Chengdang Wang, and Ting Wu. 2009. "Fibronectin Promotes Tyrosine Phosphorylation of Paxillin and Cell Invasiveness in the Gastric Cancer Cell Line AGS." *Tumori* 95: 769–779.
- Lin, C L, L a Bristol, L Jin, M Dykes-Hoberg, T Crawford, L Clawson, and J D Rothstein. 1998. "Aberrant RNA Processing in a Neurodegenerative Disease: The Cause for Absent EAAT2, a Glutamate Transporter, in Amyotrophic Lateral Sclerosis." *Neuron* 20 (3) (March): 589–602.
- Liu, Shouchun, William B Kiosses, David M Rose, Marina Slepak, Ravi Salgia, James D Griffin, Christopher E Turner, Martin a Schwartz, and Mark H Ginsberg. 2002. "A Fragment of Paxillin Binds the Alpha 4 Integrin Cytoplasmic Domain (tail) and Selectively Inhibits Alpha 4-Mediated Cell Migration." *The Journal of Biological Chemistry* 277 (23) (June 7): 20887–94.
- Lo Giudice, Temistocle, Federica Lombardi, Filippo Maria Santorelli, Toshitaka Kawai, and Antonio Orlandi. 2014. "Hereditary Spastic Paraplegia: Clinical-Genetic Characteristics and Evolving Molecular Mechanisms." *Experimental Neurology* 261 (June 20): 518–539.
- Logroscino, Giancarlo, Bryan J Traynor, Orla Hardiman, Adriano Chiò, Robert J Swingle, Andrea Millul, Emma Benn, and Ettore Beghi. 2010. "Incidence of Amyotrophic Lateral Sclerosis in Europe." *Journal of Neuronal Neurosurg Psychiatry* 81 (4): 385–390.
- Lowery, Laura Anne, and David Van Vactor. 2009. "The Trip of the Tip : Understanding the Growth Cone Machinery." *Nature Reviews. Molecular Cell Biology* 10 (5): 332–343. doi:10.1038/nrm2679.The.
- Lunn, J Simon, Stacey a Sakowski, Bhumsoo Kim, Andrew a Rosenberg, and Eva L Feldman. 2009. "Vascular Endothelial Growth Factor Prevents G93A-SOD1-Induced Motor Neuron Degeneration." *Developmental Neurobiology* 69 (13) (November): 871–84.
- Mazaki, Yuichi, Hiroshi Uchida, Okio Hino, Shigeru Hashimoto, and Hisataka Sabe. 1998. "Paxillin Isoforms in Mouse." *The Journal of Biological Chemistry* 273 (35): 22435–22441.
- McGoldrick, Philip, Peter I Joyce, Elizabeth M C Fisher, and Linda Greensmith. 2013. "Rodent Models of Amyotrophic Lateral Sclerosis." *Biochimica et Biophysica Acta* 1832 (9) (September): 1421–36.

- McLean, Jesse, Hsueh-Ning Liu, Denise Miletic, Yuan Cheng Weng, Ekaterina Rogaeva, Lorne Zinman, Jasna Kriz, and Janice Robertson. 2010. "Distinct Biochemical Signatures Characterize Peripherin Isoform Expression in Both Traumatic Neuronal Injury and Motor Neuron Disease." *Journal of Neurochemistry* 114 (4) (August): 1177–92.
- McLean, Jesse, Shangxi Xiao, Keigo Miyazaki, and Janice Robertson. 2008. "A Novel Peripherin Isoform Generated by Alternative Translation Is Required for Normal Filament Network Formation." *Journal of Neurochemistry* 104 (6) (March): 1663–73.
- Medeiros, Nelson a, Dylan T Burnette, and Paul Forscher. 2006. "Myosin II Functions in Actin-Bundle Turnover in Neuronal Growth Cones." *Nature Cell Biology* 8 (3) (March): 215–26.
- Meiri, David, Christopher B Marshall, Melissa a Greeve, Bryan Kim, Marc Balan, Fernando Suarez, Chris Bakal, et al. 2012. "Mechanistic Insight into the Microtubule and Actin Cytoskeleton Coupling through Dynein-Dependent RhoGEF Inhibition." *Molecular Cell* 45 (5) (March 9): 642–55.
- Mercado, Pablo Arrisi, Youhna M Ayala, Maurizio Romano, Emanuele Buratti, and Francisco E Baralle. 2005. "Depletion of TDP 43 Overrides the Need for Exonic and Intronic Splicing Enhancers in the Human apoA-II Gene." *Nucleic Acids Research* 33 (18) (January): 6000–10.
- Mesngon, Mariano T, Cataldo Tarricone, Sachin Hebbar, Aimee M Guillotte, E William Schmitt, Lorene Lanier, Andrea Musacchio, Stephen J King, and Deanna S Smith. 2006. "Regulation of Cytoplasmic Dynein ATPase by Lis1." *The Journal of Neuroscience : The Official Journal of the Society for Neuroscience* 26 (7) (February 15): 2132–9.
- Mitchell, David J, Kiev R Blasier, Erin D Jeffery, Mitchell W Ross, Ashok K Pullikuth, Dong Suo, Juyeon Park, et al. 2012. "Trk Activation of the ERK1/2 Kinase Pathway Stimulates Intermediate Chain Phosphorylation and Recruits Cytoplasmic Dynein to Signaling Endosomes for Retrograde Axonal Transport." *The Journal of Neuroscience : The Official Journal of the Society for Neuroscience* 32 (44) (October 31): 15495–510.
- Möhl, Christoph, Norbert Kirchgessner, Claudia Schäfer, Bernd Hoffmann, and Rudolf Merkel. 2012. "Quantitative Mapping of Averaged Focal Adhesion Dynamics in Migrating Cells by Shape Normalization." *Journal of Cell Science* 125 (Pt 1) (January 1): 155–65.
- Monkhouse, W. Stanley. 2007. *Master Medicine: Clinical Anatomy*. Second Edi. Elsevier Health Sciences.

- Moughamian, Armen J, and Erika L F Holzbaur. 2012. *23 – Cytoplasmic Dynein Dysfunction and Neurodegenerative Disease. Dyneins: Structure, Biology and Disease*. Elsevier. <http://dx.doi.org/10.1016/B978-0-12-382004-4.10023-8>.
- Murakami, T, I Nagano, T Hayashi, Y Manabe, M Shoji, Y Setoguchi, and K Abe. 2001. "Impaired Retrograde Axonal Transport of Adenovirus-Mediated E. Coli LacZ Gene in the Mice Carrying Mutant SOD1 Gene." *Neuroscience Letters* 308 (3) (August 10): 149–52.
- Myers, Kenneth a, Irina Tint, C Vidya Nadar, Yan He, Mark M Black, and Peter W Baas. 2006. "Antagonistic Forces Generated by Cytoplasmic Dynein and Myosin-II during Growth Cone Turning and Axonal Retraction." *Traffic (Copenhagen, Denmark)* 7 (10) (October): 1333–51.
- Nicholls, D, and D Atewell. 1990. "The Release and Uptake of Excitatory Amino Acids." *Trends in Pharmacological Sciences* 11 (11): 462–468.
- Niebrój-Dobosz, Irena, Dorota Dziewulska, and Hubert Kwieciński. 2004. "Oxidative Damage to Proteins in the Spinal Cord in Amyotrophic Lateral Sclerosis (ALS)." *Folia Neuropathologica / Association of Polish Neuropathologists and Medical Research Centre, Polish Academy of Sciences* 42 (3) (January): 151–6.
- Noreau, Anne, Patrick a Dion, and Guy a Rouleau. 2014. "Molecular Aspects of Hereditary Spastic Paraplegia." *Experimental Cell Research* 325 (1) (July 1): 18–26.
- Ori-McKenney, Kassandra M, and Richard B Vallee. 2011. "Neuronal Migration Defects in the Loa Dynein Mutant Mouse." *Neural Development* 6 (1) (January): 26.
- Ou, S H, F Wu, D Harrich, L F García-Martínez, and R B Gaynor. 1995. "Cloning and Characterization of a Novel Cellular Protein, TDP-43, That Binds to Human Immunodeficiency Virus Type 1 TAR DNA Sequence Motifs." *Journal of Virology* 69 (6) (June): 3584–96.
- Palazzo, Alexander F, and Gregg G Gundersen. 2002. "Microtubule-Actin Cross-Talk at Focal Adhesions." *Science's STKE : Signal Transduction Knowledge Environment* 2002 (139) (July 2): pe31.
- Parsons, J. T. 2003. "Focal Adhesion Kinase: The First Ten Years." *Journal of Cell Science* 116 (8) (April 15): 1409–1416.
- Pfister, K Kevin, Paresh R Shah, Holger Hummerich, Andreas Russ, James Cotton, Azlina Ahmad Annuar, Stephen M King, and Elizabeth M C Fisher. 2006. "Genetic Analysis of the Cytoplasmic Dynein Subunit Families." *PLoS Genetics* 2 (1) (January): e1.

- Piao, Yue-shan, Koichi Wakabayashi, Akiyoshi Kakita, Mitsunori Yamada, Shin-taro Hayashi, Takashi Morita, Fusahiro Ikuta, Kiyomitsu Oyanagi, and Hitoshi Takahashi. 2003. "Neuropathology with Clinical Correlations of Sporadic Amyotrophic Lateral Sclerosis : 102 Autopsy Cases Examined Between 1962 and 2000." *Brain Pathology* 12: 10–22.
- Ponti, a, M Machacek, S L Gupton, C M Waterman-Storer, and G Danuser. 2004. "Two Distinct Actin Networks Drive the Protrusion of Migrating Cells." *Science (New York, N.Y.)* 305 (5691) (September 17): 1782–6.
- Prior, Thomas W, and Barry S Russman. 2013. *Spinal Muscular Atrophy*. <http://www.ncbi.nlm.nih.gov/books/NBK1352/>.
- Purves, Dale, George J Augustine, David Fitzpatrick, William C Hall, Anthony-Samuel LaMantia, James O McNamara, and Leonard E White. 2008. *Neuroscience*. Fourth Edi. U.S.A.: Sinauer Associates, Inc.
- Ren, Xiang-dong, William B Kiosses, David J Sieg, Carol A Otey, David D Schlaepfer, and Martin Alexander Schwartz. 2000. "Focal Adhesion Kinase Suppresses Rho Activity to Promote Focal Adhesion Turnover." *Journal of Cell Science* 113: 3673–3678.
- Renton, Alan E, Adriano Chiò, and Bryan J Traynor. 2014. "State of Play in Amyotrophic Lateral Sclerosis Genetics." *Nature Neuroscience* 17 (1) (January): 17–23.
- Ricketts, Thomas. 2012. "Assessment of an Allelic Series of Mouse TDP43 Mutations." <http://discovery.ucl.ac.uk/1349526/2/ThomasRickettsThesisBLANKEDIMAGES.pdf>.
- Robberecht, Wim, and Thomas Philips. 2013. "The Changing Scene of Amyotrophic Lateral Sclerosis." *Nature Reviews. Neuroscience* 14 (4) (April): 248–64.
- Robertson, Janice, Mohammad M Doroudchi, Minh Dang Nguyen, Heather D Durham, Michael J Strong, Gerry Shaw, Jean-Pierre Julien, and Walter E Mushynski. 2003. "A Neurotoxic Peripherin Splice Variant in a Mouse Model of ALS." *The Journal of Cell Biology* 160 (6) (March 17): 939–49.
- Rosen, Daniel R, Teepu Siddique, David Patterson, Denise A Figlewicz, Peter Sapp, Afif Nentati, Deirdre Donaldson, et al. 1993. "Mutations in Cu/Zn Superoxide Dismutase Gene Are Associated with Familial Amyotrophic Lateral Sclerosis." *Letters to Nature* 362 (4): 59–62.
- Rosse, Carine, Katrina Boeckeler, Mark Lynch, Simone Radtke, David Frith, Karin Barnouin, Ali Sayed Morsi, Majid Hafezparast, Michael Howell, and Peter J Parker. 2012. "Binding of Dynein Intermediate Chain 2 to Paxillin Controls Focal

- Adhesion Dynamics and Migration." *Journal of Cell Science* 125 (Pt 16) (August 15): 3733–8.
- Rossor, Alexander M, Bernadett Kalmar, Linda Greensmith, and Mary M Reilly. 2012. "The Distal Hereditary Motor Neuropathies." *Journal of Neurology, Neurosurgery, and Psychiatry* 83 (1) (January): 6–14.
- Rothstein, Jeffrey D, Marleen Van Kammen, Allan I Levey, Lee J Martin, and Ralph W Kunc. 1995. "Selective Loss of Glial Glutamate Transporter GLT-1 in Amyotrophic Lateral Sclerosis." *Annals of Neurology* 38 (1): 73–84.
- Rothstein, J D.; Martin, L J.;Kunc, R W. 1992. "Decreased Glutamate Transport by the Brain and Spinal Cord in Amyotrophic Lateral Sclerosis" (326): 1464–1468.
- Rothweiler, Ulli, Espen Åberg, Kenneth a Johnson, Tom E Hansen, Jorunn B Jørgensen, and Richard a Engh. 2011. "p38 α MAP Kinase Dimers with Swapped Activation Segments and a Novel Catalytic Loop Conformation." *Journal of Molecular Biology* 411 (2) (August 12): 474–85.
- Roux, Philippe P, and John Blenis. 2004. "ERK and p38 MAPK-Activated Protein Kinases : A Family of Protein Kinases with Diverse Biological Functions." *Microbiology and Molecular Biology Reviews* 68 (2): 320–344.
- Saccon, Rachele a, Rosie K a Bunton-Stasyshyn, Elizabeth M C Fisher, and Pietro Fratta. 2013. "Is SOD1 Loss of Function Involved in Amyotrophic Lateral Sclerosis?" *Brain : A Journal of Neurology* 136 (Pt 8) (August): 2342–58. doi:10.1093/brain/awt097. <http://www.pubmedcentral.nih.gov/articlerender.fcgi?artid=3722346&tool=pmcentrez&rendertype=abstract>.
- Schaller, M D. 2001. "Paxillin: A Focal Adhesion-Associated Adaptor Protein." *Oncogene* 20 (44) (October 1): 6459–72.
- Schaller, Michael D, and J Thomas Parsons. 1995. "pp125 FAK -Dependent Tyrosine Phosphorylation of Paxillin Creates a High-Affinity Binding Site for Crk." *Molecular and Cellular Biology* 15 (5): 2635–2645.
- Scheswohl, Danielle M, Jessica R Harrell, Zenon Rajfur, Guanghua Gao, Sharon L Campbell, and Michael D Schaller. 2008. "Multiple Paxillin Binding Sites Regulate FAK Function." *Journal of Molecular Signaling* 3 (January): 1.
- Schiavo, Giampietro, Linda Greensmith, Majid Hafezparast, and Elizabeth M C Fisher. 2013. "Cytoplasmic Dynein Heavy Chain: The Servant of Many Masters." *Trends in Neurosciences* 36 (11) (November): 641–51.
- Scoto, Mariacristina, Alexander M Rossor, Matthew B Harms, Sebahattin Cirak, Mattia Calissano, Stephanie Robb, Adnan Y Manzur, et al. 2014. "Novel

Mutations Expand the Clinical Spectrum of Cytoplasmic Dynein Heavy Chain 1 (DYNC1H1)-Associated Spinal Muscular Atrophy." *J. Neurol., In Press*.

Sephton, Chantelle F, Shannon K Good, Stan Atkin, Colleen M Dewey, Paul Mayer, Joachim Herz, and Gang Yu. 2010. "TDP-43 Is a Developmentally Regulated Protein Essential for Early Embryonic Development." *The Journal of Biological Chemistry* 285 (9) (February 26): 6826–34.

Shan, Xiu, Po-Min Chiang, Donald L Price, and Philip C Wong. 2010. "Altered Distributions of Gemini of Coiled Bodies and Mitochondria in Motor Neurons of TDP-43 Transgenic Mice." *Proceedings of the National Academy of Sciences of the United States of America* 107 (37) (September 14): 16325–30.

Shaw, P J, V Forrest, P G Ince, J P Richardson, and H J Wastell. 1995. "CSF and Plasma Amino Acid Levels in Motor Neuron Disease: Elevation of CSF Glutamate in a Subset of Patients." *Neurodegeneration : A Journal for Neurodegenerative Disorders, Neuroprotection, and Neuroregeneration* 4 (2) (June): 209–16.

Sheng, Morgan, Grant Mcfadden, and Michael E Greenberg. 1990. "Membrane Depolarization and Calcium c-Fos Transcription via Phosphorylation of Transcription Factor CREB." *Neuron* 4: 571–582.

Shu, Tianzhi, Ramses Ayala, Minh-dang Nguyen, Zhigang Xie, Joseph G Gleeson, and Li-huei Tsai. 2004. "Ndel1 Operates in a Common Pathway with LIS1 and Cytoplasmic Dynein to Regulate Cortical Neuronal Positioning 77 Avenue Louis Pasteur." *Neuron* 44 (10): 263–277.

Sieg, David J, Christof R Hauck, Dusko Ilic, Candice K Klingbeil, Erik Schaefer, H Caroline, and David D Schlaepfer. 2000. "FAK Integrates Growth-Factor and Integrin Signals to Promote Cell Migration." *Nature Cell Biology* 2 (May): 249–256.

Siegel, Allan, and Hreday N Sapru. 2010. *Essential Neuroscience*. Second Edi. Lippincott Williams and Wilkins.

Siklos, L, J Engelhardt, Y Harati, RG Smith, F Joo, and SH Appel. 1996. "Ultrastructural Evidence for Altered Calcium in Motor Nerve Terminals in Amyotrophic Lateral Sclerosis." *Annals of Neurology* 39 (2): 203–16.

Singer, Mike a, Jeffrey M Statland, Gil I Wolfe, and Richard J Barohn. 2007. "Primary Lateral Sclerosis." *Muscle & Nerve* 35 (3) (March): 291–302.

Spada, Albert La. 2011. *Spinal and Bulbar Muscular Atrophy*.

Sreedharan, Jemeen, Ian P Blair, Vineeta B Tripathi, Xun Hu, Caroline Vance, Steven Ackerley, Jennifer C Durnall, et al. 2008. "All Use Subject to JSTOR Terms and Conditions TDP-43 Mutations Sporadic Amyotrophic Lateral Sclerosis." *Science* 319: 1668–1672.

- Stallings, Nancy R, Krishna Puttaparthi, Christina M Luther, Dennis K Burns, and Jeffrey L Elliott. 2010. "Progressive Motor Weakness in Transgenic Mice Expressing Human TDP-43." *Neurobiology of Disease* 40 (2) (November): 404–14.
- Stanciu, Madalina, Ying Wang, Ruth Kentor, Nancy Burke, Simon Watkins, Geraldine Kress, Ian Reynolds, et al. 2000. "Persistent Activation of ERK Contributes to Glutamate-Induced Oxidative Toxicity in a Neuronal Cell Line and Primary Cortical Neuron Cultures." *Journal of Biological Chemistry* 275 (16) (April 14): 12200–12206.
- Stribl, Carola, Aladin Samara, Dietrich Trümbach, Regina Peis, Manuela Neumann, Helmut Fuchs, Valerie Gailus-Durner, et al. 2014. "Mitochondrial Dysfunction and Decrease in Body Weight of a Transgenic Knock-in Mouse Model for TDP-43." *The Journal of Biological Chemistry* 289 (15) (April 11): 10769–84.
- Strong, Michael J, Kathryn Volkening, Robert Hammond, Wencheng Yang, Wendy Strong, Cheryl Leystra-Lantz, and Christen Shoesmith. 2007. "TDP43 Is a Human Low Molecular Weight Neurofilament (hNFL) mRNA-Binding Protein." *Molecular and Cellular Neurosciences* 35 (2) (June): 320–7.
- Suter, Daniel M, Andrew W Schaefer, Paul Forscher, and New Haven. 2004. "Microtubule Dynamics Are Necessary for Src Family Kinase-Dependent Growth Cone Steering." *Current Biology : CB* 14: 1194–1199.
- Suzuki, Hiroaki, Yoshio Shibagaki, Seisuke Hattori, and Massaki Matsuoka. 2014. "Nuclear TDP-43 Causes Neuronal Toxicity by Escaping from the Inhibitory Regulation by hnRNPs." *Oxford Journals*: 1–51.
- Swarup, Vivek, Daniel Phaneuf, Christine Bareil, Janice Robertson, Guy a Rouleau, Jasna Kriz, and Jean-Pierre Julien. 2011. "Pathological Hallmarks of Amyotrophic Lateral Sclerosis/frontotemporal Lobar Degeneration in Transgenic Mice Produced with TDP-43 Genomic Fragments." *Brain : A Journal of Neurology* 134 (Pt 9) (September): 2610–26.
- T, Atsumi. 1981. "The Ultrastructure of Intramuscular Nerves in Amyotrophic Lateral Sclerosis." *Acta Neuropathologica* 55 (3): 193–8.
- Talacko, a a, and P C Reade. 1990. "Progressive Bulbar Palsy: A Case Report of a Type of Motor Neuron Disease Presenting with Oral Symptoms." *Oral Surgery, Oral Medicine, and Oral Pathology* 69 (2) (February): 182–4.
- Tanaka, E, T Ho, and M W Kirschner. 1995. "The Role of Microtubule Dynamics in Growth Cone Motility and Axonal Growth." *The Journal of Cell Biology* 128 (1-2) (January): 139–55.
<http://www.pubmedcentral.nih.gov/articlerender.fcgi?artid=2120332&tool=pmcentrez&rendertype=abstract>.

- Tanida, Isei, Takashi Ueno, and Eiki Kominami. 2004. "LC3 Conjugation System in Mammalian Autophagy." *The International Journal of Biochemistry & Cell Biology* 36 (12) (December): 2503–18.
- Tojkander, Sari, Gergana Gateva, and Pekka Lappalainen. 2012. "Actin Stress Fibers--Assembly, Dynamics and Biological Roles." *Journal of Cell Science* 125 (Pt 8) (April 15): 1855–64.
- Tollervey, James R, Tomaž Curk, Boris Rogelj, Michael Brieese, Matteo Cereda, Melis Kayikci, Julian König, et al. 2011. "Characterizing the RNA Targets and Position-Dependent Splicing Regulation by TDP-43." *Nature Neuroscience* 14 (4) (April): 452–8.
- Touriol, Christian, Stéphanie Bornes, Sophie Bonnal, Sylvie Audigier, Hervé Prats, Anne-Catherine Prats, and Stéphan Vagner. 2003. "Generation of Protein Isoform Diversity by Alternative Initiation of Translation at Non-AUG Codons." *Biology of the Cell* 95 (3-4) (May 16): 169–178.
- Treisman, Richard. 1992. "The Serum Response Element." *Trends in Biochemical Sciences* 17 (October): 423–426.
- Tsai, Kuen-Jer, Chun-Hung Yang, Yen-Hsin Fang, Kuan-Hung Cho, Wei-Lin Chien, Wei-Ting Wang, Tzu-Wei Wu, Ching-Po Lin, Wen-Mei Fu, and Che-Kun James Shen. 2010. "Elevated Expression of TDP-43 in the Forebrain of Mice Is Sufficient to Cause Neurological and Pathological Phenotypes Mimicking FTLD-U." *The Journal of Experimental Medicine* 207 (8) (August 2): 1661–73.
- Turner, Christopher E, Michael C Brown, Joseph A Perrotta, M C Riedy, Sotiris N Nikolopoulos, A Rosa Mcdonald, Shubha Bagrodia, Sheila Thomas, and Phillip S Leventhal. 1999. "Paxillin LD4 Motif Binds PAK and PIX through a Novel 95-kD Ankyrin Repeat, ARF–GAP Protein: A Role in Cytoskeletal Remodeling" 145 (4): 851–863.
- Tynan, S H, M a Gee, and R B Vallee. 2000. "Distinct but Overlapping Sites within the Cytoplasmic Dynein Heavy Chain for Dimerization and for Intermediate Chain and Light Intermediate Chain Binding." *The Journal of Biological Chemistry* 275 (42) (October 20): 32769–74.
- Vallee, Richard B, Richard J McKenney, and Cassandra M Ori-McKenney. 2012. "Multiple Modes of Cytoplasmic Dynein Regulation." *Nature Cell Biology* 14 (3) (March): 224–30.
- Vallee, Richard B, Garrett E Seale, and Jin-Wu Tsai. 2010. "Emerging Roles for Myosin II and Cytoplasmic Dynein in Migrating Neurons and Growth Cones." *Trends in Cell Biology* 19 (7): 347–355.
- Vallés, Ana M, Maud Beuvin, and Brigitte Boyer. 2004. "Activation of Rac1 by Paxillin-Crk-DOCK180 Signaling Complex Is Antagonized by Rap1 in Migrating

- NBT-II Cells." *The Journal of Biological Chemistry* 279 (43) (October 22): 44490–6. doi:10.1074/jbc.M405144200.
<http://www.ncbi.nlm.nih.gov/pubmed/15308668>.
- Vicente-Manzanares, Miguel, Xuefei Ma, Robert S Adelstein, and Alan Rick Horwitz. 2009. "Non-Muscle Myosin II Takes Centre Stage in Cell Adhesion and Migration." *Nature Reviews. Molecular Cell Biology* 10 (11) (November): 778–90.
- Watanabe, M, M Dykes-Hoberg, V C Culotta, D L Price, P C Wong, and J D Rothstein. 2001. "Histological Evidence of Protein Aggregation in Mutant SOD1 Transgenic Mice and in Amyotrophic Lateral Sclerosis Neural Tissues." *Neurobiology of Disease* 8 (6) (December): 933–41.
- Wegorzewska, Iga, Shaughn Bell, Nigel J Cairns, Timothy M Miller, and Robert H Baloh. 2009. "TDP-43 Mutant Transgenic Mice Develop Features of ALS and Frontotemporal Lobar Degeneration." *Proceedings of the National Academy of Sciences of the United States of America* 106 (44) (November 3): 18809–14.
- Wiedemann, F R, K Winkler, a V Kuznetsov, C Bartels, S Vielhaber, H Feistner, and W S Kunz. 1998. "Impairment of Mitochondrial Function in Skeletal Muscle of Patients with Amyotrophic Lateral Sclerosis." *Journal of the Neurological Sciences* 156 (1) (January): 65–72.
- Wijesekera, Lokesh C, and P Nigel Leigh. 2009. "Amyotrophic Lateral Sclerosis." *Orphanet Journal of Rare Diseases* 4 (January).
- Wils, Hans, Gernot Kleinberger, Jonathan Janssens, Sandra Pereson, Geert Joris, Ivy Cuijt, Veerle Smits, Chantal Ceuterick-de Groote, Christine Van Broeckhoven, and Samir Kumar-Singh. 2010. "TDP-43 Transgenic Mice Develop Spastic Paralysis and Neuronal Inclusions Characteristic of ALS and Frontotemporal Lobar Degeneration." *Proceedings of the National Academy of Sciences of the United States of America* 107 (8) (February 23): 3858–63.
- Winton, Matthew J, Lionel M Igaz, Margaret M Wong, Linda K Kwong, John Q Trojanowski, and Virginia M-Y Lee. 2008. "Disturbance of Nuclear and Cytoplasmic TAR DNA-Binding Protein (TDP-43) Induces Disease-like Redistribution, Sequestration, and Aggregate Formation." *The Journal of Biological Chemistry* 283 (19) (May 9): 13302–9.
- Worms, P M. 2001. "The Epidemiology of Motor Neuron Diseases: A Review of Recent Studies." *Journal of the Neurological Sciences* 191 (1-2) (October 15): 3–9.
- Wu, Lien-Szu, Wei-Cheng Cheng, Shin-Chen Hou, Yu-Ting Yan, Si-Tse Jiang, and C-K James Shen. 2010. "TDP-43, a Neuro-Pathosignature Factor, Is Essential for Early Mouse Embryogenesis." *Genesis (New York, N.Y. : 2000)* 48 (1) (January): 56–62.

- Wu, Lien-Szu, Wei-Cheng Cheng, and C-K James Shen. 2012. "Targeted Depletion of TDP-43 Expression in the Spinal Cord Motor Neurons Leads to the Development of Amyotrophic Lateral Sclerosis-like Phenotypes in Mice." *The Journal of Biological Chemistry* 287 (33) (August 10): 27335–44.
- Xiao, Shangxi, Sonja Tjostheim, Teresa Sanelli, Jesse R McLean, Patrick Horne, Yuxin Fan, John Ravits, Michael J Strong, and Janice Robertson. 2008. "An Aggregate-Inducing Peripherin Isoform Generated through Intron Retention Is Upregulated in Amyotrophic Lateral Sclerosis and Associated with Disease Pathology." *The Journal of Neuroscience : The Official Journal of the Society for Neuroscience* 28 (8) (February 20): 1833–40.
- Xu, Ya-Fei, Tania F Gendron, Yong-Jie Zhang, Wen-Lang Lin, Simon D'Alton, Hong Sheng, Monica Castanedes Casey, et al. 2010. "Wild-Type Human TDP-43 Expression Causes TDP-43 Phosphorylation, Mitochondrial Aggregation, Motor Deficits, and Early Mortality in Transgenic Mice." *The Journal of Neuroscience : The Official Journal of the Society for Neuroscience* 30 (32) (August 11): 10851–9.
- Xu, Ya-Fei, Yong-Jie Zhang, Wen-Lang Lin, Xiangkun Cao, Caroline Stetler, Dennis W Dickson, Jada Lewis, and Leonard Petrucelli. 2011. "Expression of Mutant TDP-43 Induces Neuronal Dysfunction in Transgenic Mice." *Molecular Neurodegeneration* 6 (1) (January): 73.
- Yuan, Aidong, Takahiro Sasaki, Asok Kumar, Corrinne M Peterhoff, Mala V Rao, Ronald K Liem, Jean-Pierre Julien, and Ralph A Nixon. 2012. "Peripherin Is a Subunit of Peripheral Nerve Neurofilaments: Implications for Differential Vulnerability of CNS and PNS Axons." *The Journal of Neuroscience* 32 (25): 8501–8508.
- Zaidel-Bar, Ronen, Ron Milo, Zvi Kam, and Benjamin Geiger. 2007. "A Paxillin Tyrosine Phosphorylation Switch Regulates the Assembly and Form of Cell-Matrix Adhesions." *Journal of Cell Science* 120 (Pt 1) (January 1): 137–48.
- Zanetta, Chiara, Monica Nizzardo, Chiara Simone, Erika Monguzzi, Nereo Bresolin, Giacomo P Comi, and Stefania Corti. 2014. "Molecular Therapeutic Strategies for Spinal Muscular Atrophies: Current and Future Clinical Trials." *Clinical Therapeutics* 36 (1) (January 1): 128–40.
- ZELKO, IGOR N, THOMAS J MARIANI, and RODNEY J FOLZ. 2002. "Superoxide Dismutase Multigene Family: A Comparison of the CuZn-SOD (SOD1), Mn-SOD (SOD2), and EC-SOD (SOD3) Gene Structures, Evolution, and Expression." *Free Radical Biology & Medicine* 33 (3): 337–349.
- Zhang, Yong-Jie, Thomas Caulfield, Ya-Fei Xu, Tania F Gendron, Jaime Hubbard, Caroline Stetler, Hiroki Sasaguri, et al. 2013. "The Dual Functions of the Extreme N-Terminus of TDP-43 in Regulating Its Biological Activity and Inclusion Formation." *Human Molecular Genetics* 22 (15) (August 1): 3112–22.

Zhang, Yong-Jie, Ya-Fei Xu, Casey Cook, Tania F Gendron, Paul Roettges, Christopher D Link, Wen-Lang Lin, et al. 2009. "Aberrant Cleavage of TDP-43 Enhances Aggregation and Cellular Toxicity." *Proceedings of the National Academy of Sciences of the United States of America* 106 (18) (May 5): 7607–12.

DYNC1H1 mutation alters transport kinetics and ERK1/2-cFos signalling in a mouse model of distal spinal muscular atrophy

Caroline A. Garrett,¹ Muruj Barri,¹ Anna Kuta,² Violetta Soura,¹ Wenhan Deng,¹ Elizabeth M. C. Fisher,² Giampietro Schiavo³ and Majid Hafezparast¹

¹ School of Life Sciences, University of Sussex, Falmer, Brighton, BN1 9QG, UK

² Department of Neurodegenerative Disease, Institute of Neurology, University College London, Queen Square, London WC1N 3BG, UK

³ Sobell Department of Motor Neuroscience and Movement Disorders, Institute of Neurology, University College London, Queen Square, London WC1N 3BG, UK

Correspondence to: Majid Hafezparast,
School of Life Sciences,
University of Sussex,
Falmer, Brighton,
BN1 9QG, UK
E-mail: m.hafezparast@sussex.ac.uk

Mutations in the gene encoding the heavy chain subunit (DYNC1H1) of cytoplasmic dynein cause spinal muscular atrophy with lower extremity predominance, Charcot–Marie–Tooth disease and intellectual disability. We used the legs at odd angles (Loa) (DYNC1H1^{F580Y}) mouse model for spinal muscular atrophy with lower extremity predominance and a combination of live-cell imaging and biochemical assays to show that the velocity of dynein-dependent microtubule minus-end (towards the nucleus) movement of EGF and BDNF induced signalling endosomes is significantly reduced in Loa embryonic fibroblasts and motor neurons. At the same time, the number of the plus-end (towards the cell periphery) moving endosomes is increased in the mutant cells. As a result, the extracellular signal-regulated kinases (ERK) 1/2 activation and c-Fos expression are altered in both mutant cell types, but the motor neurons exhibit a strikingly abnormal ERK1/2 and c-Fos response to serum-starvation induced stress. These data highlight the cell-type specific ERK1/2 response as a possible contributory factor in the neuropathological nature of *Dync1h1* mutations, despite generic aberrant kinetics in both cell types, providing an explanation for how mutations in the ubiquitously expressed DYNC1H1 cause neuron-specific disease.

Keywords: cytoplasmic dynein; endosomes; Loa; motor neurons; ERK 1/2

Abbreviations: ERK1/2 = extracellular signal-regulated kinases 1/2; Loa = Legs at odd angles; MAP kinase = mitogen activated protein kinase; MEF = mouse embryonic fibroblast

Introduction

Cytoplasmic dynein is a 1.2 MDa complex responsible for the majority of minus-end (also referred to as retrograde in axons) directed microtubule-dependent trafficking within cells. At the core of the complex is a DYNC1H1 heavy chain homodimer.

The C-terminus of each dynein heavy chain is the site of ATP hydrolysis, essential for powering the complex along microtubules, which also bind at this end. Amino acids 446–800 in the N-terminus (residues 1 to ~1400), associate with dynein intermediate and light intermediate chains (Tynan *et al.*, 2000), plus accessory and regulatory proteins including dynactin (reviewed in Vallee

Received January 17, 2014. Revised February 21, 2014. Accepted March 5, 2014.

© The Author (2014). Published by Oxford University Press on behalf of the Guarantors of Brain. All rights reserved.

For Permissions, please email: journals.permissions@oup.com

et al., 2012; Carter, 2013; Kikkawa, 2013; Schiavo *et al.*, 2013). These components are required for dynein function and/or help confer specificity for cargo, including organelles such as endosomes, which have vital roles in responding to external stimuli, environmental fluctuations, stressors and implementing general housekeeping functions.

Mutations within dynein heavy chain are causative for spinal muscular atrophy with lower extremity predominance (SMA-LED), Charcot-Marie-Tooth disease type 2 (CMT2), microcephaly, and intellectual disability (reviewed in Schiavo *et al.*, 2013). Moreover, mutations in the p150 subunit of dynactin have been linked to motor neuron disease (Puls *et al.*, 2003, 2005; Munch *et al.*, 2004). The severity of these diseases highlights the importance of cytoplasmic dynein in cellular function; however, the overlapping symptoms of many of the aforementioned diseases poses the question of why there is a disproportionate impact on neuronal cells. To address this question we compared two distinct cell types: mouse embryonic fibroblasts (MEFs); and motor neurons, both derived from the legs at odd angles (*Loa*) mouse.

Loa mice carry a F580Y mutation within the dynein heavy chain. *Dync1h1^{Loa/Loa}* (from here on referred to as *Loa/Loa*) mice have severe loss of spinal anterior horn motor neurons (Hafezparast *et al.*, 2003), impairment of cortical lamination (Ori-McKenney and Vallee, 2011) and die perinatally, whereas *Dync1h1^{+/-Loa}* (referred to as *+/-Loa*) manifest an age-related neuromuscular deficit and sensory neuropathy (Hafezparast *et al.*, 2003; Chen *et al.*, 2007; Ilieva *et al.*, 2008; Wiggins *et al.*, 2012). At the molecular level, the *Loa* mutation has been shown to adversely affect dynein complex assembly (Deng *et al.*, 2010) and processivity (Ori-McKenney *et al.*, 2010).

Motor neurons rely on trophic signalling mediated by TrkB (tropomyosin-related kinase B)—a member of the receptor tyrosine kinase (RTK) superfamily—for survival. Upon binding of brain-derived neurotrophic factor (BDNF) to TrkB, the receptor is activated by dimerization and autophosphorylation. The catalytically active BDNF-TrkB complexes are then endocytosed and the progression of these 'signalling endosomes' along the endocytic pathway for signalling in the soma, followed by degradation in the lysosomes requires the activity of cytoplasmic dynein (Yano *et al.*, 2001; Bhattacharyya *et al.*, 2002; Heerssen *et al.*, 2004). Similar to the BDNF-TrkB trafficking in motor neurons, activation of epidermal growth factor receptor (EGFR) by EGF triggers the endocytosis of EGF-EGFR complexes and their targeting to late endosomes/lysosomes in a dynein-dependent process in MEFs (Bonifacino and Traub, 2003).

The function of the signalling endosomes is particularly important in neuronal cells in which receptor-ligand complexes undergo long range translocation from nerve termini to the cell body using the dynein-dependent retrograde transport machinery. Activation of the BDNF or EGF receptors initiates a transient signalling cascade involving Ras and Raf upstream of extracellular signal-regulated kinases (ERK) 1/2. On the other hand, sustained activation of ERK1/2 involves CT10 regulator of kinase (CRK) adaptor proteins and the small GTP protein RAP1 (Nguyen *et al.*, 1993). BDNF also stimulates additional intracellular signalling cascades including phospholipase C γ (PLC γ) and phosphoinositide 3-kinase (PI3K) (reviewed in Harrington and Ginty, 2013).

Moreover, transient and sustained activation of ERK1/2 in neuronal cells have been shown to alter their morphological characteristics and cellular differentiation (Tanaka *et al.*, 1993; Ji *et al.*, 2010). Downstream of ERK1/2, transcription of the immediate early gene *c-Fos* can be promoted through ELK1. *c-Fos* dimerizes with *c-Jun* to form the AP1 complex to initiate transcription of genes important for cell survival, growth, proliferation and differentiation. Owing to the location of the *Loa* mutation, it would be reasonable to predict that a delayed degradation of the signal due to an impairment of receptor-ligand complex trafficking to the lysosomes would likely lead to prolonged activation of ERK1/2 and an increase in immediate early gene expression.

Thus, to explore the cell-type specific effects of the *Loa* mutation, we specifically looked at the endocytic trafficking of BDNF and EGF and their associated ERK1/2 signalling (Burke *et al.*, 2001; Howe *et al.*, 2001; Howe and Mobley, 2004; Driskell *et al.*, 2007; Taub *et al.*, 2007; Schuster *et al.*, 2011). Our data show generic aberrations in transport kinetics in two distinct cell types MEFs and motor neurons, both of which harbour the *Loa* mutation. Endosomes in *Loa* cells display reduced minus-end directed velocity and increased plus-end directed movements. The *Loa* phenotype is associated with increased numbers of side-steps that are both slower and smaller than in wild-type cells. We also show cell-specific alterations in ERK1/2 and the immediate early gene *c-Fos* expression. Specifically, *Loa/Loa* MEFs are not affected by serum deprivation, as measured by ERK1/2 levels in comparison with wild-type cells, and in response to EGF stimulation ERK1/2 activation is sustained. In contrast, *Loa* motor neurons are markedly more affected by nutrient deprivation than their wild-type controls, as shown by increased levels of phosphorylated ERK1/2 (pERK1/2) and *c-Fos*. We suggest that these cell-type specific responses are contributing mechanisms resulting in the *DYNC1H1* neuropathogenesis that arise from mutations in this ubiquitously expressed protein.

Materials and methods

Cell culture

MEFs were cultured in Dulbecco's modified Eagles medium supplemented with 15% HyClone™ foetal bovine serum (Fisher), 1% penicillin/streptomycin and 1% L-glutamine. They were cultured at 37°C with 3% O₂ and 5% CO₂. Starvation media consisted of the same without the addition of serum. EGF stimulation (20 ng/ml) was applied as a continuous stimulation for biochemical analysis. A 10-min pulse of EGF-Alexa Fluor® 546 (Molecular Probes) was used for live-cell imaging, or EGF-Alexa Fluor® 555 (Invitrogen) for fixed-cell imaging.

Embryonic Day 13 motor neurons were dissected and cultured based on an established protocol (Camu and Henderson, 1994) with minor modifications; motor neuron culture media (Neurobasal® media plus B27 supplement, 0.25% glutamine, 0.1% β -mercaptoethanol, 2% horse serum, 0.1% fungizone, 1% penicillin/streptomycin) were supplemented with 0.1 ng/ml GDNF (R&D systems), 0.5 ng/ml CNTF and 0.1 ng/ml BDNF (Invitrogen). Cells were incubated at 37°C in 5% CO₂. During 2-h serum starvation, cells were incubated in motor neuron culture medium lacking horse serum.

For live-cell imaging motor neurons or MEFs were rinsed and replenished with warmed motor neuron or MEF starvation medium, respectively; however, the Neurobasal® medium or Dulbecco's modified Eagles medium was replaced in both instances with Leibovitz L-15 CO₂-independent medium. Imaging was undertaken at 37°C. BDNF at a concentration of 5 ng/ml was used for motor neuron stimulation and this was applied either as a 10-min 'pulse' for live-cell imaging or left as 'continuous' stimulation for cell signalling assays. pHrodo™ dextran 40 µg/ml (Invitrogen) was simultaneously applied for live-cell imaging. For ERK1/2 and JNK inhibition assays, cells were treated with 10 µM and 50 µM of U0126 and SP600125 (both from Sigma), respectively.

Cell lysis and λ-protein phosphatase treatment

Cells were lysed in 25 mM Tris-HCl, pH 7.4, 150 mM NaCl, 1 mM EDTA, 1% NP40, 5% glycerol, protease and phosphatase inhibitors 1 and 2 (Sigma). Lysates were incubated on ice for 15 min before centrifugation. Protein concentration was determined using BCA Protein Assay Kit (Pierce). In selected cases, equal volumes were loaded onto electrophoresis gels for western blot. For λ-protein phosphatase assays, 1.5×10^6 wild-type MEFs were seeded in complete medium and incubated overnight as described above. Next day, the complete culture medium was replaced with serum-free medium and after 2 h the cells were stimulated with 20 ng/ml of EGF for 60 min. Cells were lysed as above, but without the phosphatase inhibitors. Twenty micrograms of each protein sample was treated with 2000 units of λ-protein phosphatase (New England Biolabs) in a 50 µl reaction volume at 30°C for 30 min.

Immunoblotting and immunocytochemistry

Cell lysates were loaded onto 4–12% NuPAGE® gradient gels and proteins detected using the following antibodies: phospho-p44/42 MAPK (ERK1/2) Thr202/Tyr204 (New England Biolabs), c-Fos (Santa Cruz Biotechnology), phospho-SAPK/JNK T183/Y185 (Cell Signalling), β-actin (Sigma), phospho-XRCC1S485/T488 (Bethyl Laboratories). A c-Fos blocking peptide was utilized following manufacturer's instructions (Santa Cruz). Quantification was carried out using ImageJ gel analysis software. Data were transferred to Excel and GraphPad Prism for data representation and two-tailed *t*-test or two-way ANOVA analysis.

Cells were fixed in 4% paraformaldehyde before permeabilization with 0.1% Triton™ X-100, blocked for 60 min in 2% bovine serum albumin and then stained with anti-α-tubulin (Upstate). Coverslips were mounted using ProLong® gold anti-fade reagent with DAPI (Invitrogen).

Image acquisition and analysis

For EGF particle assays, fixed-cell images were obtained using FITC, Cy5 and DAPI filters. Deconvolved images were analysed with the aid of standard ImageJ programs. Probability distribution frequencies were plotted by measuring EGF-containing vesicle size in pixels and converting this to µm² from the pixels:microns microscopy image scale.

Live-cell images were collected at 10 min and 30 min post-removal of growth factor and tracks required an overall net retrograde migration to be included in the analysis. Live cell images were captured every 2 s for 1 min duration in MEFs and every 3 s for 2 min in

motor neurons, using a Delta Vision microscope (Applied Precision). The ImageJ 'Manual Tracking' plugin (Fabrice P. Cordelieres) was used to gather track information. Both live cell imaging and fixed cell assays were analysed with the assistance of Excel and GraphPad Prism using the Mann-Whitney U-test. Kymographs were produced using software from the MacBiophotonics ImageJ for microscopy users.

Results

Aberrant transport kinetics in *Loa/Loa* mouse embryonic fibroblasts

To examine the impact of the *Loa* mutation on growth factor transport and degradation, we serum starved wild-type and *Loa/Loa* MEFs for 2 h before stimulation with 20 ng/ml EGF-Alexa Fluor® 555 for 10 min. MEFs were then rinsed and fixed for imaging after 0-, 10-, 30- and 60-min chase. To ensure differences were not a reflection of cell size (Rishal *et al.*, 2012), the analysed areas of 37 cells from each genotype were compared. No significant difference was found (wild-type = $2057 \pm 89.3 \mu\text{m}^2$ and *Loa/Loa* = $1992 \pm 86.7 \mu\text{m}^2$) (Fig. 1C).

At 0-min chase both wild-type and *Loa/Loa* had similar numbers of EGF-containing endosomes: 746.9 ± 103.8 and 781.9 ± 74.9 , respectively (Fig. 1A and B). However by 10-min chase there were significantly more EGF-AlexaFluor® 555 containing vesicles remaining in *Loa/Loa* when compared to wild-type cells (wild-type = 454.6 ± 34.6 , *Loa/Loa* = 753.5 ± 71.2 , $P = 0.0014$).

By 30-min a distinct reduction in particle numbers in both genotypes was apparent, although, quantification remained higher in *Loa/Loa* than in wild-type (289.5 ± 29.3 and $231.529.3 \pm 26.9$, respectively). The 60-min chase highlighted significance once again with wild-type particles having reduced to 108 ± 10.1 and *Loa/Loa* to only 148.1 ± 9.9 ($P = 0.0152$).

Due to the prominent difference in EGF-containing vesicles at 10 min we sought to distinguish between delayed convergence of early endosomes and a delay in EGF degradation. We then plotted the probability distributions of EGF-positive vesicles as a function of the area of EGF-containing organelles. In wild-type MEFs endosome size was greater than in *Loa/Loa* at both 0- and 30-min chase; however, by 60-min this difference was less marked (Fig. 1D). As early endosomes increase in size during fusion events leading to their maturation, these data suggest that the *Loa* mutation delays the progression of endocytosed EGF along the endocytic pathway.

To gain further insight into endosomal movement, live-cell imaging was carried out. We used an assay similar to that shown in Fig. 1, but instead of fixing the cells, they were rinsed, left in CO₂-independent media at 37°C and chased for 10 and 30 min (Fig. 2A–D). Minus-end directed transport velocity is conventionally measured as positive movements towards the nucleus whereas plus-end directed transport velocity is represented as negative.

Initial observations of the minus-end directed movements identified a distinct lack of fast carriers moving at velocities above 2 µm/s in *Loa/Loa*, and 60% less moving at velocities above 1 µm/s at both time points (Fig. 2C). In both genotypes, the majority of displacements occurred at speeds below 0.25 µm/s.

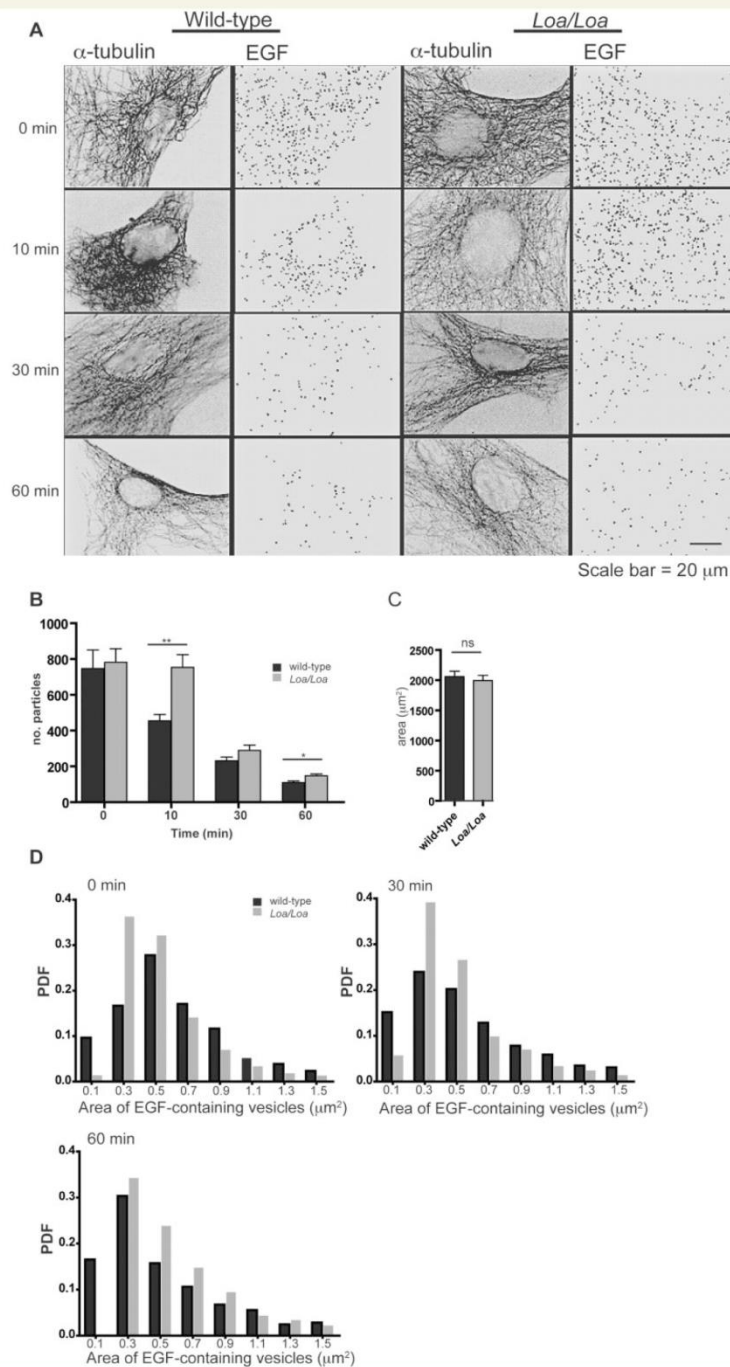


Figure 1 EGF-Alexa Fluor[®] 555 processing is altered in *Loa* MEFs. (A) Representative images of EGF-Alexa Fluor[®] 555 in wild-type and *Loa/Loa* MEFs after a 10-min pulse. Images taken at 0-, 10-, 30- and 60-min chase show increased numbers of EGF-containing vesicles in *Loa/Loa* compared with wild-type MEFs over time. Scale bar = 20 μ m. (B) Quantification of the number of EGF-Alexa Fluor[®] 555 vesicles remaining in MEFs at each chase time (asterisks represent *P*-values of *P* = 0.001 at 10 min and 0.015 at 60 min; *n* = 15). (C) Average area analysed for vesicle counting was the same in wild-type and *Loa/Loa* MEFs, *n* = 37. (D) Histograms depicting a probability distribution frequency (PDF) of area of vesicles containing labelled EGF. After EGF stimulation, *Loa/Loa* MEFs show a delay in forming large vesicles.

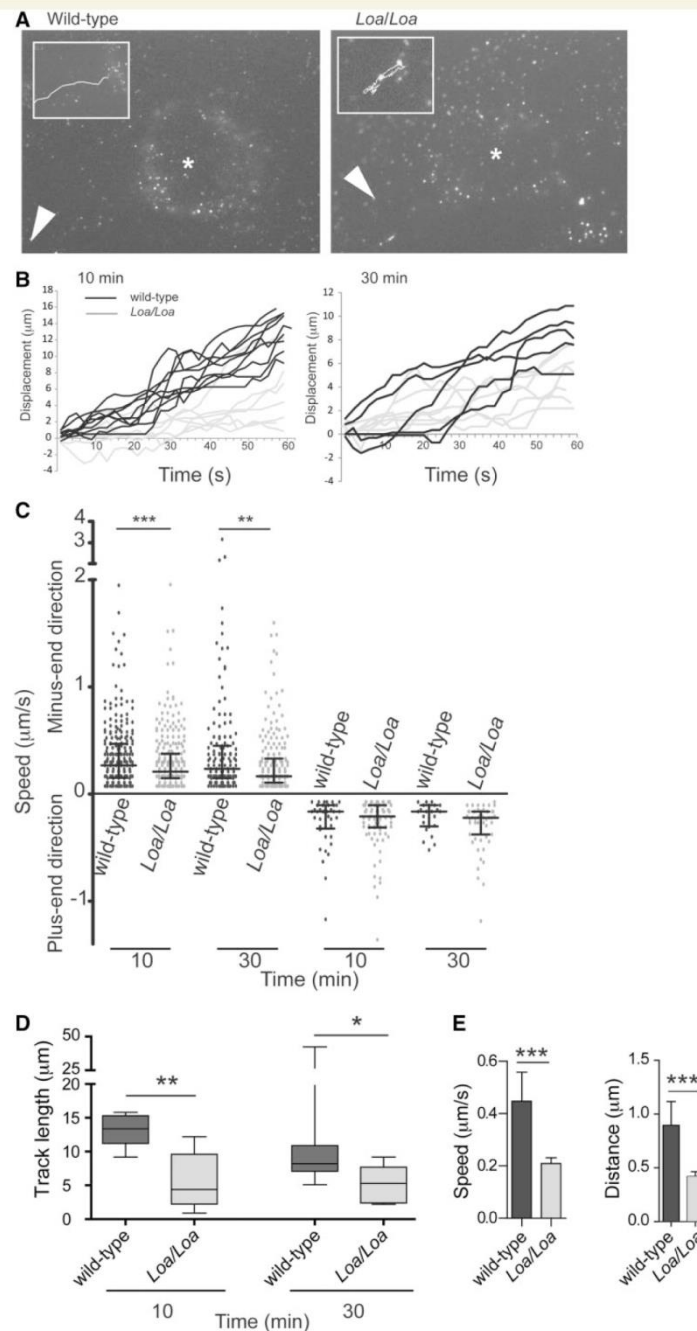


Figure 2 Endosome trafficking is aberrant in *Loa*. (A) Representative tracks from wild-type and *Loa/Loa* MEFs. Arrowheads and asterisks indicate the tracked endosomes and nuclei, respectively. As shown in the magnified insets, the *Loa/Loa* path seems shorter and more ambiguous than in wild-type. (B) Representative track displacements in wild-type and *Loa/Loa* at 10- and 30-min chase. (C) The velocity of dynein-dependent minus-end directed transport is reduced in *Loa/Loa* at 10 ($P < 0.0001$) and 30 min ($P < 0.007$) chase. Plus-end directed transport velocity is not significantly different across the genotypes. (D) Overall track length is reduced in *Loa/Loa* compared with wild-type at 10- and 30-min chase ($P = 0.002$ at 10 min and $P = 0.044$ at 30 min). Data analysed are from sample sizes of $n = 349$ movements for wild-type from 13 tracks (four cells) and 419 movements from 15 tracks (five cells), for *Loa/Loa*, at 10 min; $n = 232$ movements for wild-type from eight tracks (five cells) and 337 movements for *Loa/Loa* from 12 tracks (six cells). (E) Sideward velocity and distance travelled are reduced in *Loa/Loa* compared with wild-type ($P = 0.0003$ for both assays). For sideward speed and distance analysis, measurements from 10-min and 30-min chase were pooled together. Asterisks represent the indicated P -values.

This was not surprising as many endosomes remain static for several seconds before longer movements were made.

Analysis of dynein-dependent minus-end directed transport velocities highlighted a significant shift towards slower velocity in *Loa/Loa* at 10- and 30-min chase (Fig. 2C). The minus-end directed movements were significantly slower in *Loa/Loa* compared with that in wild-type MEFs at both 10 min (medians of 0.11 $\mu\text{m/s}$ and 0.17 $\mu\text{m/s}$, respectively; $P < 0.0001$) and 30 min (medians of 0.07 $\mu\text{m/s}$ and 0.11 $\mu\text{m/s}$, respectively; $P < 0.007$). Plus-end directed transport velocities were not significantly different across the time points or genotypes (Fig. 2C).

To determine whether the altered dynamics of *Loa/Loa* velocities compared with wild-type was sufficient to affect the overall displacement, all tracks (76% of total tracks measured) that remained in focus for at least 96% of frames were analysed. Displacement in *Loa/Loa* was significantly reduced when compared to wild-type at 10-min chase ($P = 0.002$) (Fig. 2D). Track length ranged from 9.2 μm to 15.8 μm (median 13.4 μm) in wild-type and 0.90 μm to 12.2 μm (median 4.4 μm) in *Loa/Loa*. This trend remained at 30 min, with wild-type total displacement ranging from 5.1 μm to 42.3 μm (median 8.2 μm) and 2.2 μm to 9.2 μm (median 5.3 μm) in *Loa/Loa*.

In addition, we found movements that were neither minus-end nor plus-end directed, but sideward relative to the main travelling direction of the endosome. Approximately 5% of wild-type movements across both chase points were classed as side steps, whereas in *Loa/Loa* this number was increased to ~7%. When measuring the velocity and distance of these sideward movements it was found that in *Loa/Loa* the velocity was significantly slower [means of 0.45 (± 0.1 SEM) $\mu\text{m/s}$ and 0.21 (± 0.02 SEM) $\mu\text{m/s}$ for wild-type and *Loa/Loa*, respectively, $P = 0.0003$] and movement was over shorter distances [0.90 (± 0.2 SEM) μm and 0.42 (± 0.5 SEM) μm for wild-type and *Loa/Loa*, respectively ($P = 0.0003$)] (Fig. 2E). These might represent the off-axis movements of dynein, observed by several studies (Reck-Peterson *et al.*, 2006; DeWitt *et al.*, 2012; Qiu *et al.*, 2012), in which dynein uses its flexibility to step on neighbouring protofilaments and microtubules for navigating through a crowded cytoplasm. The observed slower sideward speed and smaller distance travelled by dynein in *Loa* MEFs might reflect a reduced flexibility of dynein to reach neighbouring microtubules, caused by impaired dynein complex assembly and binding to dynactin (Deng *et al.*, 2010).

Together these data show aberrant transport kinetics in *Loa/Loa* MEFs, which may delay maturation of early endosomes into late endosomes and multivesicular bodies.

Transport kinetics are impaired in +/Loa motor neurons

As cytoplasmic dynein mutations have been linked to several neurological diseases (Puls *et al.*, 2003, 2005; Munch *et al.*, 2004; Schiavo *et al.*, 2013), it was important to assess transport parameters in neuronal cells. Although deficits in both motor and sensory neurons have been identified in the *Loa* mouse, we chose

to examine intracellular transport kinetics within motor neurons, to advance our earlier work (Hafezparast *et al.*, 2003), which identified impairments in axonal retrograde transport in this cell type.

Embryonic motor neurons were dissected at embryonic Day 13 and maintained in culture for 1 week. The motor neurons isolated from *Loa* embryos looked indistinguishable from those derived from embryos expressing green fluorescent protein (GFP) under control of the motor neuron specific transcription factor, homeobox gene 9 (*Hb9*). Only cells with large soma, single axon and complex dendritic arborization were analysed.

Because of the dominant nature of dynein mutations in human pathologies (Schiavo *et al.*, 2013), we decided that +/*Loa* motor neurons would be more representative of human disease than *Loa/Loa* and thus carried out live-cell imaging comparisons between wild-type and +/*Loa*.

For live-cell tracking in motor neuron axons, and in the absence of a fluorophore-conjugated BDNF, we starved the motor neurons for 2 h and stimulated them with native BDNF to induce activation of its receptor TrkB and increase the BDNF-TrkB-containing endosomal pool. We then used the pH-sensitive fluorescent dye pHrodoTM linked to dextran to detect the endosomes and analyse the global axonal retrograde transport of endocytic and phagocytic organelles in these cells. The majority of tracking was from DIC (differential interference contrast) images of axons in which vesicles >500 nm were clearly visible, many co-located with pHrodoTM fluorescence.

The range of velocities observed in motor neuron tracking experiments were similar to those seen in MEFs, from $-1.36 \mu\text{m/s}$ (plus-end directed, or anterograde) to $\sim 2 \mu\text{m/s}$ (minus-end directed or retrograde) and were in agreement with those observed in our previous study (Kieran *et al.*, 2005). There were also fewer endosomes moving at speeds in excess of 1 $\mu\text{m/s}$ in +/*Loa* compared to wild-type at both 10- and 30-min chase (30% less at 10 min and 70% less at 30 min) (Fig. 3A and B).

Minus-end directed movements identified a trend for slower velocities in +/*Loa* at 10 min, which reached significance at 30-min chase ($P = 0.01$) (Fig. 3B). Moreover, the velocity of minus-end directed movements decreased in +/*Loa* between 10 and 30-min chase ($P = 0.0001$). Interestingly, although plus-end directed velocity was not significantly different between the genotypes at 10-min chase, there was an increased propensity towards movements in this direction in +/*Loa* compared to wild-type motor neurons, which had a distinct lack of such movements during the 30-min chase (Fig. 3B). Upper and lower ranges of track displacement in +/*Loa* compared to wild-type were distinctly different at 10 min (20.4 μm to 61.0 μm in wild-type and 4.2 μm to 55.4 μm in +/*Loa*) and at 30-min chase (14.1 μm to 42.2 μm for wild-type and 7.6 μm to 33 μm for +/*Loa*) (Fig. 3C). These differences, however, were not statistically significant ($P = 0.2$ and 0.9, respectively).

Taken together, these data show that the *Loa* mutation causes a significant impairment to endosomal axonal transport, determining not only a reduction in minus-end directed velocity and overall track length, but also a tendency towards increased plus-end movements.

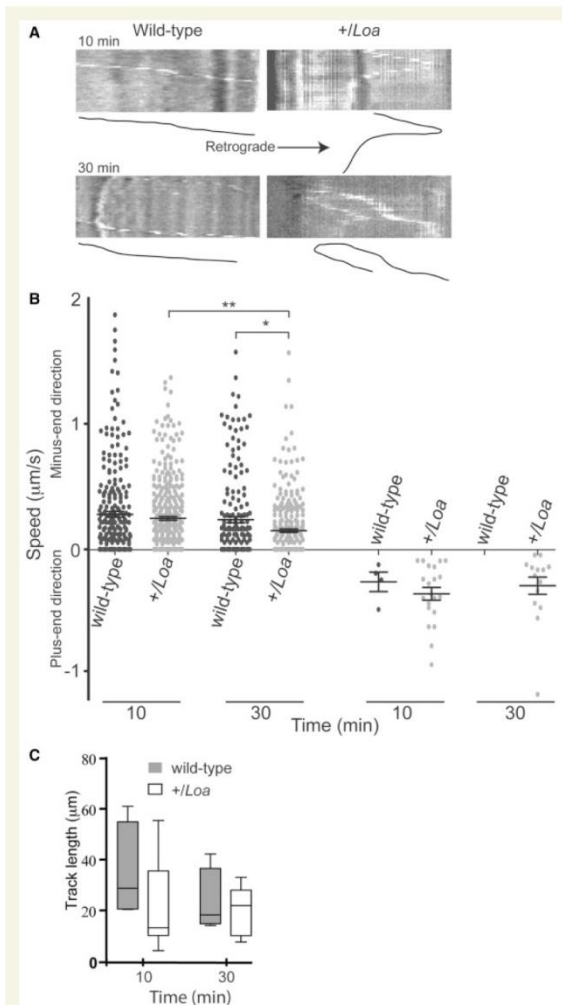


Figure 3 Global retrograde trafficking after BDNF stimulation is aberrant in *Loa* motor neurons. (A) Kymographs of trafficking in wild-type and +/Loa motor neurons. Kymograph traces are shown schematically as lines under each kymograph. (B) Minus-end and plus-end directed movements in wild-type and +/Loa motor neurons. The velocity of dynein-dependent minus-end directed transport is significantly reduced in +/Loa at 30-min chase, when compared with wild-type ($P = 0.01$) and between the 10-min and 30-min chase times ($P = 0.0001$). Plus-end directed movements are more frequent in +/Loa motor neurons, but velocities are not significantly different between the genotypes. (C) Track displacement at 10- and 30-min chase. For each chase time analysed 'n' values were as follows; at 10 min, wild-type $n = 257$ movements from eight tracks (five cells) and $n = 373$ displacements from eight tracks (seven cells) for +/Loa. At 30-min wild-type $n = 194$ movements from seven tracks (three cells) and for +/Loa, $n = 314$ movements from eight tracks (three cells). Asterisks represent the indicated P -values.

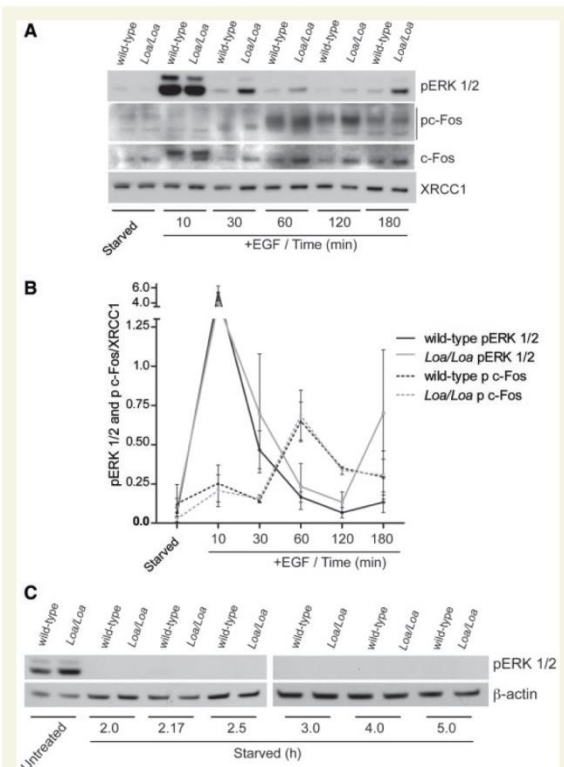


Figure 4 Aberrant signalling in *Loa/Loa* MEFs. (A) ERK1/2 activation is prolonged in *Loa/Loa* up to and including 180 min, without significant increases in c-Fos and pc-Fos levels compared with wild-type. (B) Quantification of pERK1/2 and pc-Fos levels in *Loa/Loa* and wild-type. pERK1/2 declines before there is an increase in pc-Fos. (C) In comparison to untreated controls, wild-type and *Loa/Loa* MEF cells did not have detectable levels of pERK1/2 during 5 h of serum starvation.

Prolonged ERK1/2 activation and increased c-Fos in *Loa/Loa* mouse embryonic fibroblasts

We next investigated the effect of the delayed trafficking of the EGF-containing signalling endosomes on ERK1/2, a well-established downstream effector of EGF-initiated signalling. Wild-type and *Loa/Loa* MEFs were serum starved for 2 h before stimulation with 20 ng/ml EGF. Cells were lysed at 10, 30, 60, 120, and 180 min after stimulation.

A peak of phosphorylated ERK1/2 (pERK1/2) was apparent at 10 min post-stimulation. This activation was transient and by 60 min the wild-type levels of pERK1/2 were nearing those of the serum-starved control (Fig. 4A and B). In contrast, pERK1/2 activation was found to be more sustained in *Loa/Loa* such that at 30 min post-stimulation there was on average a 1.5-fold increase in pERK1/2 levels in *Loa/Loa*. At 60, 120, and 180 min, the fold increases were 1.4, 1.2, and 5.3, respectively, when compared to wild-type (Fig. 4A and B). Two-way ANOVA analysis of these

data revealed that EGF had a significant effect over all the time points for both genotypes [$F(5,24) = 61.11$, mean square = 19.35, $P < 0.0001$], and although there was a trend in higher levels of pERK1/2 in *Loa/Loa* MEFs, its overall effect did not reach significance [$F(1,24) = 0.13$, mean square = 0.04, $P = 0.73$]. There was no significant interaction between the genotypes and time [$F(5,24) = 2.12$, mean square = 0.67, $P = 0.1$], indicating that the pattern of response to EGF is similar in *Loa* and wild-type MEFs over the observed time points. Mitogens are known to induce a biphasic activation of pERK1/2 (reviewed in [Meloche and Pouyssegur, 2007](#)) and the second peak at 120-min time point is likely to represent this phenomenon (Fig. 4B).

It was important to clarify that the tendency towards increased levels of pERK in mutant MEFs was not due to prolonged serum starvation, as in some cell types, ERK1/2 is known to become active in response to serum deprivation to induced autophagy for cell survival. To test this, MEFs were serum-starved for up to 5 h and pERK1/2 levels were examined. pERK1/2 was not detectable in the serum starved MEFs when compared to the untreated control cells (Fig. 4C).

Prolonged activation of ERK1/2 led us to hypothesize that the expression of immediate early genes could be significantly increased as a result. As pERK1/2, through ELK1, activates the transcription of c-Fos we chose to compare the levels of c-Fos in wild-type and *Loa/Loa* MEFs stimulated with EGF. The identity of the c-Fos bands on western blots was determined by λ -protein phosphatase treatment and c-Fos blocking peptide (Supplementary Fig. 1).

Although low in abundance, we found 0.9-fold less c-Fos in *Loa/Loa* compared with wild-type after serum starvation (Fig. 4A and Supplementary Fig. 2). However, after EGF stimulation c-Fos levels were increased in *Loa/Loa* on average by 1.5-, 1.6-, 1.6-, 1.1- and 2.1-fold at 10, 30, 60, 120, and 180 min, respectively.

As expected levels of stable phosphorylated c-Fos (pc-Fos) were found to be low after serum starvation of the MEFs. After stimulation with 20 ng/ml EGF a delay of at least 30 min was observed before the Ras/Raf/ERK pathway resulted in a significant increase in c-Fos phosphorylation (Fig. 4B); however, the c-Fos phosphorylation profile in *Loa/Loa* was similar to wild-type (Fig. 4B). Moreover, we did not observe any difference in proliferation rates between *Loa/Loa* and wild-type MEFs (Supplementary Fig. 3).

In summary, these data reveal that the F580Y mutation in *Dync1h1* results in a trend towards prolonged activation of ERK1/2 in response to EGF stimulation in *Loa* MEFs. Moreover, this prolonged activation is not a result of serum starvation, but likely due to delayed maturation and trafficking of EGF-containing endosomes towards the lysosome. These changes are, however, not dramatic enough to have a significant impact on transcriptional and phosphorylation profiles of c-Fos or the proliferation response in *Loa* MEFs.

Aberrant ERK1/2 activation and increased c-Fos in +/Loa motor neurons

As BDNF-stimulated *Loa* motor neurons showed impaired transport kinetics similar to EGF-stimulated MEFs, we asked whether

the ERK1/2 signalling in mutant motor neurons would display the same pattern as in the corresponding MEFs. Thus, after 2 h serum starvation and subsequent stimulation with 5 ng/ml BDNF, motor neuron extracts were collected from wild-type and +/Loa at 10 and 30 min post-stimulation (Fig. 5A). pERK1/2 levels were found to be similar between wild-type and +/Loa in untreated cells (Fig. 5A and B). After 2 h starvation, however, there was a trend for pERK1/2 levels in +/Loa to be higher than those of wild-type. After BDNF stimulation, there is a slight decline in pERK1/2 levels in the wild-type over the time course of the experiment. BDNF stimulation also results in increased pERK1/2 levels in +/Loa motor neurons, which are higher than in wild-type neurons (Fig. 5A and B). This trend remains the same at longer BDNF stimulation times (Fig. 5C), indicating that BDNF-induces sustained activation of ERK1/2 in +/Loa motor neurons over time.

When looking at c-Fos activation after serum starvation and BDNF stimulation, we observed increased pc-Fos levels in starved and BDNF stimulated motor neurons in both genotypes (Fig. 5D and E). Although the increase in pc-Fos after serum starvation coincided with increased pERK1/2, we questioned whether the rise in pERK1/2 in +/Loa was sufficient to produce the dramatic pc-Fos peak observed. As nutrient deprivation is a major stress on cells, we examined whether the activation of c-Fos in motor neurons during starvation is induced by ERK1/2 and/or the stress activated protein kinases JNK and p38. To this end we treated wild-type motor neurons with U0126 (a highly selective inhibitor of MEK1 and MEK2 upstream of ERK1/2) and SP600125 (a selective inhibitor of JNK). As shown in Fig. 5F, ERK1/2 inhibition attenuates c-Fos activation during serum starvation and after stimulation with BDNF, relative to the cells with no inhibitors at each time point, whereas JNK inhibition appears to have the opposite effect, leading to increased pc-Fos levels. Analysis of p38 levels showed a slight increase in active p38 dimers in both genotypes, which declined after BDNF stimulation before increasing again after 8 h, likely as a result of depletion of BDNF (Supplementary Fig. 4). Collectively, these data show that in motor neurons, starvation induces activation of ERK1/2 and c-Fos to a greater extent in +/Loa than in wild-type. Moreover, BDNF-induced activation of ERK1/2 and c-Fos is also greater in +/Loa motor neurons when compared with wild-type.

Discussion

We began by identifying altered EGF trafficking in MEFs isolated from wild-type and *Loa/Loa* embryos. We show increased numbers of EGF vesicles in *Loa/Loa* with the greatest difference at 10-min chase (Fig. 1A and B). Moreover, we show a reduction in size of EGF-containing vesicles, which is apparent immediately following the pulse with EGF (Fig. 1D). During this time frame clathrin-coated vesicles, after uncoating, fuse to early endosomes that then mature to late endosomes. These data therefore suggest delayed endosomal maturation in the mutant cells. This observation is intriguing as we showed previously that the *Loa* mutation impairs the interactions of dynein heavy chain with dynein intermediate and light intermediate chains, and consequently p150 subunit of dynactin (Deng *et al.*, 2010). As dynein intermediate

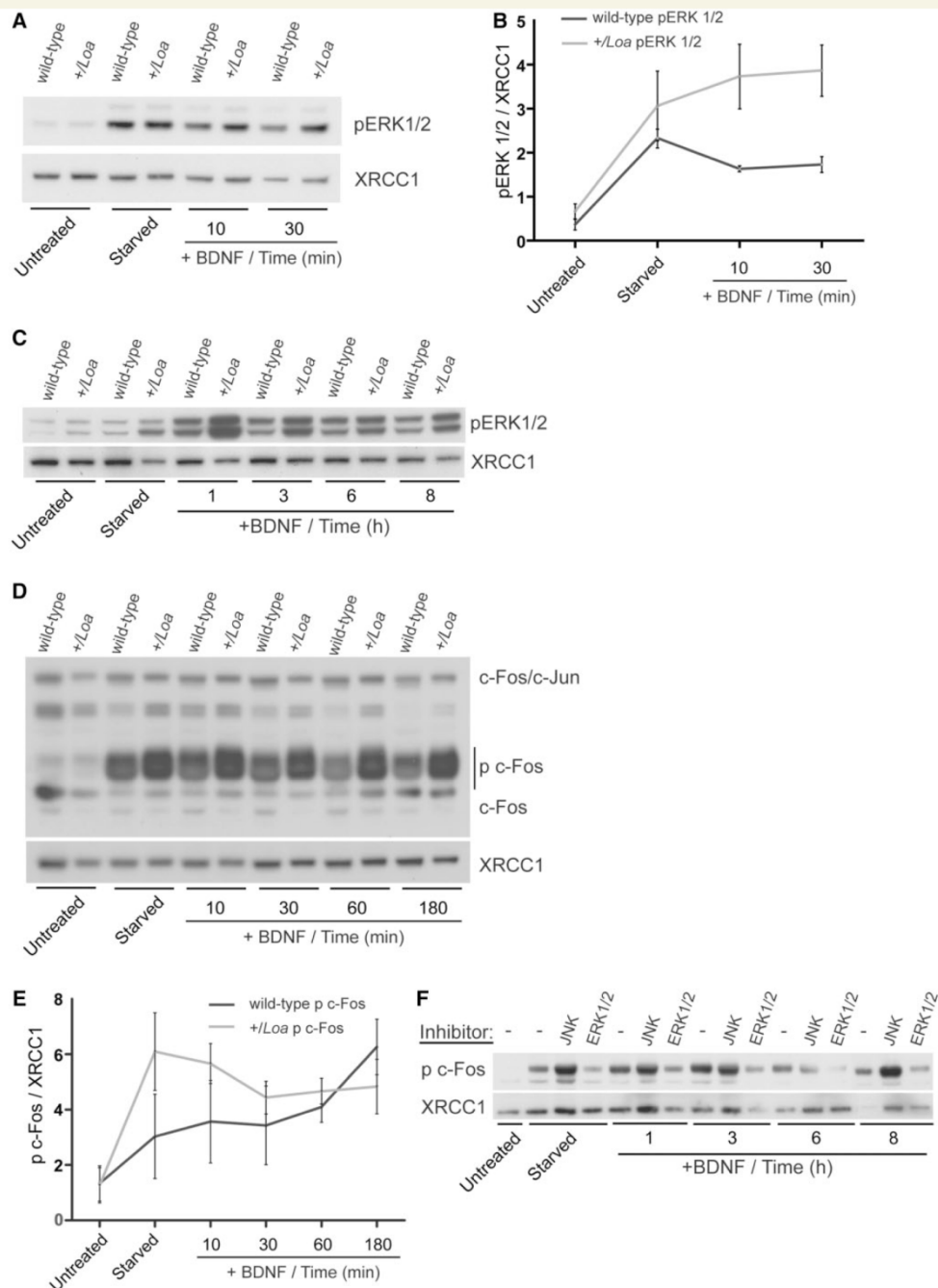


Figure 5 ERK1/2 and c-Fos are activated by serum starvation in motor neurons. (A and B) pERK1/2 levels in +/Loa motor neurons are higher than wild-type after serum starvation. +/Loa does respond to BDNF activation, but not to the same extent as wild-type. (C) Western blot analysis shows higher levels of phospho-ERK1/2 in +/Loa than in the wild-type motor neurons following starvation. BDNF stimulation, further increases active ERK1/2 in +/Loa motor neurons than the wild-type. A marked increase of p-ERK1/2 is observed at 1 h after stimulation with BDNF, which declines over time. (D) p c-Fos is dramatically induced by serum deprivation, followed by a decline in response to BDNF stimulation in +/Loa motor neurons. (E) Quantification of p c-Fos in D. (F) ERK1/2 inhibition attenuates c-Fos induction during starvation and after stimulating with BDNF. Western blot shows levels of p c-Fos in wild-type motor neurons at different time points: with no inhibition, JNK inhibitor SP600125, or U0126 MEK/ERK1/2 inhibitor. XRCC1 was used as a loading control and its signals were used to normalize ERK1/2 and c-Fos levels.

and light intermediate chains, and dynactin are regulators of cargo attachment, this finding may be indicative of impaired cargo docking to the dynein complex, delaying subsequent transport along microtubules. At later time points increased numbers of EGF-containing vesicles are found in *Loa/Loa* compared to wild-type MEFs, suggesting a delay in EGF-EGFR trafficking to the lysosomes.

Our live cell data show reduced minus-end transport velocity in *Loa* MEFs and motor neurons and an increased likelihood of plus-end directed steps. This finding bears the question of how a mutation in the cargo binding domain of dynein may affect the speed of the cargo. The answer to this question could lie in our previous finding that the *Loa* mutation impairs the interaction of dynein with dynactin (Deng *et al.*, 2010). It is also known that the number of simultaneously engaged motors affects the cargo's average speed by influencing its run length and duration of the pauses (Ori-McKenney *et al.*, 2010; and reviewed in Xu and Gross, 2012). Thus the reduced velocity of the signalling endosomes in *Loa* cells could be the result of recruitment of fewer dynein motors to the endosomes at any given time. Moreover, cooperation between cytoplasmic dynein and its opposing motor kinesin have been established including the suggestion that one cannot function in the absence of the other (Ally *et al.*, 2009). However, this is not always the case (Flores-Rodriguez *et al.*, 2011) and thus it is plausible that aberrant binding of endocytic cargo to dynein in *Loa* may result in a tug-of-war between kinesin and mutant dynein being balanced more favourably towards the plus-end directed movement of kinesin than it is towards the minus-end directed dynein movement.

A consequence of the impaired trafficking of signalling endosomes harbouring EGF in the *Loa* MEFs is a trend in higher levels of pERK1/2 without significant impact on its downstream effector c-Fos. In motor neurons, however, serum starvation induced activation of ERK1/2 in both genotypes. This is an intriguing observation as it demonstrates that the response of motor neurons to serum withdrawal is completely different to that of the MEFs. In contrast to MEFs, serum deprivation led to a striking activation of ERK1/2 and induction of active c-Fos particularly in *Loa* motor neurons (Fig. 5A–E). Moreover, the elevated pc-Fos is mainly a response to ERK1/2 activation and not the stress activated protein kinases JNK or p38, as unlike the ERK1/2 inhibitor U0126, JNK inhibitor SP600125 did not reduce pc-Fos in serum-starved motor neurons. These data indicate that firstly, the post-mitotic motor neurons are specifically equipped with a stress response machinery which activates the ERK1/2 MAP kinase pathway and their downstream effectors such as c-Fos, possibly as a protective mechanism against cellular stress; secondly, this response is exacerbated in *+/Loa* motor neurons. Moreover, on the addition of BDNF, the pERK1/2 and p-cFos levels remain higher in *+/Loa* motor neurons.

Almeida *et al.* (2005) have shown that BDNF induces transient ERK1/2 activity to promote survival in response to glutamate toxicity. In contrast, persistent ERK1/2 activity caused by glutamate-induced oxidative stress causes cell death in cortical neurons (Stanciu *et al.*, 2000; Luo and DeFranco, 2006). It is therefore possible that the tendency of *+/Loa* motor neurons to increased and persistent levels of pERK1/2, caused by impaired trafficking and delayed transport of signalling endosomes towards lysosomes,

contribute to neuronal cell death by making them more susceptible to physiological insults such as oxidative stress.

In a recent study, Mitchell *et al.* (2012) have demonstrated that in cortical neurons, BDNF stimulation of ERK1/2 leads to phosphorylation of dynein intermediate chains and recruitment of cytoplasmic dynein to signalling endosomes for retrograde transport. Intriguingly, we have previously shown that the amount of phosphorylated dynein intermediate chains is reduced in brain tissues of *Loa/Loa* mice (Deng *et al.*, 2010). Thus, it is plausible that the increased binding affinity of dynein heavy chain to the intermediate chains (Deng *et al.*, 2010) could lead to conformational changes in the intermediate chains, which may impede their phosphorylation following ERK1/2 activation by BDNF. Consequently, this would lead to impaired dynein-mediated transport of endosomes to lysosomes for degradation and consequently further accumulation of active ERK1/2 as reported here.

We have identified aberrant transport kinetics in *Loa*, which are not cell-type specific. However the effect on cell signalling is substantially different between mitotic MEFs and terminally-differentiated motor neurons. This work shows for the first time a direct comparison between two very different cell types and identifies underlying signalling events that might contribute to the neurological phenotypes of *Dync1h1* mutations.

Funding

We would like to thank funding supports from the Biotechnology and Biological Sciences Research Council (BBSRC) for M.H., C.G. and W.D., the National centre for the replacement, refinement, and reduction of animals in research (NC3Rs) for M.H. and W.D., the Saudi Arabia Ministry of Higher Education for M.B., University of Sussex for V.S.; E.F., A.K. and G.S. were supported by the ENDOCYTE Research and Training Network funded by the European Union, G.S. is funded by Cancer Research UK, and G.S. and E.F. are funded by the UK Motor Neuron Disease Association.

Supplementary material

Supplementary material is available at *Brain* online.

References

- Ally S, Larson AG, Barlan K, Rice SE, Gelfand VI. Opposite-polarity motors activate one another to trigger cargo transport in live cells. *J Cell Biol* 2009; 187: 1071–82.
- Almeida RD, Manadas BJ, Melo CV, Gomes JR, Mendes CS, Graos MM, *et al.* Neuroprotection by BDNF against glutamate-induced apoptotic cell death is mediated by ERK and PI3-kinase pathways. *Cell Death Differ* 2005; 12: 1329–43.
- Bhattacharyya A, Watson FL, Pomeroy SL, Zhang YZ, Stiles CD, Segal RA. High-resolution imaging demonstrates dynein-based vesicular transport of activated Trk receptors. *J Neurobiol* 2002; 51: 302–12.
- Bonifacino JS, Traub LM. Signals for sorting of transmembrane proteins to endosomes and lysosomes. *Annu Rev Biochem* 2003; 72: 395–447.

- Burke P, Schooler K, Wiley HS. Regulation of epidermal growth factor receptor signaling by endocytosis and intracellular trafficking. *Mol Biol Cell* 2001; 12: 1897–910.
- Camu W, Henderson CE. Rapid purification of embryonic rat motoneurons: an *in vitro* model for studying MND/ALS pathogenesis. *J Neurol Sci* 1994; 124 (Suppl): 73–4.
- Carter AP. Crystal clear insights into how the dynein motor moves. *J Cell Sci* 2013; 126: 705–13.
- Chen XJ, Levedakou EN, Millen KJ, Wollmann RL, Soliven B, Popko B. Proprioceptive sensory neuropathy in mice with a mutation in the cytoplasmic Dynein heavy chain 1 gene. *J Neurosci* 2007; 27: 14515–24.
- Deng W, Garrett C, Dombert B, Soura V, Banks G, Fisher EM, et al. Neurodegenerative mutation in cytoplasmic dynein alters its organization and dynein-dynactin and dynein-kinesin interactions. *J Biol Chem* 2010; 285: 39922–34.
- DeWitt MA, Chang AY, Combs PA, Yildiz A. Cytoplasmic dynein moves through uncoordinated stepping of the AAA+ ring domains. *Science* 2012; 335: 221–5.
- Driskell OJ, Mironov A, Allan VJ, Woodman PG. Dynein is required for receptor sorting and the morphogenesis of early endosomes. *Nat Cell Biol* 2007; 9: 113–20.
- Flores-Rodriguez N, Rogers SS, Kenwright DA, Waigh TA, Woodman PG, Allan VJ. Roles of dynein and dynactin in early endosome dynamics revealed using automated tracking and global analysis. *PLoS One* 2011; 6: e24479.
- Hafezparast M, Klocke R, Ruhrberg C, Marquardt A, Ahmad-Annuar A, Bowen S, et al. Mutations in dynein link motor neuron degeneration to defects in retrograde transport. *Science* 2003; 300: 808–12.
- Harrington AW, Ginty DD. Long-distance retrograde neurotrophic factor signalling in neurons. *Nat Rev Neurosci* 2013; 14: 177–87.
- Heerssen HM, Pazyra MF, Segal RA. Dynein motors transport activated Trks to promote survival of target-dependent neurons. *Nat Neurosci* 2004; 7: 596–604.
- Howe CL, Mobley WC. Signaling endosome hypothesis: a cellular mechanism for long distance communication. *J Neurobiol* 2004; 58: 207–16.
- Howe CL, Valletta JS, Rusnak AS, Mobley WC. NGF signaling from clathrin-coated vesicles: evidence that signaling endosomes serve as a platform for the Ras-MAPK pathway. *Neuron* 2001; 32: 801–14.
- Ilieva HS, Yamanaka K, Malkmus S, Kakinohana O, Yaksh T, Marsala M, et al. Mutant dynein (Loa) triggers proprioceptive axon loss that extends survival only in the SOD1 ALS model with highest motor neuron death. *Proc Natl Acad Sci USA* 2008; 105: 12599–604.
- Ji Y, Lu Y, Yang F, Shen W, Tang TT, Feng L, et al. Acute and gradual increases in BDNF concentration elicit distinct signaling and functions in neurons. *Nat Neurosci* 2010; 13: 302–9.
- Kieran D, Hafezparast M, Bohnert S, Dick JR, Martin J, Schiavo G, et al. A mutation in dynein rescues axonal transport defects and extends the life span of ALS mice. *J Cell Biol* 2005; 169: 561–7.
- Kikkawa M. Big steps toward understanding dynein. *J Cell Biol* 2013; 202: 15–23.
- Luo Y, DeFranco DB. Opposing roles for ERK1/2 in neuronal oxidative toxicity: distinct mechanisms of ERK1/2 action at early versus late phases of oxidative stress. *J Biol Chem* 2006; 281: 16436–42.
- Meloche S, Pouyssegur J. The ERK1/2 mitogen-activated protein kinase pathway as a master regulator of the G1- to S-phase transition. *Oncogene* 2007; 26: 3227–39.
- Mitchell DJ, Blasier KR, Jeffery ED, Ross MW, Pullikuth AK, Suo D, et al. Trk activation of the ERK1/2 kinase pathway stimulates intermediate chain phosphorylation and recruits cytoplasmic dynein to signaling endosomes for retrograde axonal transport. *J Neurosci* 2012; 32: 15495–510.
- Munch C, Sedlmeier R, Meyer T, Homberg V, Sperfeld AD, Kurt A, et al. Point mutations of the p150 subunit of dynactin (DCTN1) gene in ALS. *Neurology* 2004; 63: 724–6.
- Nguyen TT, Scimeca JC, Filloux C, Peraldi P, Carpentier JL, Van Obberghen E. Co-regulation of the mitogen-activated protein kinase, extracellular signal-regulated kinase 1, and the 90-kDa ribosomal S6 kinase in PC12 cells. Distinct effects of the neurotrophic factor, nerve growth factor, and the mitogenic factor, epidermal growth factor. *J Biol Chem* 1993; 268: 9803–10.
- Ori-McKenney KM, Vallee RB. Neuronal migration defects in the Loa dynein mutant mouse. *Neural Dev* 2011; 6: 26.
- Ori-McKenney KM, Xu J, Gross SP, Vallee RB. A cytoplasmic dynein tail mutation impairs motor processivity. *Nat Cell Biol* 2010; 12: 1228–34.
- Puls I, Jonnakuty C, LaMonte BH, Holzbaur EL, Tokito M, Mann E, et al. Mutant dynactin in motor neuron disease. *Nat Genet* 2003; 33: 455–6.
- Puls I, Oh SJ, Sumner CJ, Wallace KE, Floeter MK, Mann EA, et al. Distal spinal and bulbar muscular atrophy caused by dynactin mutation. *Ann Neurol* 2005; 57: 687–94.
- Qiu W, Derr ND, Goodman BS, Villa E, Wu D, Shih W, et al. Dynein achieves processive motion using both stochastic and coordinated stepping. *Nat Struct Mol Biol* 2012; 19: 193–200.
- Reck-Peterson SL, Yildiz A, Carter AP, Gennerich A, Zhang N, Vale RD. Single-molecule analysis of dynein processivity and stepping behavior. *Cell* 2006; 126: 335–48.
- Rishal I, Kam N, Perry RB, Shinder V, Fisher EM, Schiavo G, et al. A motor-driven mechanism for cell-length sensing. *Cell Rep* 2012; 1: 608–16.
- Schiavo G, Greensmith L, Hafezparast M, Fisher EM. Cytoplasmic dynein heavy chain: the servant of many masters. *Trends Neurosci* 2013; 36: 641–51.
- Schuster M, Lipowsky R, Assmann MA, Lenz P, Steinberg G. Transient binding of dynein controls bidirectional long-range motility of early endosomes. *Proc Natl Acad Sci USA* 2011; 108: 3618–23.
- Stanciu M, Wang Y, Kentor R, Burke N, Watkins S, Kress G, et al. Persistent activation of ERK contributes to glutamate-induced oxidative toxicity in a neuronal cell line and primary cortical neuron cultures. *J Biol Chem* 2000; 275: 12200–6.
- Tanaka S, Hattori S, Kurata T, Nagashima K, Fukui Y, Nakamura S, et al. Both the SH2 and SH3 domains of human CRK protein are required for neuronal differentiation of PC12 cells. *Mol Cell Biol* 1993; 13: 4409–15.
- Taub N, Teis D, Ebner HL, Hess MW, Huber LA. Late endosomal traffic of the epidermal growth factor receptor ensures spatial and temporal fidelity of mitogen-activated protein kinase signaling. *Mol Biol Cell* 2007; 18: 4698–710.
- Tynan SH, Gee MA, Vallee RB. Distinct but overlapping sites within the cytoplasmic dynein heavy chain for dimerization and for intermediate chain and light intermediate chain binding. *J Biol Chem* 2000; 275: 32769–74.
- Vallee RB, McKenney RJ, Ori-McKenney KM. Multiple modes of cytoplasmic dynein regulation. *Nat Cell Biol* 2012; 14: 224–30.
- Wiggins LM, Kuta A, Stevens JC, Fisher EM, von Bartheld CS. A novel phenotype for the dynein heavy chain mutation Loa: altered dendritic morphology, organelle density, and reduced numbers of trigeminal motoneurons. *J Comp Neurol* 2012; 520: 2757–73.
- Xu J, Gross SP. Biophysics of dynein *in vivo*. In: King SM, editor. *Dyneins: structure, biology and disease*. London: Academic Press; 2012. p. 191–206.
- Yano H, Lee FS, Kong H, Chuang J, Arevalo J, Perez P, et al. Association of Trk neurotrophin receptors with components of the cytoplasmic dynein motor. *J Neurosci* 2001; 21: RC125.